

NASA CR-134778

D6-42392

LOW-SPEED AND ANGLE-OF-ATTACK EFFECTS ON SONIC AND NEAR-SONIC INLETS

T. E. Hickcox, R. L. Lawrence, J. Syberg, and D. R. Wiley

March 1975

(NASA-CR-134778) LOW SPEED AND ANGLE OF ATTACK EFFECTS ON SONIC AND NEAR-SONIC INLETS (Boeing Commercial Airplane Co., Seattle) 207 p HC \$7.25	N75-19184
CSCL 01A	Unclas 14663
	G3/02

Prepared under contract NAS3-18035 by
Boeing Commercial Airplane Company
P.O. Box 3707
Seattle, Washington 98124



for
Lewis Research Center
NATIONAL AERONAUTICS AND SPACE ADMINISTRATION

1. Report No. NASA CR-134778	2. Government Accession No.	3. Recipient's Catalog No.	
4. Title and Subtitle LOW-SPEED AND ANGLE-OF-ATTACK EFFECTS ON SONIC AND NEAR-SONIC INLETS		5. Report Date March 1975	6. Performing Organization Code
		8. Performing Organization Report No. D6-42392	
7. Author(s) T. E. Hickcox, R. L. Lawrence, J. Syberg, and D. R. Wiley		10. Work Unit No.	
9. Performing Organization Name and Address Boeing Commercial Airplane Company P.O. Box 3707 Seattle, Washington 98124		11. Contract or Grant No. NAS3-18035	
		13. Type of Report and Period Covered Contractor Report	
12. Sponsoring Agency Name and Address National Aeronautics and Space Administration Washington, D.C. 20546		14. Sponsoring Agency Code	
		15. Supplementary Notes Project Manager, Robert J. Antl, V/STOL and Noise Division, NASA Lewis Research Center, Cleveland, Ohio	
16. Abstract The objective of the analysis and tests described in this report is to determine the effects of forward velocity and angle of attack on sonic and near-sonic inlet aerodynamic performance penalties and acoustic suppression characteristics. The tests demonstrate that translating centerbody and radial vane sonic inlets, and QCSEE high throat Mach number inlets, can be designed to operate effectively at forward speed and moderate angle of attack with good performance and noise suppression capability. The performance and noise suppression trends demonstrated at forward speed and 0° inflow angle are similar to those measured in an earlier investigation in which the same inlets were operated statically in front of model scale fans. The radial vane inlet at approach (vanes installed) shows aerodynamic performance penalties larger than those exhibited by the translating centerbody and QCSEE high Mach number inlets to obtain comparable noise reductions. Careful redesign of inlet lips has led to good aerodynamic performance at high angles of attack and crosswind for all inlets. Axisymmetric compressible flow analysis is shown to allow accurate prediction of sonic flow conditions, and thus to be an effective design tool.			
17. Key Words (Suggested by Author(s)) Noise attenuation Forward velocity Sonic inlets Near-sonic inlets Angle of attack		18. Distribution Statement Unclassified—unlimited	
19. Security Classif. (of this report) Unclassified	20. Security Classif. (of this page) Unclassified	21. No. of Pages 202	22. Price* \$3.00

TABLE OF CONTENTS

	Page
SUMMARY	1
INTRODUCTION	5
TEST APPARATUS	7
Inlet Test Models	7
Translating Centerbody Inlet	7
Radial Vane Inlet	7
QCSEE High Throat Mach Number Inlets	8
Test Facility	8
Inlet Locations in the Wind Tunnel	8
Siren Noise Source	9
Δ SPL Measurement Limitations	9
Instrumentation Sensors	11
Microphone Locations	11
Data Acquisition and Reduction	11
Performance Data	11
Acoustic Data	12
Test Procedures	14
ANALYTICAL INLET DESIGN	15
Sonic Inlets	15
QCSEE High Throat Mach Number Inlet	17
Diffuser Design	17
Lip Design	18
External Cowl Design	18
TEST RESULTS	19
Evaluation Criteria	19
Summary of Inlet Performance	20
Translating Centerbody Inlet	20
Radial Vane Inlet	20
QCSEE High Throat Mach Number Inlets	21
Detailed Results	21
Translating Centerbody Inlet	21
Radial Vane Inlet	26
QCSEE High Throat Mach Number Inlets	28
Dynamic Pressure Distortion	31
CONCLUSIONS	33
RECOMMENDATIONS	35

PRECEDING PAGE BLANK NOT FILMED

TABLE OF CONTENTS—Concluded

	Page
SYMBOLS	37
REFERENCES	39

LIST OF FIGURES

No.		Page
1	Inlet Concepts Investigated at Forward Speed and Angle of Attack	41
2	Typical Test Arrangement—Translating Centerbody Inlet A1 Installed at $\alpha = 0^\circ$	42
3	Variation of Recovery With Noise Reduction—Translating Centerbody Inlet A1 at $\alpha = 0^\circ$	43
4	Variation of Distortion With Noise Reduction—Translating Centerbody Inlet A1 at $\alpha = 0^\circ$	44
5	Variation of Recovery and Distortion With Noise Reduction—Translating Centerbody Inlets A1, A2, and A3 at $\alpha = 20^\circ$, $V = 185$ km/h (100 kn)	45
6	Variation of Recovery With Noise Reduction—Radial Vane Inlet B at $\alpha = 0^\circ$	46
7	Variation of Distortion With Noise Reduction—Radial Vane Inlet B at $\alpha = 0^\circ$	47
8	Variation of Recovery and Distortion With Noise Reduction—QCSEE High Mach Number Inlets C1, C4, and C5 at $\alpha = 0^\circ$, $V = 148$ km/h (80 kn)	48
9	Variation of Recovery and Distortion With Noise Reduction—QCSEE High Mach Number Inlets C1, C4, and C5 at $\alpha = 20^\circ$, $V = 306$ km/h (165 kn)	49
10	Inlet Model Parts	50
11	Translating Centerbody Inlets A1, A2, and A3—Approach and Takeoff Positions	51
12	Translating Centerbody Inlet A1 Approach—Pressure Instrumentation	53
13	Boundary Layer Rake Probe Locations	55
14	Radial Vane Inlet B—Pressure Instrumentation	57
15	Radial Vane Inlet B—Vane Cross Section	59
16	Radial Vane Inlet B—Static Pressure Taps	60
17	QCSEE High Mach Number Inlet C1—Pressure Instrumentation	61
18	QCSEE High Mach Number Inlets C2 and C2-A—Pressure Instrumentation	63
19	QCSEE High Mach Number Inlet C3—Pressure Instrumentation	65
20	QCSEE High Mach Number Inlet C4—Pressure Instrumentation	67
21	QCSEE High Mach Number Inlet C5—Pressure Instrumentation	69
22	Boeing 9-Ft by 9-Ft Low-Speed Wind Tunnel	71
23	Wind Tunnel Inlet Locations at Test Angles of Attack	72
24	Translating Centerbody Inlet A1 Takeoff— $\alpha = 0^\circ$	73
25	Radial Vane Inlet B Takeoff (Vanes Removed)— $\alpha = 0^\circ$	74
26	Translating Centerbody Inlet A1 Approach— $\alpha = 20^\circ$	75
27	Radial Vane Inlet B Approach— $\alpha = 35^\circ$	76
28	QCSEE High Mach Number Inlet C1— $\alpha = 50^\circ$	77
29	Translating Centerbody Inlet A1— $\alpha = 90^\circ$	78
30	Typical Measured Noise Signature—Siren Noise Signal SPL Versus Frequency	79
31	Siren ΔP and Siren Noise Flanking Path Effects (Inlet A1)	80
32	Effect of Inlet Airflow on SPL at Siren Monitor Microphone	81
33	Microphone Locations in the Wind Tunnel	82

LIST OF FIGURES—Continued

No.		Page
34	Data Reduction Flow Diagram	83
35	SPL and \overline{SPL} Versus C_D^* for Translating Centerbody Inlet A2— $\alpha = 20^\circ$, V = 185 km/h (100 kn)	84
36	Effect of Tunnel Wall Reflections on SPL for a Broadband, Omnidirectional Noise Source	85
37	Design Envelop for Sonic Inlet (Based on YC-14 Airplane)	86
38	Effect of Centerbody on Cowl Lip Mach Number Distribution for Translating Centerbody Inlet—Takeoff, V = 0, $M_2 = 0.514$	87
39	Surface Mach Number Distribution for Translating Centerbody Inlet— Takeoff, Configuration 1, V = 0	88
40	Surface Mach Number Distribution for Translating Centerbody Inlet— Approach, Configuration 1, V = 0	89
41	Lip Contraction Ratio Effects for Translating Centerbody Inlet—Takeoff, V = 0	90
42	Cowl Lip Shape Effects for Translating Centerbody Inlet—Takeoff, V = 0	91
43	Cowl Lip Shape Effects for Radial Vane Inlet—Takeoff, V = 0	92
44	Variation of Shape Factor and Surface Mach Number With Diffuser Shape—QCSEE High Mach Number Inlet	93
45	Effect of Lip Aspect Ratio on Lip Mach Numbers—QCSEE High Mach Number Inlet	94
46	Effect of Forward Speed on Cowl Lip Mach Number Distributions— QCSEE High Mach Number Inlet	95
47	Translating Centerbody Inlet A1—Performance Summary	96
48	Translating Centerbody Inlets A2 and A3 Approach— Performance Summary	97
49	Radial Vane Inlet B—Performance Summary	98
50	QCSEE High Mach Number Inlets C1, C4, and C5—Performance Summary	99
51	Boundary Layer Profiles for Translating Centerbody Inlet A1 at Takeoff— $\alpha = 90^\circ$, V = 65 km/h (35 kn)	100
52	Compressor Face Total Pressure Recovery Maps for Translating Centerbody Inlet A1 at Takeoff— $\alpha = 90^\circ$, V = 65 km/h (35 kn)	101
53	Inlet Cowl Mach Number Distribution for Translating Centerbody Inlet A1 at Takeoff— $\alpha = 90^\circ$, V = 65 km/h (35 kn)	103
54	Translating Centerbody Inlet A1 Distortion and Recovery Performance at Takeoff— $\alpha = 90^\circ$, V = 65 km/h (35 kn)	105
55	Compressor Face Total Pressure Recovery Maps for Translating Centerbody Inlet A1 at Approach— $\alpha = 0^\circ$	106
56	Compressor Face Total Pressure Recovery Maps for Translating Centerbody Inlet A1 at Approach—V = 0	107
57	Compressor Face Total Pressure Recovery Maps for Translating Centerbody Inlet A1 at Approach— $\alpha = 20^\circ$, V = 185 km/h (100 kn)	108
58	Translating Centerbody Inlet A1 Distortion and Recovery Performance at Approach	109

LIST OF FIGURES—Continued

No.	Page
59	Translating Centerbody Inlet A2 Distortion and Recovery Performance at Approach— $\alpha = 35^\circ$, $V = 148$ km/h (80 kn) 111
60	Compressor Face Total Pressure Recovery Maps for Translating Centerbody Inlet A2 at Approach— $\alpha = 35^\circ$, $V = 148$ km/h (80 kn) 112
61	Translating Centerbody Inlet A2 Distortion and Recovery Performance at Approach— $\alpha = 20^\circ$, $V = 259$ km/h (140 kn) 114
62	Translating Centerbody Inlet A2 Acoustic Performance at Approach— $\alpha = 20^\circ$, $V = 259$ km/h (140 kn) 115
63	Compressor Face Total Pressure Recovery Maps for Translating Centerbody Inlet A2 at Approach— $\alpha = 20^\circ$, $V = 259$ km/h (140 kn) 116
64	Translating Centerbody Inlet A3 Distortion and Recovery Performance at Approach— $\alpha = 35^\circ$, $V = 148$ km/h (80 kn) 118
65	Translating Centerbody Inlet A3 Distortion and Recovery Performance at Approach— $\alpha = 20^\circ$, $V = 259$ km/h (140 kn) 118
66	Translating Centerbody Inlet A3 Acoustic Performance at Approach— $\alpha = 20^\circ$, $V = 259$ km/h (140 kn) 119
67	Translating Centerbody Inlet A2 Distortion and Recovery Performance at Approach— $\alpha = 20^\circ$, $V = 185$ km/h (100 kn) 120
68	Translating Centerbody Inlet A2 Acoustic Performance at Approach— $\alpha = 20^\circ$, $V = 185$ km/h (100 kn) 121
69	Translating Centerbody Inlet A3 Distortion and Recovery Performance at Approach— $\alpha = 20^\circ$, $V = 185$ km/h (100 kn) 122
70	Translating Centerbody Inlet A3 Acoustic Performance at Approach— $\alpha = 20^\circ$, $V = 185$ km/h (100 kn) 123
71	Comparison of Analysis With Data for Translating Centerbody Inlet A1 at Takeoff— $V = 0$, $C_D^* = 0.963$ 124
72	Comparison of Analysis With Data for Translating Centerbody Inlet A1 at Takeoff— $V = 259$ km/h (140 kn), $C_D^* = 0.980$ 125
73	Comparison of Analysis With Data for Translating Centerbody Inlet A1 at Takeoff— $V = 324$ km/h (175 kn) for Analysis, $V = 306$ km/h (165 kn) for Data; $C_D^* = 0.980$ 126
74	Comparison of Analysis With Data for Translating Centerbody Inlet A1 at Approach— $V = 0$, $C_D^* = 0.914$ 127
75	Comparison of Analysis With Data for Translating Centerbody Inlet A1 at Approach— $V = 0$, $C_D^* = 0.963$ 128
76	Comparison of Analysis With Data for Translating Centerbody Inlet A1 at Approach— $V = 148$ km/h (80 kn), $C_D^* = 0.914$ 129
77	Comparison of Analysis With Data for Translating Centerbody Inlet A1 at Approach— $V = 259$ km/h (140 kn), $C_D^* = 0.941$ 130
78	Comparison of Analysis With Data for Translating Centerbody Inlet A1 Diffuser Separation— $\alpha = 0^\circ$ 131
79	Comparison of Analysis With Data for Translating Centerbody Inlet A1 Cowl Surface Mach Number Distribution at Takeoff— $\alpha = 90^\circ$, $V = 65$ km/h (35 kn), $C_D^* = 0.963$ 132

LIST OF FIGURES—Continued

No.		Page
80	Comparison of Cowl Surface Mach Number Distributions for Translating Centerbody Inlets A1, A2, and A3 at Approach, Windward Cowl— $\alpha = 35^\circ$, $V = 148$ km/h (80 kn)	133
81	Comparison of Centerbody Surface Mach Number Distributions for Translating Centerbody Inlets A1, A2, and A3 at Approach, Leeward Centerbody— $\alpha = 35^\circ$, $V = 148$ km/h (80 kn)	134
82	Radial Vane Inlet B Distortion and Recovery Performance at Takeoff— $\alpha = 0^\circ$, $V = 315$ km/h (170 kn)	135
83	Radial Vane Inlet B Distortion and Recovery Performance at Takeoff— $\alpha = 90^\circ$, $V = 65$ km/h (35 kn)	135
84	Radial Vane Inlet B Acoustic Performance at Takeoff— $\alpha = 20^\circ$, $V = 315$ km/h (170 kn)	136
85	Radial Vane Inlet B Acoustic Performance at Takeoff— $\alpha = 0^\circ$, $V = 315$ km/h (170 kn)	137
86	Radial Vane Inlet B Acoustic Performance at Takeoff— $\alpha = 20^\circ$, $V = 259$ km/h (140 kn)	138
87	Radial Vane Inlet B Acoustic Performance at Takeoff— $\alpha = 0^\circ$, $V = 0$	139
88	Compressor Face Total Pressure Recovery Maps for Radial Vane Inlet B at Takeoff— $\alpha = 90^\circ$, $V = 65$ km/h (35 kn)	140
89	Compressor Face Total Pressure Recovery Maps for Radial Vane Inlet B at Approach	142
90	Inlet Cowl Mach Number Distribution for Radial Vane Inlet B at Approach	144
91	Radial Vane Inlet B Distortion and Recovery Performance at Approach— $\alpha = 0^\circ$, $V = 148$ km/h (80 kn)	145
92	Radial Vane Inlet B Distortion and Recovery Performance at Approach— $\alpha = 35^\circ$, $V = 185$ km/h (100 kn)	145
93	Radial Vane Inlet B Acoustic Performance at Approach— $\alpha = 0^\circ$, $V = 0$	146
94	Radial Vane Inlet B Acoustic Performance at Approach— $\alpha = 0^\circ$, $V = 148$ km/h (80 kn)	147
95	Radial Vane Inlet B Acoustic Performance at Approach— $\alpha = 0^\circ$, $V = 185$ km/h (100 kn)	148
96	Radial Vane Inlet B Acoustic Performance at Approach— $\alpha = 0^\circ$, $V = 259$ km/h (140 kn)	149
97	Comparison of Analysis With Data for Radial Vane Inlet B at Takeoff— $V = 0$, $C_D^* = 0.941$	150
98	Comparison of Analysis With Data for Radial Vane Inlet B at Takeoff— $V = 0$, $C_D^* = 0.980$	151
99	Comparison of Analysis With Data for Radial Vane Inlet B at Takeoff— $V = 148$ km/h (80 kn), $C_D^* = 0.970$	152
100	Comparison of Analysis With Data for Radial Vane Inlet B at Takeoff— $V = 148$ km/h (80 kn), $C_D^* = 0.982$	153
101	Comparison of Analysis With Data for Radial Vane Inlet B at Takeoff— $V = 259$ km/h (140 kn), $C_D^* = 0.991$	154

LIST OF FIGURES—Continued

No.		Page
102	Comparison of Analysis With Data for Radial Vane Inlet B at Takeoff— $V = 324$ km/h (175 kn), $C_D^* = 0.991$	155
103	QCSEE High Mach Number Inlet C1 Distortion and Recovery Performance— $\alpha = 50^\circ$, $V = 148$ km/h (80 kn)	156
104	QCSEE High Mach Number Inlet C1 Distortion and Recovery Performance— $\alpha = 90^\circ$, $V = 65$ km/h (35 kn)	156
105	Compressor Face Total Pressure Recovery Maps for QCSEE High Mach Number Inlet C1— $\alpha = 50^\circ$, $V = 148$ km/h (80 kn)	157
106	Inlet Cowl Mach Number Distribution for QCSEE High Mach Number Inlet C1— $\alpha = 50^\circ$, $V = 148$ km/h (80 kn)	158
107	Compressor Face Total Pressure Recovery Maps for QCSEE High Mach Number Inlet C1— $\alpha = 0^\circ$, $V = 0$	159
108	QCSEE High Mach Number Inlet C1 Distortion and Recovery Performance— $\alpha = 0^\circ$, $V = 0$	160
109	QCSEE High Mach Number Inlet C Performance Summary— $\alpha = 50^\circ$, $\alpha = 90^\circ$	161
110	QCSEE High Mach Number Inlet C4 Distortion and Recovery Performance— $\alpha = 50^\circ$, $V = 148$ km/h (80 kn)	162
111	QCSEE High Mach Number Inlet C4 Distortion and Recovery Performance— $\alpha = 50^\circ$, $V = 140$ km/h (75 kn)	162
112	Compressor Face Total Pressure Recovery Maps for QCSEE High Mach Number Inlet C4 $\alpha = 50^\circ$, $V = 140$ km/h (75 kn)	163
113	QCSEE High Mach Number Inlet C5 Distortion and Recovery Performance— $\alpha = 50^\circ$, $V = 140$ km/h (75 kn)	164
114	Comparison of Analysis With Data for QCSEE High Mach Number Inlet C1— $V = 0$, $C_D^* = 0.959$	165
115	Comparison of Analysis With Data for QCSEE High Mach Number Inlet C1— $V = 148$ km/h (80 kn), $C_D^* = 0.959$	166
116	Comparison of Analysis With Data for QCSEE High Mach Number Inlet C4— $V = 0$, $C_D^* = 0.959$	167
117	Comparison of Analysis With Data for QCSEE High Mach Number Inlet C4— $V = 148$ km/h (80 kn), $C_D^* = 0.959$	168
118	Comparison of Analysis With Data for QCSEE High Mach Number Inlet C5— $V = 0$, $C_D^* = 0.959$	169
119	Comparison of Analysis With Data for QCSEE High Mach Number Inlet C5— $V = 148$ km/h (80 kn), $C_D^* = 0.959$	170
120	Cowl Mach Number Distributions for QCSEE High Mach Number Inlet C1— $\alpha = 50^\circ$, $V = 148$ km/h (80 kn), $C_D^* = 0.963$	171
121	Cowl Mach Number Distributions for QCSEE High Mach Number Inlet C1— $\alpha = 90^\circ$, $V = 65$ km/h (35 kn), $C_D^* = 0.963$	172
122	Cowl Mach Number Distributions for QCSEE High Mach Number Inlet C4— $\alpha = 50^\circ$, $V = 148$ km/h (80 kn), $C_D^* = 0.941$	173
123	Cowl Mach Number Distributions for QCSEE High Mach Number Inlet C4— $\alpha = 90^\circ$, $V = 65$ km/h (35 kn), $C_D^* = 0.963$	174

LIST OF FIGURES—Concluded

No.		Page
124	Cowl Mach Number Distributions for QCSEE High Mach Number Inlet C5— $\alpha = 50^\circ$, $V = 148$ km/h (80 kn), $C_D^* = 0.931$	175
125	Cowl Mach Number Distributions for QCSEE High Mach Number Inlet C5— $\alpha = 90^\circ$, $V = 65$ km/h (35 kn), $C_D^* = 0.946$	176
126	Effect of C_D^* on ΔP_{rms} for Translating Centerbody Inlets A2 and A3 at Approach— $\alpha = 20^\circ$	177
127	Effect of C_D^* on ΔP_{rms} for Radial Vane Inlet B at Approach— $\alpha = 0^\circ$	178
128	Effect of C_D^* on ΔP_{rms} for Radial Vane Inlet B at Takeoff— $\alpha = 0^\circ$	179
129	Effect of C_D^* on ΔP_{rms} for Radial Vane Inlet B at Takeoff— $\alpha = 20^\circ$	180
130	Effect of C_D^* on ΔP_{rms} for QCSEE High Mach Number Inlet C1— $\alpha = 0^\circ$	181

LIST OF TABLES

No.		Page
1	Translating Centerbody Inlet A Coordinates and Centerbody Translations	182
2	Translating Centerbody Inlet A Cross-Sectional Areas	183
3	Translating Centerbody Inlet A1 Static Pressure Taps	184
4	Radial Vane Inlet B Coordinates	186
5	Radial Vane Inlet B Static Pressure Taps	187
6	Principal Geometric Characteristics of QCSEE Inlets C1 through C5	189
7	QCSEE High Mach Number Inlet C Coordinates	190
8	QCSEE High Mach Number Inlet C Static Pressure Taps	195
9	Microphone Locations Relative to Inlet Entrance Center	198
10	Translating Centerbody Inlet A1 Operating Characteristics at Takeoff	198
11	Translating Centerbody Inlet A1 Airflow Characteristics at Takeoff— $\alpha = 90^\circ$, $V = 65$ km/h (35 kn)	199
12	Translating Centerbody Inlet A1 Operating Characteristics at Approach	199
13	Translating Centerbody Inlets A2 and A3 Operating Characteristics at Approach	200
14	Radial Vane Inlet B Operating Characteristics	201
15	QCSEE High Mach Number Inlet C Operating Characteristics	202

SUMMARY

The need to develop quieter airplanes for commercial airlines is being increasingly emphasized. To achieve substantial airplane noise reductions, especially as required for small-airport and night operations, it is important to be able to reduce radiated inlet noises by 10 to 30 dB or more; the sonic or high throat Mach number inlet concept has demonstrated this capability in static tests involving model scale fans. The objective of the analysis and tests described in this report is to determine the effects of forward velocity and angle of attack on sonic and near-sonic inlet aerodynamic performance penalties and acoustic suppression characteristics.

The tests demonstrate that translating centerbody and radial vane sonic inlets, and QCSEE high throat Mach number inlets, can be designed to operate effectively at forward speed and moderate angle of attack with good performance and noise suppression capability. The performance and noise suppression trends demonstrated at forward speed and 0° inflow angle are similar to those measured when the same inlets were operated statically in front of model scale fans. (The results of the earlier sonic inlet tests are described in reference 1.) The radial vane inlet at approach (vanes installed) shows aerodynamic performance penalties larger than those exhibited by the translating centerbody and QCSEE high Mach number inlets to obtain comparable noise reductions. Careful redesign of inlet lips has led to good aerodynamic performance at high angles of attack and crosswind for all inlets. Axisymmetric compressible flow analysis is shown to allow accurate prediction of sonic inlet flow conditions, and thus to be an effective design tool.

The inlet concepts investigated are shown in figures 1(a) through (c). The translating centerbody inlet—inlets A1, A2, and A3 in figure 1(a)—is designed to handle inlet maximum airflows 1.25 times the approach airflow when the centerbody is in the A1 approach position; the “takeoff” and “approach” positions of the centerbody provide the respective throat areas. Intermediate centerbody locations A2 and A3 were explored to allow for more extreme inlet inflow angles (α , angle of attack). Location A2 provides 1% more throat area than A1, and A3 provides 4% more. The radial vane inlet, shown in figure 1(b), is designed for the same throat area ratio as the translating centerbody inlet. The approach throat area is obtained with the vanes exposed, and the takeoff throat area is obtained by removing the vanes; in an airplane installation, the vanes would be folded into the cowl for takeoff and cruise. An inlet designed for QCSEE application, inlet C4, is shown in figure 1(c). This inlet concept relies on a variable-geometry engine to maintain relatively constant airflow demands, or on acoustic lining to achieve noise suppression at reduced approach airflows. The translating centerbody inlet and the radial vane inlet are the same hardware tested in front of a model scale fan under static conditions (ref. 1). A total of five inlets for QCSEE application—C inlets—were tested; they have identical diffusers but differ with respect to the contours of the cowl lip.

The tests were conducted in the Boeing low-speed propulsion wind tunnel at forward velocities up to 315 km/h (170 kn) and inflow angles up to 90° . Compressor face recovery and distortion were measured with 84 probe positions; diffuser boundary layers also were measured, and cowl and centerbody pressure distributions were obtained. A siren noise source signal was generated downstream in the inlet duct and monitored external to the

inlet with microphones flush-mounted on the wind tunnel wall. A J-47 engine supplied suction to vary inlet airflow. Figure 2 shows a typical test arrangement.

The variation of recovery and distortion with noise reduction for inlet A1 is shown in figures 3 and 4; data are shown for $\alpha = 0^\circ$ and V (forward velocity) = 0 and 148 km/h (80 kn). \overline{SPL} is obtained from the averaged reading of four microphones flush-mounted on the tunnel wall. The $\Delta \overline{SPL}$ value is found by subtracting the \overline{SPL} at 3 kHz (the siren noise source fundamental frequency) from the maximum \overline{SPL} at 3 kHz observed at lower inlet airflows near the idle speed of the J-47. In some cases the tunnel noise floor prevented measurement of $\Delta \overline{SPL} > 30$ to 35 dB. At $V = 148$ km/h (80 kn) in the approach configuration, $\Delta \overline{SPL} > 25$ dB is obtainable at recovery > 0.99 and distortion $< 5\%$. At the same forward speed in the takeoff configuration, $\Delta \overline{SPL}$ of about 15 dB is available at recovery > 0.99 and distortion $\sim 6\%$. Results from the fan test of reference 1 are shown in figures 3 and 4 for comparison. The reference ΔPNL is calculated by scaling the model spectra to the STF 369C engine size and extrapolating levels to the 500-ft location at 50° . The main conclusion is that the tests reported here show the same general trends of recovery and distortion variation with noise reduction as the fan model tests. The fan model performed better statically, in part because the fan suction creates flow uniformity near the compressor face. In addition, a bellmouth entry to the inlet was used in the fan tests, causing better flow conditions in the throat and diffuser. The trends shown by the current test are better at forward velocity than at the static condition (and better than the fan model results), probably because the cowl lip functions better.

The aerodynamic performance and noise reduction characteristics of the translating centerbody in the A1, A2, and A3 positions are compared in figure 5 for $\alpha = 20^\circ$ and $V = 185$ km/h (100 kn). The A2 and A3 positions produce trends similar to those for A1 (approach) at 148 km/h (80 kn). However, the angle of attack and forward velocity cause cowl diffuser separation at the A1 position (approach), and this is reflected in decreased recovery and increased distortion for the same $\Delta \overline{SPL}$. Thus distortion will be reduced and recovery increased if the centerbody is translated aft for angle-of-attack operation.

The aerodynamic performance and noise characteristics of the radial vane inlet, inlet B, are shown in figures 6 and 7. At 148 km/h (80 kn), approach configuration, $\Delta \overline{SPL} > 25$ dB is not obtained until recovery falls below 0.94 and distortion exceeds 12%. Compared to the approach operation of the translating centerbody inlet, this is poor performance. In the takeoff configuration (vaness removed), $\Delta \overline{SPL}$ of 25 dB is available at a recovery > 0.99 and distortion $< 5\%$ at 148 km/h (80 kn); this performance is better than is the case for the A1 inlet at the same velocity. At approach, performance at forward velocity and at the static condition is nearly the same, and the static performance is similar to the fan model performance of reference 1. This is probably because the flow around the inlet lip is not as important as the flowfield through the vanes in suppressing the noise. In the takeoff configuration, with the vanes removed, good performance characteristics are obtained, and forward velocity improves performance; these effects are similar to those found for inlet A.

The various QCSEE (C inlet) designs have similar characteristics at $\alpha = 0^\circ$, $V = 148$ km/h (80 kn), and $\alpha = 20^\circ$, $V = 306$ km/h (165 kn), as shown in figures 8 and 9. Inlet C1 has the initial Boeing lip design, C4 has the final Boeing lip design, and C5 is the NASA-selected lip design. All C inlets have a common diffuser. The inlets exhibit very good characteristics at

$\alpha = 0^\circ$, showing $\Delta \overline{\text{SPL}} > 25$ dB at recovery of 0.99 and distortion of 4%; the throat Mach number at this condition is near the design value of 0.79. At $\alpha = 20^\circ$ and $V = 306$ km/h (165 kn), $\Delta \overline{\text{SPL}} > 25$ dB is available at a small decrease in recovery and a distortion increase; thus the inlet performs well with an increase in α and V .

An important part of the QCSEE inlet performance objectives is operation at $\alpha = 50^\circ$, $V = 148$ km/h (80 kn), and $\alpha = 90^\circ$, $V = 65$ km/h (35 kn). The initial Boeing design, C1, performs well at $\alpha = 0^\circ$ and $\alpha = 20^\circ$, but flow separation occurs at the specified higher angles of attack. Based on test information about inlet C1, lip modifications were made and the C4 Boeing design evolved. Both the Boeing inlet, C4, and the NASA inlet, C5, meet the design objective of separation-free operation near the design throat Mach number of 0.79; aerodynamic and noise performance at $\alpha = 0^\circ$ and $\alpha = 20^\circ$ is good for both inlets (figures 8 and 9).

INTRODUCTION

Sonic inlets have been under investigation for a number of years as a means by which large reductions of forward radiated engine fan and compressor noise can be obtained. NASA, Boeing, and other organizations have demonstrated the basic feasibility and potential of the device, and, more recently, Boeing developed under NASA contract an expanded technology base for sonic inlets (ref. 1). The Boeing/NASA investigation evaluated and compared a number of configuration concepts with respect to aerodynamic and noise performance, mechanical design feasibility, and overall system considerations. The tests were conducted in an anechoic chamber at zero forward speed; turbomachinery provided the noise source.

The basic objective of the present investigation is to determine the effects of forward velocity and angle of attack on sonic inlet aerodynamic performance and acoustic suppression; a siren provides the noise source. Two of the most promising concepts of the previous investigation were selected for this evaluation: the translating centerbody sonic inlet, and the radial vane sonic inlet. In addition, a third configuration was investigated, a NASA-selected design for QCSEE application. The QCSEE design is a nonvariable geometry inlet to be operated near 0.79 throat Mach number; the translating centerbody inlet and the radial vane inlet have variable geometry to allow for large variations of inlet airflow.

PRECEDING PAGE BLANK NOT FILMED

TEST APPARATUS

INLET TEST MODELS

The three inlet test models were (1) translating centerbody sonic inlet, (2) radial vane sonic inlet, and (3) high throat Mach number inlet (for QCSEE application). The translating centerbody inlet (A inlets) and the radial vane inlet (B inlet) were the same hardware used in the earlier sonic inlet investigation (ref. 1) except that new cowl lips were manufactured and attached to the forward end of the original cowl diffusers. The inlets for QCSEE application (C inlets) were manufactured specifically for this test; five C inlets were tested, all with a common diffuser, but each with a uniquely contoured cowl lip attached to the forward end. A photograph of the three types of inlets and their respective parts appears in figure 10.

TRANSLATING CENTERBODY INLET

The translating centerbody inlet (inlet A) was tested with the centerbody in two basic positions—in the forward position for approach (A1 approach), and in the aft position for takeoff (A1 takeoff). Due to angle-of-attack problems encountered when the centerbody was in the basic approach position, two alternate positions (A2 approach and A3 approach) were also evaluated. A composite sketch of the three approach positions and the takeoff position of the centerbody is presented in figure 11.

Inlet coordinates and centerbody translations are given in table 1; table 2 provides hilite, throat, and compressor face areas. Figure 12 shows the pressure instrumentation for inlet A1 approach, indicating locations of the static pressure taps, compressor face rakes, boundary layer rake, and dynamic probes. The static taps indicated by an open circle are the same taps used in the earlier Boeing/NASA investigation (ref. 1); new taps are shown by an X. Model stations for the pressure taps are given in table 3. Figure 13 shows the boundary layer rake configuration, as well as the rake location on the cowl and the centerbody, for all three types of inlets investigated.

RADIAL VANE INLET

Figure 14 provides a scaled sketch of the radial vane inlet, inlet B, showing locations of the static pressure taps, compressor face rakes, boundary layer rake, dynamic probes, and radial vanes. The centerbody and the portion of the cowl aft of the parting line ($X/L^* = 1.14$) are the same hardware used in the tests of reference 1, except that new pressure taps and a boundary layer rake have been added. The vanes also are the same hardware. A new forward cowl has been made for the present investigation.

The coordinates of inlet B are given in table 4; table 5 gives the surface pressure taps. The approach throat area—minimum area between the vanes—is 368.6 cm^2 (57.13 in^2), and the takeoff throat area—vanes removed—is 482.3 cm^2 (74.75 in^2). The latter area was determined by a compressible potential flow calculation.

There are 36 radial vanes, symmetrical in shape and spaced 10° apart, center to center. The vane surfaces are linear elements that intersect on the inlet centerline when projected. All

PRECEDING PAGE BLANK NOT FILMED

cross sections are similar; the reference plane cross section is shown and its coordinates listed in figure 15. Locations of static pressure taps in the vanes are shown in figure 16.

QCSEE HIGH THROAT MACH NUMBER INLETS

The QCSEE-type inlets, C inlets, were manufactured specifically for this test. Five versions—all with a common diffuser but with five different lips that can be attached to the forward end—were investigated. The principal geometric characteristics of inlets C1 through C5 are given in table 6. Inlet C2 was manufactured with a noticeable ridge on the hilite, and some testing was done with this inlet as delivered. To determine if inlet performance was affected by the ridge, inlet C2 was sanded smooth. The sanded configuration is called inlet C2-A.

Figures 17 through 21 provide scaled sketches of the C inlets, indicating locations of the static pressure taps, compressor face rakes, boundary layer rake, and dynamic probes. The model parting line for the inlet lips is at $X/L^* = 1$, i.e., 2.54 cm (1 in) downstream of the minimum cowl diameter or throat.

Coordinates for inlets C1 through C5 are given in table 7. (Table 7(b), which lists inlet C2-A coordinates, identifies C2 coordinates only where they are different from the sanded configuration.) Coordinates of the static pressure taps are given in table 8. All taps for inlets C1, C2, and C2-A are located at the same values of X/L^* .

All QCSEE C inlets have the same throat and compressor face areas—507.52 cm² (78.67 in²) and 607.37 cm² (94.14 in²), respectively. Inlets C1, C2, C2-A, and C4 have the same hilite area—736.00 cm² (114.08 in²); the hilite areas for C3 and C5 are 720.69 cm² (111.71 in²) and 743.02 cm² (115.17 in²), respectively.

TEST FACILITY

The test program was conducted in the Boeing low-speed wind tunnel, which has a nominal test section of 2.74 m by 2.74 m (9 ft by 9 ft). Tunnel airflow is induced through a honeycomb screen system, a large area reduction, the test section, the tunnel diffuser section, and through a turboprop power source. The inlet airflow passes through the inlet and is ducted through the tunnel floor to an external ducting system that includes a venturi meter. The suction source for the inlet airflow is a turbojet engine. Figure 22 shows an external view of the tunnel.

INLET LOCATIONS IN THE WIND TUNNEL

The test angles of attack are established by using various combinations of duct pieces downstream of the inlet. The ducting for $\alpha = 0^\circ$ is shown in figure 23. At 0° , the inlet centerline is 117 cm (46 in) above the floor of the test section, which has an overall height of 262 cm (103 in). Figure 23 also shows inlet locations for other inflow angles used in the test. Photographs of various inlet configurations installed in the wind tunnel at the inflow angles tested are presented in figures 24 through 29.

SIREN NOISE SOURCE

The location of the siren noise source is shown in figures 24 through 27. The siren rotating disk axis is at a right angle to the inlet centerline, and the siren noise is ducted directly into the inlet pipe at a point where inlet flow velocities are always less than 60 m/s. During each test, the siren is run at constant speed and pressure ratio. The siren noise signal radiates into the duct and then traverses the duct and passes through the inlet into the wind tunnel test section. The siren noise source produces an acoustic signal composed of a fundamental tone and its harmonics. A typical siren signal spectrum is shown in figure 30. The amplitude of the siren tone harmonics decreases as harmonic number increases, but the siren signal amplitudes for the fundamental frequency and several harmonics are available for testing. The fundamental frequency of the siren signal was set at 3 kHz for the inlet tests; data were obtained at 3, 6, 9, 12, 15, and 18 kHz.

The acoustic output of the siren depends on the pressure difference across the siren chopper (rotor) plate. The supply gauge pressure to the chopper plate was maintained at $3.45 \times 10^5 \text{ N/m}^2$ (50 psig), with the siren air vented into the inlet flow duct. Inlet flow duct pressure varied slightly with inlet airflow, causing some variation in the pressure difference across the chopper plate. A test was performed to determine the change in acoustic level that would result from these variations. With inlet AI installed, noise measurements were made in the wind tunnel test section for three values of siren supply pressure with no inlet airflow. The $\overline{\text{SPL}}$ results are shown in the three upper curves in figure 31. The siren supply gauge pressures were 2.76, 3.45, and $5.17 \times 10^5 \text{ N/m}^2$ (40, 50, and 75 psig, respectively). For the total change of 2.41 N/m^2 (35 psig) pressure difference across the siren, the largest change in $\overline{\text{SPL}}$ was 4 dB at 9 kHz.

The range of pressure differences across the siren encountered during inlet testing was from $3.45 \times 10^5 \text{ N/m}^2$ (no inlet flow) to $3.47 \times 10^5 \text{ N/m}^2$ (maximum inlet flow). This range corresponds to a 0.03-dB variation in $\overline{\text{SPL}}$, so report data have not been adjusted for the duct pressure variations.

It was not useful to monitor the siren signal level inside the inlet flow duct by measuring $\overline{\text{SPL}}$ at a single location. The measurement location was in the inlet duct directly across from the siren, and here $\overline{\text{SPL}}$'s were strongly influenced by acoustic reflections (standing wave patterns) that were altered by airflow in the duct and by changes in duct configuration. The duct configuration changes with angle of attack, and the duct end conditions change when different inlets are installed. Siren monitor microphone $\overline{\text{SPL}}$ measurements for two frequencies at various inlet airflows are compared in figure 32. No significant trend of $\overline{\text{SPL}}$ versus inlet airflow is indicated, and so siren output was not corrected for inlet airflow.

$\Delta \overline{\text{SPL}}$ MEASUREMENT LIMITATIONS

Previous efforts to measure the noise suppression available from sonic and near-sonic inlets indicate that a test facility must provide the dynamic range capability required to measure

noise reductions ($\Delta \overline{\text{SPL}}$'s) of 20 to 30 dB. The dynamic range of the Boeing facility could be limited by the following:

- siren source noise that propagates to the microphones via paths other than upstream through the inlet (“flanking paths”)
- wind tunnel propeller noise
- wind tunnel turboprop compressor noise
- J-47 engine (suction source for inlet flow) noise
- wind tunnel boundary layer noise
- electronic noise in the data acquisition system

The actual dynamic range for a given test run depends on combinations of the preceding limiters, and the facility resolution of $\Delta \overline{\text{SPL}}$ can be determined only during test operation. Prior to test, however, an examination of the effect of siren noise source flanking paths was made. After the siren noise level emitted from inlet A1 with no inlet airflow was measured, the inlet was closed by a cap—which resulted in an acoustic transmission loss > 20 dB—and the siren noise level was measured again. The difference in levels ($\Delta \overline{\text{SPL}}$) was 17 dB at 3 kHz, less than the desired dynamic range of 20 to 30 dB. To correct the situation, the hard surfaces of the inlet flow duct and siren case were acoustically insulated with a layer of Scottfelt as shown in figure 27. The measurement process was repeated, and the dynamic range ($\Delta \overline{\text{SPL}}$) increased to 27.5 dB at 3 kHz. Since the cap allows some noise transmission, the dynamic range for measurement of the reduction of siren noise at 3 kHz—the fundamental siren frequency—is greater than 27.5 dB, and greater than the siren harmonics values indicated in figure 31.

Wind tunnel propeller noise occurs at frequencies well below the 3-kHz siren fundamental, but the wind tunnel turboprop compressor has a narrow band noise at a center frequency of 7.5 kHz, which can be filtered out from the siren tones occurring at 6 kHz and 9 kHz (figure 30). The J-47 engine noise contains tones at 2 kHz and 5 kHz; these also can be filtered from the siren tones. Note that the data in figure 30 are for $V = 185$ km/h (100 kn) and $C_D^* = 0.39$; at other tunnel velocities and airflows, the measurements indicate that the frequency and levels of the J-47 tones change but that the turboprop compressor tone does not change.

The microphones on the wind tunnel wall are immersed in a turbulent boundary layer that produces a broadband noise level over a wide frequency range. The boundary layer noise masked the siren noise at frequencies greater than 12 kHz, and also at 9 kHz for some wind tunnel velocities and inlet flow conditions. At the highest wind tunnel velocities, $\Delta \overline{\text{SPL}}$ measurements are limited to 10 dB at 12 kHz; however, at $V = 0$, data at 15 kHz and 18 kHz can be obtained. (For measurements at the latter frequencies, noise from the J-47 engine dictates the dynamic range lower limit.)

Electronic noise in the data acquisition system did not limit measurement of SPL at any of the siren noise frequencies. The ratio of measured noise to electronic noise exceeded 20 dB for all data acquired.

An unexplained noise source was encountered during the tests of the QCSEE C inlets at $C_D^* > 0.98$. The source was broadband and controlled the background noise level for the frequency range of 12 to 20 kHz. The SPL measured in a 40-Hz bandwidth for this noise is about 85 dB for 12, 15, and 18 kHz. The noise was observed at all microphone locations and is not believed to be an instrumentation problem.

INSTRUMENTATION SENSORS

Pressures and temperatures are sensed with transducers and thermocouples and are passed through amplifiers, signal conditioners, and digital voltmeters into a quick-look computer. Compressor face dynamic pressures for selected runs were recorded on tape and monitored on oscilloscopes. Dynamic pressure sensors were Kulite transducers (25-psi-rated). Acoustic sensors were B&K microphones.

MICROPHONE LOCATIONS

Microphone locations are shown in figure 33. Locations 01, 02, 03, and 04 (indicated by circles) are parallel to the inlet centerline and are used for the $\alpha = 0^\circ$ tests. Locations 201, 202, 203, 204, and 205 (shown by triangles) are used for the $\alpha = 20^\circ$ tests. All locations are parallel to the inlet centerline except 201. Locations 05F and 205 are used for wind-off tests (centerline microphone, figure 25); 05S is used for some wind-on tests.

All microphones were positioned with their diaphragms (sensing elements) flush-mounted on the tunnel walls except 05F, 05S, and 205. These were oriented with geometric axes parallel to the wind tunnel airflow and diaphragms facing upstream. They were protected by an aerodynamically streamlined windscreen (B&K UA 0385 noise cone). The probe microphone assembly was supported by a strut that could be mounted from either the wind tunnel floor or the ceiling. A microphone was located in the main inlet duct directly opposite the siren noise source duct. It was flush-mounted in the duct wall and was in line of sight with the siren.

The distance r from the inlet entrance center to microphone locations is given in table 9. The magnitude of angle ϕ , between the inlet centerline and the line from the inlet entrance center to the microphone location, is also given in the table.

DATA ACQUISITION AND REDUCTION

PERFORMANCE DATA

Performance data were acquired and reduced through techniques standard to Boeing and the industry. The specific data handling procedures used for this investigation are shown in

figure 34. The calculations are made with English units and are then converted to SI units as follows:

English units	Conversion multipliers	SI units
in ²	6.4516	cm ²
lb/in ²	6894.7572	pascals (N/m ²)
R	5/9	K
lb/s	0.45359237	kg/s
lb/s-ft ²	4.8824276	kg/s-m ²
kn (U.S.)	1.852	km/h

The total pressure recovery at the compressor face, $P_{T2} AV/P_{T REF}$, is based on the area-weighted average of all measured total pressures. Since there are 7 probes on each of 4 rakes, and each rake is positioned in 3 circumferential locations, the total pressure average contains 84 measurements. The total pressure distortion at the compressor face is the maximum total pressure minus the minimum total pressure (as indicated by any of the 84 measurements) divided by the average.

In this report, performance and acoustic data are presented as a function of inlet flow coefficient, C_D^* . This parameter is defined as the measured airflow divided by the ideal maximum (choked throat) airflow for the same area; it is equal to $1/(A/A^*)_{TH}$. The corresponding throat Mach number can easily be found from A/A^* in compressible flow tables. C_D^* is used because it is a convenient parameter for comparing the effect of changes in inlet airflow for airplane and engine applications. In addition, the maximum C_D^* achievable in a given inlet is a measure of the inlet throat blockage caused by boundary layer and flow nonuniformity.

Narrowband (4-Hz) analyses of selected recordings for the Kulite dynamic pressure sensors were performed over the frequency interval of 10 Hz to 2000 Hz. Spectra for the dynamic pressure typically were smooth, broadband noise. Therefore, the rms readings are not influenced by narrowband noise spectral components, and, hence, the ΔP_{rms} values are good measures of the dynamic pressures.

ACOUSTIC DATA

The microphones were equipped with resistor heaters and kept several degrees warmer than the temperature of the surrounding air to prevent condensation from forming internally. The B&K 2615 cathode followers for the microphones were mechanically isolated from wind tunnel vibrations, and flexible adapters (B&K UA 0123) were used between the microphones and the cathode followers. Sensitivity calibration of the microphones was performed at the start and end of each test interval and each test day with a B&K 4220 piston phone.

Voltage signals from the microphone systems were recorded on a 14-track magnetic tape recorder along with signals for voice, time code, and siren rotor rpm, and signals from the 25-psi-rated Kulite pressure transducers in the inlet total pressure rake. Readings for the rms output of the Kulite transducers were made during the tests; they were band-limited to the frequency interval of 10 Hz to 2000 Hz.

With the use of a Federal Scientific Model UA 6 Real Time Narrow Band Analyzer, SPL data from the tape recordings were reduced to graphs of SPL versus frequency; a typical example is given in figure 30. The normal frequency bandwidth for the analyzer was 40 Hz, and the maximum frequency for the data reduction was 20 kHz.

The recorded SPL data include background noise. However, the siren signal is resolved by a filtering process, and the SPL is measured for each tone. Since the siren noise emitted by the test inlet decreases in amplitude as C_D^* is increased, SPL graphs for some test conditions do not resolve the siren tones from the background noise. The procedure used to determine SPL values for the siren tones was the following: if the siren tone was resolved from the background noise by more than 3 dB, the SPL was read at the siren tone frequency and then tabulated; if the resolution of the siren tone was less than 3 dB, the SPL value was tabulated as a "less than" ($SPL <$) value. Resolution in dB is used here to mean the dB difference between the value for a peak in the spectrum and the value, smoothly interpolated, that would occur at the same frequency if the peak were removed. Use of this procedure results in some siren tone SPL levels that are high by as much as 3 dB. In these cases, the effect on reported results is that siren or noise *reduction* by a test inlet is conservatively indicated.

The measured siren noise in the wind tunnel test section external to the inlet depends on the siren noise level emitted by the inlet, the acoustic directivity of the inlet, and the reflective paths from the hard wind tunnel surfaces to the measurement location. Both the noise level emitted by the inlet and the directivity of the inlet change as inlet flow parameters are changed, thus causing changes in the total siren noise measured at a particular location. These combined effects tend to mask inlet-emitted noise level trends. The effects are reduced if SPL's are established as averages of measurements at several locations. These averages are analogous to a space-averaged SPL measurement.

Siren noise measurements for each of four microphone locations and their arithmetic mean are shown in figure 35. SPL and \overline{SPL} versus inlet C_D^* are plotted for four siren harmonic frequencies. The SPL data for individual microphone locations scatter around the \overline{SPL} curve. The combined effects for broadband noise of acoustic reflections in the test section and SPL averaging can be seen by comparing the two data curves shown in figure 36. Measurements of the SPL produced by a broadband, omnidirectional noise source in an anechoic field and in the wind tunnel test section are compared. The noise source was located in the wind tunnel in the approximate area where the inlet hilites were placed. If the free-field (anechoic) measurement had been made with a flush-mounted wall microphone, the lower curve would be raised by 6 dB and would then agree, to within 2 dB, with the measurement made in the wind tunnel. The close agreement for a broadband, omnidirectional noise source does not imply that measurements made under the same conditions for a narrowband, directional noise source would agree this closely. It does indicate, however, that the averaging of SPL measurements from the four locations is a reasonable

procedure. Acoustic test results are presented using the average $\overline{\text{SPL}}$ of the SPL's measured by four flush-mounted microphones in the wind tunnel wall.

For convenience in this report, noise reduction values of $\overline{\text{SPL}}$ are formed by subtracting the $\overline{\text{SPL}}$ at a given C_D^* , usually at 3 kHz, from the maximum $\overline{\text{SPL}}$ for any nonzero airflow condition, where the $\overline{\text{SPL}}$ values are four-microphone averages. Other reference levels of $\overline{\text{SPL}}$ from which $\overline{\text{SPL}}$ reductions would be measured could be chosen. One procedure would be to compute $\overline{\text{SPL}}$ reductions where the reference condition would be static flow ($V = 0$) for the inlet and the wind tunnel; however, for many of the inlets tested, this condition produced a lower $\overline{\text{SPL}}$ than measured at some higher C_D^* values, and the result was inlet $\overline{\text{SPL}}$ amplification. Two other reference choices were considered: (1) a value for $\overline{\text{SPL}}$ equal to the highest value of $\overline{\text{SPL}}$ measured for any C_D^* value, including static inlet flow; and (2) a value at a set C_D^* near the minimum operating points for the inlets ($\overline{\text{SPL}}$ data for higher C_D^* would be reported, and data for lower C_D^* would be discarded). Use of these alternates for $\overline{\text{SPL}}$ reference levels leads to conflicting results, possibly due to inlet directivity effects. The changes observed in $\overline{\text{SPL}}$ at low C_D^* values are not well understood.

Inlet noise reductions determined with a siren noise source probably understate the inlet acoustic performance obtainable with a fan noise source. More of the energy of fan noise is distributed into higher-order acoustic modes than is the case for the siren source. Reported results indicate that noise in the higher-order modes is suppressed to a greater degree than noise in the lower-order modes in sonic inlets (ref. 2).

The trends of $\overline{\text{SPL}}$ versus C_D^* reported here are for noise emitted from the inlet; these trends do not address other airplane noise sources, such as the bypass fan exhaust, the engine case, the jet exhaust, the combustor, the turbomachinery, or the airframe. Hence $\overline{\text{SPL}}$ noise reductions in this report should *not* be interpreted as *airplane* noise reductions that would be achieved with the application of a flight inlet.

TEST PROCEDURES

A typical test run started with a tunnel warmup to provide for steady tunnel speeds. The jet engine for the inlet airflow was set for idle, and acoustic and performance data were recorded with the rake at the first position. After acoustic data were recorded, rake data were recorded at the second and third positions. The entire process required about three minutes. At this point, the on-line computer worked about 1-1/2 minutes while the jet engine controls were advanced to set an increased inlet airflow for the next point. Sometimes this procedure would cause an increase or decrease in tunnel speed, and in these cases appropriate adjustments were made. During a number of runs, alternate procedures were tried, such as setting inlet airflow and slowly bringing the tunnel speed up. No hysteresis was found, probably because of the dependency between inlet airflow and tunnel speed. Since the angle-of-attack changes require a tunnel shutdown, it was not possible to explore continuous change in α .

ANALYTICAL INLET DESIGN

SONIC INLETS

Under contract NAS3-15574 (ref. 1), two sonic inlet models were developed in a static test program. High noise suppression and good aerodynamic performance were demonstrated with these models, one of which was a translating centerbody single-passage inlet and the other a radial vane multipassage inlet. A discussion of the analytical design procedure used to develop these inlets is presented in reference 1.

Since the primary objective of the present program is to evaluate the effects of forward speed and angle of attack, the goal of the analytical work was to design a lip for each of the existing sonic inlet diffusers that would provide acceptable performance within the inlet operating envelope. The design envelope used for this program is shown in figure 37 in terms of inlet angle of attack versus forward speed. This envelope is similar to that used on the Boeing AMST (YC-14) airplane.

Selection of the initial lip configurations was based on an inviscid study of the lip flow at the static condition as well as on a combined viscous/inviscid study at forward speeds. The design tool is a transonic potential flow program that can be combined with a compressible boundary layer program at forward speed. The potential flow program uses relaxation methods to calculate two-dimensional or axisymmetric transonic potential flows; the boundary layer program uses a finite difference approach to solve a set of partial differential equations for conservation of mass and energy and the rate of change of streamwise momentum in the boundary layer. In the combined version, the program automatically iterates viscous and inviscid solutions a specified number of times.

The design approach for the sonic inlet lips included a study that examined the effects of varying contraction ratio, lip length, and lip shape. The study was conducted at the static condition because the most severe lip flow at zero degrees angle of attack occurs at zero velocity. In addition, an analysis of results available from tests of conventional inlets revealed that the peak lip Mach number at a given angle of attack (or crosswind condition) will decrease if the peak Mach number at the static condition is reduced, for example, by increasing the contraction ratio. It was therefore assumed that the lip that produces the best Mach number distribution at the static condition also will be the best configuration for angle of attack or crosswind conditions. The lip study was first conducted on the translating centerbody inlet. The experience gained from this effort was then applied to study of the radial vane inlet.

Previous analytical and experimental work on conventional subsonic inlets conducted at Boeing has indicated that a near-optimum lip shape is obtained by using the "super-ellipse" curve define by

$$(X/a)^{2.2} + (R/b)^{2.2} = 1; a/b = 2.5$$

This is confirmed in reference 3, which presents an analytical investigation of the effect of subsonic inlet lip geometry on the lip Mach number distribution at various angles of attack.

Since the effect of the centerbody on the lip Mach number distribution is relatively small, as shown in figure 38, the super-ellipse curve was used for the basic configuration. The translating centerbody inlet surface Mach number distributions for takeoff and approach are shown in figures 39 and 40, respectively. In both cases, a deceleration occurs just inside the inlet hilite before the flow reaccelerates into the throat region. This deceleration (or adverse pressure gradient) will cause boundary layer transition, an increase in the growth rate of the boundary layer, and a deterioration of the boundary layer profile. At increasing angle of attack the adverse gradient will become more severe, thus aggravating the problems associated with the boundary layer. Therefore, an effort was made to minimize or eliminate the gradient without increasing the local Mach numbers in the throat region. The lip contraction ratio was the first parameter studied. Lip Mach number distributions at takeoff airflow (one-dimensional throat Mach number of 0.90) for a super-ellipse with contraction ratios of 30%, 35%, and 40% are shown in figure 41. The contraction ratio here is defined as

$$CR = \left(\frac{A_{HI}}{A_{TH}} - 1 \right) 100 (\%)$$

where A_{TH} is the minimum flow area with the centerbody removed. The fact that a higher contraction ratio lip improves inlet performance at the static condition is clearly demonstrated in figure 41. The peak Mach number and thus the adverse gradient decrease rapidly with increasing CR.

Since no maximum diameter was specified for the sonic inlets, it was decided to use the 35% CR lip as a basis for further analytical study. This CR results in a hilite diameter approximately equal to the fan face diameter. Cowl wall thickness at the fan face typically is in the order of 10% to 15% of the fan face radius. The inlet fineness ratio (i.e., hilite diameter/maximum cowl diameter) is thus between 0.85 and 0.90—a reasonable number for a low-drag cowl design. In addition, the 35% CR is compatible with the design envelope (for example, a 34% CR is used on the YC-14 inlet).

To further reduce the adverse gradient, a curvature study of the elliptical equation

$$(X/a)^n + (R/b)^m = 1$$

was conducted. The study showed that an increase in the exponent n and a decrease in the exponent m serve to increase the radius of curvature in the critical lip area just inside the hilite. Lip Mach number distributions for two such configurations are compared with the $n = m = 2.2$ super-ellipse in figure 42. For configuration 9, the Mach number distribution is almost flat, with only a small gradient near the throat. Configuration 16 has a small adverse gradient just inside the hilite, followed by a long, favorable gradient to the throat. Configurations 9 and 16 have identical peak Mach numbers (1.05) just inside the hilite, but the adverse gradient for configuration 9 is located closer to the throat, and the boundary layer has less distance to redevelop before it reaches the diffuser region downstream of the throat. Configuration 16 is the best lip configuration for the translating centerbody inlet.

A similar study was conducted on the radial vane inlet, and the results show that lip flow requirements for both types of sonic inlets are similar. Radial vane inlet lip Mach number distributions for the three most promising configurations are shown in figure 43. These shapes are similar to those found for the translating centerbody inlet. Again, configuration 16, with a 35% CR, is the best choice; it was therefore selected as the lip configuration for the radial vane inlet.

For the most promising lip configurations, a combined viscous/inviscid study was conducted at forward speeds to aid in lip selection and to identify the airflows or throat Mach numbers at which separation problems might be encountered. For the translating centerbody inlet, an attempt was also made to predict the angle-of-attack inlet pressure distribution with the use of empirical information, and to evaluate the boundary layer shape in the throat region during such severe inlet flow conditions. Comparisons between these predictions and the test data are shown in "Test Results," the next section of this report.

QCSEE HIGH THROAT MACH NUMBER INLET

A new inlet was designed for the QCSEE engine application. The objective was to develop, through analysis and testing, an inlet that will meet the performance requirements and design objectives summarized following:

(1) Performance

- No inlet separation at an angle of attack of 50° and a forward speed of 148 km/h (80 kn)
- No inlet separation with a 65-km/h (35-kn), 90° crosswind during static operation

(2) Design

- Takeoff throat Mach number = 0.79
- Inlet length to fan diameter $L/D = 1.0$
- Noise reduction at takeoff ≥ 13 PNdB, including the effect of the noise treatment required for approach conditions. (The inlet was designed for the over-the-wing QCSEE engine, for which the approach airflow is lower than the takeoff airflow. Since the model designed and fabricated under the present contract is a hard-wall inlet, the noise reduction goal is somewhat less than 13 PNdB.)

The design approach involves three areas of effort: the diffuser, the lip, and the external cowl. The spinner has the over-the-wing contour specified by NASA Lewis.

DIFFUSER DESIGN

The diffuser design concept is based on previous Boeing inlet design experience. The approach was to use curves with constant second derivatives and to avoid long, straight sections at high inclination relative to the inlet centerline. A maximum slope (dR/dX) of 0.2

(11.31°) was used. Several diffuser contours were developed and examined, some with rapid initial diffusion (smaller radius of curvature near the throat) and others with less rapid diffusion (larger radius of curvature near the throat).

It was found that with less rapid initial diffusion (and, as a result, lower maximum area before the spinner is encountered), adverse pressure gradients in the diffuser are reduced, as is the tendency for the flow to reaccelerate. Also, the combined viscous/inviscid analysis at forward speed shows an improvement in the boundary layer shape factor. Mach number and shape factor H_1 distributions for two diffuser contours are compared in figure 44. An H_1 value above 1.8 corresponds to a distorted velocity profile, and the boundary layer computer program usually indicates separation if H_1 is between 2.2 and 2.5. A "full" profile corresponds to $H_1 = 1.3$. The line labeled D3 in the figure has the lowest peak value of H_1 and therefore is the diffuser contour chosen for the QCSEE inlet.

LIP DESIGN

Selection of the lip contraction ratio was governed by the stringent requirement of separation-free operation at $\alpha = 50^\circ$, $V = 148$ km/h (80 kn), $M_{TH} = 0.79$. Based on extrapolation of existing information (YC-14 model tests) about the effect of throat Mach number and contraction ratio on angle-of-attack performance, a contraction ratio of 45% was selected.

A lip aspect ratio (major-to-minor axis ratio) of 2.5 was chosen for initial analysis based on experience with subsonic inlets and the design of the two sonic inlets. Results showed that, for the QCSEE inlet, this lip produces a strong adverse pressure gradient with a tendency for the flow to be supersonic near the throat. A lip aspect ratio of 3.0 was then investigated. A comparison of lip aspect ratios for the same lip shape is shown in figure 45. The 3.0 aspect ratio lip reduces the peak Mach number at the entrance to the throat region and also reduces the adverse pressure gradient by increasing the radius of curvature in the throat region.

As indicated by previous analysis, the shape of the inlet lip can strongly affect the lip Mach number distribution at both static and forward speeds. Several of the sonic inlet lip shapes were examined at static condition, but they were found to result in undesirable Mach number peaks just inside the hilite. New lip shapes were studied, and the best of these were analyzed at a forward speed of 148 km/h (80 kn) using the combined viscous/inviscid analysis program. This analysis indicates that the super-ellipse is the best overall lip shape with the lowest peak Mach number. The lip defined by $(X/a)^{2.2} + (R/b)^{2.2} = 1$; $a/b = 3.0$, $CR = 45\%$, was therefore selected for the initial QCSEE inlet configuration. Lip Mach number distributions at the static and the 148-km/h (80-kn) conditions for this lip are shown in figure 46.

EXTERNAL COWL DESIGN

With the selected contraction ratio of 45% and the limitation on maximum cowl diameter, a high fineness ratio (DHI/DMAX) is required. Two values of fineness ratio were examined, one of 0.902, for an axisymmetric inlet, and one of 0.870, for a nonaxisymmetric inlet that has a variable contraction ratio around the circumference. Little difference was found between the two fineness ratios, so the 0.902 fineness ratio for the axisymmetric inlet was chosen. The external lip shape is a simple ellipse with a 6.6:1 aspect ratio, $(X/a)^2 + (R/b)^2 = 1$; $a/b = 6.6$.

TEST RESULTS

The objective of the tests is to evaluate the performance and noise characteristics of the translating centerbody, radial vane, and QCSEE high Mach number inlets. In particular, forward speed and angle-of-attack effects are important. For this investigation, the figures of merit are:

- compressor face recovery
- compressor face distortion
- acoustic suppression characteristics, and
- dynamic pressure distortion

Data for these parameters are available for each of the three inlet types evaluated. In addition, boundary layer data were taken just downstream of the throat for all cowls, and on the centerbody of the translating centerbody inlet models. During test operation, on-line data plots were made of mass flow parameters and of static pressures in the throat region. These data help establish the gross stability (or stationarity) of inlet operation and are useful in identifying transitory stall regions.

EVALUATION CRITERIA

To identify whether or not an inlet is "working" or "operating satisfactorily," some arbitrary criteria must be developed. Following are the evaluation criteria established for this investigation:

- (1) Is there a high recovery and a significant acoustic suppression near the "knee" of the curve, i.e., just prior to the point where recovery drops sharply as C_D^* increases?
 - takeoff-recovery ≥ 0.98 ; acoustic suppression ≥ 10 dB ($\Delta \overline{SPL}$)
 - approach-recovery ≥ 0.97 ; acoustic suppression ≥ 15 dB ($\Delta \overline{SPL}$)
- (2) Is the distortion at the knee within reasonable limits, that is, $\leq 10\%$?
 - If distortion $\geq 10\%$, the operating point should be moved to a lower C_D^* where the distortion limit is not exceeded. (It should not be inferred that engines exist or will be built to accept a 10% distortion level and the associated compressor face distortion pattern.)
- (3) Is the airflow relatively stable?
 - Inlets in steady stall from the diffuser are acceptable if the distortion limits are not exceeded.

- Inlets operating with gross transitory stall are considered unstable.

(4) What are the likely inlet airflow requirements for the particular forward speed and angle of attack?

These criteria formed the basis on which subjective evaluations were made of the capabilities of the inlets to work satisfactorily.

SUMMARY OF INLET PERFORMANCE

TRANSLATING CENTERBODY INLET

The performance results for translating centerbody inlet A1 are summarized in figure 47. The inlet performs well at all important tunnel velocities and inflow angles in the takeoff mode, figure 47(a). Crosswind operation ($\alpha = 90^\circ$) at $V = 65$ km/h (35 kn) is rated as marginal because of a higher-than-acceptable distortion level (14%) that is due, primarily, to losses on the cowl lip. At takeoff, inlet A1 attenuates the 3-kHz siren source noise by more than 16 dB ($\Delta \overline{\text{SPL}}$) at $\alpha = 0^\circ$, and by at least 10 dB ($\Delta \overline{\text{SPL}}$) at $\alpha = 20^\circ$.

In the approach mode, figure 47(b), inlet A1 works fairly well at $\alpha = 0^\circ$. (Since operation at $V = 0$ is not required during approach, the marginal performance at $V = 0$ is not significant.) Operation is poor, however, at angle of attack, where significant transitory stall and high distortion occur. If inlet airflow is reduced to bring the distortion level within limits or to eliminate the stall (at $\alpha = 20^\circ$), siren source noise suppression is decreased to only one or two dB ($\Delta \overline{\text{SPL}}$) at 3 kHz.

To provide performance improvements at high angle of attack in the approach mode, two intermediate centerbody positions were evaluated, called inlet A2, located 2.54 cm (1.0 in) aft of A1 approach, and inlet A3, 3.81 cm (1.5 in) aft of A1 approach. Inlet A2 has 1% more approach throat area than A1; inlet A3 has 4% more than A1. Figure 48, which summarizes results, indicates that the performance of A2 and A3 is superior to A1 at $\alpha = 20^\circ$; A2 and A3 performance is marginal at $\alpha = 35^\circ$. Some instabilities and cowl separation occur at low airflows, and some centerbody separation occurs at higher airflows.

Although not shown in figure 48, the effects of using A2 and A3 as the intermediate centerbody positions for the A1 design at the A1 approach power settings—and at $\alpha = 20^\circ$ and $V = 185$ km/h (100 kn)—are worthy of mention. Under these operating conditions, the distortion and recovery criteria are met. With respect to noise suppression, A2 performs marginally—just meeting the criterion with a 20-dB ($\Delta \overline{\text{SPL}}$) suppression—and A3 performs poorly, with only a 12-dB ($\Delta \overline{\text{SPL}}$) suppression. However, if the 20° inflow angles are required primarily for emergency-type operation, the reduced noise suppression is not a serious problem.

RADIAL VANE INLET

Radial vane inlet B exhibits aerodynamically stable inlet flow, high recovery, and low distortion throughout all the conditions tested. It does not, however, meet the acoustic noise suppression criterion for the approach mode ($\Delta \overline{\text{SPL}} \geq 15$ dB). For this reason, inlet B

operation is rated as marginal at all approach conditions that require suppression (figure 49). Noise suppression is inhibited by the vanes, possibly because they create a different type of high Mach number flowfield.

QCSEE HIGH THROAT MACH NUMBER INLETS

QCSEE inlets C1, C4, and C5 perform well at inflow angles of 0° and 20° : aerodynamic performance is good, and noise attenuation > 22 dB ($\Delta\overline{\text{SPL}}$), recovery ≥ 0.98 , and distortion $\leq 10\%$ are available. At $\alpha = 50^\circ$ and $\alpha = 90^\circ$, however, inlet C1—the first QCSEE model tested—performs poorly, exhibiting separation and unsteady flows (figure 50).

Inlets C2, C3, and C4 were designed to improve aerodynamic performance at $\alpha = 50^\circ$ and $\alpha = 90^\circ$ while maintaining good aerodynamic and acoustic performance at the 0° and 20° inflow angles. Inlets C4 and C5 exhibit good operation at $\alpha = 90^\circ$ and meet the design criterion of separation-free operation at $M_{\text{TH}} = 0.79$, $\alpha = 50^\circ$, and $V = 148$ km/h (80 kn). Both C4 and C5 provide, in addition, noise reductions ≥ 22 dB ($\Delta\overline{\text{SPL}}$) at $\alpha = 0^\circ$ and $\alpha = 20^\circ$. Some separation was encountered for C4 and C5 at $M_{\text{TH}} < 0.79$, $\alpha = 50^\circ$, and $V = 148$ km/h (80 kn). The inlets were tested at $V = 140$ km/h (75 kn), and inlet C4 performance was better at the slightly decreased forward speed.

DETAILED RESULTS

TRANSLATING CENTERBODY INLET

Takeoff

An aim of the translating centerbody investigation is to develop inlet lips that, when added to the diffuser section defined in reference 1, provide acceptable inlet operation over the design envelope shown in figure 47. The most severe test of inlet lip performance occurs at low speed and maximum airflow, i.e., when the inlet is in the takeoff position. Inlet A1 operating characteristics at takeoff are summarized in table 10.

It is possible to operate the inlet at all the forward speeds and inflow angles tested. (It should be noted, however, that distortion exceeds the 10% criterion at $\alpha = 90^\circ$ and $V = 65$ km/h (35 kn).) The 3-kHz siren noise source signal is suppressed 16 to 24 dB ($\Delta\overline{\text{SPL}}$) at $\alpha = 0^\circ$ and 10 to 19 dB ($\Delta\overline{\text{SPL}}$) at $\alpha = 20^\circ$, showing that inlet A1 operates as an effective sound suppressor at takeoff.

The most severe test of inlet lip performance occurs at 90° crosswind at 65 km/h (35 kn). As shown in figure 51, the cowl boundary layer is separated at low inlet airflows for this case, but at higher airflows (above $M_{\text{TH}} = 0.7$), the boundary layer is attached. (Separated profiles have total pressures that are equal to the wall static pressure near the wall.) The centerbody boundary layer is attached for all conditions except hard choke ($M_{\text{TH}} = 0.806$). When the inlet is operating at crosswind and low inlet flows, gross inlet lip separation occurs; this is reflected in large separation regions at the compressor face, figure 52(a), and in relatively constant static pressure through the diffuser, as indicated by constant Mach numbers in figure 53(a). As inlet airflow increases, the separated region decreases in size and moves away from the center of the compressor face and toward the

lower lip. When this occurs, the diffuser works better, as shown by a rising pressure gradient. The lip is still separated near the hilite, however, and static pressures are constant through the throat region, figures 52(b) and (c) and 53(b) and (c). Further increases in inlet airflow result in attached flow over the lip, in the throat region, and in the diffuser, (d), (e), and (f) in figures 52 and 53. As the inlet airflow increases toward choking, shock-induced losses cause increased distortion and reduced recovery, (g) and (h) in figures 52 and 53. The corresponding distortion and performance curves are shown in figure 54; corresponding boundary layer data appear in figure 51. Table 11 summarizes inlet A1 airflow characteristics for crosswind operation.

Approach

Inlet A1.—Inlet A1 operating characteristics at approach are summarized in table 12. As indicated by the data, the inlet functions well in the approach mode at 0° inflow angle and tunnel velocities of 148, 185, and 259 km/h (80, 100, and 140 kn, respectively). The compressor face recovery maps in figures 55(a), (b), and (c) show excellent flow at this angle of attack and these velocities. The maps plot the flow just prior to the knee of the recovery curve. An example of the flow just beyond the knee is given in figure 55(d) for the case of $\alpha = 0^\circ$, $V = 259$ km/h (140 kn). The distortion level is 10%, and, as shown, regions of unsymmetrical separation appear. This map corresponds to a siren noise reduction of about 25 dB ($\Delta\overline{SPL}$) at 3 kHz.

Although operation at 0° inflow angle is not actually required at the static condition ($V = 0$) for approach, table 12 shows marginal performance at zero tunnel speed. The separation that causes the unsteady inlet flow and reduced performance at this condition occurs near 0° on the cowl. The compressor face recovery map in figure 56(a), which is for a point just beyond the knee of the recovery curve, clearly shows this separation. (The map corresponds to a siren noise reduction of about 13 dB ($\Delta\overline{SPL}$) at 3 kHz.) As shown in figures 56(b) and (c), similar unsymmetrical trends appear for $\alpha = 20^\circ$ and $\alpha = 35^\circ$ at the static condition.

Compressor face recovery maps for several inlet airflows at $\alpha = 20^\circ$ and $V = 185$ km/h (100 kn) appear in figure 57. The operation is limited by unsteady flow and separation. Raw data show that the cowl boundary layer is separated in the diffuser for the C_D^* values shown in figures 57(a) and (b), and attached for those shown in figures 57(c) and (d). The centerbody boundary layer is attached in the diffuser for all cases. Despite cowl diffuser separation, operation at $C_D^* = 0.798$ —figure 57(a)—is acceptable because of the very low distortion level. However, a small increase in inlet airflow, to $C_D^* = 0.864$, yields the distortion and separation shown in figure 57(b). A further increase, from $C_D^* = 0.864$ to $C_D^* = 0.980$, improves both recovery and distortion, figure 57(c), and when the flow is increased to $C_D^* = 0.986$, the inlet moves toward a hard choke pattern, figure 57(d). These effects are shown in the recovery and distortion curves of figure 58(a). Note that inlet operation is unsatisfactory at high C_D^* ; inlet airflow can be reduced to the stable operating region, but when C_D^* is lowered to avoid a high distortion level, significant noise suppression is eliminated (table 12).

The preceding discussion shows that inlet A1 does not meet the approach criteria at $\alpha = 20^\circ$, $V = 185$ km/h (100 kn). This is true generally for angle-of-attack operation, and, as shown in the performance summary curves of figures 58(a) through (d), recovery and distortion are

generally poor. On-line data show that inlet airflow at the angles of attack and forward speeds evaluated is somewhat unstable. The static pressure in the throat region seems to be more unstable than gross airflow, which is only slightly unstable. These conditions indicate that the inlet is probably in transitory stall.

Inlets A2 and A3.—The translating centerbody was tested in two additional configurations obtained by translating the centerbody aft 2.54 cm (1.0 in)—inlet A2—and 3.81 cm (1.5 in)—inlet A3. These configurations represent two centerbody positions that could be used to improve angle-of-attack performance at approach. They could be controlled as a function of power setting and inlet inflow angle. As the centerbody is retracted, the throat area increases, thereby decreasing the Mach number and available noise reduction at a constant power setting. The A2 and A3 inlet designs are aimed at achieving satisfactory approach operation at angle of attack while obtaining significant noise reduction at slightly reduced throat Mach numbers.

Inlet A2 and A3 approach operating characteristics are summarized in table 13. Since inlet A1 provides acceptable operation at $\alpha = 0^\circ$, inlets A2 and A3 were tested only at angle of attack. Both A2 and A3 provide operation superior to A1 at $\alpha = 20^\circ$ and $\alpha = 35^\circ$.

Inlet A2: Inlet A2 appears to operate satisfactorily within the design envelope for approach conditions (see figure 48), although performance is marginal at $\alpha = 35^\circ$ and $V = 148$ km/h (80 kn). At the latter condition the cowl boundary layer is separated in the diffuser and the airflow is unsteady for $C_D^* < 0.94$. At $C_D^* = 0.86$, this is reflected in distortion slightly greater than 10%; distortion is $< 10\%$, however, at $C_D^* = 0.72$ and 0.94 , as shown in figure 59. The compressor face maps in figures 60(a), (b), and (c) clearly show the cowl separation for $C_D^* < 0.9$; this separation is the cause of the unsteadiness and marginal performance at low inlet airflows. The compressor face map in figure 60(d), however, shows that at a slightly higher inlet airflow, $C_D^* = 0.944$, the cowl boundary layer is attached, leading to a dramatic improvement in distortion and recovery. At this C_D^* value, the centerbody shows losses that prevent even better performance. Further increases in inlet airflow increase centerbody losses and result in a normal choking pattern, figures 60(e) through (g).

Although inlet A2 shows some unstable airflows for $C_D^* < 0.84$ when operated at $\alpha = 20^\circ$ and $V = 259$ km/h (140 kn), as observed on-line, recovery and distortion performance is more than adequate, as indicated in figure 61. Siren noise source suppression curves for this condition are shown in figure 62. If the inlet were operated at $C_D^* = 0.975$ (recovery = 0.98, distortion = 10%), a siren noise source reduction of 22 dB ($\Delta\overline{SPL}$) at 3 kHz is available. Operation is also possible at other C_D^* values; for example, at $C_D^* = 0.94$ (recovery = 0.99, distortion = 6%), a reduction of 15 dB ($\Delta\overline{SPL}$) is available at 3 kHz. The compressor face maps in figures 63(a) through (g) show the flow characteristics of inlet A2 at 259 km/h (140 kn) and $\alpha = 20^\circ$. The cowl shows some separation at the lowest airflow tested, figure 63(a); however, this separation is limited, and it does not reach the centerbody, as it does in the case of low airflow at 148 km/h (80 kn), $\alpha = 35^\circ$, figure 60(a). The cowl remains attached as airflow increases, figures 63(b) through (e), resulting in good performance despite centerbody separation.

Inlet A3: Inlet A3 appears to operate satisfactorily within the design envelope for approach conditions (see figure 48), although, like inlet A2, it performs marginally at $\alpha = 35^\circ$, $V = 148$ km/h (80 kn). The flow characteristics at this condition are similar to inlet A2, but the distortion characteristics are slightly poorer (figure 64). Since data were not taken at $C_D^* \sim 0.94$ for inlet A3, it is not certain that performance is satisfactory at this important point. (Compare figures 59 and 64.)

The performance and acoustic characteristics at $\alpha = 20^\circ$, $V = 259$ km/h (140 kn) are presented in figures 65 and 66; these curves show trends similar to inlet A2, figures 61 and 62. Compressor face maps and pressure distributions also show similar trends for this run.

Operation at Approach with a Constant Power Setting.—The design size of a translating centerbody inlet is determined by the airflow at approach and the maximum airflow (usually at maximum power setting). The ratio of these airflows determines how widely the throat area ratio must be varied to maintain high throat Mach numbers. For the A inlets, this ratio is assumed to be 0.8 (approach to takeoff). If the centerbody is retracted from the A1 approach condition and the power setting remains constant, the throat area increases and the throat Mach number decreases. Since $C_D^* = (A^*/A)_{TH}$ and the hilite corrected airflow $WCAHI \sim C_D^* \cdot A_{TH}$, then, in order to maintain a constant airflow,

$$\frac{(WCAHI)_{A1}}{(WCAHI)_{A2}} = 1 = \frac{(C_D^* \cdot A_{TH})_{A1}}{(C_D^* \cdot A_{TH})_{A2}}, \text{ and}$$

$$(C_D^*)_{A2} = (C_D^*)_{A1} \cdot \frac{(A_{TH})_{A1}}{(A_{TH})_{A2}}$$

where WCAHI is the corrected airflow per unit of AHI.

Thus if inlet A1 is operating at 185 km/h (100 kn) approach speed at $\alpha = 0^\circ$ and $C_D^* = 0.975$ (table 12), and the engine must suddenly operate at $\alpha = 20^\circ$ (e.g., for an emergency), then a translation of the centerbody to the A2 position will cause the inlet C_D^* to be:

$$(C_D^*)_{A2} = 0.975 (0.99) = 0.965$$

For inlet A2 at $\alpha = 20^\circ$, $V = 185$ km/h (100 kn), and $C_D^* = 0.965$, recovery is 0.99 and distortion is 6% (figure 67), and the $\Delta\overline{SPL}$ is 20 dB (figure 68) instead of 30 dB (table 12 at 0° , 185 km/h). Operation at the same angle of attack and forward speed with the centerbody translated aft to the A3 position requires

$$(C_D^*)_{A3} = 0.975 (0.96) = 0.935$$

This provides recovery of 0.995 and distortion of 5%, as shown in figure 69, and acoustic suppression of 12 dB ($\Delta\overline{SPL}$ at 3 kHz), figure 70.

Comparison of Analysis With Data

A comparison of the predicted and measured surface Mach number distributions for a static case in the takeoff configuration is given in figure 71. The static analysis does not include viscous effects. The agreement is close until the throat region on the centerbody, where the importance of viscous effects are more significant. The measured Mach number is higher at the centerbody throat because of boundary layer displacement thickness effects, which also cause higher cowl surface Mach numbers in the diffuser. Centerbody separation is evident in the data, and the measured downstream cowl Mach number is higher relative to analysis due to the effective area change. The important aspects of the flow into the throat region are predicted well.

Comparisons for the takeoff mode where the analysis includes boundary layer effects are given in figures 72 and 73. Some centerbody separation is evident in both figures, although reattachment is indicated for the case of $V = 324$ km/h (175 kn). Separation was not predicted, but the analysis did show very high H_j values (above 2.2), indicating that separation could occur because of highly distorted velocity profiles. The data and analysis are in reasonable agreement into the throat region. For the case shown in figure 73 (324 km/h (175 kn) for analysis, 306 km/h (165 kn) for data), centerbody separation effects are limited, and the results agree in the diffuser.

Comparisons of analysis with data at two different throat Mach numbers for the static condition at approach are given in figures 74 and 75. The analysis at a nominal throat Mach number of 0.8 ($C_D^* = 0.963$), shown in figure 75, has more pronounced Mach number peaks in the throat and stronger adverse gradients downstream than the 0.7 nominal throat Mach number ($C_D^* = 0.914$) analysis of figure 74. This "peaking" is not seen in the measured data, probably because the flowfield is modified by the boundary layer. Except for the predicted peaks, the data and analysis agree closely for both throat Mach numbers through and past the throat, but separation is indicated in the diffuser. The data from the appropriate compressor face distortion maps show that the diffuser separates on the cowl. Comparisons between analysis and data for the approach configuration at two forward speeds are presented in figures 76 and 77. In both cases, the agreement between predicted and measured data is excellent through the entire inlet.

The predicted regions of diffuser separation as a function of forward speed and C_D^* are compared with test data in figure 78; both takeoff and approach are shown. Since C_D^* was not precisely defined in the testing, the measured data show the approximate value at which separation was encountered. For the approach configuration, the test results indicate that the inlet operates without separation at slightly higher flow coefficients (or throat Mach numbers) than predicted; for the takeoff configuration, data show that the inlet separates at slightly lower throat Mach numbers than predicted. The value of X/L^* at which separation occurs was correctly predicted for both configurations.

As discussed previously in this report, in the "Analytical Design" section, an analysis was made to predict the windward internal cowl surface Mach number distribution for the translating centerbody inlet in the takeoff configuration with a 65-km/h (35-kn) crosswind. The predicted Mach number distribution, together with test data, is presented in figure 79. The data are for a lower C_D^* value than the analysis. Overall, the agreement between

prediction and test results is good. The only significant difference occurs at the hilite, where the Mach number in the data is higher. This higher number is probably the result of a discontinuity in radius of curvature between the inner and outer contour at the hilite.

Inlet A1 angle-of-attack performance in the approach configuration was not satisfactory. The problem did not involve the lip, but rather the diffuser. To provide improved performance, the diffuser was analyzed with the centerbody translated aft slightly to change the diffuser area distribution while causing only minimal changes in throat area. The surface Mach number distributions for inlets A1, A2, and A3 at $\alpha = 35^\circ$ and $V = 148$ km/h (80 kn) are presented in figure 80 for the windward side of the cowl and in figure 81 for the leeward side of the centerbody for similar throat Mach numbers. Inlet A1 exhibits a diffuser separation (also identified on the cowl windward side in the compressor face distortion maps); inlets A2 and A3 do not show separation. In addition, A2 shows a lower peak cowl Mach number than A3 (figure 80). There is evidence of possible centerbody separation in the diffuser for inlet A1, but not for inlets A2 and A3 (figure 81). Inlet A2 has the lowest peak Mach number.

From the preceding, it is concluded that inlets A2 and A3 are improvements over A1, and that A2 may be slightly better than A3.

RADIAL VANE INLET

A new cowl lip was designed to fit the radial vane sonic inlet described in reference 1. The aim was to test the performance at forward speed and angle of attack, and, if appropriate, to redesign the lip to improve the operating characteristics.

Takeoff

Radial vane inlet B provides excellent performance and noise reduction characteristics in the takeoff configuration (vanes removed), as shown in table 14(a). The flow is stable for all operating conditions, recovery is generally high, distortion is low, and the noise curves roll off at lower CD^* than is the case for approach. Recovery and distortion, although variable, are good for most runs. The best recovery and distortion occur at $\alpha = 0^\circ$, $V = 315$ km/h (170 kn), figure 82, and the poorest occur at $\alpha = 90^\circ$, $V = 65$ km/h (35 kn), figure 83. The noise level curves for takeoff are similar for all inflow angles and tunnel speeds tested; the roll-off of sound level with CD^* is shown in figures 84 through 87.

The flow remains attached to the cowl for nearly all inlet airflows at all inflow angles and at all tunnel velocities. The compressor face maps for the test run showing the poorest aerodynamic performance are given in figures 88(a) through (h). Only figure 88(a), which maps total pressure recovery at a throat Mach number of 0.163, shows cowl separation (at the hilite). All other conditions mapped in figure 88 show attached flow and normal patterns approaching choked flow.

Approach

At approach (vanes exposed), the radial vane inlet exhibits aerodynamically stable inlet flows, high recovery, and low distortion throughout all the conditions tested. However, the

acoustic suppression does not meet the evaluation criterion outlined earlier (see figure 49 and table 14). For this reason, the inlet operation is rated as marginal at all approach conditions that require acoustic suppression. Suppression of the siren noise signal is inhibited apparently by the presence of the vanes. The cause of comparatively poor acoustic suppression may be related to the fact that the C_D^* required for acceptable performance is lower for this inlet at approach than for any other inlet tested at approach or takeoff, thus indicating increased blockage due to boundary layer and flow nonuniformity.

A study of the approach compressor face maps in figures 89(a) through (h) reveals that the vanes are "straightening" the flow and that the total pressure loss patterns are not dependent on either forward speed or angle of attack. The corrected inlet airflows contained in these maps are nearly the same at inflow angles of 0° , 20° , and 35° at various tunnel speeds. The loss patterns show concentration of low total pressure near the centerbody, even at $\alpha = 20^\circ$ and $\alpha = 35^\circ$. A boundary layer analysis made prior to the test runs indicated that separation would occur on the trailing edge of the vanes at relatively low vane throat Mach numbers, and that vane blockage would be greater near the centerbody. It was predicted that the vane separation would result in reduced recovery and increased distortion, and that the variation in vane blockage would result in more gradual inlet choking, starting near the centerbody and progressing across the vane. The test results confirm these predictions.

The cowl lip pressure distribution differs for each of the conditions of figure 89, but the diffuser pressure gradients are almost identical. The pressure distributions on the cowl for four selected conditions are presented in figures 90(a) through (d).

Unlike the takeoff recovery and distortion performance curves, which are variable, the approach performance curves for all test runs are nearly identical. The two curves that show the widest variations are for $V = 148$ km/h (80 kn) at $\alpha = 0^\circ$ and $V = 185$ km/h (100 kn) at $\alpha = 35^\circ$, figures 91 and 92, respectively. The approach noise curves for the radial vane inlet are shown in figures 93 through 96; these can be compared with the A inlet approach curves in figures 62, 68, and 70. The radial vane approach curves differ from curves typical of other inlets in that the roll-off of the noise level is delayed and steeper. (Note that the noise curves for the radial vane inlet at takeoff, figures 84 through 87, are much more favorable than at approach.) The noise level roll-off at approach generally occurs at $C_D^* > 0.95$, but the operating C_D^* usually is < 0.95 , table 14(b). The result is low $\Delta \overline{SPL}$'s and a rating of marginal operation at approach.

Comparison of Analysis With Data

Full flowfield predictions require a three-dimensional analysis for the approach configuration because the vanes are in the flow passage; therefore, they were made only for the takeoff configuration. (Approximate analyses were made for the approach configuration.)

Comparisons of analysis with data for static conditions at two different inlet flows are shown in figures 97 and 98. In both cases, the hilite Mach number of the data is higher than analysis. As with the translating centerbody inlet, this may be due to a break in curvature at the hilite. The figures show that the Mach number across the lip is slightly

lower in the data, compared to analysis, but that the analysis and data agree very well with respect to the shape of the curve. The agreement in the throat region is very close. In the diffuser, the data show a higher Mach number than analysis; this is as expected, since the analysis for static conditions does not include boundary layer displacement thickness effects.

Comparisons between analysis and data for surface Mach numbers at $V = 148$ km/h (80 kn) are made in figures 99 and 100. The lower throat Mach number data, figure 99, show very good agreement with the analysis, although there is some variation in the diffuser. At the higher throat Mach number, figure 100, the data show a definite Mach number peaking behind the throat in the diffuser. This is associated with choking and resultant shocks. The higher data Mach numbers in the diffuser are a result of the higher corrected airflow, together with boundary layer distortion and thickening due to the shocks in the diffuser.

Comparisons of data and analysis at $V = 259$ km/h (140 kn) and $V = 324$ km/h (175 kn) are shown in figures 101 and 102, respectively. In both cases, the agreement between data and analysis is very good. The locally higher Mach numbers in the diffuser upstream of the compressor face station may be due to excessive boundary layer distortion or local separation and reattachment.

QCSEE HIGH THROAT MACH NUMBER INLETS

The aim of the investigation of the QCSEE inlet designs is to explore an inlet/engine concept where the inlet provides noise attenuation at high throat Mach numbers with a fixed inlet geometry. Variable geometry in the engine system provides the thrust variations required for approach, takeoff, and cruise, thereby keeping the inlet corrected airflow requirements nearly the same for these operating modes. In addition, consideration is given to using peripheral acoustic lining to provide noise attenuation for lower airflows. However, the inlets were tested without acoustic lining. The rationale for the design of the various C inlets is described in the "Analytical Inlet Design" section that appears earlier in this report.

Inlet C1

The performance and characteristics of inlet C1 are given in figure 50 and table 15(a). The inlet operates well at $\alpha = 0^\circ$ and $\alpha = 20^\circ$, with suppression of the siren source noise signal ranging from 25 to 34 dB (Δ SPL) at 3 kHz. At $\alpha = 50^\circ$, $V = 148$ km/h (80 kn) and $\alpha = 90^\circ$, $V = 65$ km/h (35 kn), flow separation is encountered.

The recovery and distortion curves for the high angle-of-attack conditions are shown in figures 103 and 104. Compressor face maps for $\alpha = 50^\circ$, $V = 148$ km/h (80 kn) are shown in figures 105(a) through (d); cowl static pressure distributions are shown in figures 106(a) through (d). For all inlet airflows, losses are concentrated at the 180° position on the cowl; lip separation occurs for the lower airflow shown in figure 106(a), and diffuser separation occurs for the larger airflows in figures 106(b) through (d). These separations are associated with the severe distortion patterns of figures 105(a) through (d). The lip design does not produce the type of pressure distribution necessary for proper operation of the diffuser.

Although inlet operation is good at $V = 0$, $\alpha = 0^\circ$, some instability occurs at high airflows. Operation is stable at $C_D^* \sim 0.95$ or less—see, for example, figures 107(a) and (b)—but transitory stall occurs for $C_D^* > 0.95$, and nonaxisymmetric separation losses appear, figures 107(c) and (d). Analysis of pressure distributions (see the discussion following on “Comparison of Analysis with Data”) shows that diffuser separation is occurring for the case of figure 107(c). The recovery and distortion are very good below $C_D^* = 0.97$ (figure 108), which is the value of C_D^* for the compressor face map shown in figure 107(c).

Inlets C2, C3, and C4

Since inlet C1 performance at $\alpha = 50^\circ$ and $\alpha = 90^\circ$ is poor, additional cowl lips were designed to improve performance at these high angles of attack while maintaining good performance and suppression characteristics at $\alpha = 0^\circ$ and $\alpha = 20^\circ$. Inlets C2, C3, and C4 are designs developed to gain such improvements.

Figure 109 presents a performance summary for the C inlets at the high angles of attack. Inlets C2 and C2-A (C2 was designated as C2-A after the inlet hilite region was smoothed) show improved recovery and reduced distortion at $\alpha = 90^\circ$. Inlet C3 does not improve recovery or distortion at $\alpha = 50^\circ$ and $V = 148$ km/h (80 kn), so no further testing was done on this inlet. Inlet C4 and inlet C5, the NASA design, provide the best operation. Both inlets show separation-free operation near the design throat Mach number of 0.79 ($C_D^* \sim 0.957$) and meet the design objective. However, separation and distortion $> 10\%$ occur at lower airflows. Therefore, inlets C4 and C5 were each tested for one run at 140 km/h (75 kn); inlet C4 shows a small improvement in distortion.

The summary of inlet C4 operation is given in figure 50 and table 15(b). The characteristics of inlet C4 are similar to those for C1 at $\alpha = 0^\circ$ and $\alpha = 20^\circ$. At $\alpha = 50^\circ$ and $\alpha = 90^\circ$, the performance is much improved, with stable operation indicated at both $\alpha = 90^\circ$, $V = 65$ km/h (35 kn) and $\alpha = 50^\circ$, $V = 148$ km/h (80 kn). At the 50° condition, however, inlet separation is experienced at low airflows, leading to reduced recovery and increased distortion (figure 110). The operation is therefore rated as marginal in table 15(b). An additional test case was run at 140 km/h (75 kn), and the stable operating range and performance increased (figure 111). This condition is rated as good in table 15(b). Compressor face maps for this run are presented in figures 112(a) through (d).

Inlet C5

The design of inlet C5 was furnished by NASA for test evaluation. The results are summarized in figure 50 and table 15(c). Good inlet operation, comparable to inlet C4, is provided. Like C4, the operation of C5 at $\alpha = 50^\circ$ and $V = 148$ km/h (80 kn) at high airflows is good. However, it is rated as marginal in the table due to unstable operating characteristics at low airflows. A test was run at $\alpha = 50^\circ$, $V = 140$ km/h (75 kn), but the inlet operation is still unstable at lower airflows. Inlet C5 recovery and distortion are shown in figure 113. The poor operation at C_D^* between 0.54 and 0.65 is caused by unstable separation (observed on-line). Comparable unstable operation was not observed on-line for inlet C4, and data were not taken below $C_D^* = 0.75$ (figure 111).

Comparison of Analysis With Data

Several variations of the QCSEE inlet were analyzed and tested, the important ones being C1, C4, and C5. All have the same diffuser and spinner, but differ in lip and external cowl shape. The design of inlet C1 is based on potential flow analysis at 0° inflow angle for static and 148-km/h (80-kn) conditions. The design of inlets C3 and C4 is based on examination of the angle of attack and crosswind results for the inlets previously tested, and selection of lip shapes that redistribute lip curvature to improve on earlier results. Inlet C5 employs a lip shape developed by NASA Lewis.

Comparisons of analysis and data for the static and 148-km/h (80-kn) conditions are given for inlet C1 in figures 114 and 115, for inlet C4 in figures 116 and 117, and for inlet C5 in figures 118 and 119. A high-aspect-ratio lip shape was chosen for inlet C1, the initial configuration, because it provides the lowest lip Mach number peak and the lowest strength of the adverse pressure gradient into the diffuser. The lip Mach number peak gets higher and the adverse gradient into the diffuser stronger as the lip aspect ratio goes down (C4 and C5). The C1 static case, shown in figure 114, indicates unexpected diffuser separation, while the lip and throat flow agree very well. Small differences in diffuser Mach number distribution are evident for other cases, but analysis and data are in excellent agreement. The diffuser Mach numbers are higher in figure 114 due to these separation effects. The potential flow analysis is a design aid that provides very good flowfield definition.

An important conclusion drawn from the C inlet design study is that the analysis for 0° angle of attack is not a sufficient tool if severe angle of attack and crosswind requirements must be met. The long lip of C1 proved to have very high Mach numbers and strong adverse pressure gradients at high angle of attack and crosswind. Figures 120 and 121 provide such data for $\alpha = 50^\circ$, $V = 148$ km/h (80 kn), and $\alpha = 90^\circ$, $V = 65$ km/h (35 kn), respectively.

Inlet C4 was designed to improve high angle-of-attack performance. The external cowl is more blunt, to reduce the hilite Mach number peak, and the lip aspect ratio and shape are changed to redistribute the local radius of curvature—thus changing the Mach number distribution. The results for $\alpha = 50^\circ$, $V = 148$ km/h (80 kn), and $\alpha = 90^\circ$, $V = 65$ km/h (35 kn), shown in figures 122 and 123, respectively, meet the desired objectives. The hilite Mach number peaks are reduced, and a more favorable Mach number distribution across the lip and into the diffuser is achieved. In addition, the apparent diffuser separation is reduced or eliminated.

Inlet C5, the NASA Lewis design, has a lip shape that is shorter but otherwise very similar to that of C4. It is therefore not surprising that the results for $\alpha = 50^\circ$, $V = 148$ km/h (80 kn), and $\alpha = 90^\circ$, $V = 65$ km/h (35 kn), shown in figures 124 and 125, respectively, are very similar to C4 results for these inflow angles and forward speeds. The C5 results show that the hilite Mach number peak is much reduced and the diffuser separation is reduced or eliminated compared with C1 data.

DYNAMIC PRESSURE DISTORTION

Dynamic pressure instrumentation caused considerable difficulty during testing. Limited data are available, however, and ΔP_{rms} values are given for some of the inlets in figures 126 through 130. (See figures 12, 14, and 17 for locations of the dynamic probes.)

The highest dynamic distortion levels are recorded for inlet C1 near choke, reaching nearly 6% (figure 130). However, for most cases shown, dynamic distortion levels are low over the normal operating range of the inlets. Inlets A2 and A3 are the exceptions, showing slightly higher levels (figure 126).

Forward speed does not materially change the dynamic distortion for any of the inlets except inlet C1 (figure 130).

CONCLUSIONS

- At 0° inflow angles, the aerodynamic performance generally shows improvement with forward velocity for the inlets tested.
- The aerodynamic performance penalties generally are more severe at angle of attack; however, all inlets that had poor or marginal operation were modified and retested, and significant improvements resulted.
- There is no consistent trend in the variation of acoustic suppression characteristics with forward velocity at 0° inflow angle; however, QCSEE high Mach number inlets C4 and C5 show a reduction in noise suppression at forward velocity relative to the $V = 0$ measurements.
- All inlets tested provide significant noise suppression at increasing throat airflow; only the radial vane inlet at approach (vanes exposed) shows large aerodynamic penalties to obtain large noise suppression.
- The translating centerbody, as designed, functions well at all conditions except approach at 20° and 35° inflow angles; by controlling the centerbody as a function of power setting and inflow angle, it is possible to maintain satisfactory performance by trading only a small amount of noise suppression.
- Both the NASA and the Boeing QCSEE inlet designs provide good aerodynamic performance and noise suppression at high throat Mach numbers. At 50° inflow angle and forward velocity of 148 km/h (80 kn), separation-free operation is obtained near the design throat Mach number of 0.79; however, separation is experienced at lower airflows, and distortion is 12%.
- The variation of recovery and distortion with noise suppression for the translating centerbody and radial vane inlets follows the trends shown in reference 1 for similar inlets operated in front of a model scale fan. Note, however, that the data of reference 1 for the model fan were scaled to PNL, which includes directivity effects, while the noise signal reductions reported here are for a siren source and are uncorrected $\Delta\overline{\text{SPL}}$'s at the siren fundamental frequency of 3 kHz.
- Except for the radial vane inlet at approach, measured noise reductions ($\Delta\overline{\text{SPL}}$ at 3 kHz) are generally 20 to 30 dB at recoveries > 0.97 and distortion levels $< 10\%$. In many instances, however, the facility noise floor limited the amount of reduction that could be measured, and values of 30 to 40 dB as shown in the tests of reference 1 are probable.
- Although poor inlet aerodynamic performance is associated with separation and instability, some evidence indicates that separation in the diffuser increases noise suppression, probably because of the higher Mach numbers in the separated diffuser.

PRECEDING PAGE BLANK NOT FILMED

- Suitable design techniques may be combined with experimental techniques to produce proof of the feasibility of sonic inlet designs for engines with maximum-to-approach corrected airflow ratios ~ 1.25 . These techniques may also be used to rapidly design inlets for application to variable-geometry engines, such as those for the QCSEE concept.
- Axisymmetric analysis tools are effective and accurate means for predicting inlet flow characteristics at the static condition and at forward speed (for symmetrical inlets); for a particular geometry, Mach number distributions, separation, and incipient separation are readily identifiable.
- Axisymmetric analysis must be combined with experience and judgement to evolve designs for good angle-of-attack performance. Testing is required to evaluate a given design and to make a final selection.

RECOMMENDATIONS

- For QCSEE-type application concepts, acoustic lining may be required for noise suppression at approach. The effect of the acoustic lining on aerodynamic performance and noise suppression at takeoff airflow needs to be investigated.
- It is evident that significant noise suppression is obtained while all flow within the inlet is subsonic. Investigations are needed (such as refracting inlet studies) to identify the exact mechanisms involved in these noise suppressions.
- A weakness in the design tools is the lack of proven three-dimensional flow analysis capability applicable to high throat Mach number inlet design. Data from the present investigation and from other tests can be used to support the development of needed three-dimensional analyses.

SYMBOLS

GENERAL

A	area, cm ² or m ² (cross-sectional)
A*	cross-sectional area required for a given mass flow expanded to Mach 1
C _D *	inlet flow coefficient—measured mass flow divided by calculated inviscid one-dimensional mass flow at M _{TH} ≈ 1.0 through A _{TH} at PT REF
CR	contraction ratio, %, [(A _{HI} /A _{MIN cowl}) - 1] (100)
D	diameter, cm or m
FR	fineness ratio, R _{HI} /R _{MAX Cowl}
H _i	boundary layer shape factor, $H_i = \frac{\int_0^\delta [1-(u/u_e)] dy}{\int_0^\delta (u/u_e) [1-(u/u_e)] dy}$
L	inlet length, cm or m
L*	2.54 cm
M	Mach number
P	pressure, N/m ²
R	radius from inlet centerline
r	vector distance from inlet entrance center to microphone
SPL	sound pressure level, dB, re: 20 μN/m ²
$\overline{\text{SPL}}$	sound pressure level averaged from four microphones
V	velocity, km/h (also kn)
X	distance downstream from minimum cowl diameter, cm
α	inlet inflow angle (angle of attack), degrees
θ	rotational angle clockwise about inlet centerline looking downstream, degrees
φ	angle between inlet centerline and vector r to microphone location, degrees

PRECEDING PAGE BLANK NOT FILMED

SUBSCRIPTS

AV	average
HI	inlet hilite
MAX	maximum
MIN	minimum
REF	tunnel
S	static
T	total
TH	inlet throat
2	compressor face

OTHER

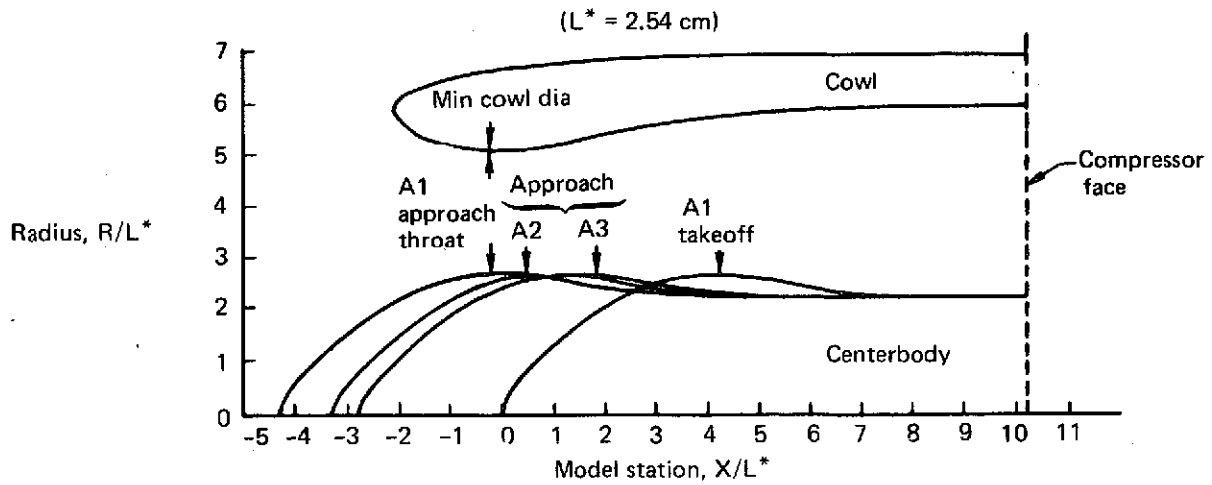
Distortion $100(P_{T \text{ MAX}} - P_{T \text{ MIN}})/P_{T \text{ AV}}$ at the compressor face

ΔP_{rms} $\left\{ \frac{1}{T} \int_{-T/2}^{T/2} (\Delta P)^2 dt \right\}^{1/2}$, where ΔP is fluctuating pressure limited to the frequency band between 10 Hz and 2000 Hz

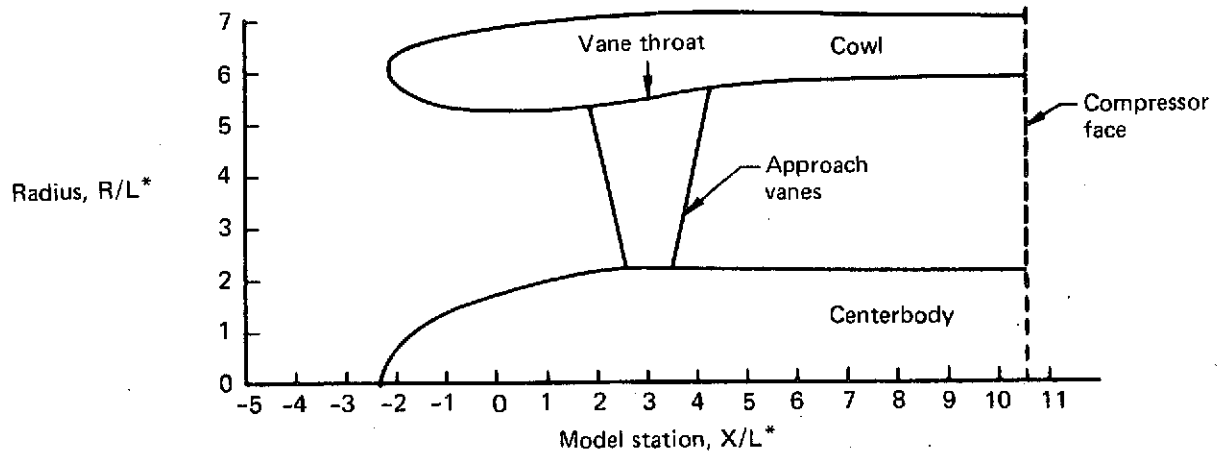
Recovery $P_{T2 \text{ AV}}/P_{T \text{ REF}}$

REFERENCES

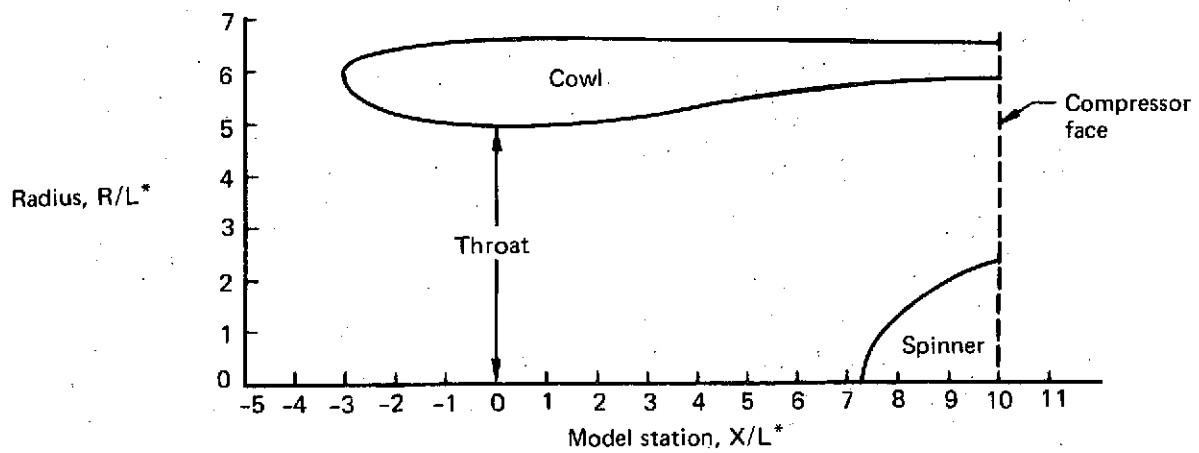
1. Klujber, F; Bosch, J. C.; Demetrick, R. W.; and Robb, W. L.: *Investigation of Noise Suppression by Sonic Inlets for Turbofan Engines*. The Boeing Company, July 1973.
Volume I—Program Summary. NASA CR 121126 (Boeing document D6-40855).
Volume II—Appendixes. NASA CR 121127 (Boeing document D6-40855-1).
Volume III—An Experimental Investigation of the Internal Noise Field of Two Model Axisymmetric Sonic Inlets. NASA CR 121128 (Boeing document D6-40818).
2. Shaut, L. A.: *Results of an Experimental Investigation of Total Pressure Performance and Noise Reduction of an Airfoil Grid Inlet*. Boeing document D6-23276, 1969.
3. Albers, J. A.; and Miller, B. A.: *Effect of Subsonic Inlet Lip Geometry on Predicted Surface and Flow Mach Number Distribution*. NASA TN D-7446, 1973.



(a) Translating Centerbody Inlets A1, A2, and A3—Approach and Takeoff Positions



(b) Radial Vane Inlet B—Approach (Vanes in Flow)



(c) QCSEE High Mach Number Inlet C4 (Fixed Geometry)

Figure 1.—Inlet Concepts Investigated at Forward Speed and Angle of Attack

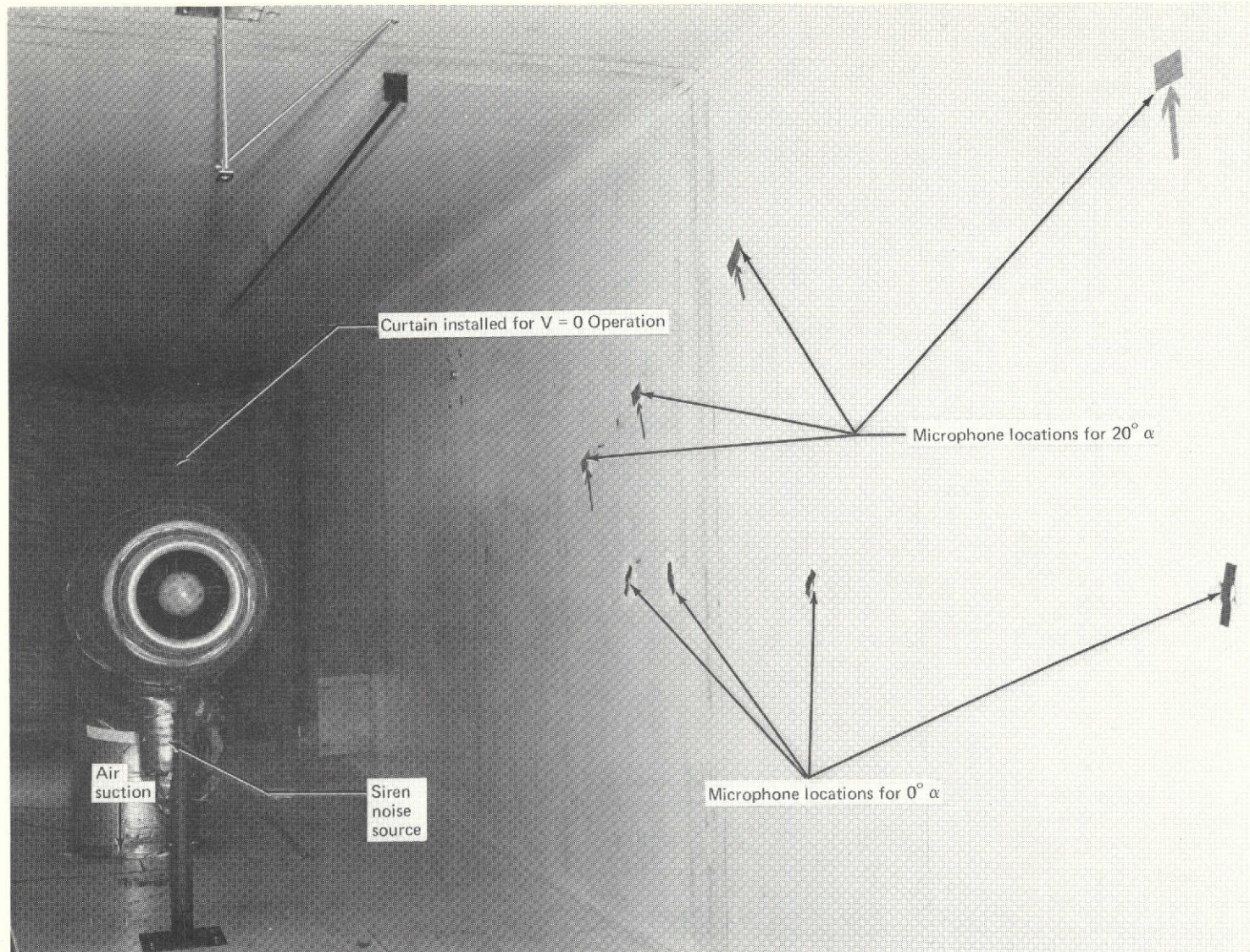
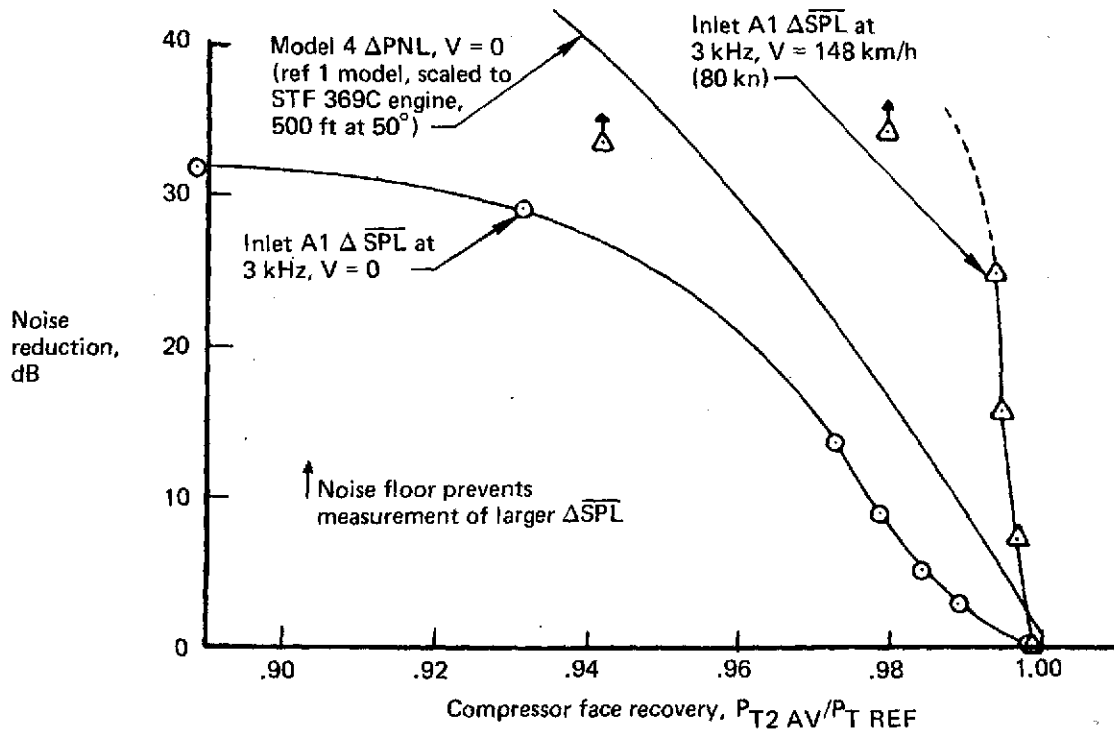
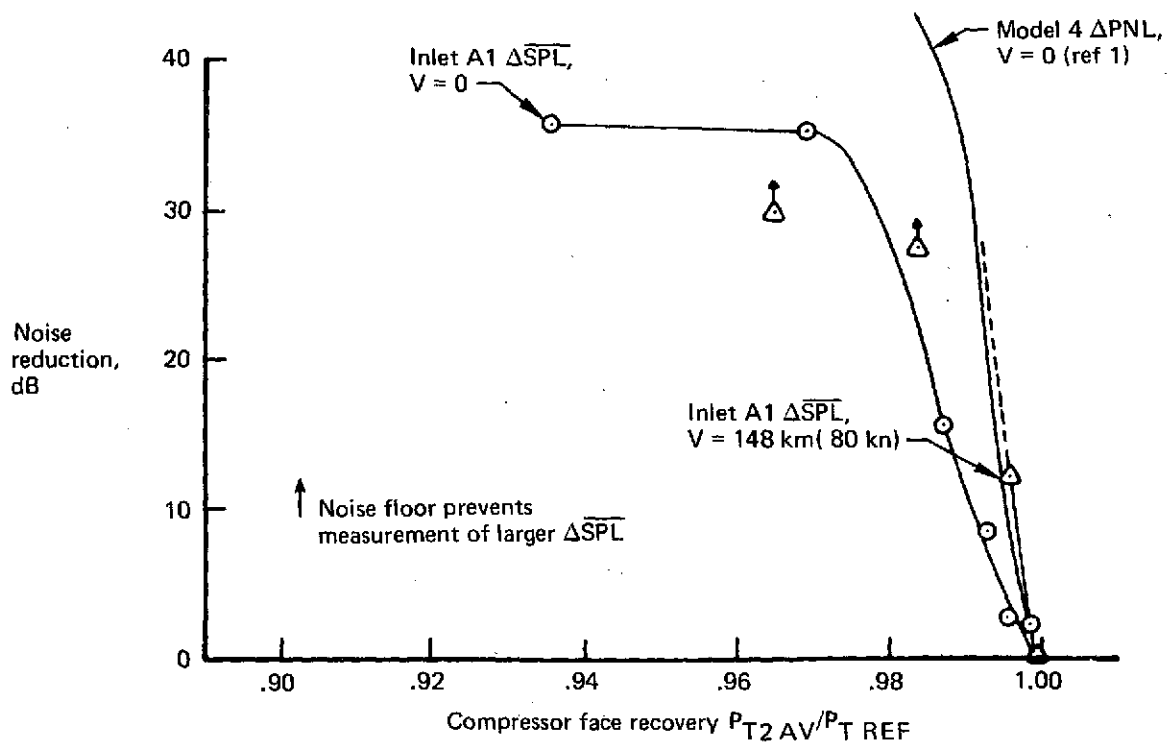


Figure 2.—Typical Test Arrangement—Translating Centerbody Inlet A1 Installed at $\alpha = 0^\circ$

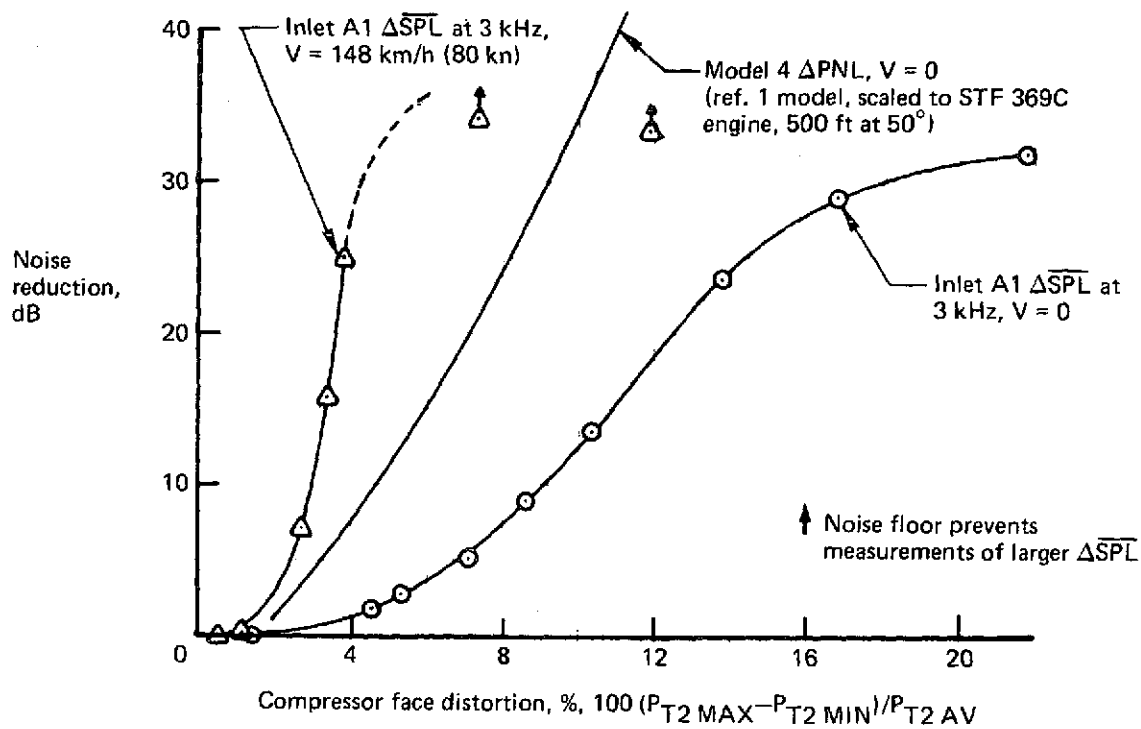


(a) Approach

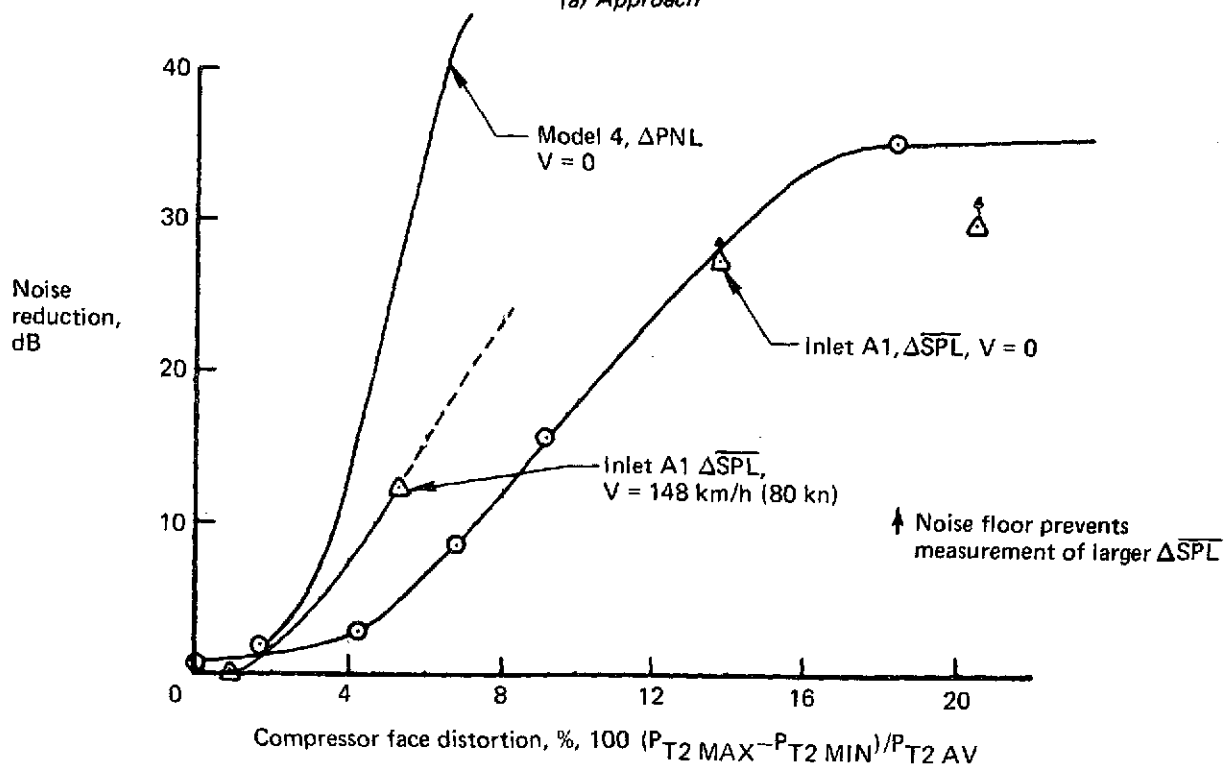


(b) Takeoff

Figure 3.—Variation of Recovery With Noise Reduction—Translating Centerbody Inlet A1 at $\alpha = 0^\circ$



(a) Approach



(b) Takeoff

Figure 4.—Variation of Distortion With Noise Reduction—Translating Centerbody Inlet A1 at $\alpha = 0^\circ$

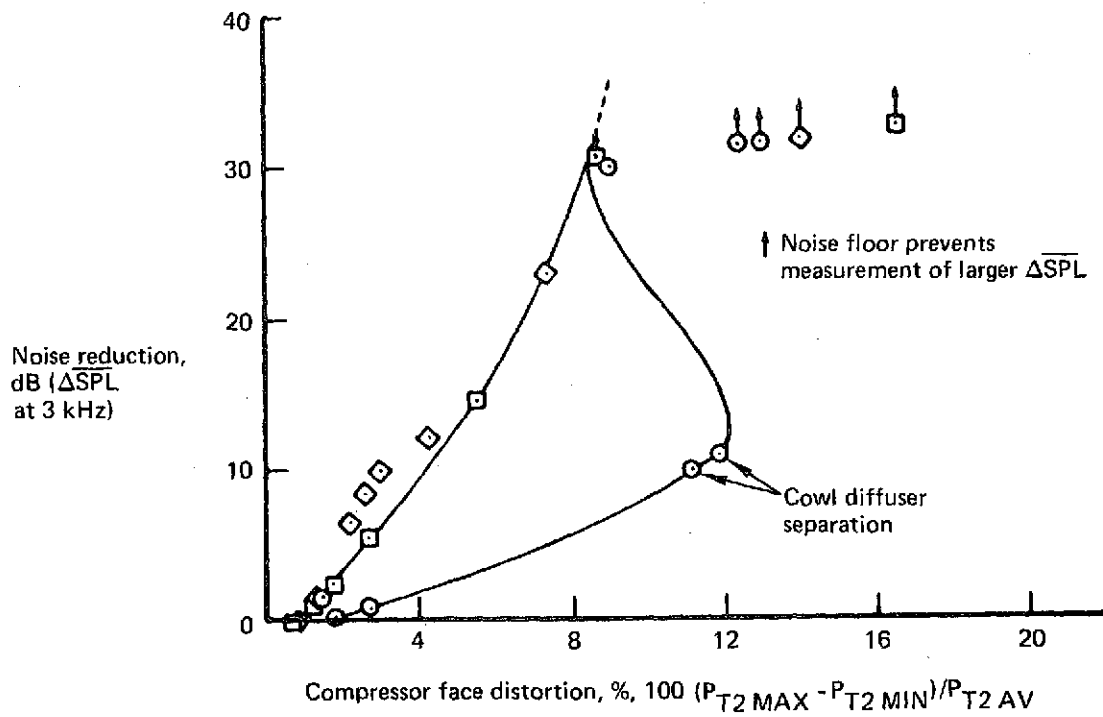
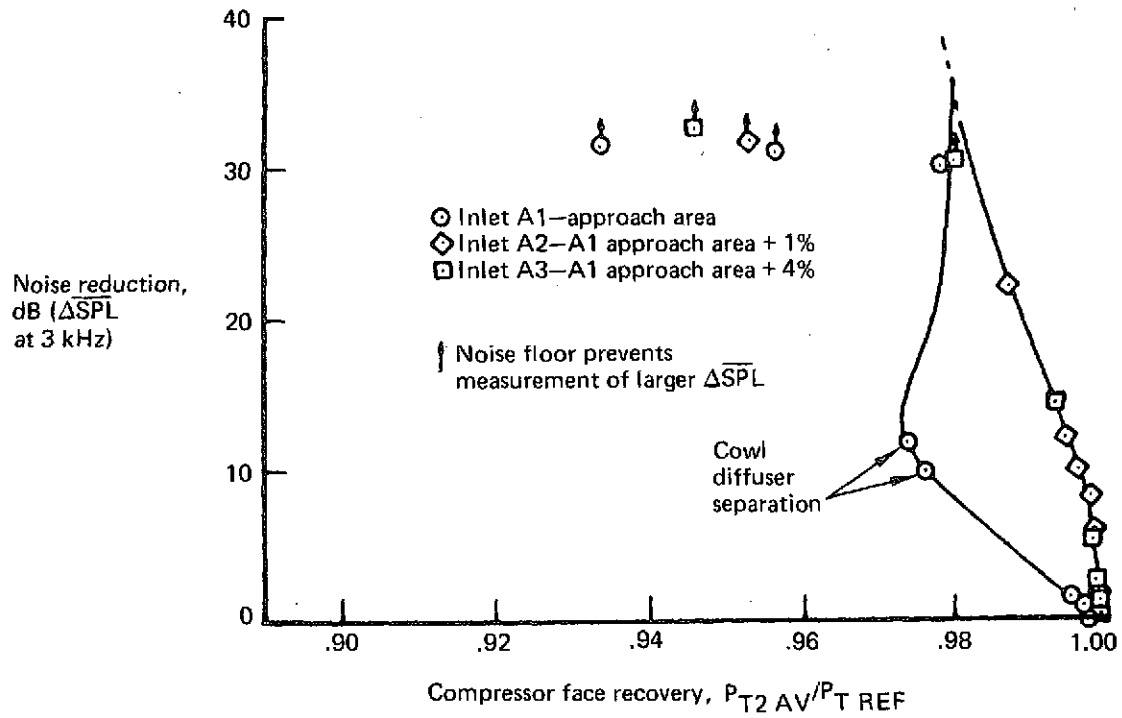
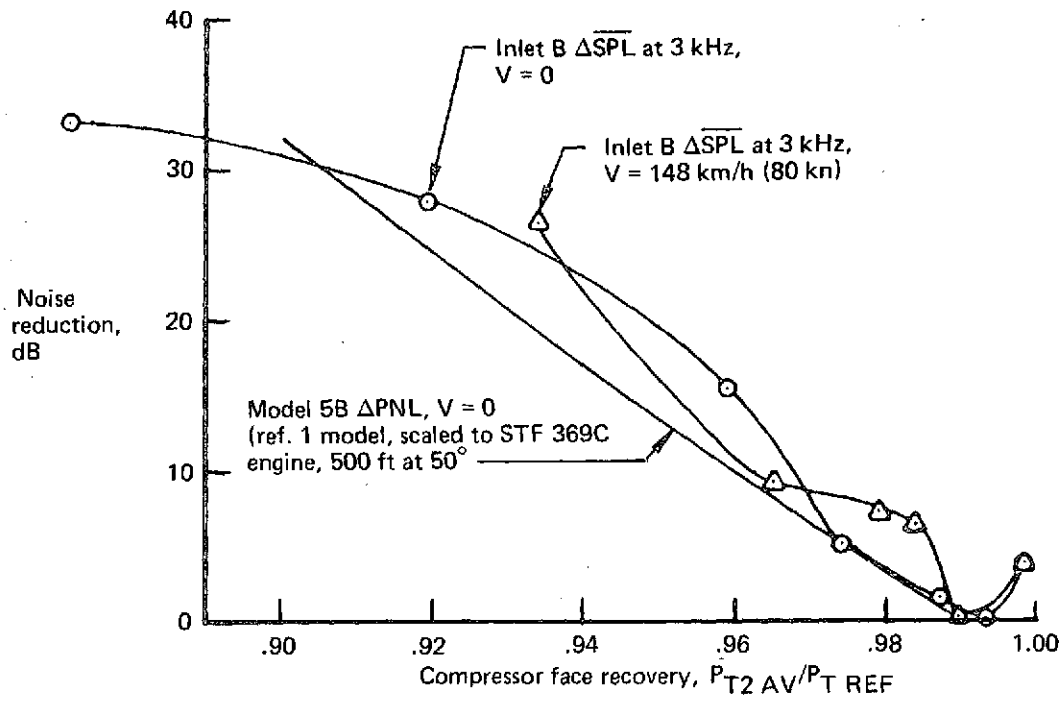
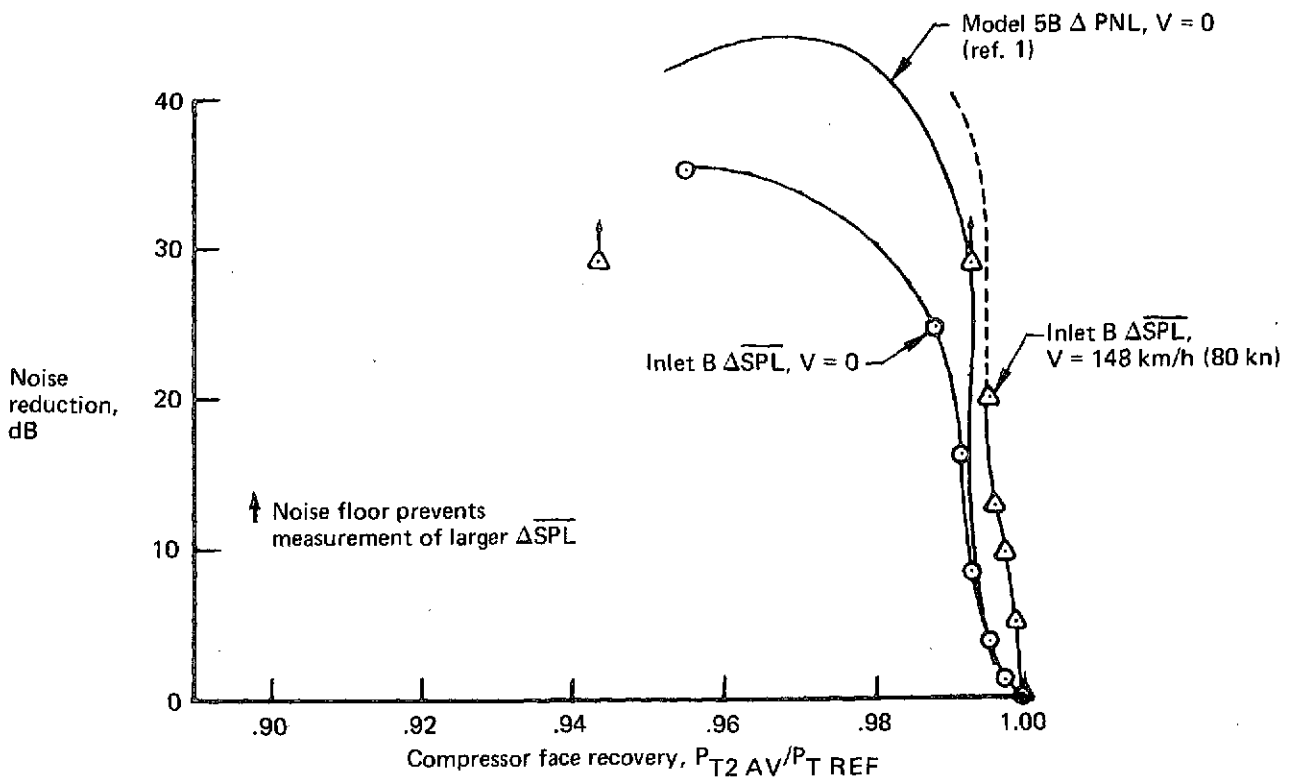


Figure 5.—Variation of Recovery and Distortion With Noise Reduction—Translating Centerbody Inlets A1, A2, and A3 at $\alpha = 20^\circ$, $V = 185 \text{ km/h (100 kn)}$

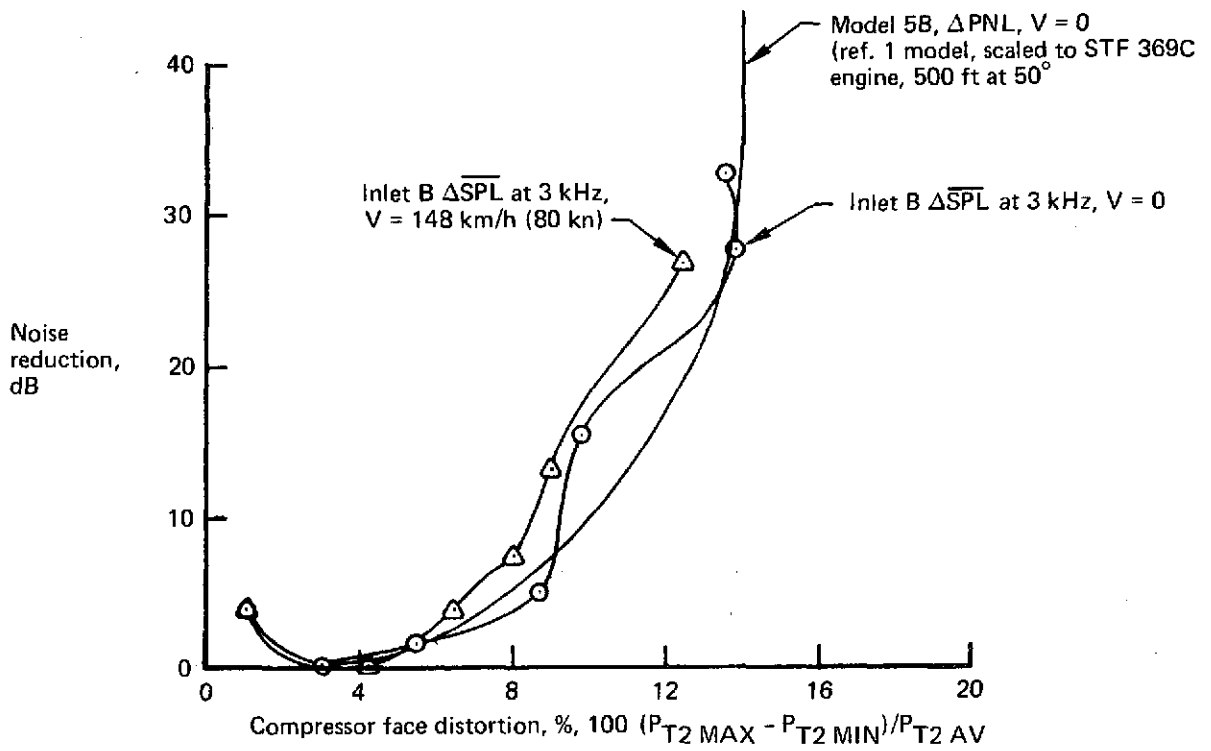


(a) Approach (Vaness Exposed)

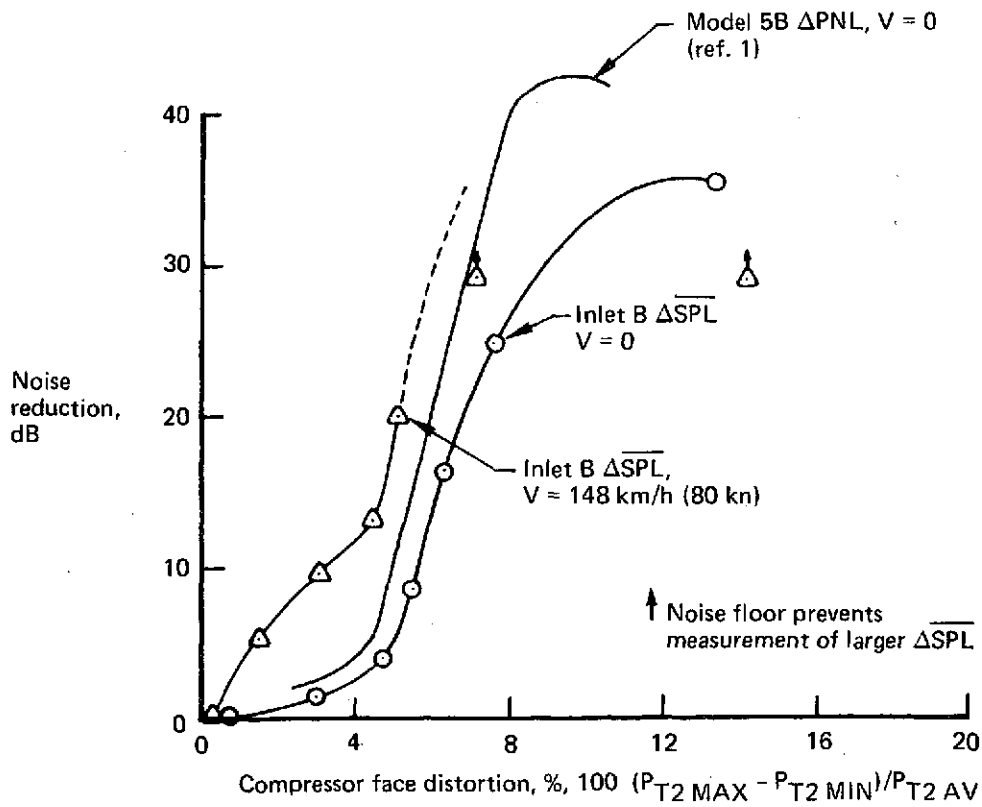


(b) Takeoff (Vaness Removed)

Figure 6.—Variation of Recovery With Noise Reduction—Radial Vane Inlet B at $\alpha = 0^\circ$



(a) Approach (Vanes Exposed)



(b) Takeoff (Vanes Removed)

Figure 7.—Variation of Distortion With Noise Reduction—Radial Vane Inlet B at $\alpha = 0^\circ$

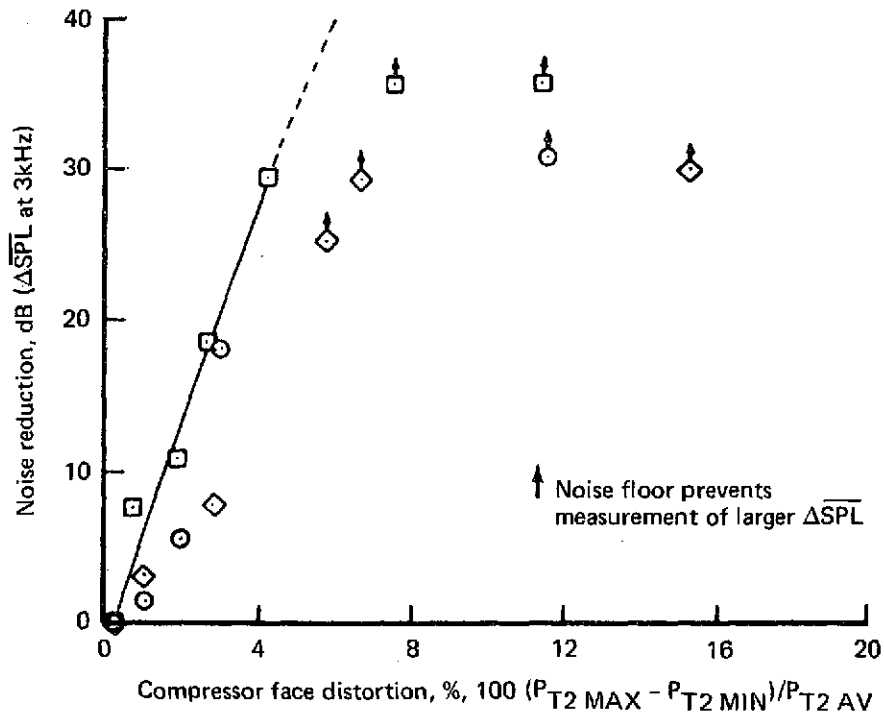
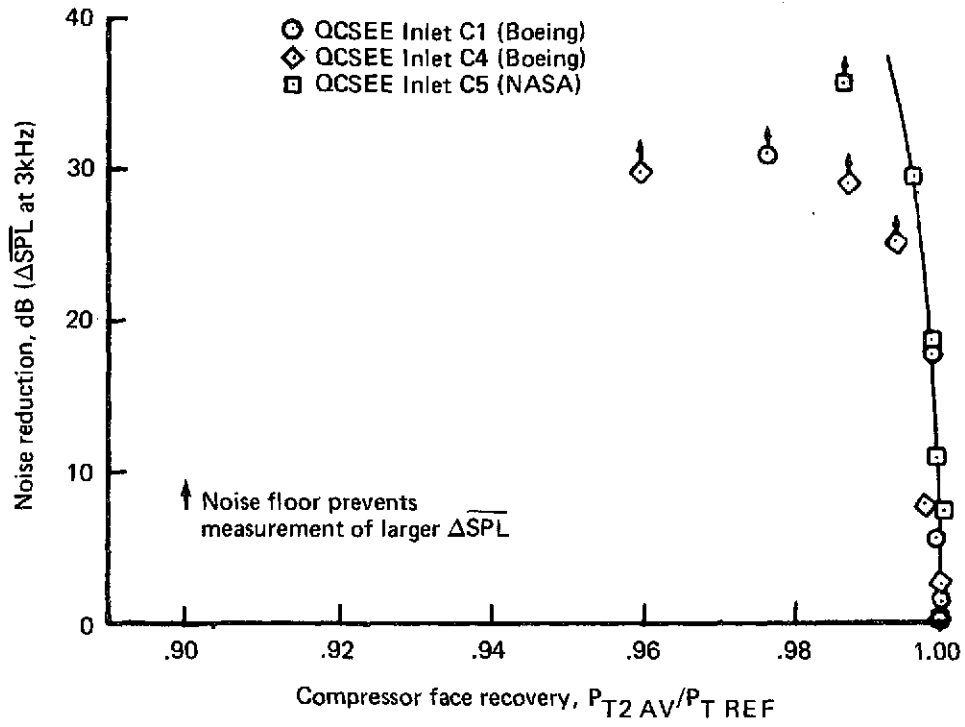


Figure 8.—Variation of Recovery and Distortion With Noise Reduction—
 QCSEE High Mach Number Inlets C1, C4, and C5 at $\alpha = 0^\circ$,
 $V = 148 \text{ km/h (80 kn)}$

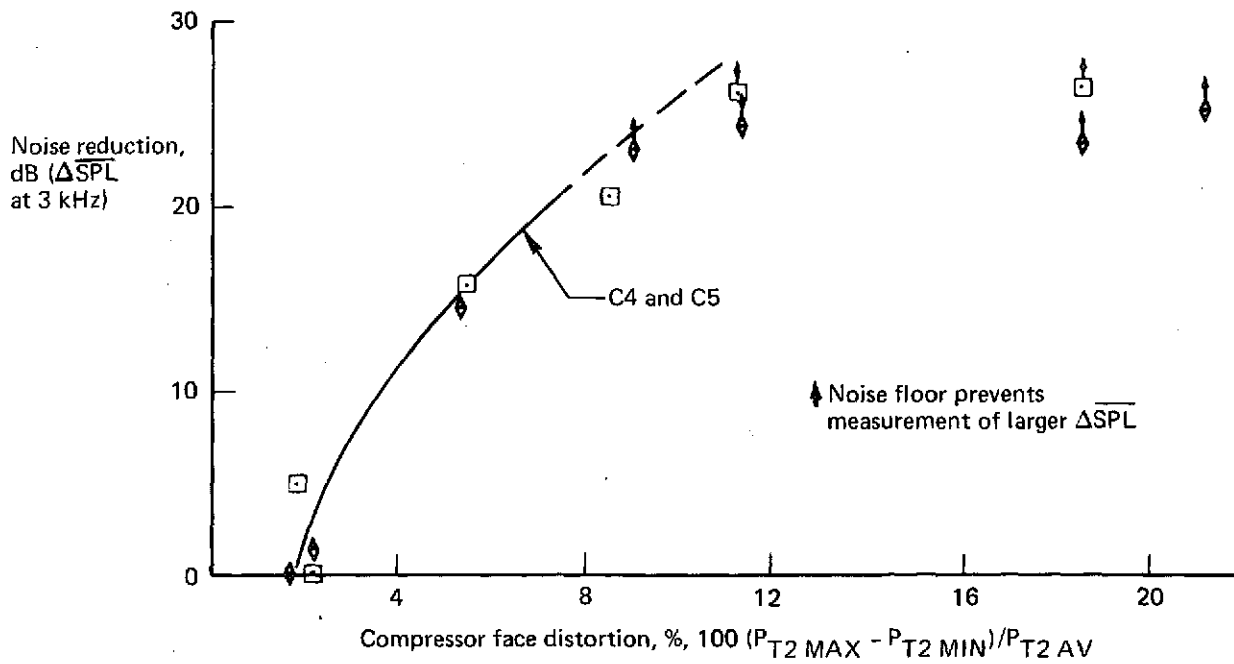
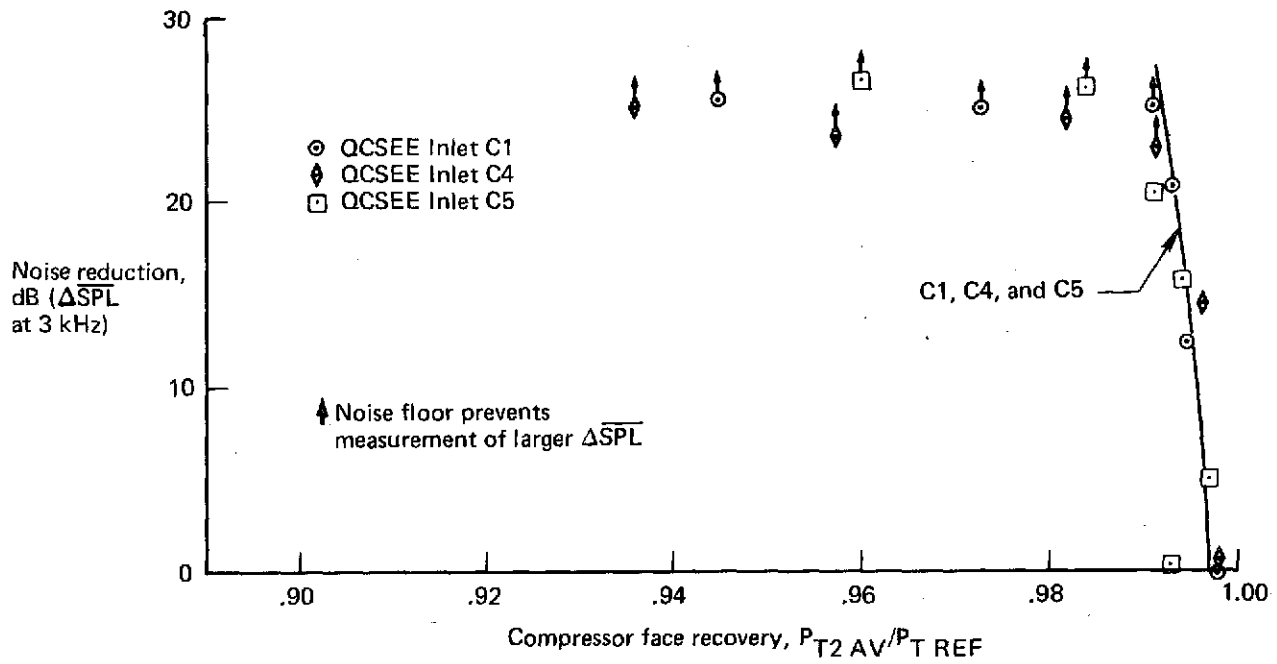


Figure 9.—Variation of Recovery and Distortion With Noise Reduction—
 QCSEE High Mach Number Inlets C1, C4, and C5 at $\alpha = 20^\circ$
 $V = 306 \text{ km/h (165 kn)}$

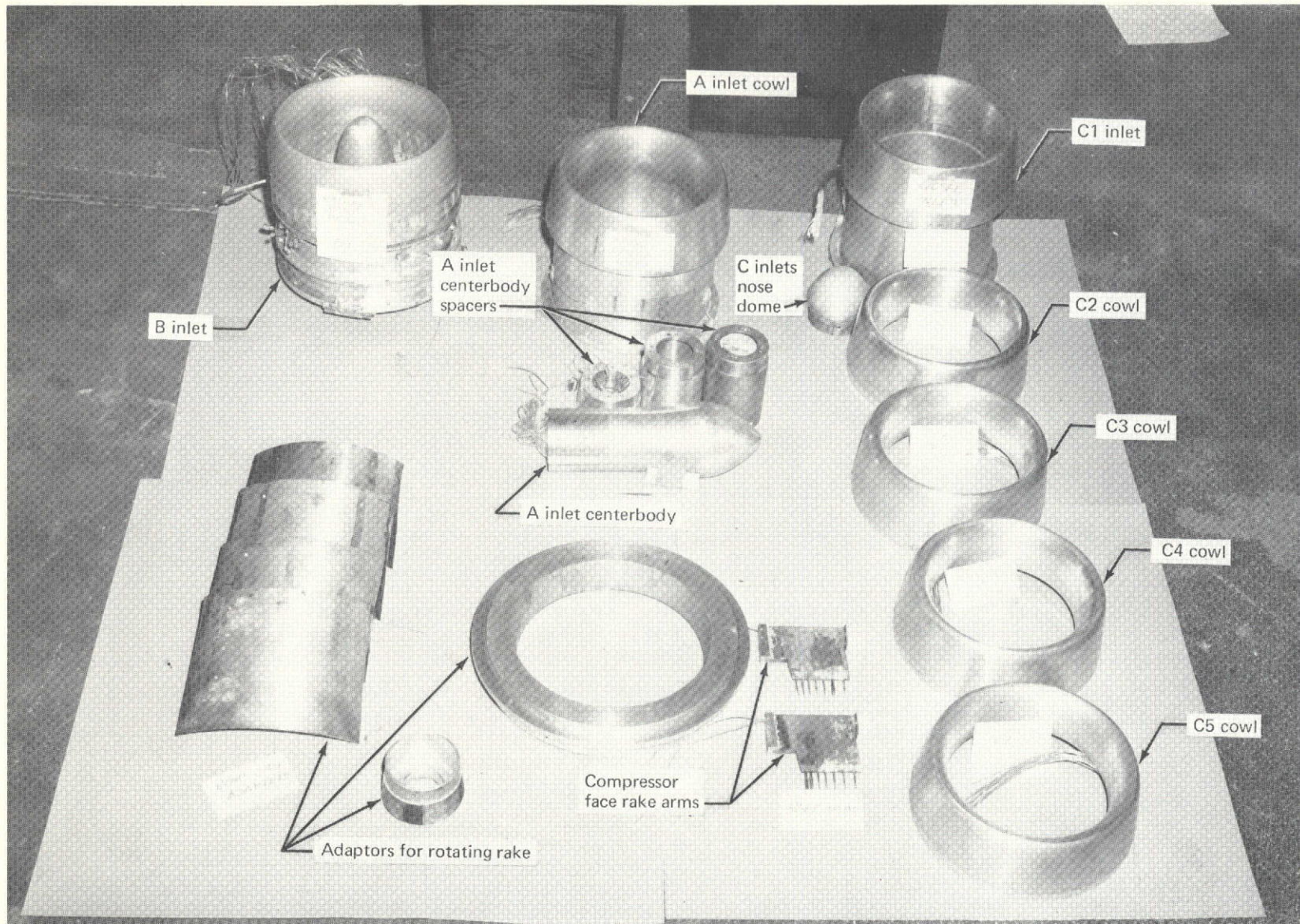


Figure 10.—Inlet Model Parts

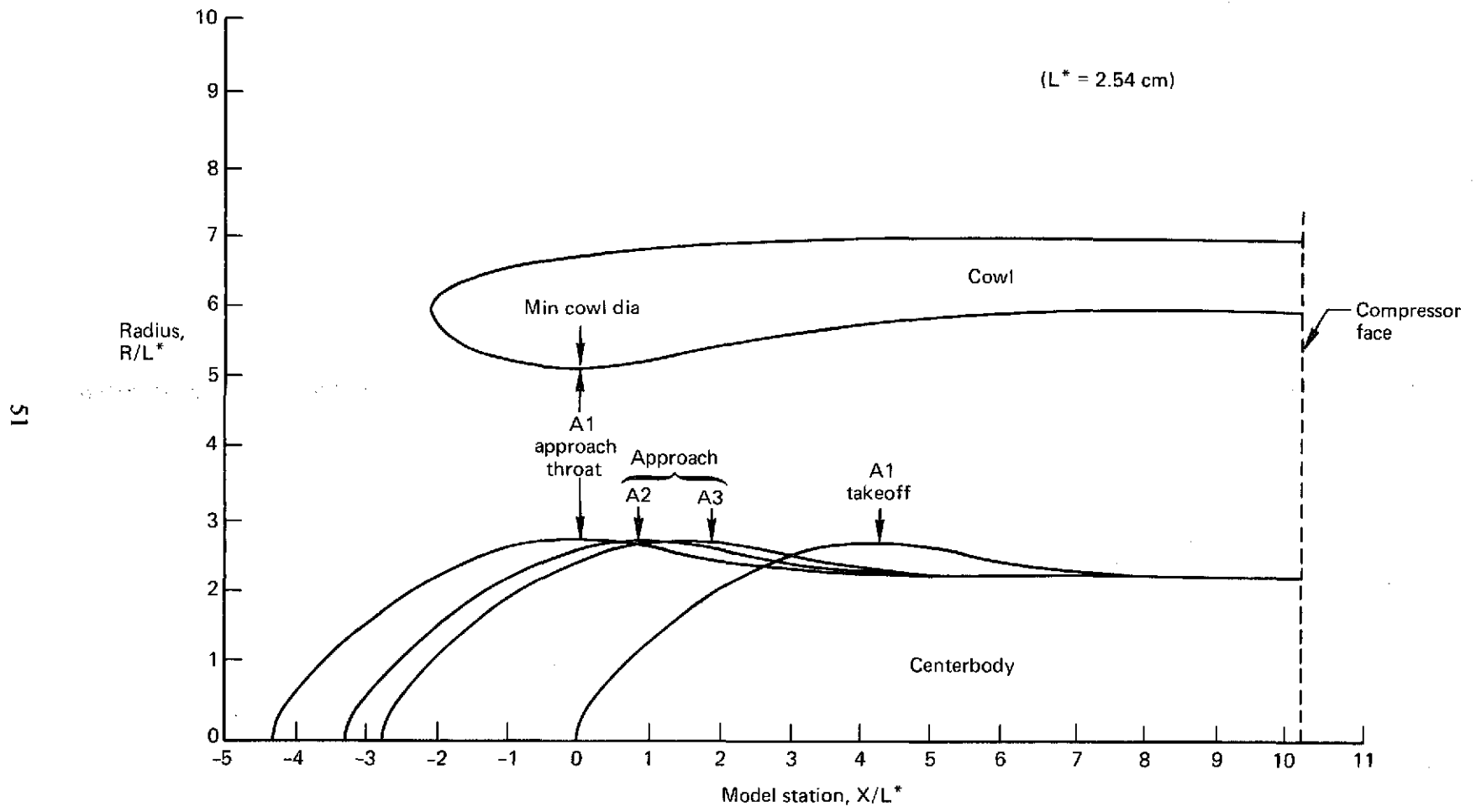
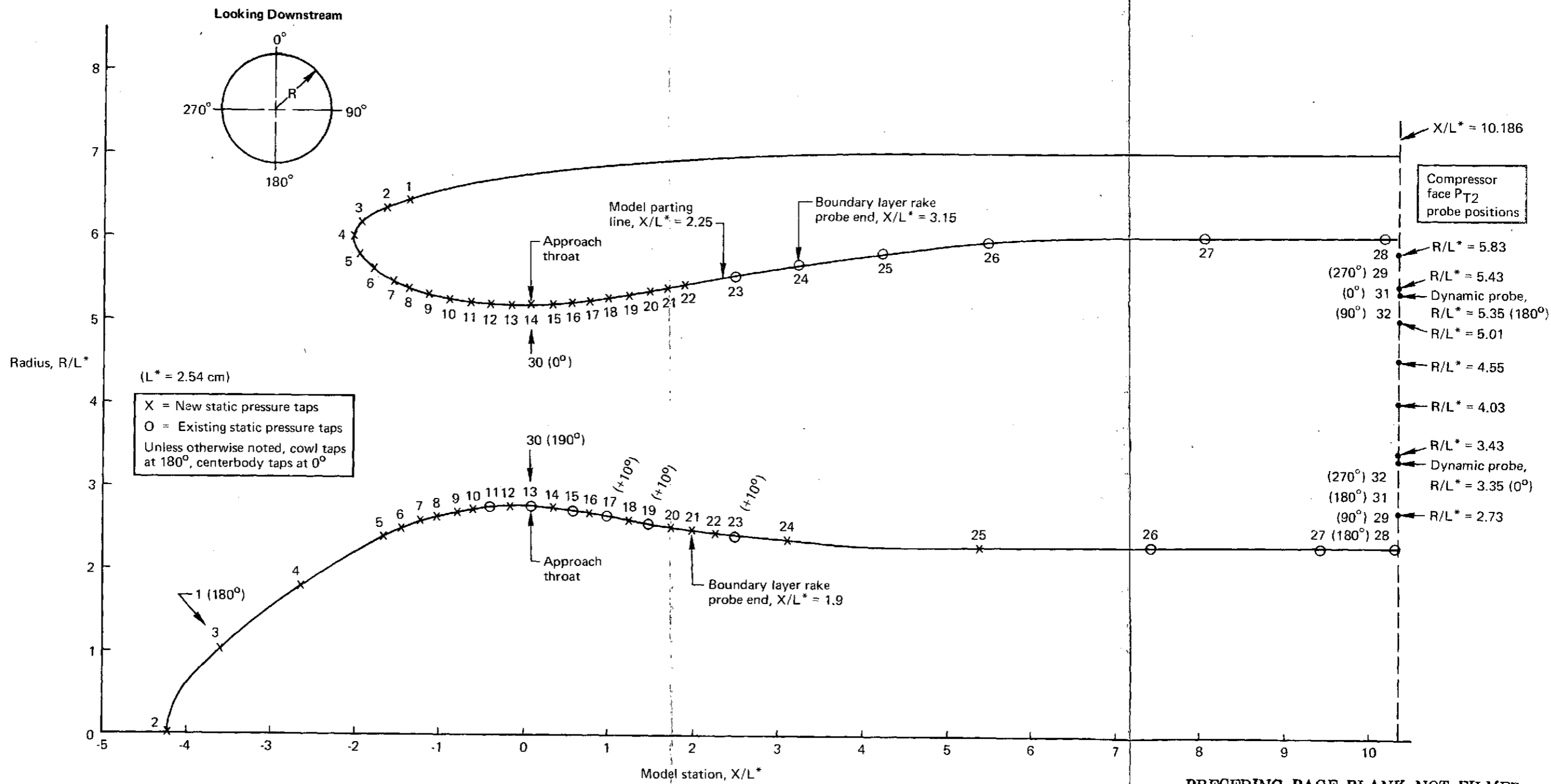


Figure 11.—Translating Centerbody Inlets A1, A2, and A3—Approach and Takeoff Positions



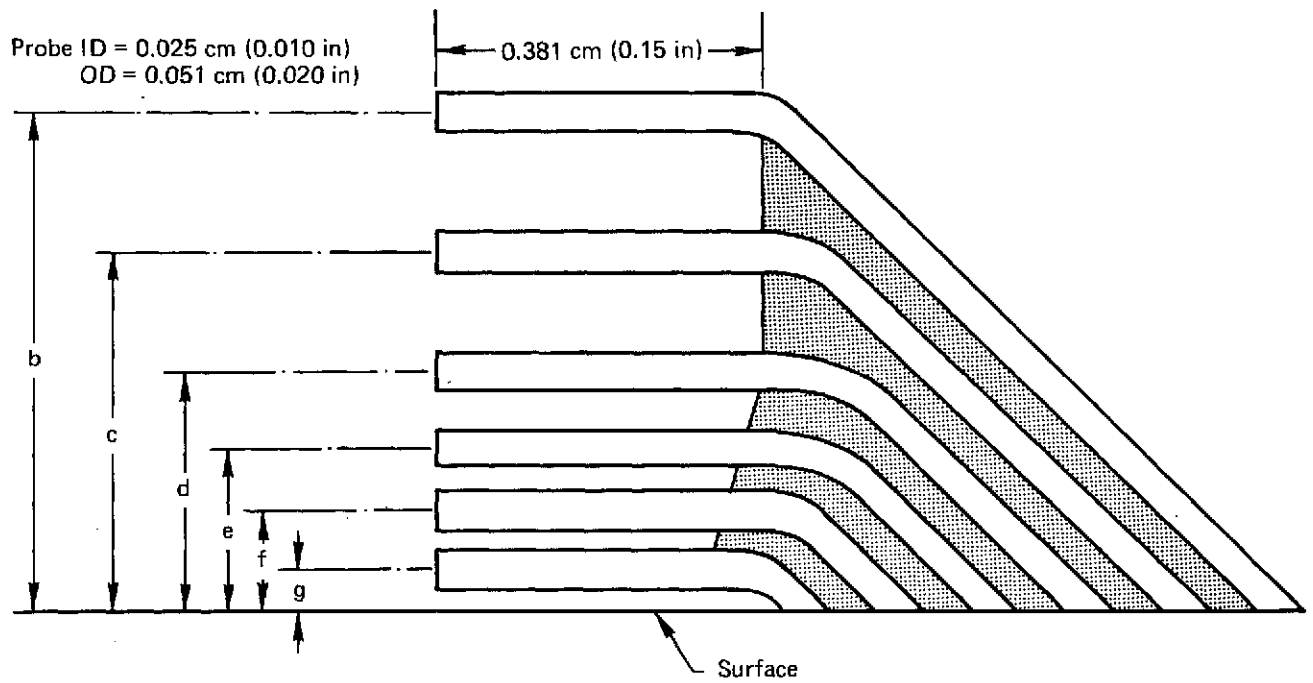
PRECEDING PAGE BLANK NOT FILMED

Figure 12.—Translating Centerbody Inlet A1 Approach—Pressure Instrumentation

FOLDOUT FRAME

FOLDOUT FRAME

Probe	Distance from surface	
	cm	in
b	0.635	0.25
c	0.457	0.18
d	0.305	0.12
e	0.203	0.08
f	0.127	0.05
g	0.051	0.02

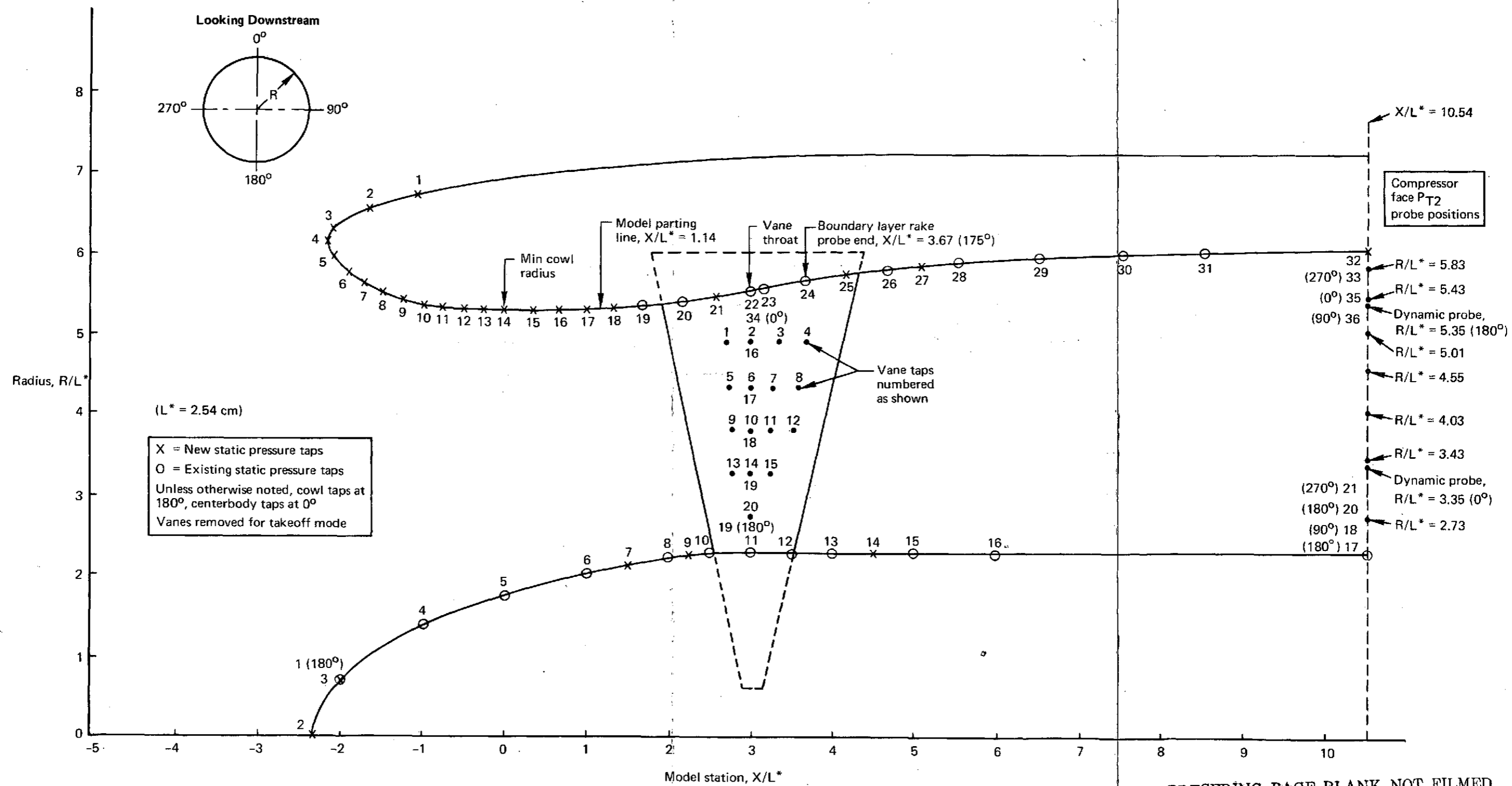


Inlet	Rake position	
	Cowl	Centerbody
A	$X/L^* = 3.15$	$X/L^* = 1.90$
B	$X/L^* = 3.67$	
C	$X/L^* = 6.00$	

Note: $L^* = 2.54\text{cm}$

Figure 13.—Boundary Layer Rake Probe Locations

PRECEDING PAGE BLANK NOT FILMED

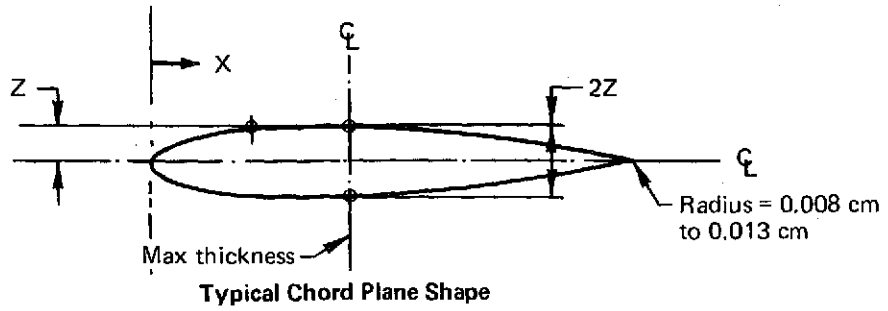


PRECEDING PAGE BLANK NOT FILMED

Figure 14.—Radial Vane Inlet B—Pressure Instrumentation

FOLDOUT FRAME

FOLDOUT FRAME



Reference Chord Plane Coordinates	
X/L*	Z/L*
0	0
0.0018	0.009
0.0290	0.033
0.0940	0.056
0.1470	0.066
0.2350	0.076
0.3530	0.083
0.4710	0.085
0.5890	0.083
0.7650	0.069
0.8830	0.052
1.0000	0.030
1.1180	0.009
1.1770	0

Note: Tolerance within ± 0.005 cm for max thickness (2Z);
 within ± 0.008 cm for all other coordinates.

Figure 15.—Radial Vane Inlet B—Vane Cross Section

PRECEDING PAGE BLANK NOT FILMED

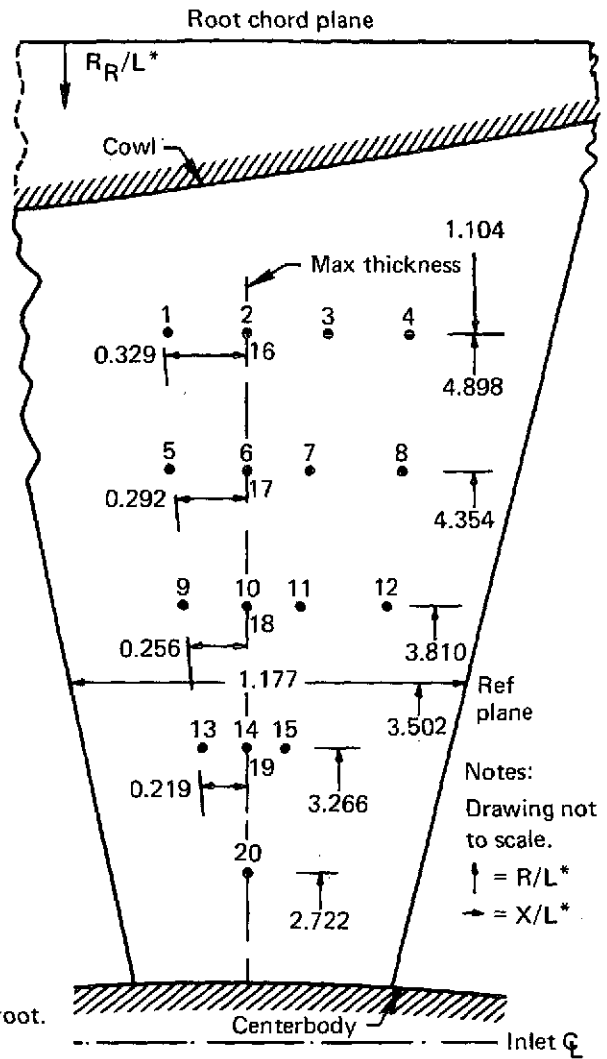
Tap no.	Part no.	Radial dist from root chord plane, R_R/L^*	Radial dist from inlet Q_L , R/L^*	Axial dist from vane max thickness, X/L^*
16	-2	1.104	4.898	0
17	-2	1.648	4.354	0
18	-2	2.192	3.810	0
19	-2	2.736	3.266	0
20	-2	3.280	2.722	0
1	-3	1.104	4.898	-0.329
2	-3	1.104	4.898	0
3	-3	1.104	4.898	0.329
4	-3	1.104	4.898	0.658
5	-4	1.648	4.354	-0.292
6	-4	1.648	4.354	0
7	-4	1.648	4.354	0.292
8	-4	1.648	4.354	0.585
9	-5	2.192	3.810	-0.256
10	-5	2.192	3.810	0
11	-5	2.192	3.810	0.256
12	-5	2.192	3.810	0.512
13	-6	2.736	3.266	-0.219
14	-6	2.736	3.266	0
15	-6	2.736	3.266	0.219

Notes:

Coordinates of contours as per drawing 5329-405.

R calculations based on distance of $R/L^* = 6.002$ from Q_L to root.

$L^* = 2.54$ cm.



Notes:
Drawing not to scale.
↑ = R/L^*
→ = X/L^*

Circumferential Locations of Vanes (Looking Downstream*)

Part no.	θ
-2	175°
-3	155°
-4	195°
-5	165°
-6	185°

*Taps on left side of vanes

Figure 16.—Radial Vane Inlet B—Static Pressure Taps

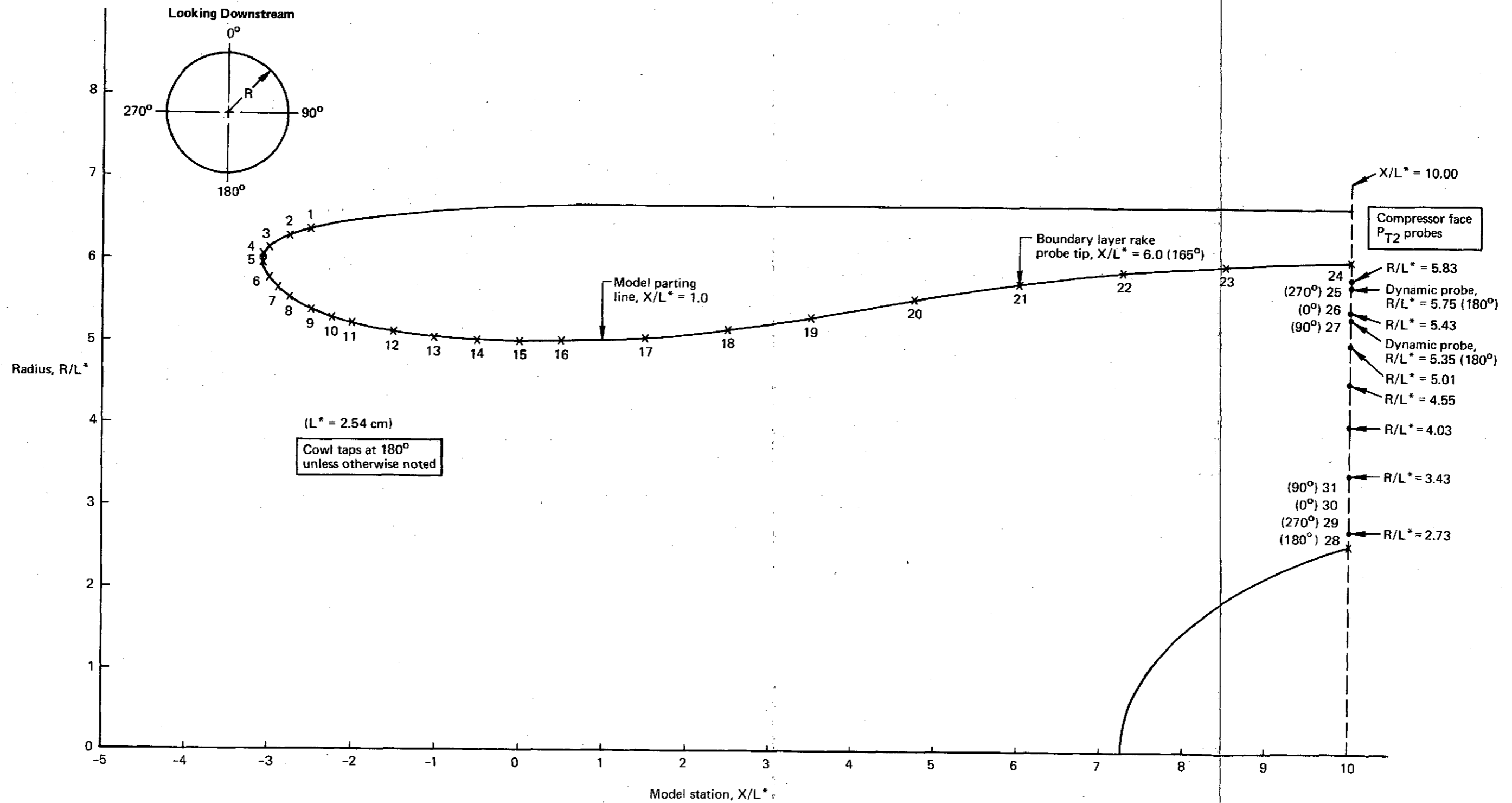
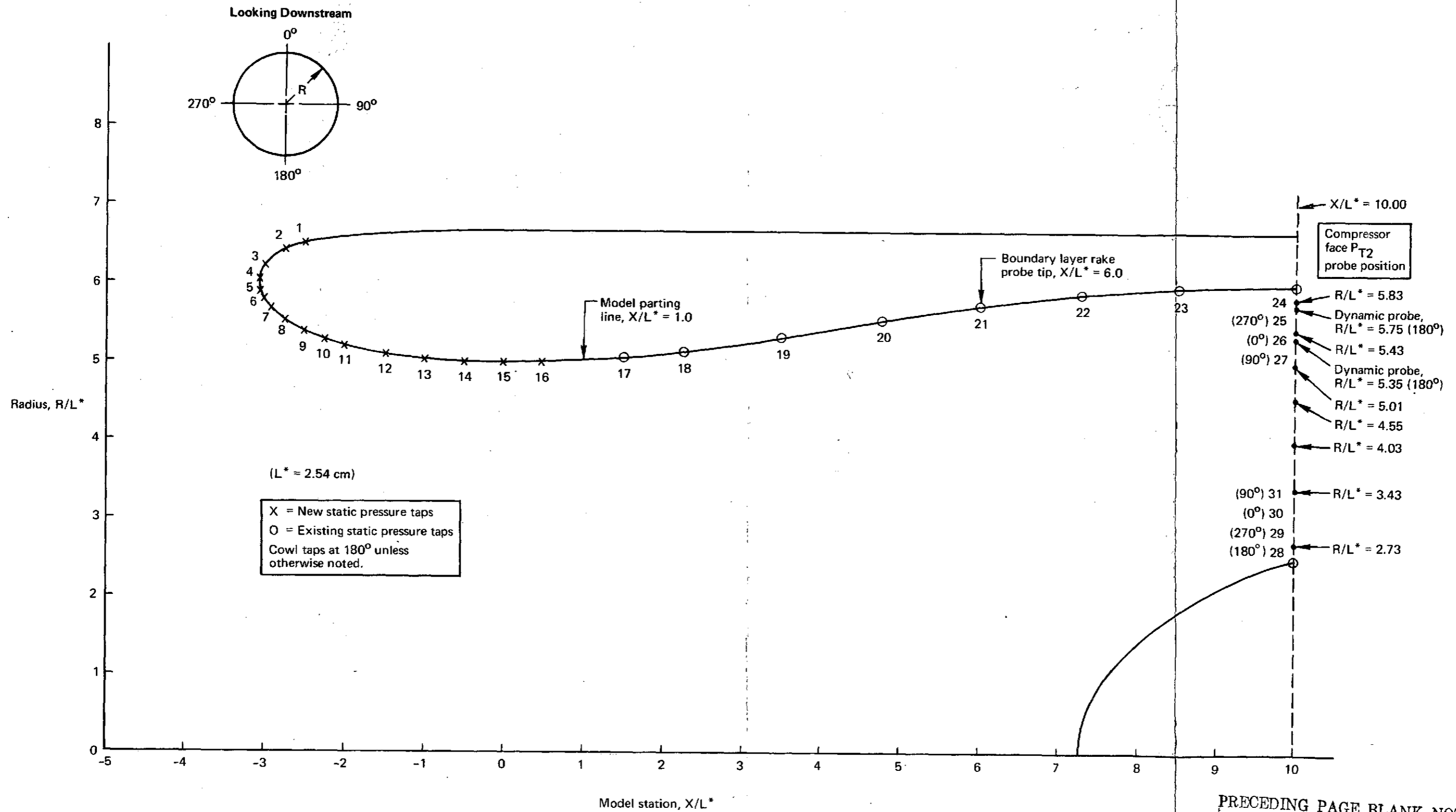


Figure 17.—QCSEE High Mach Number Inlet C1 —Pressure Instrumentation

FOLDOUT FRAME

FOLDOUT FRAME



PRECEDING PAGE BLANK NOT FILMED

Figure 18.—QCSEE High Mach Number Inlets C2 and C2-A—Pressure Instrumentation

FOLDOUT FRAME

FOLDOUT FRAME

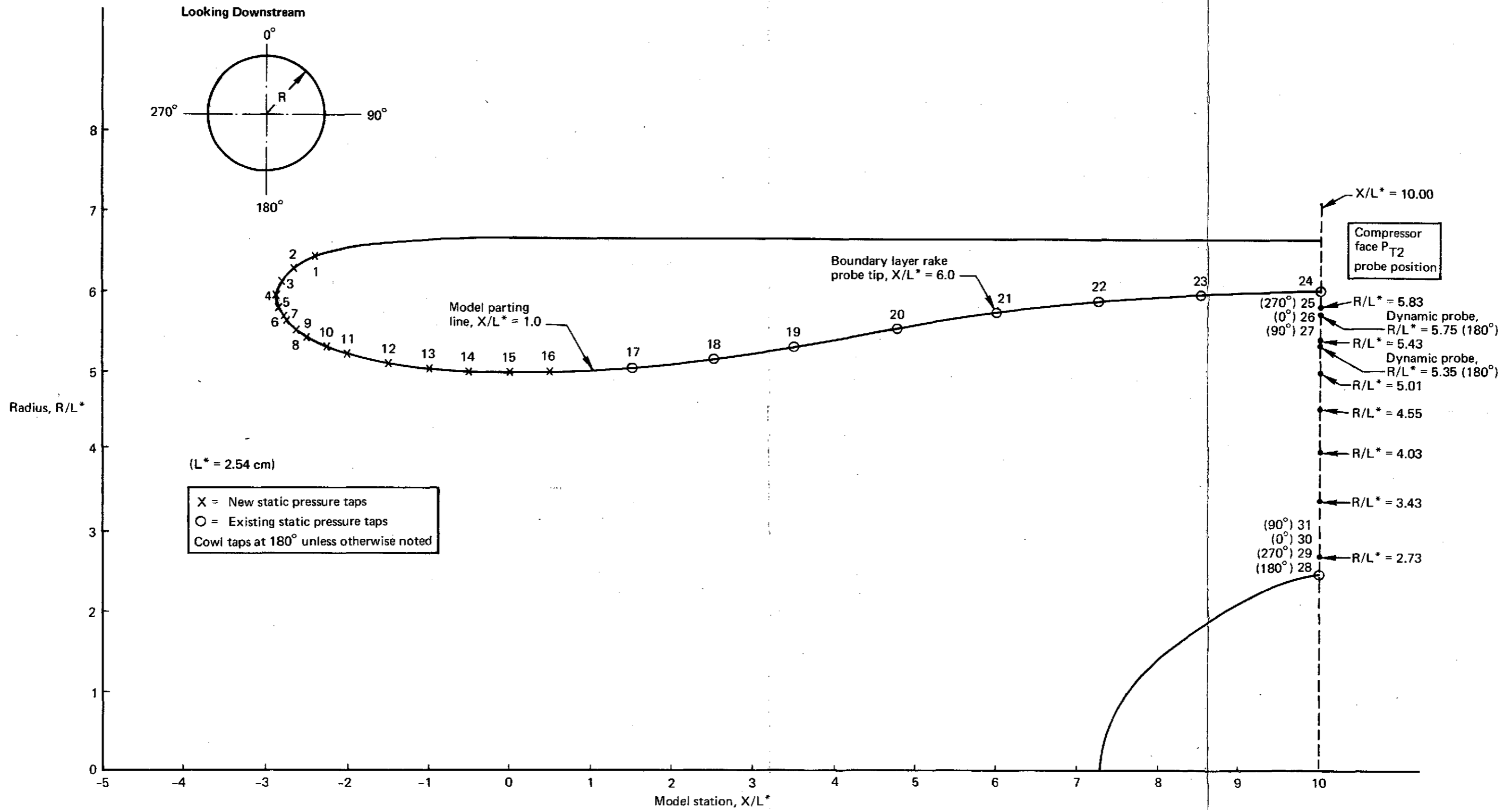
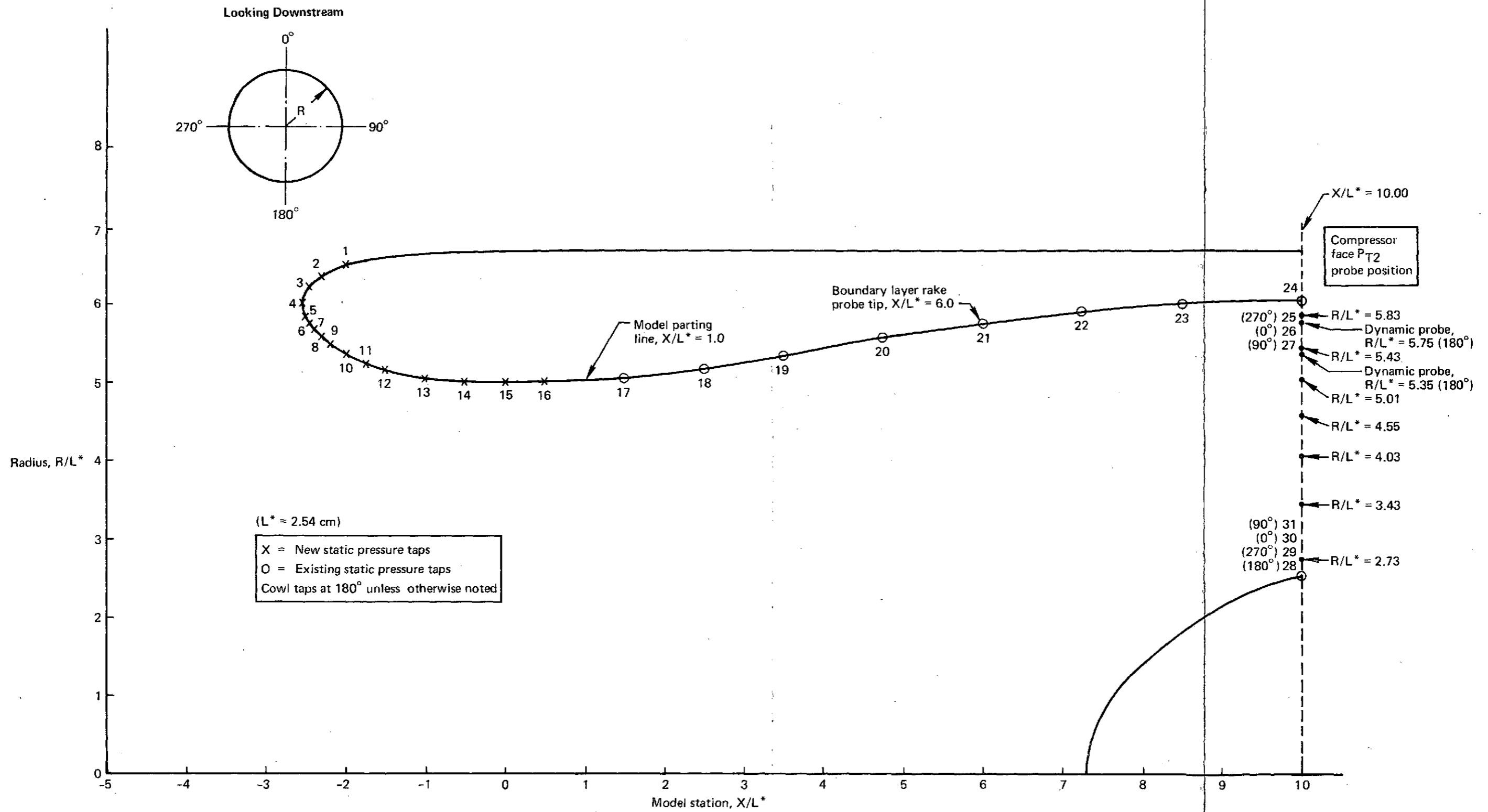


Figure 19.—OCSEE High Mach Number Inlet C3—Pressure Instrumentation

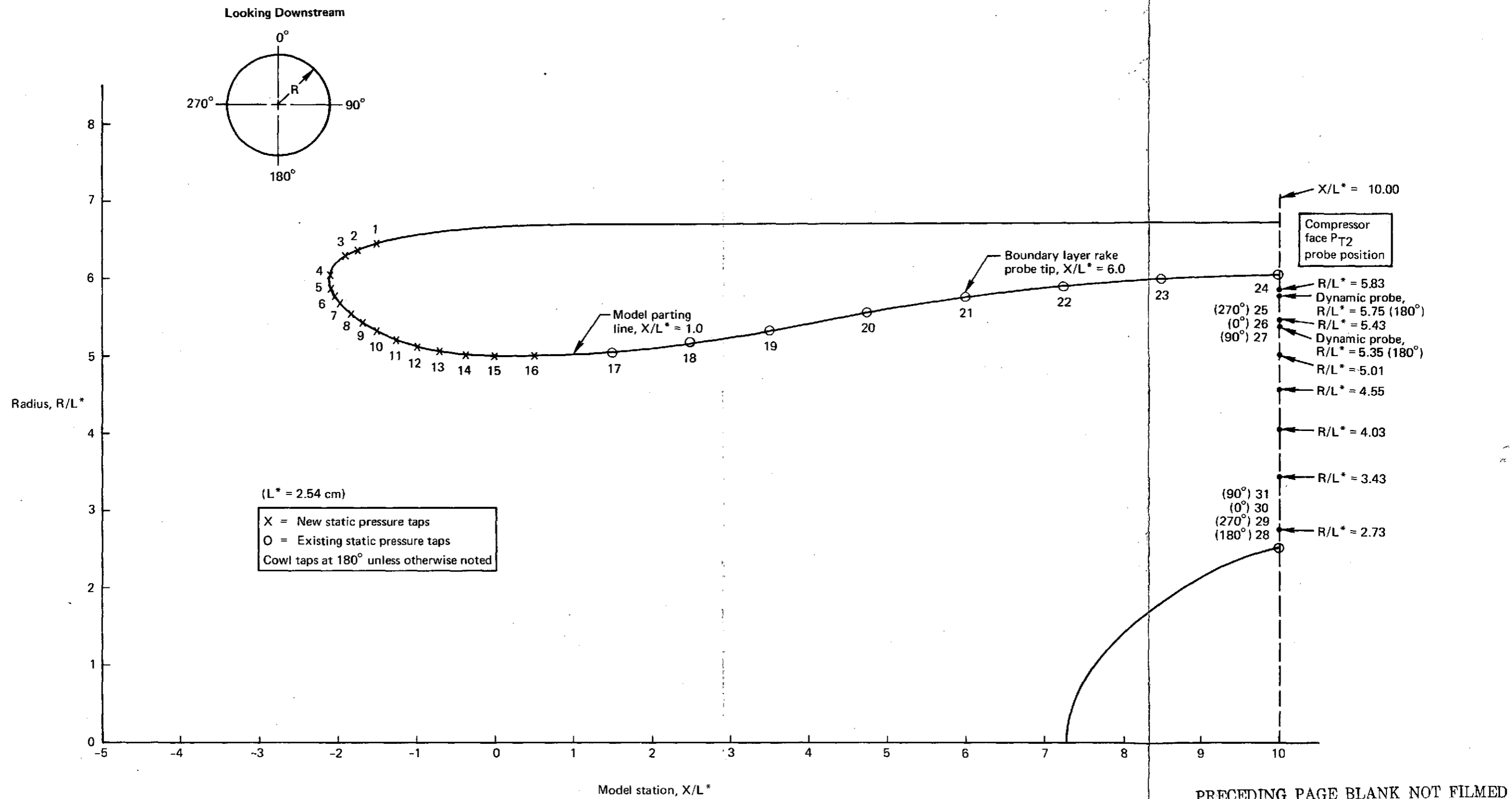
FOLDOUT FRAME

FOLDOUT FRAME



PRECEDING PAGE BLANK NOT FILMED

Figure 20.—QCSEE High Mach Number Inlet C4—Pressure Instrumentation



PRECEDING PAGE BLANK NOT FILMED

Figure 21.—QCSEE High Mach Number Inlet C5— Pressure Instrumentation

FOLDOUT FRAME

FOLDOUT FRAME

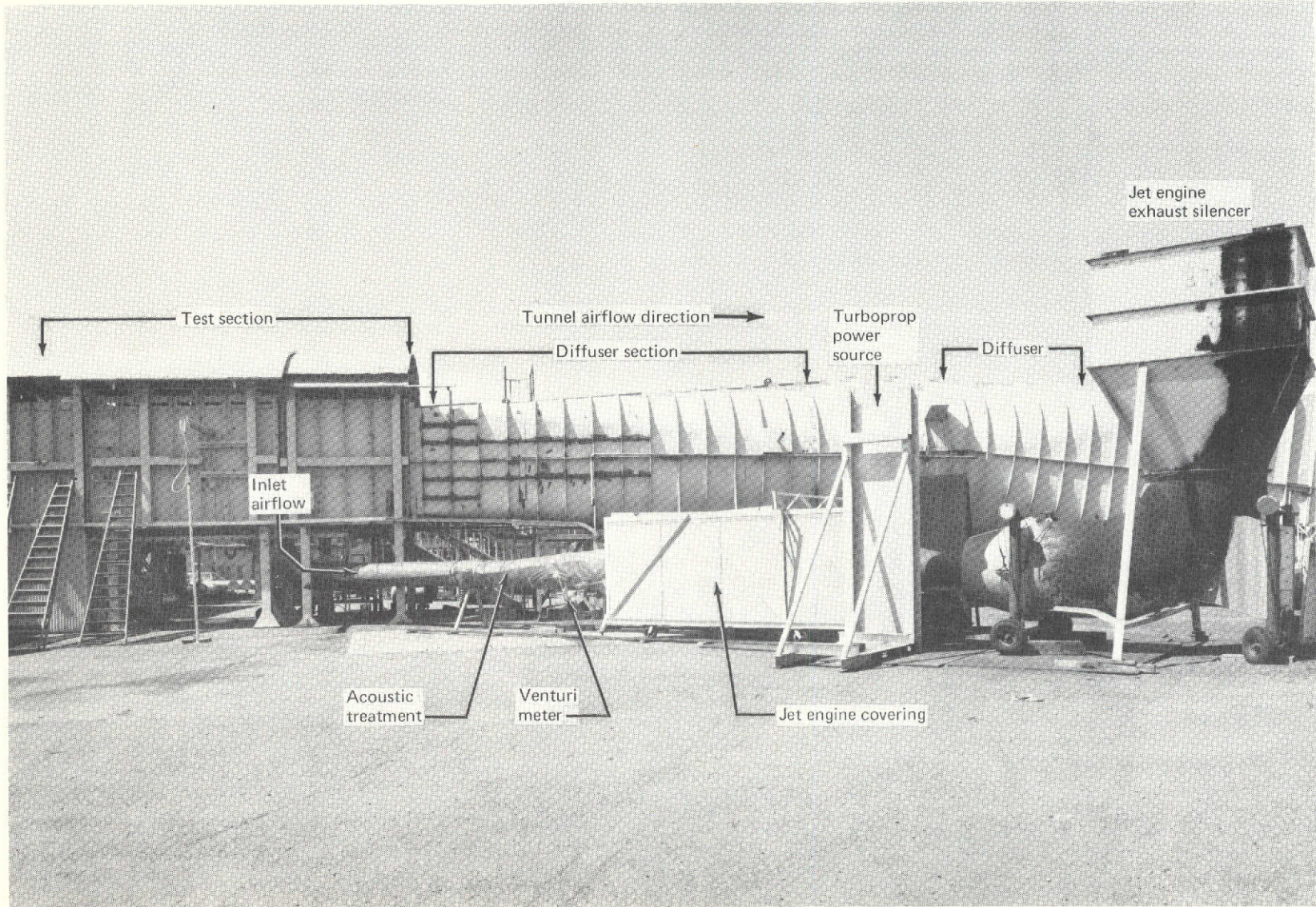


Figure 22.—Boeing 9-Ft by 9-Ft Low-Speed Wind Tunnel

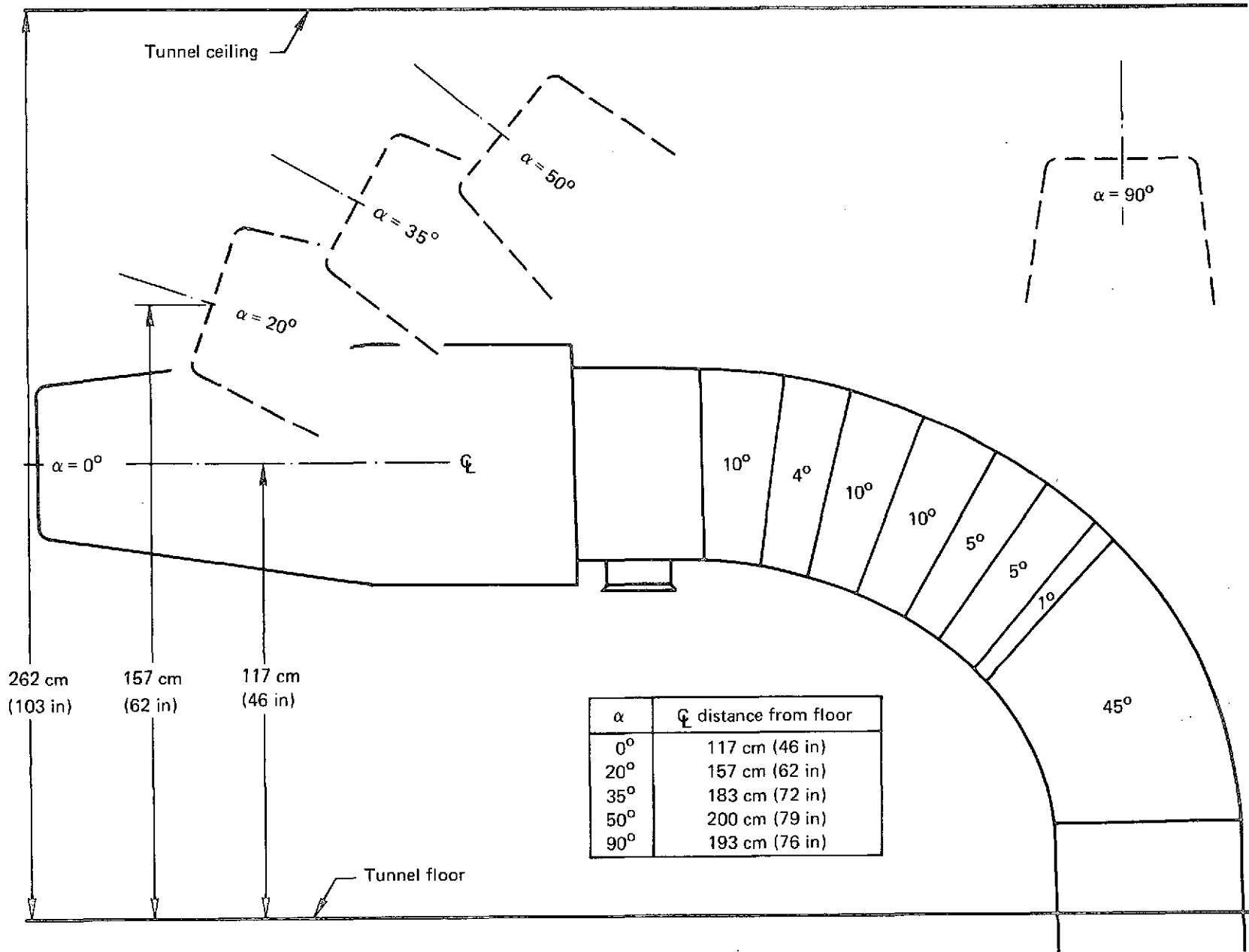


Figure 23.—Wind Tunnel Inlet Locations at Test Angles of Attack

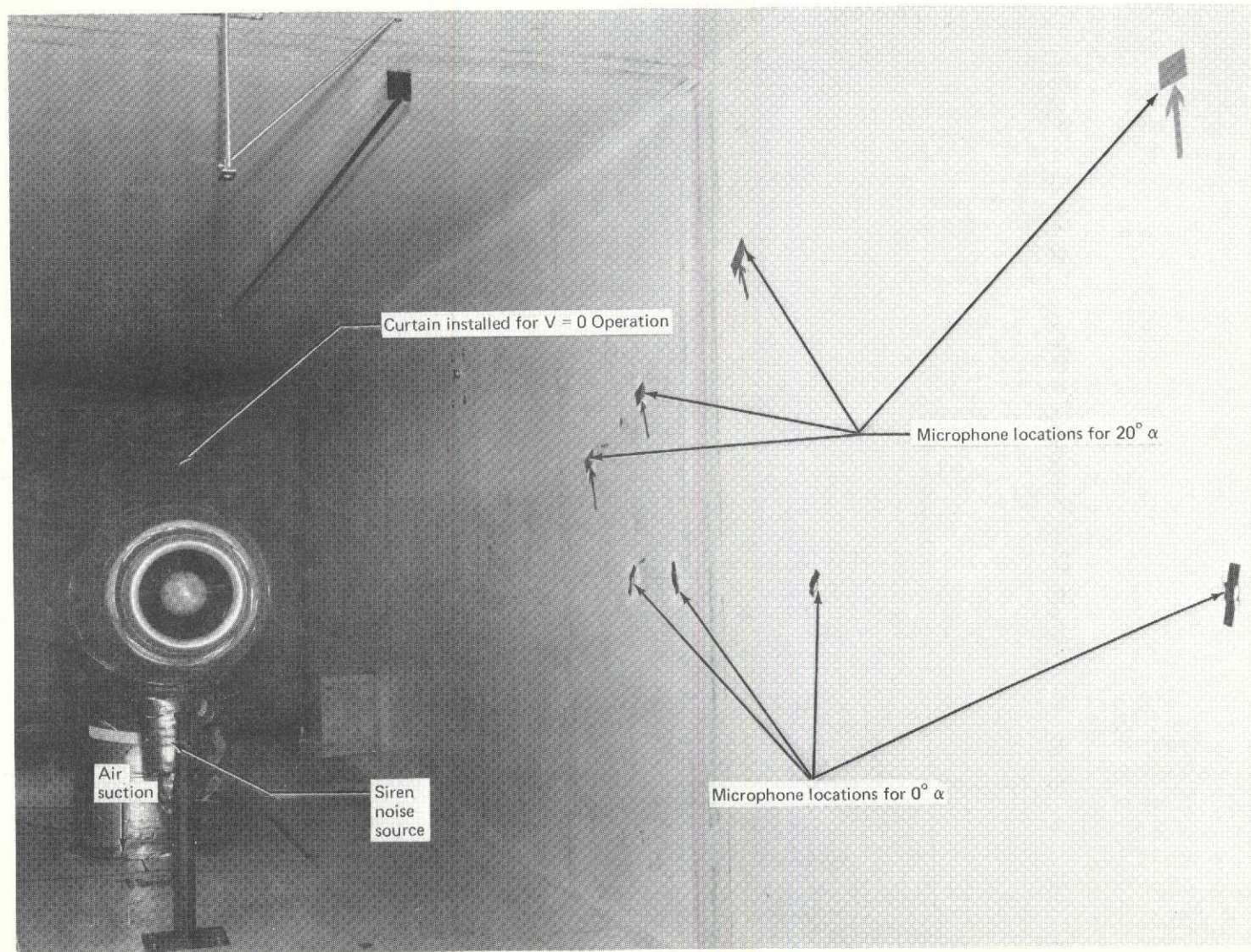


Figure 24.—Translating Centerbody Inlet A1 Takeoff— $\alpha = 0^\circ$

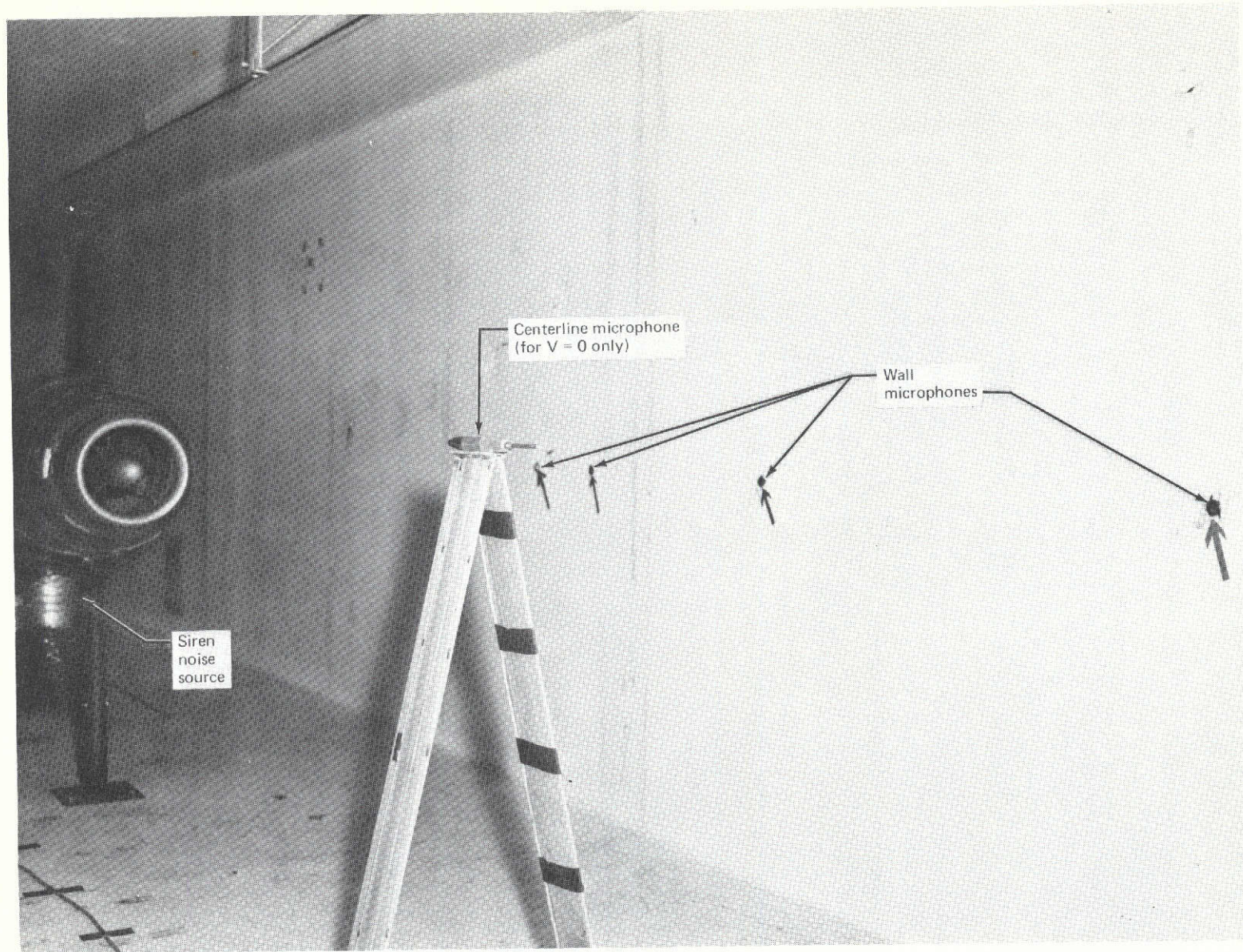


Figure 25.—Radial Vane Inlet B Takeoff (Vaness Removed)— $\alpha = 0^\circ$

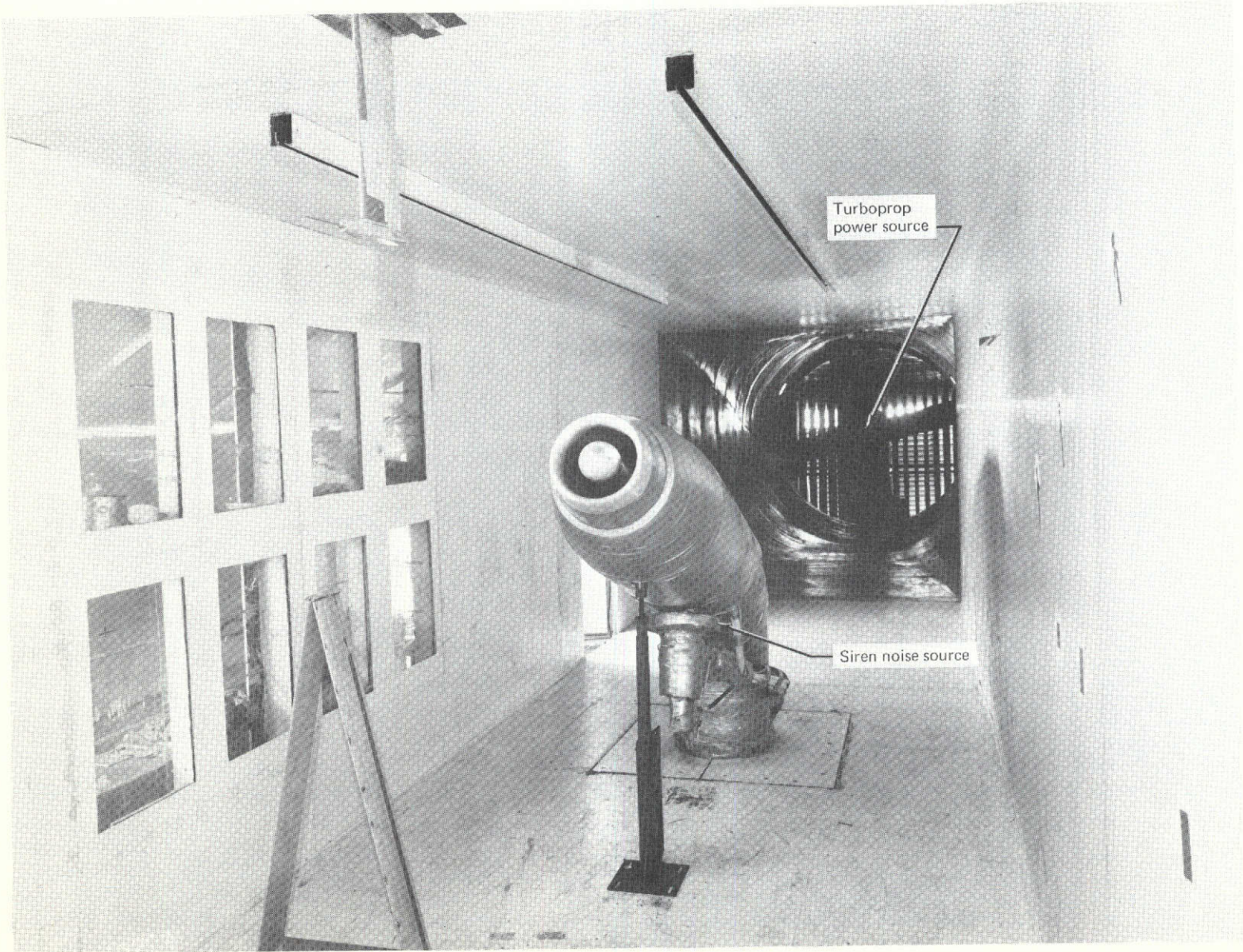


Figure 26.—Translating Centerbody Inlet A1 Approach— $\alpha = 20^\circ$

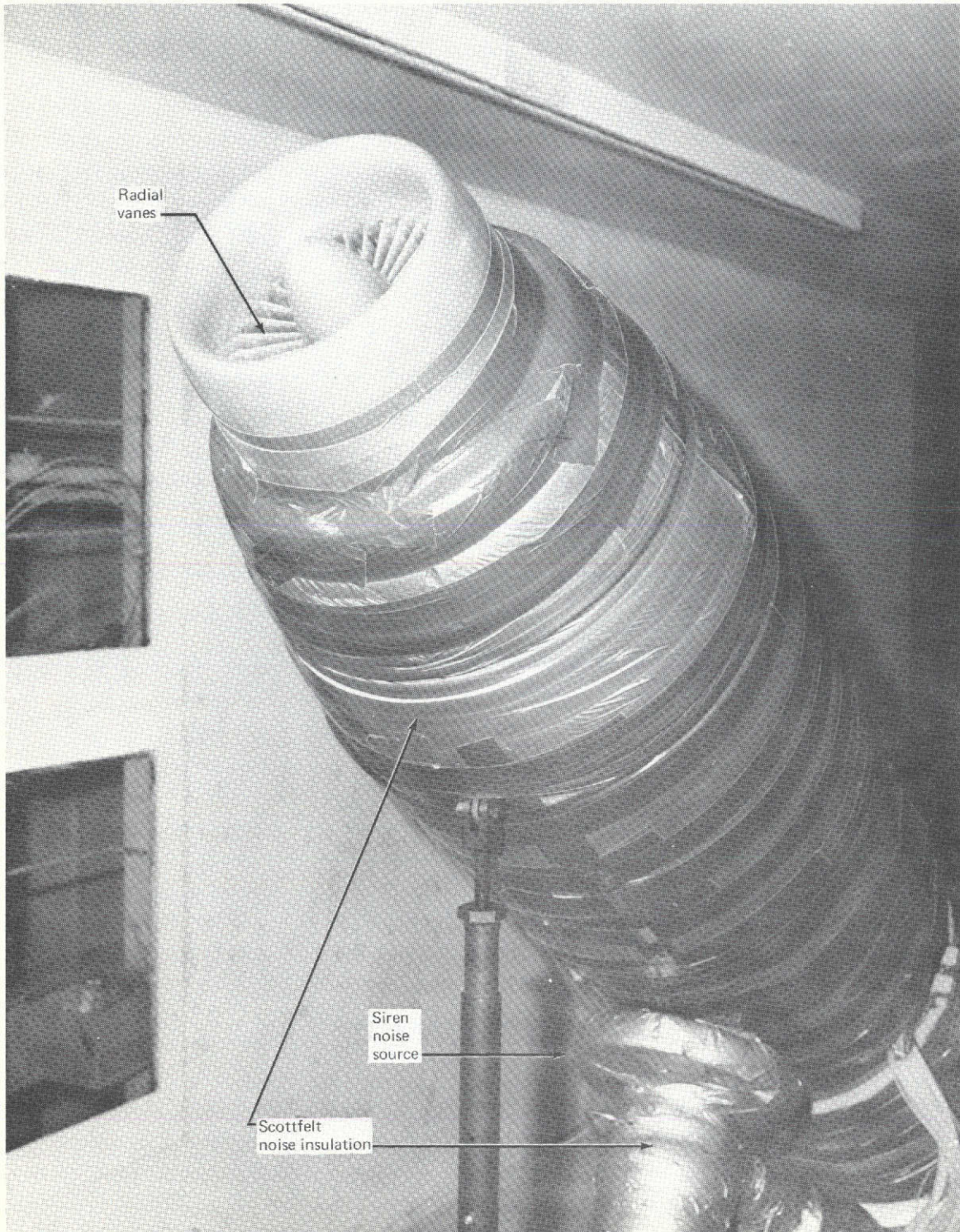


Figure 27.—Radial Vane Inlet B Approach— $\alpha = 35^\circ$

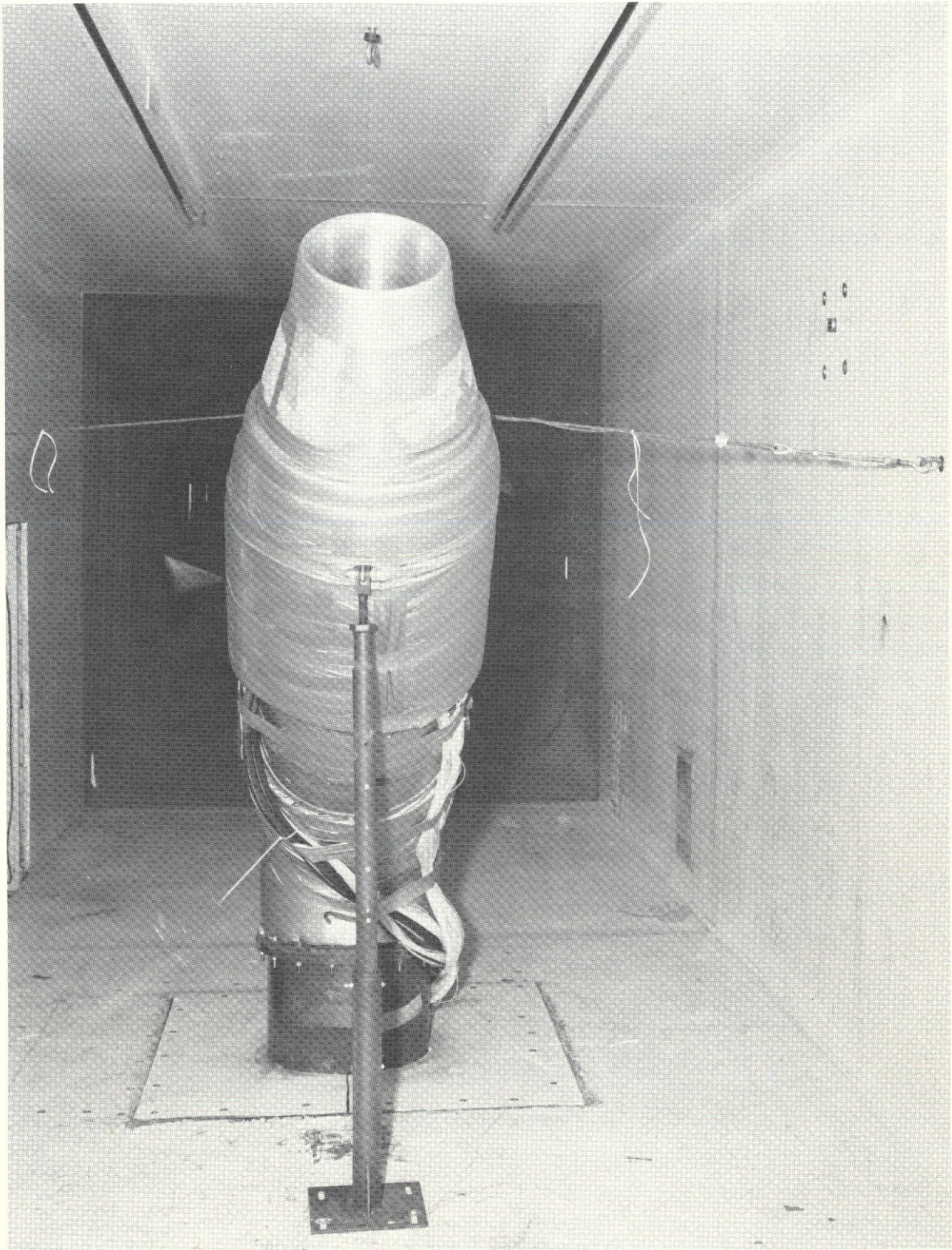


Figure 28.—QCSEE High Mach Number Inlet C1— $\alpha=50^\circ$



Figure 29.—Translating Centerbody Inlet A1 Takeoff— $\alpha = 90^\circ$

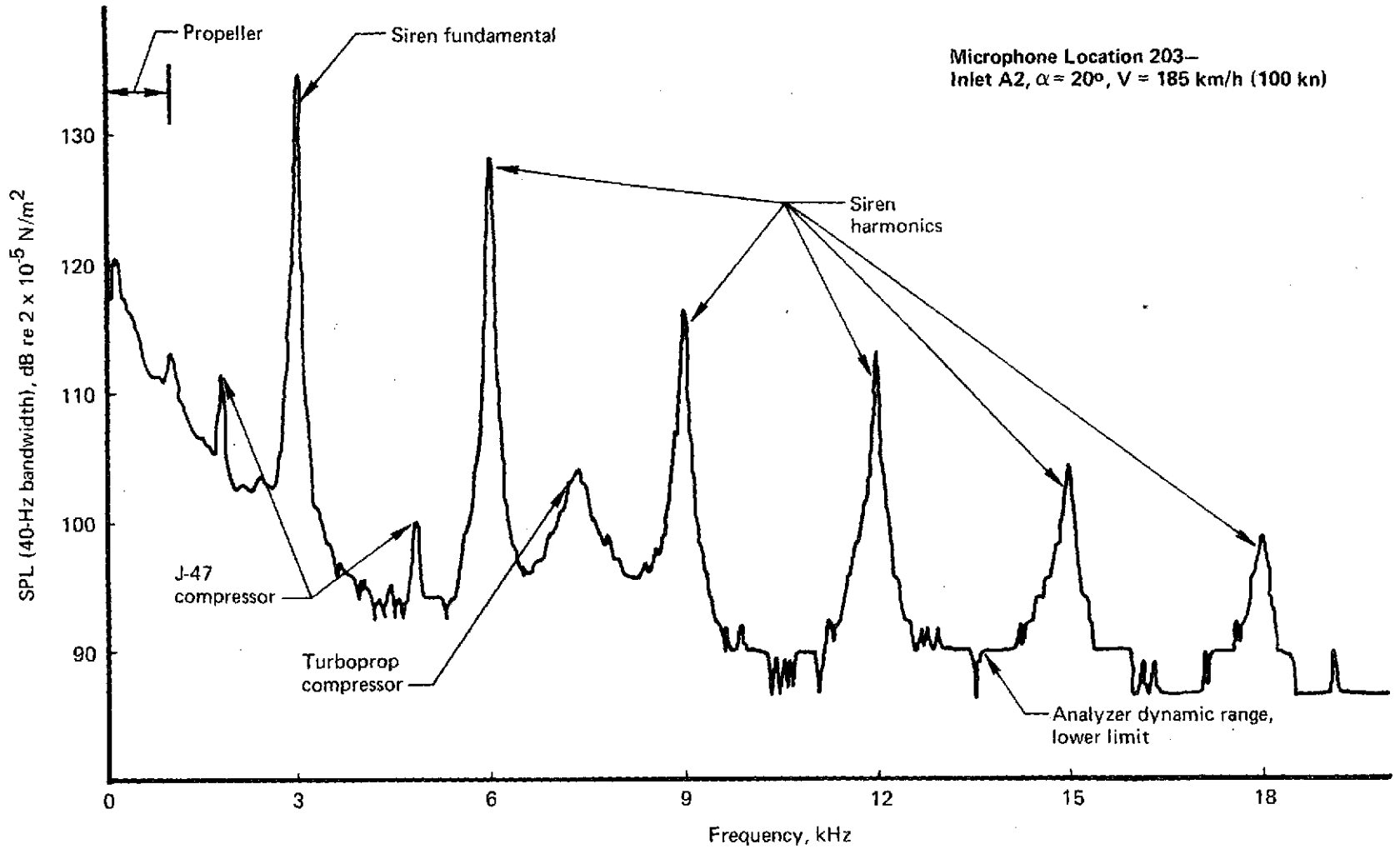


Figure 30.—Typical Measured Noise Signature—Siren Noise Signal SPL Versus Frequency

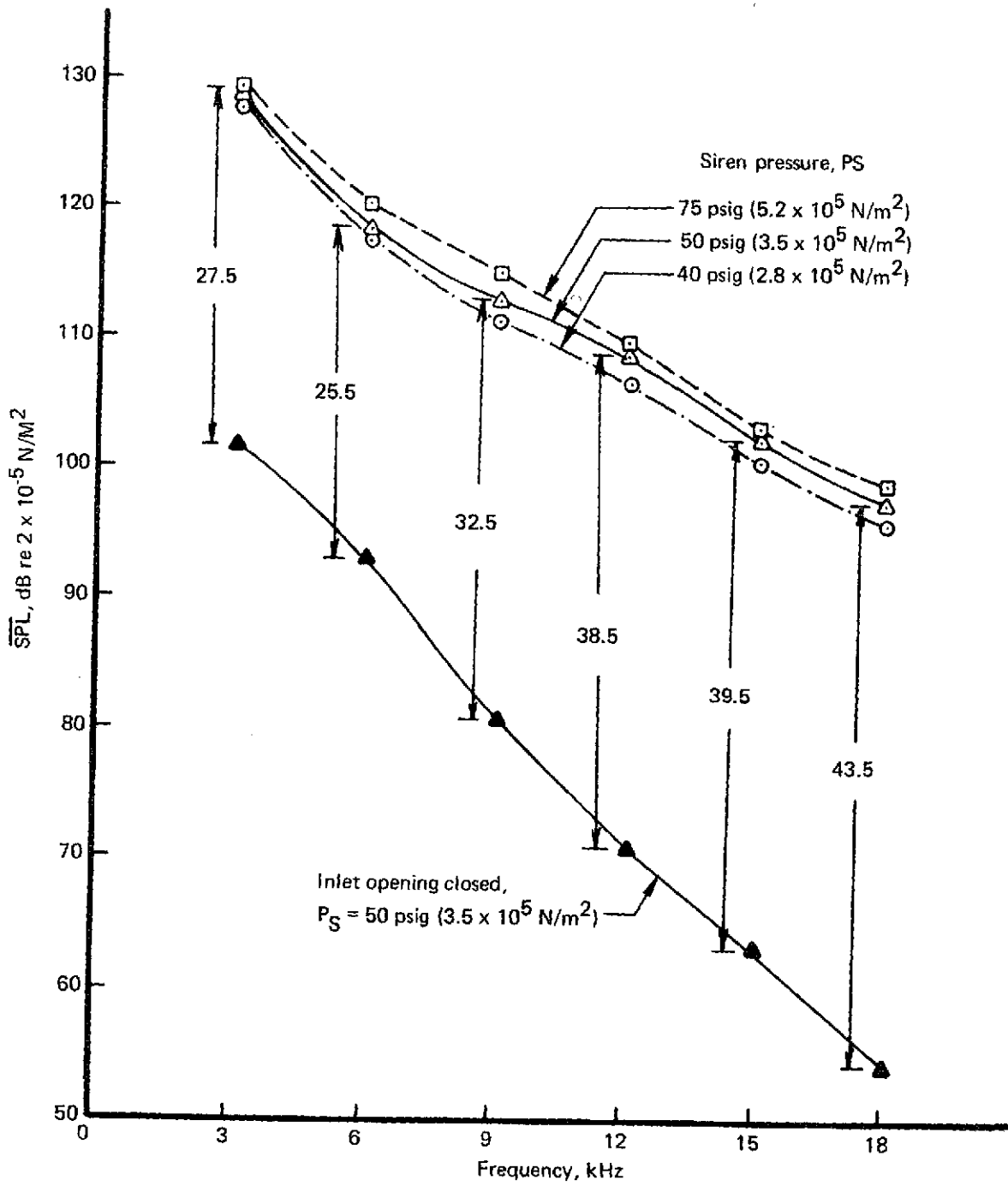
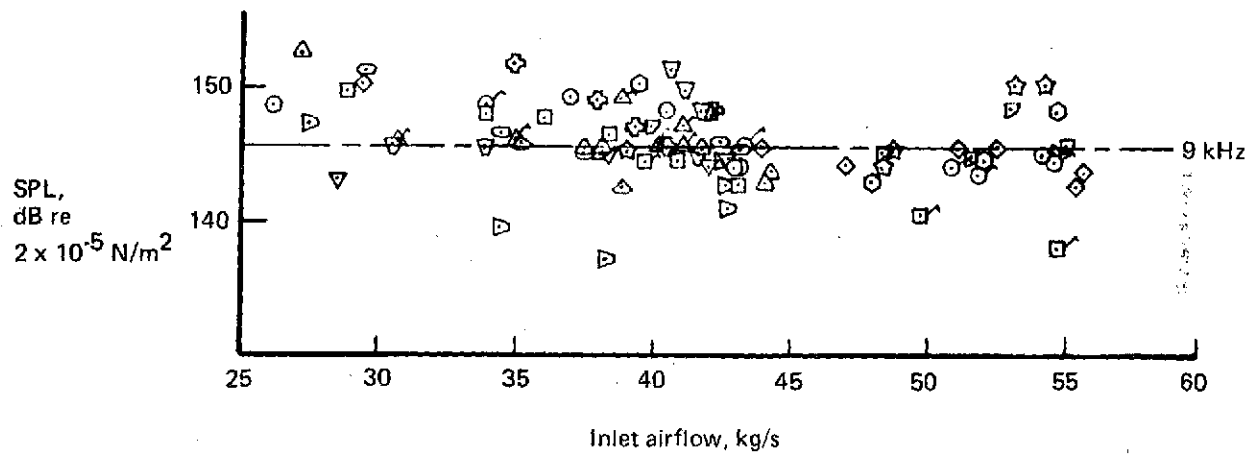
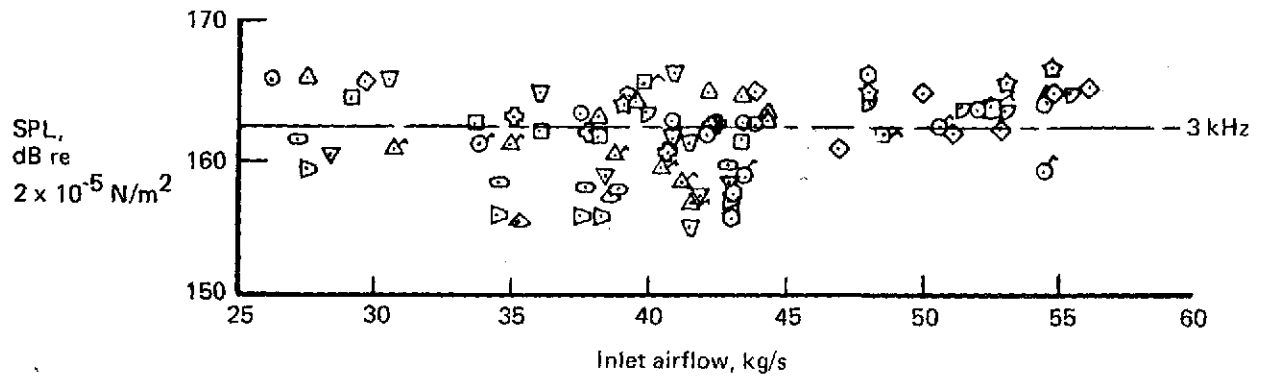


Figure 31.—Siren ΔP and Siren Noise Flanking Path Effects (Inlet A1)



Note: Data are for 13 runs at varying tunnel speed and α .

Figure 32.—Effect of Inlet Airflow on SPL at Siren Monitor Microphone

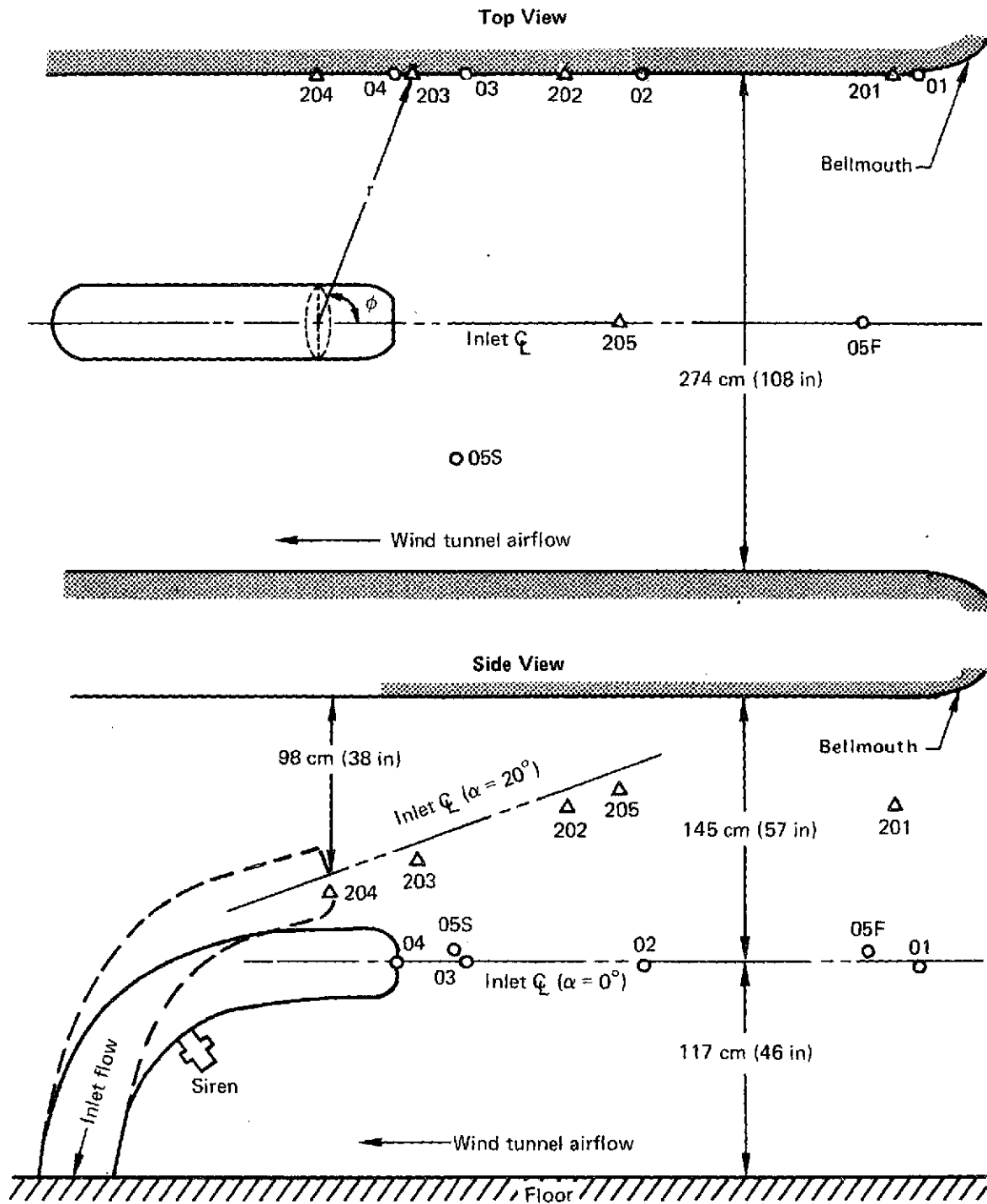


Figure 33.—Microphone Locations in the Wind Tunnel

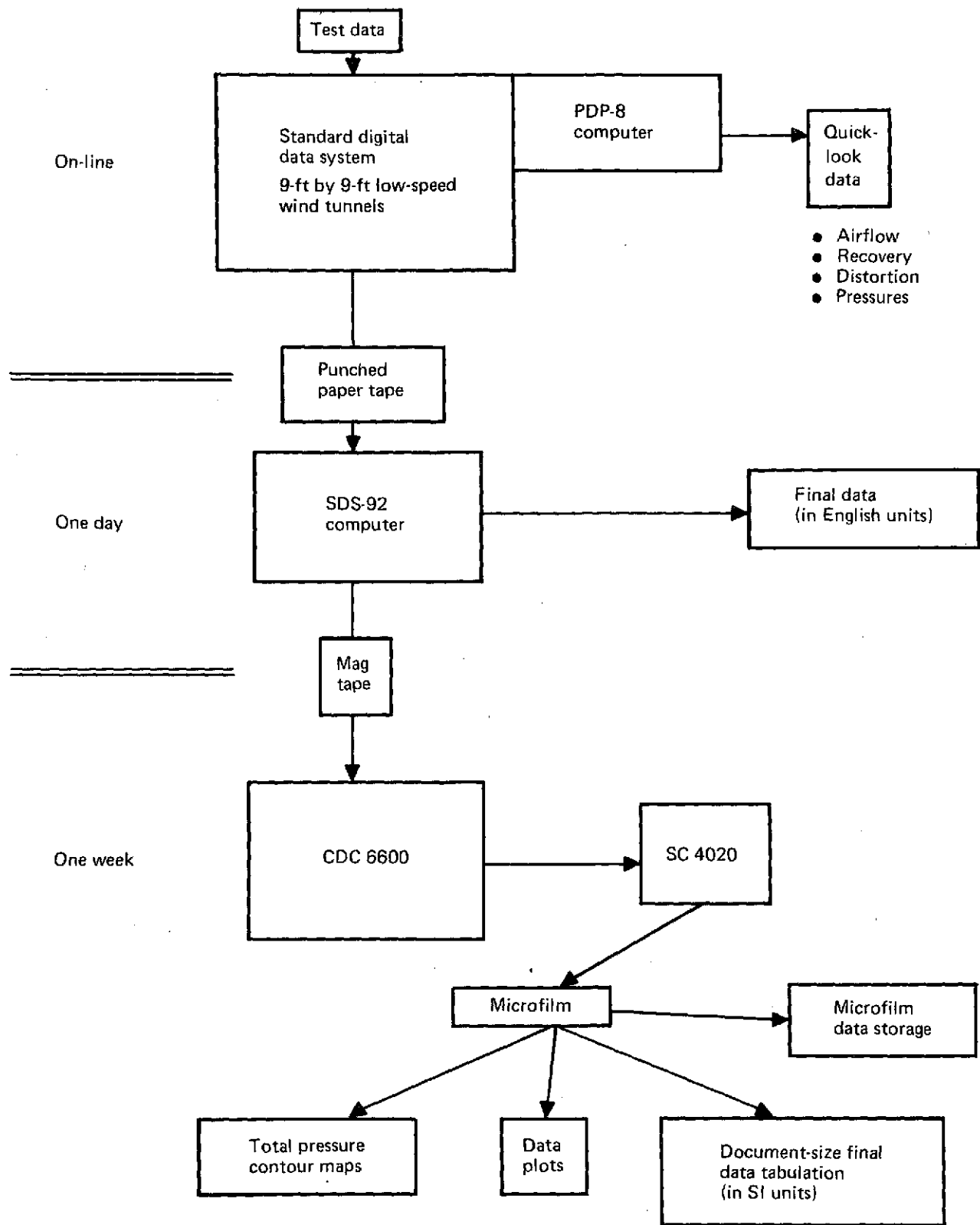


Figure 34.—Data Reduction Flow Diagram

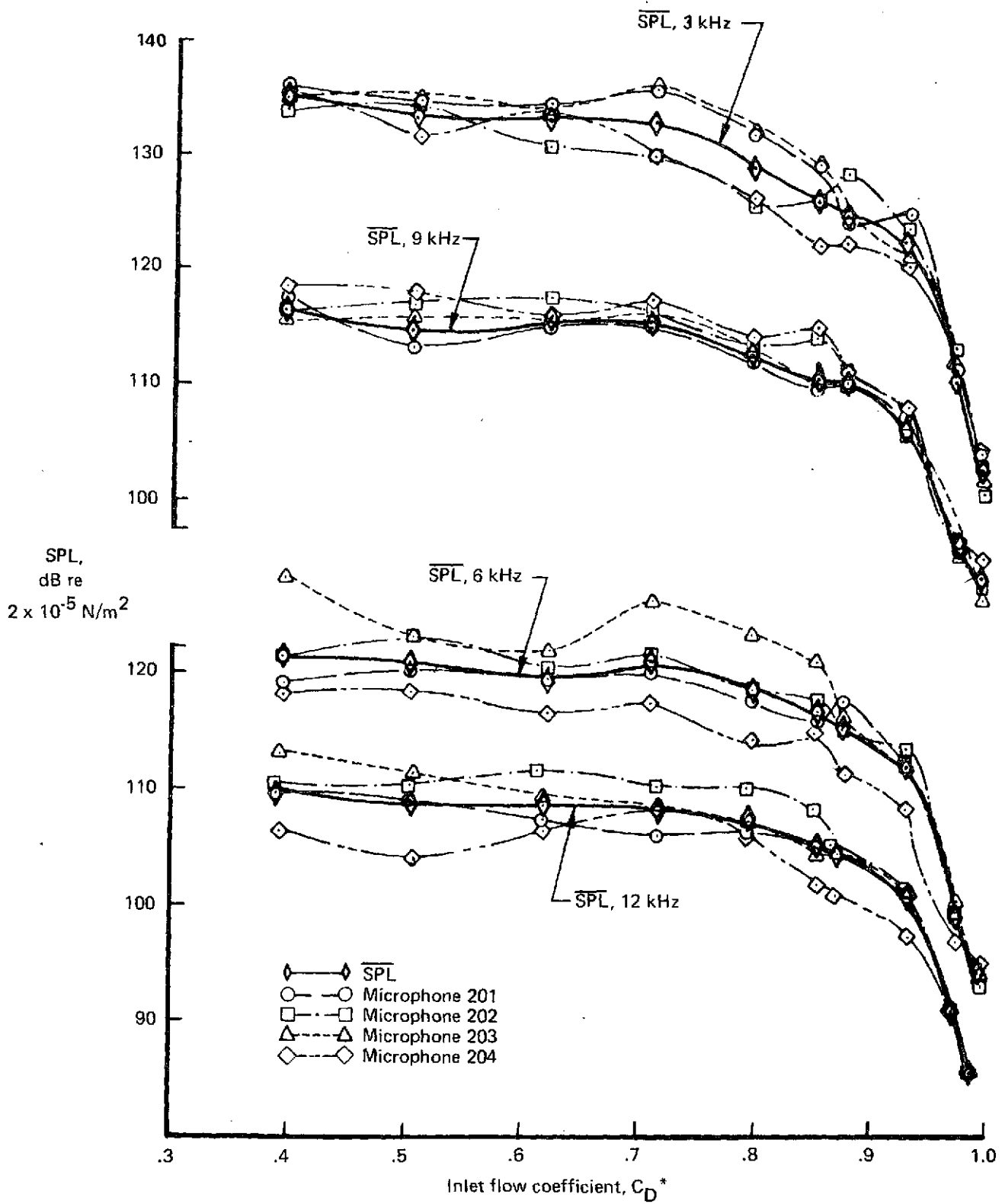


Figure 35.—SPL and $\overline{\text{SPL}}$ Versus C_D^* for Translating Centerbody Inlet A2— $\alpha = 20^\circ$, $V = 185 \text{ km/h (100 kn)}$

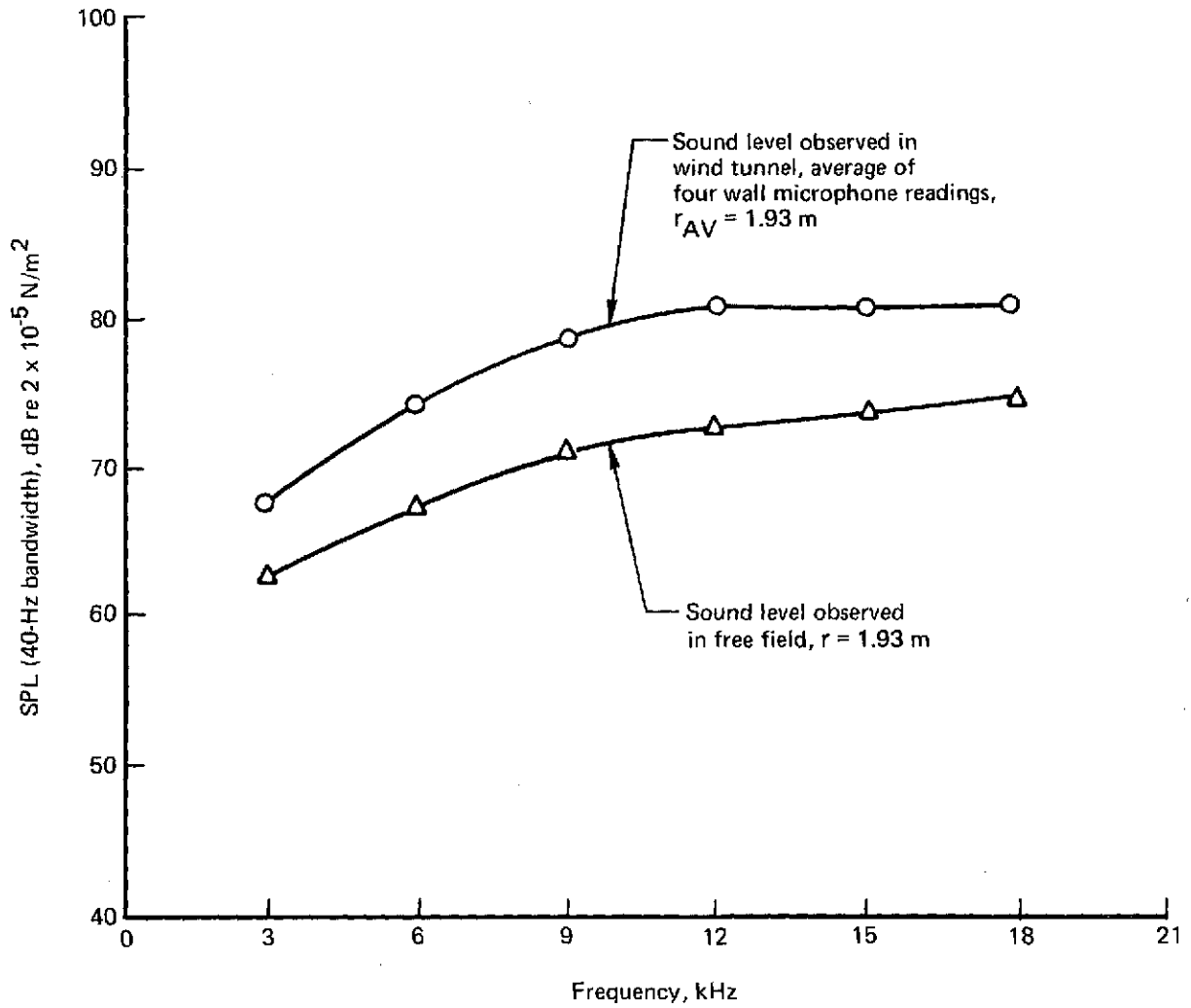


Figure 36.—Effect of Tunnel Wall Reflections on SPL for a Broadband, Omnidirectional Noise Source

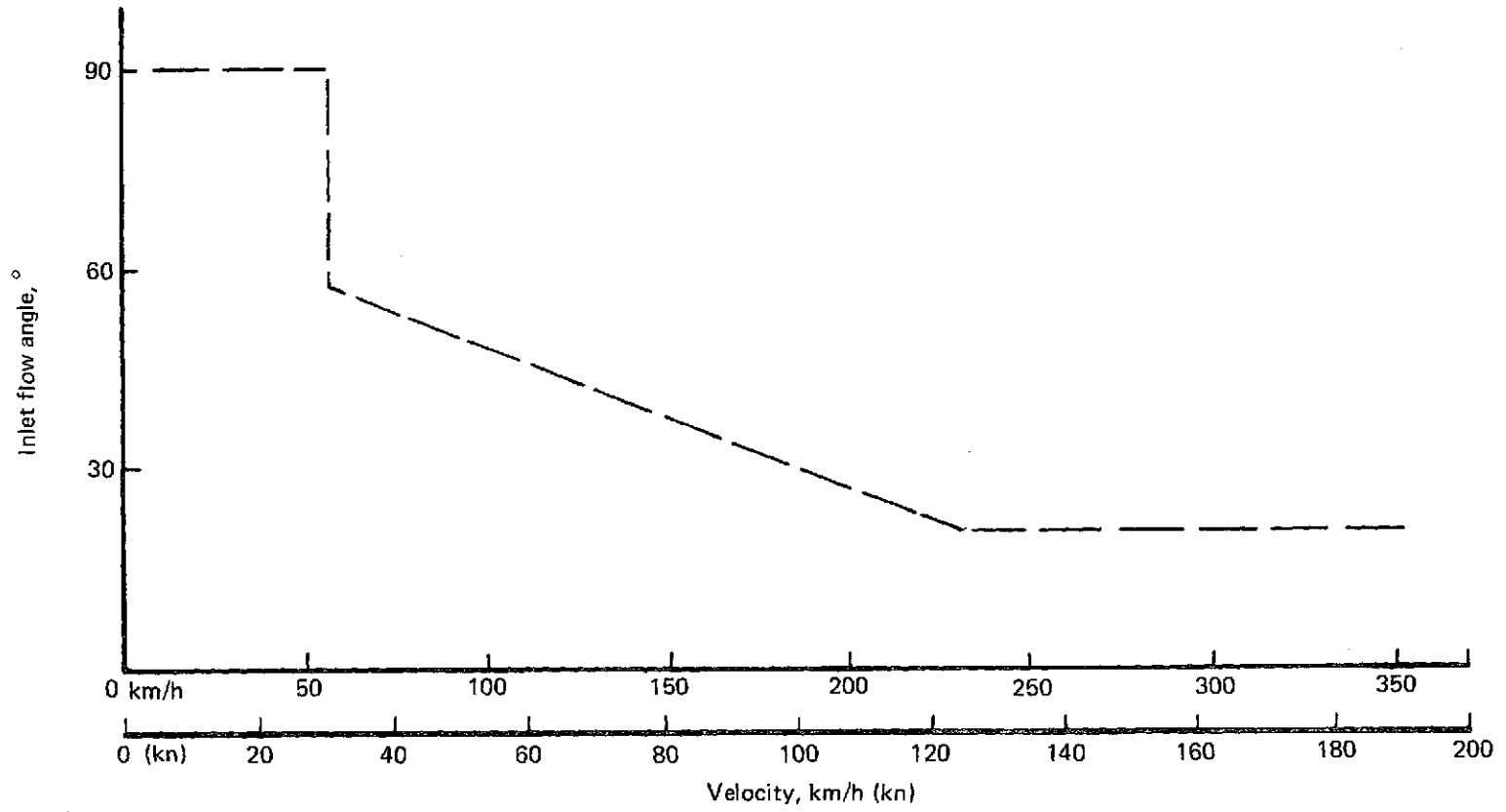


Figure 37.—Design Envelope for Sonic Inlet (Based on YC-14 Airplane)

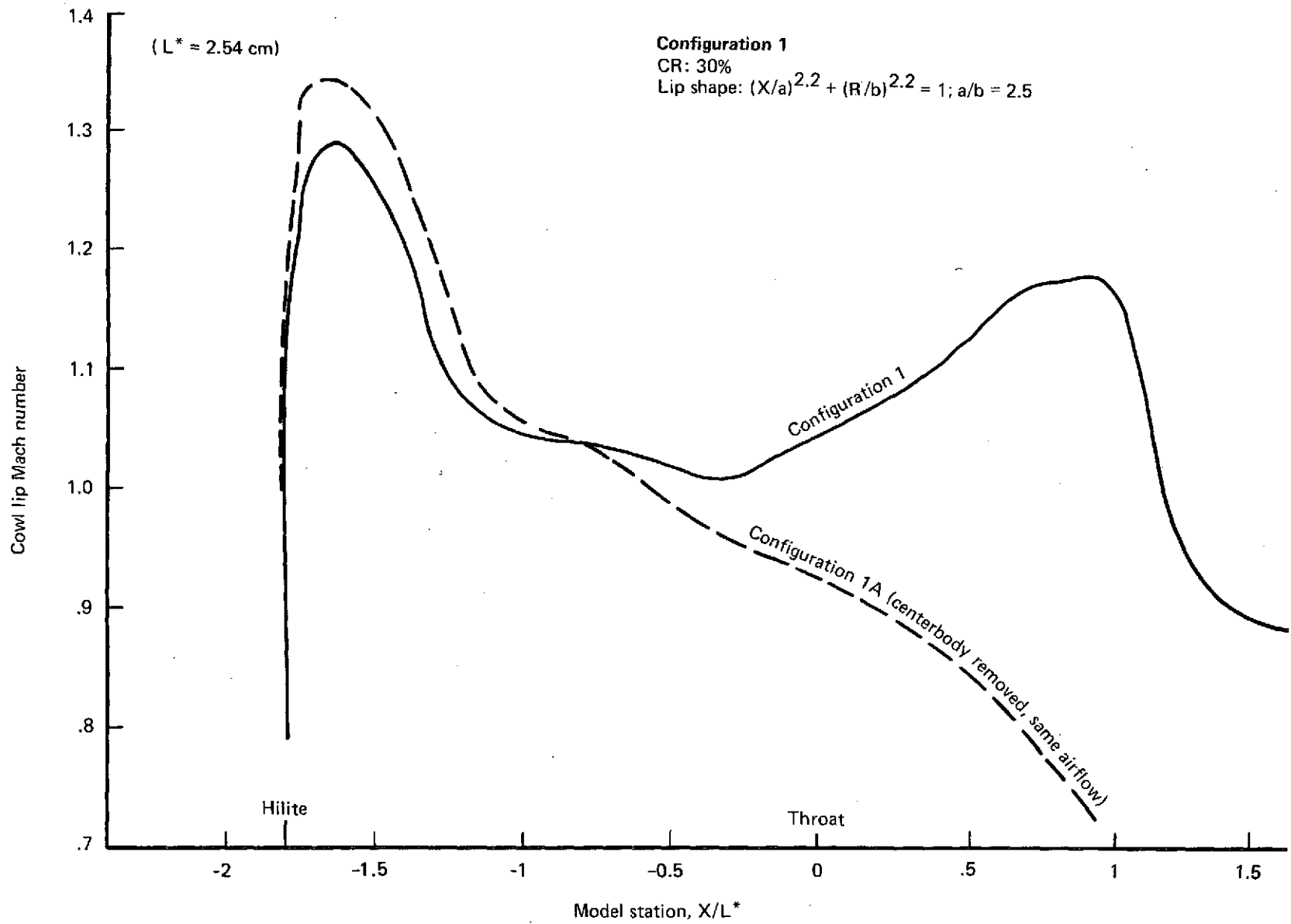


Figure 38.—Effect of Centerbody on Cowl Lip Mach Number Distribution for Translating Centerbody Inlet—Takeoff, $V = 0$, $M_2 = 0.514$

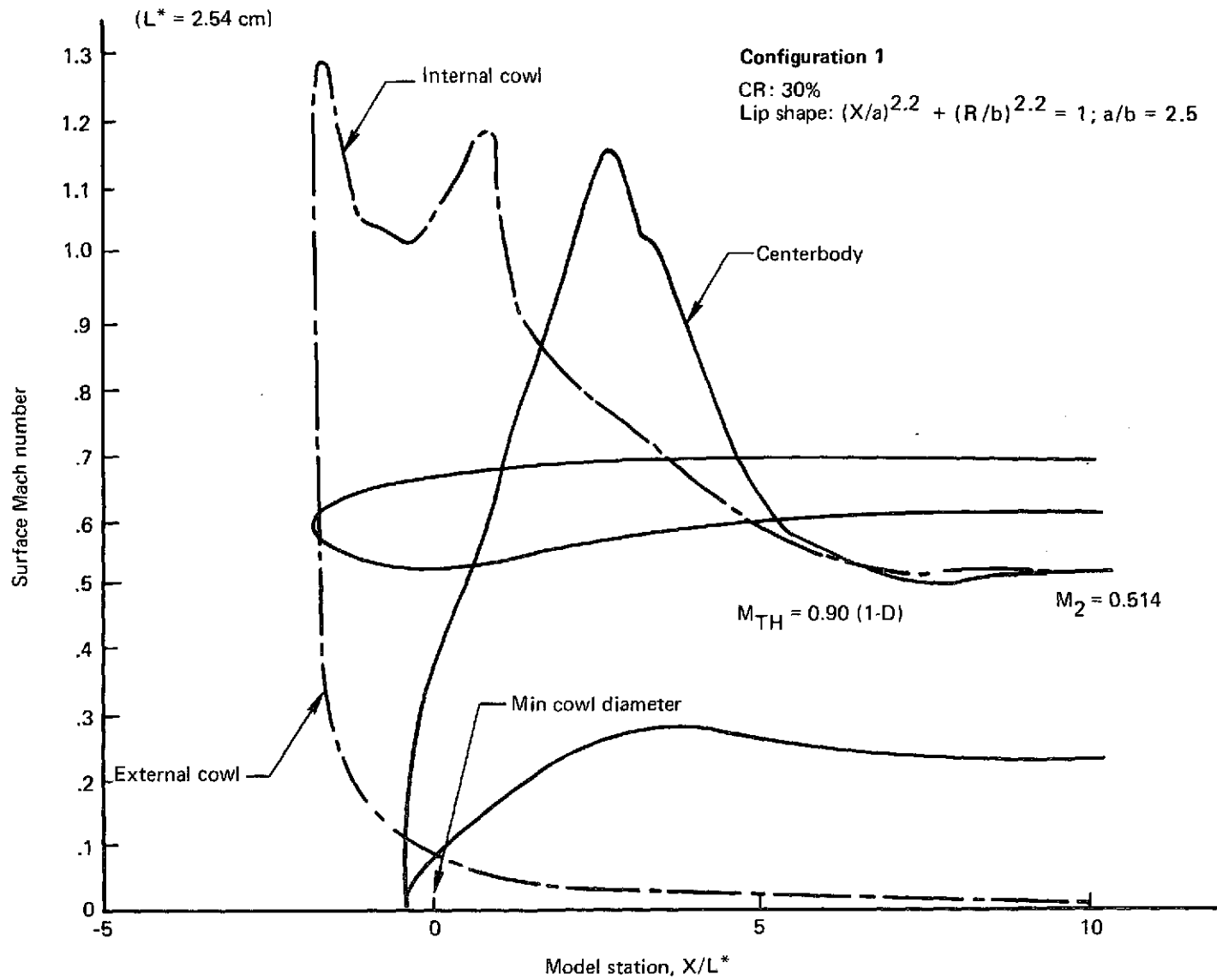


Figure 39.—Surface Mach Number Distribution for Translating Centerbody Inlet—Takeoff, Configuration 1, $V = 0$

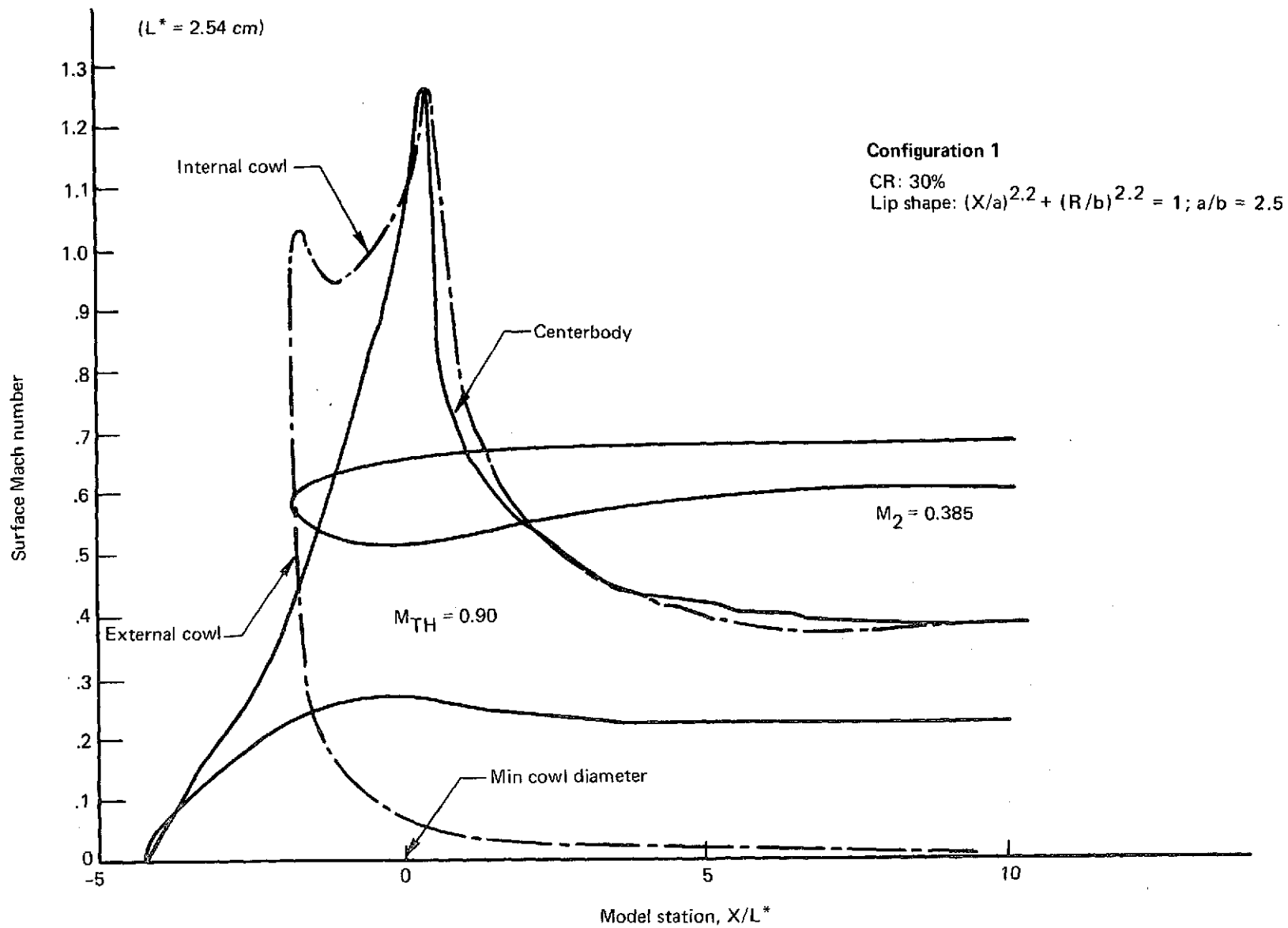


Figure 40.—Surface Mach Number Distribution for Translating Centerbody Inlet—
 Approach, Configuration 1, $V = 0$

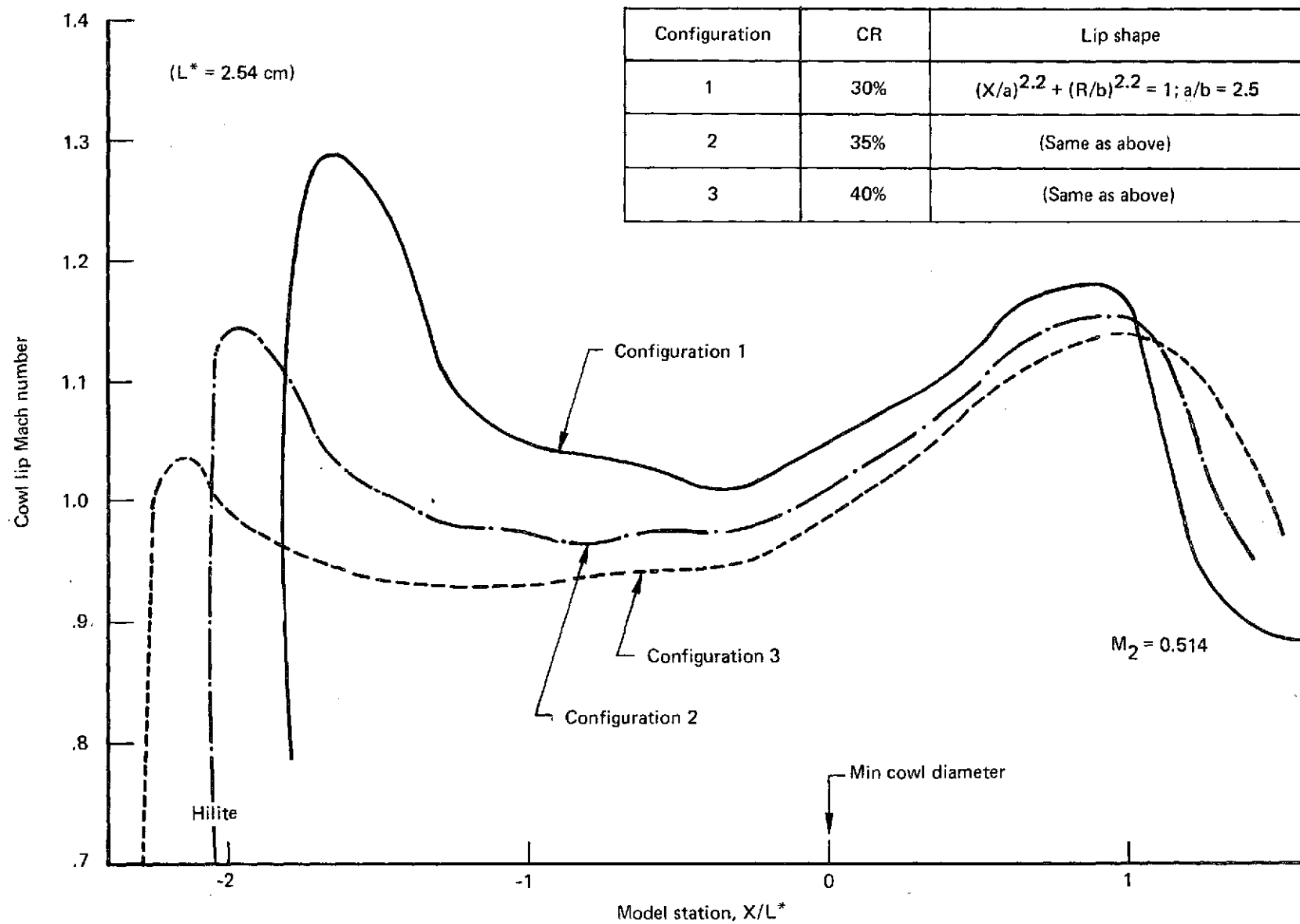


Figure 41.—Lip Contraction Ratio Effects for Translating Centerbody Inlet—Takeoff, $V = 0$

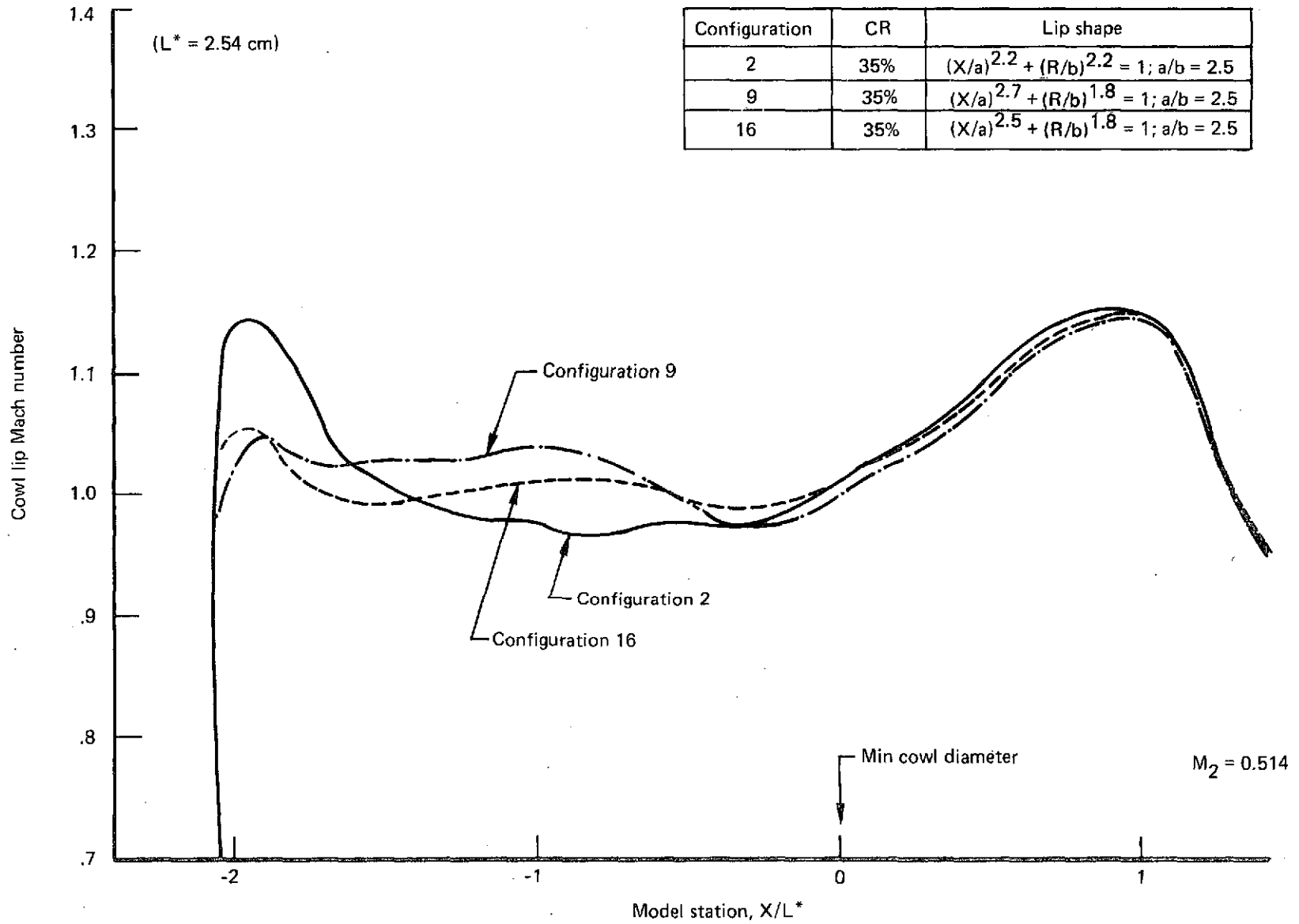


Figure 42.—Cowl Lip Shape Effects for Translating Centerbody Inlet—Takeoff, $V = 0$

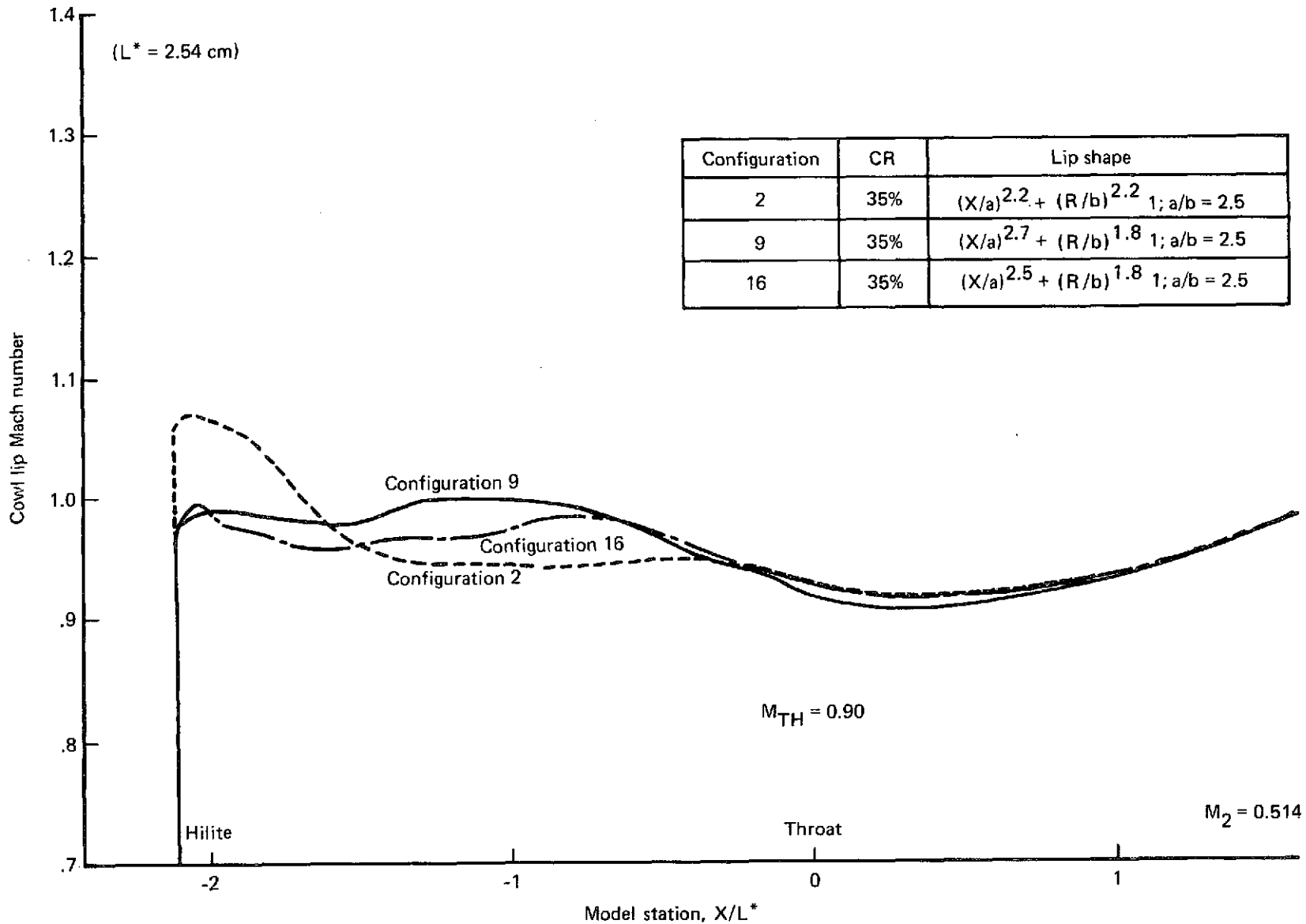


Figure 43.—Cowl Lip Shape Effects for Radial Vane Inlet—Takeoff, $V = 0$

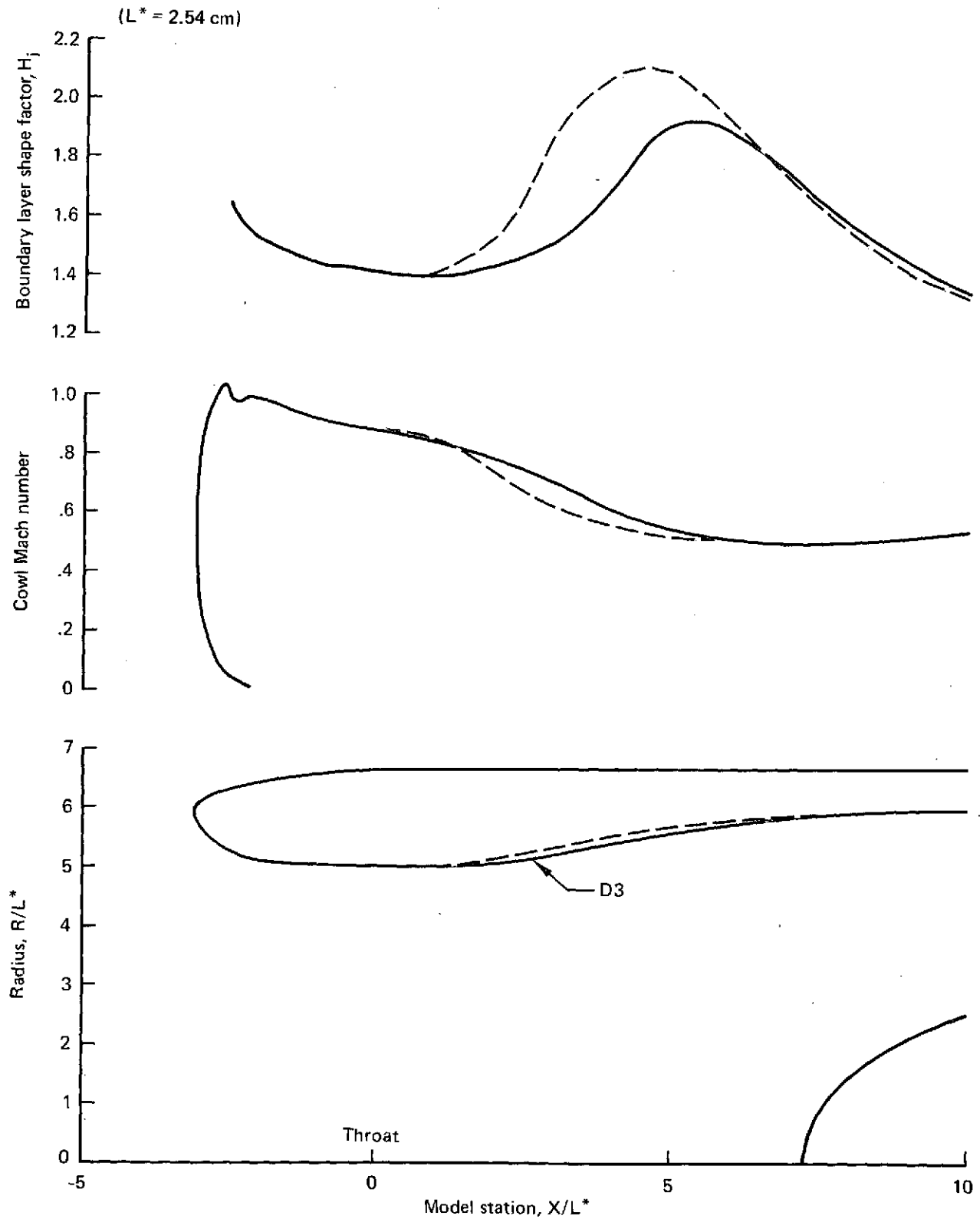


Figure 44.—Variation of Shape Factor and Surface Mach Number with Diffuser Shape—QCSEE High Mach Number Inlet

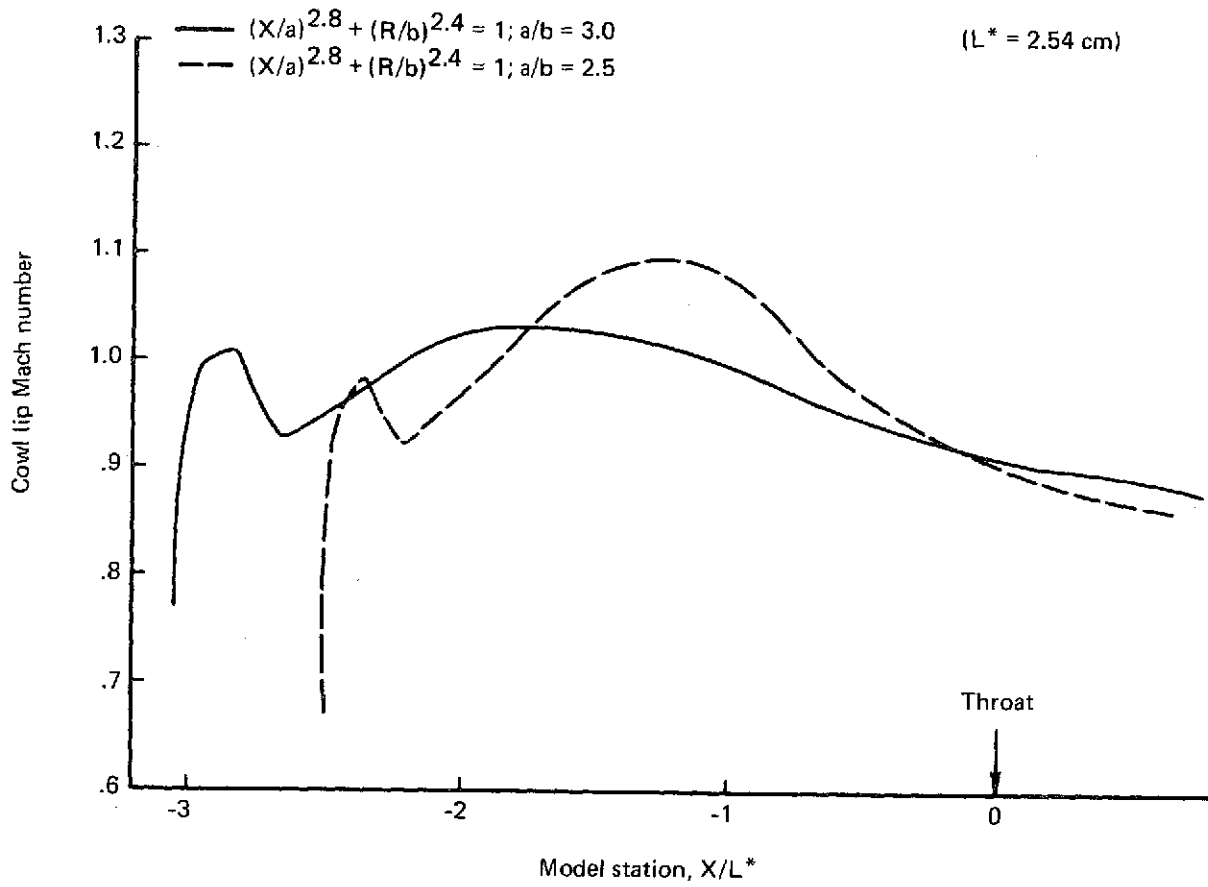


Figure 45.—Effect of Lip Aspect Ratio on Lip Mach Numbers—QCSEE
High Mach Number Inlet

C-2

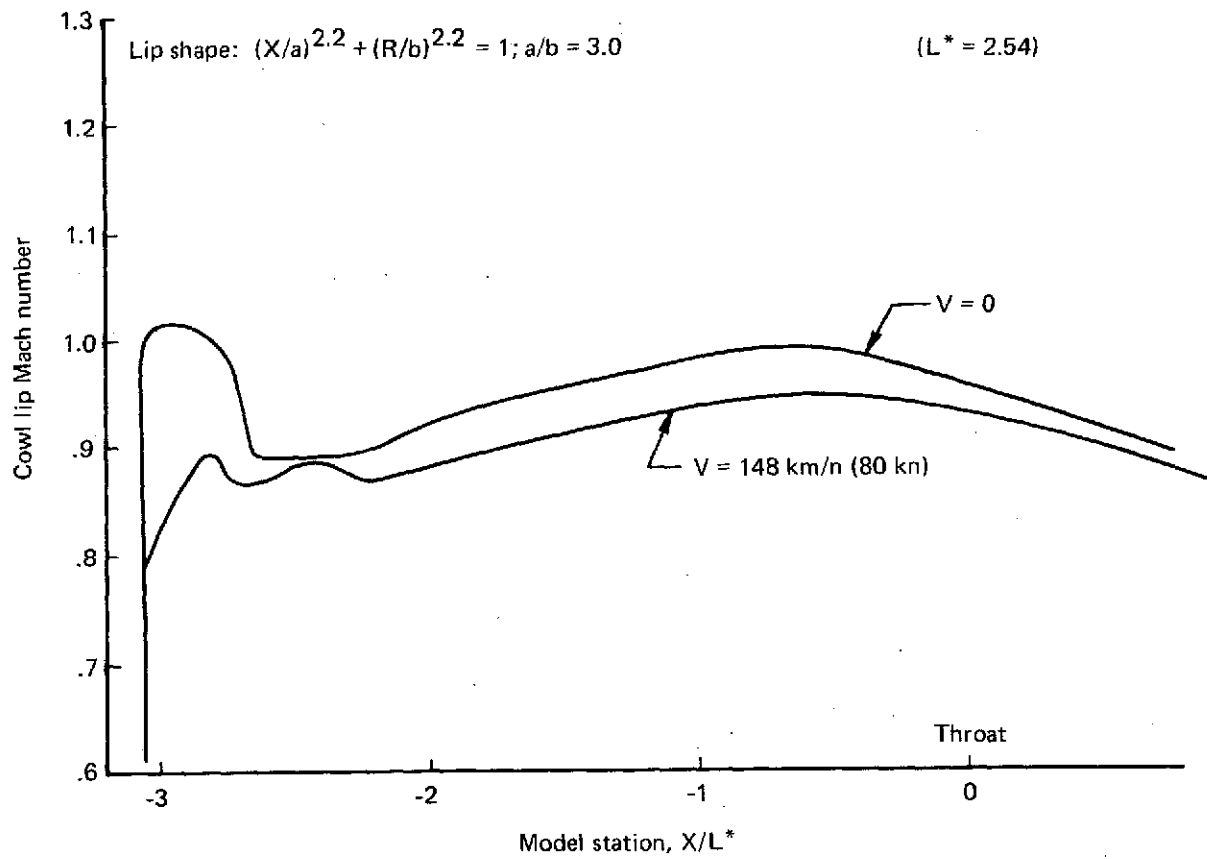


Figure 46.—Effect of Forward Speed on Cowl Lip Mach Number Distributions—
QCSEE High Mach Number Inlet

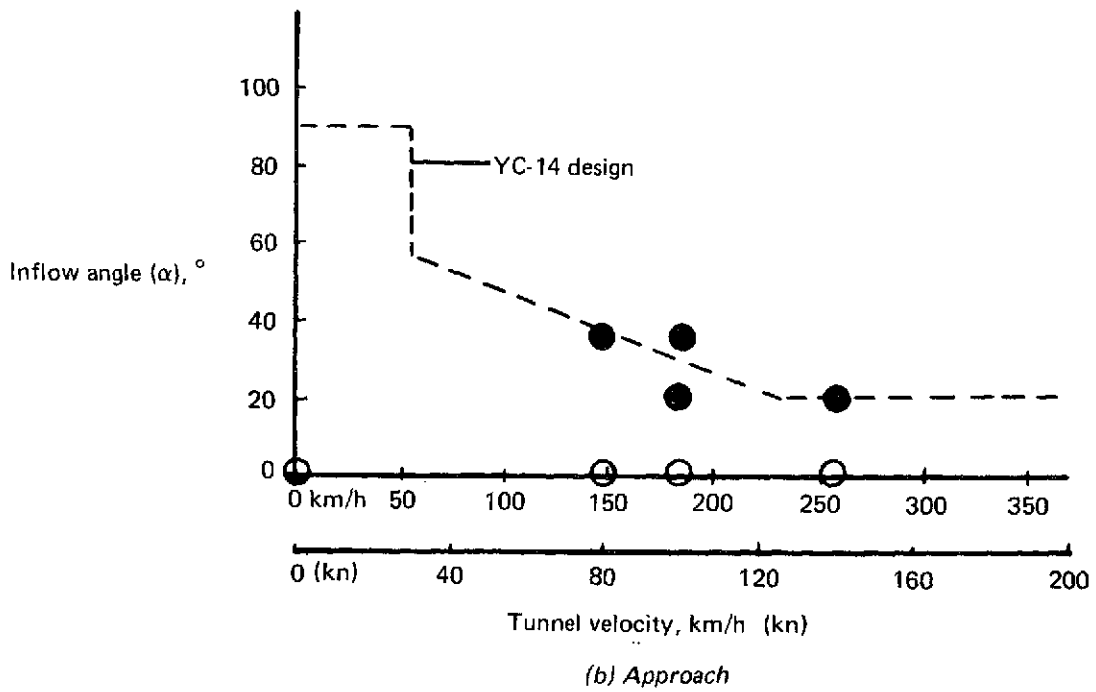
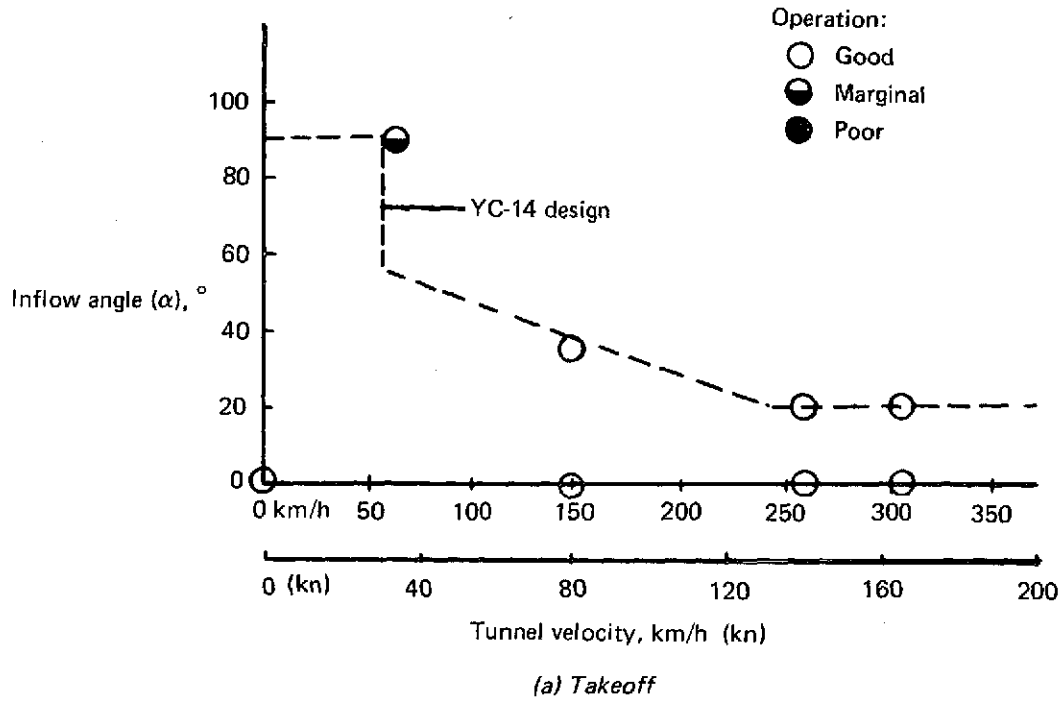
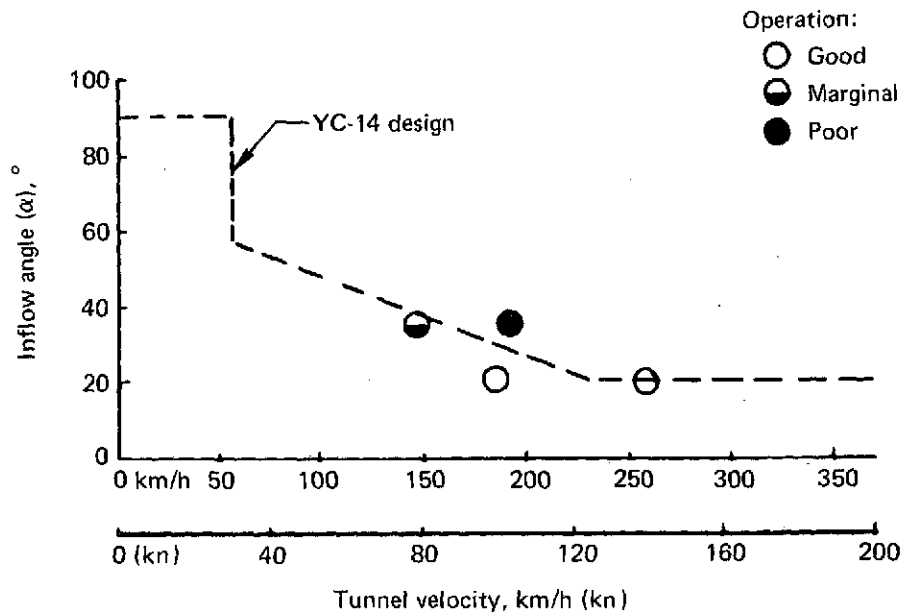
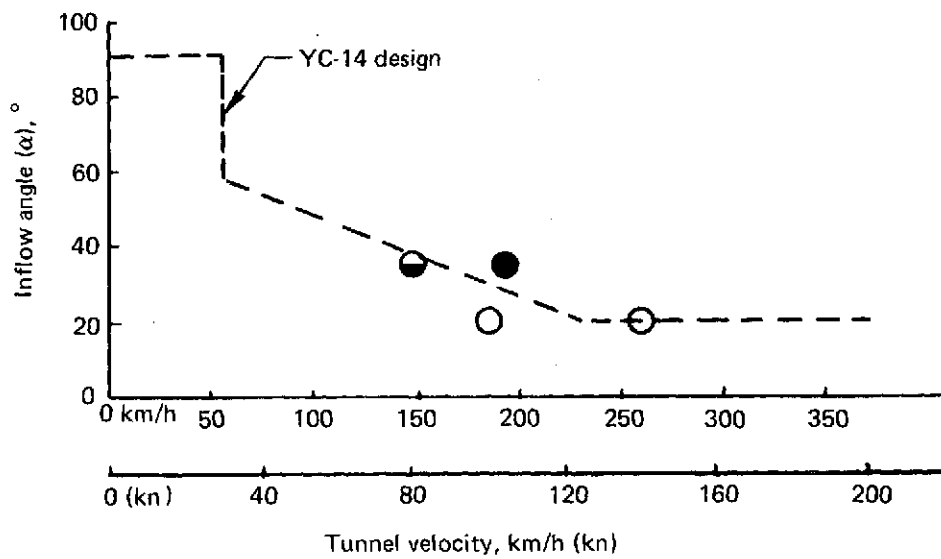


Figure 47.—Translating Centerbody Inlet A1—Performance Summary



(a) Inlet A2 Approach (1% Area Increase)



(b) Inlet A3 Approach (4% Area Increase)

Figure 48.—Translating Centerbody Inlets A2 and A3 Approach—Performance Summary

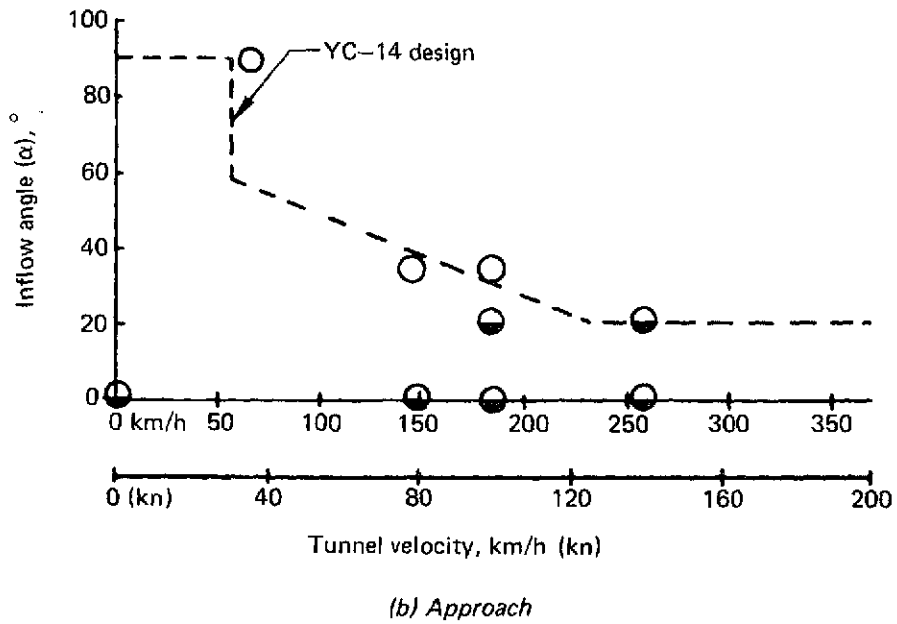
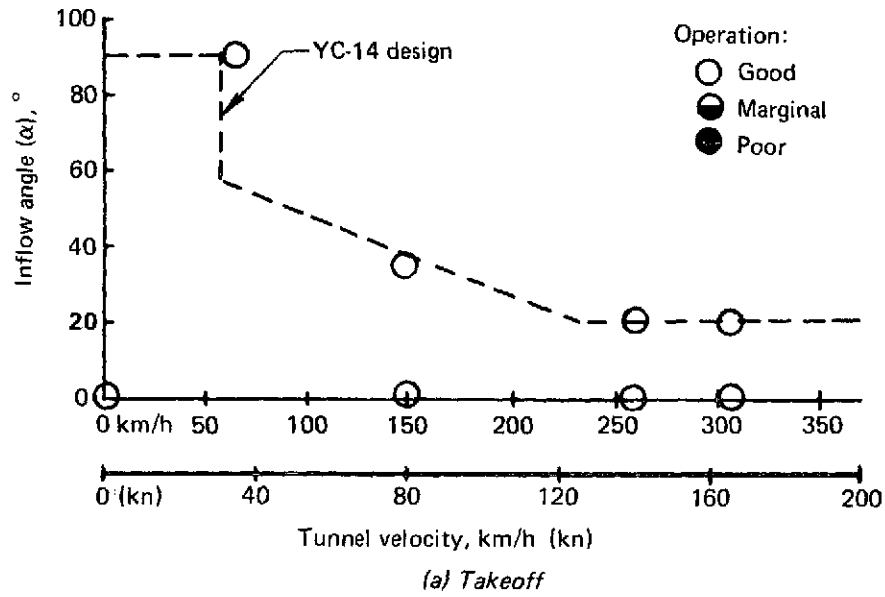


Figure 49.—Radial Vane Inlet B—Performance Summary

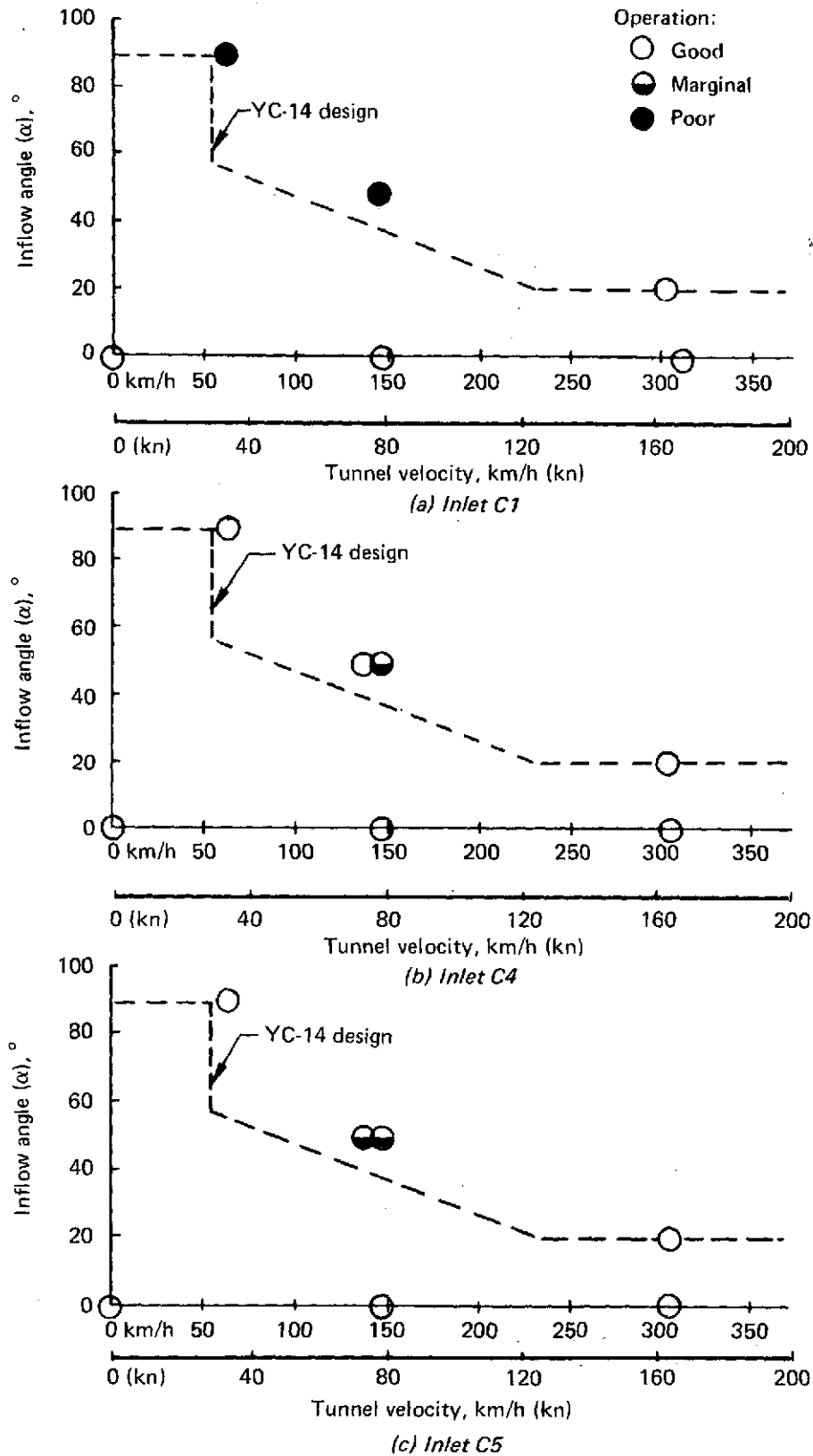
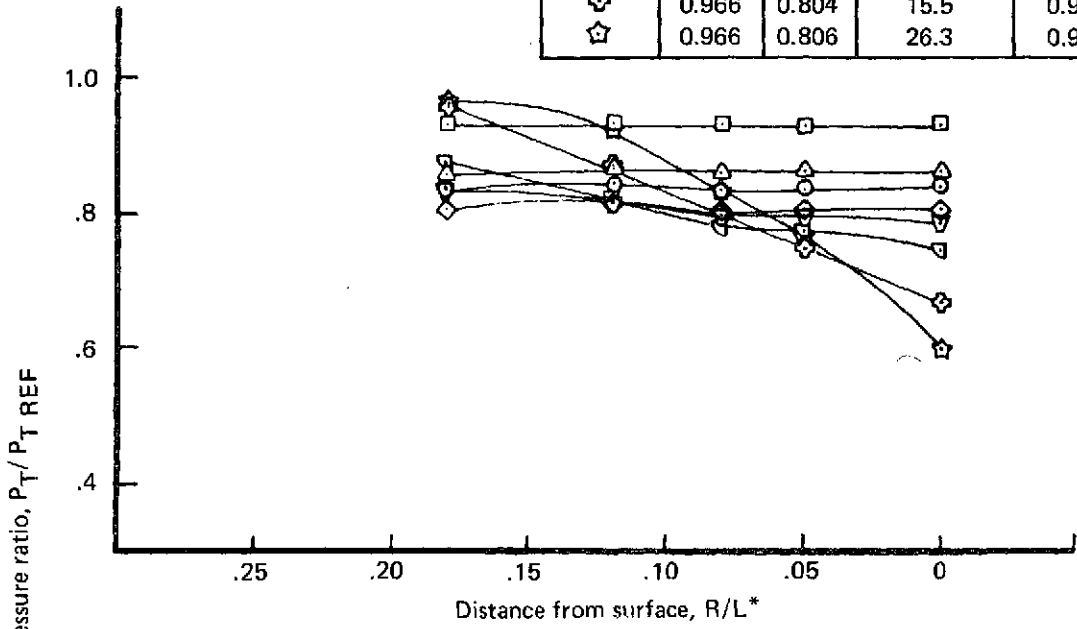
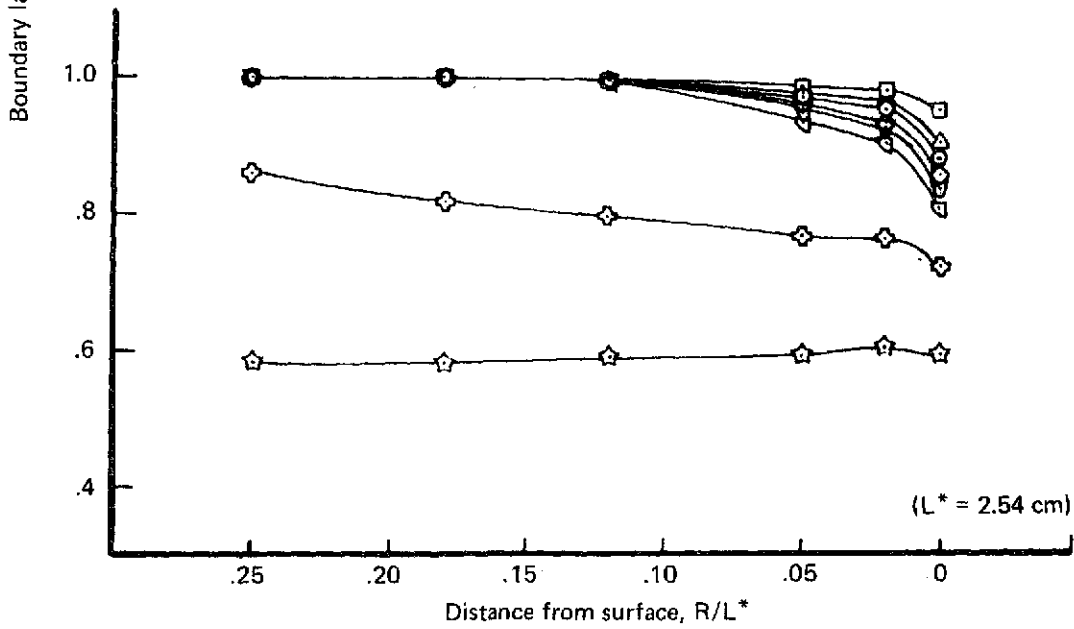


Figure 50.—QCSEE High Mach Number Inlets C1, C4, and C5—Performance Summary

Symbol	C_D^*	M_{TH}	Distortion, %	Recovery
□	0.284	0.168	5.6	0.9743
△	0.572	0.356	9.5	0.9678
○	0.657	0.422	10.7	0.9696
◇	0.783	0.536	12.2	0.9817
▽	0.872	0.637	12.9	0.9871
▽	0.928	0.722	13.8	0.9869
⊕	0.966	0.804	15.5	0.9706
☆	0.966	0.806	26.3	0.9372

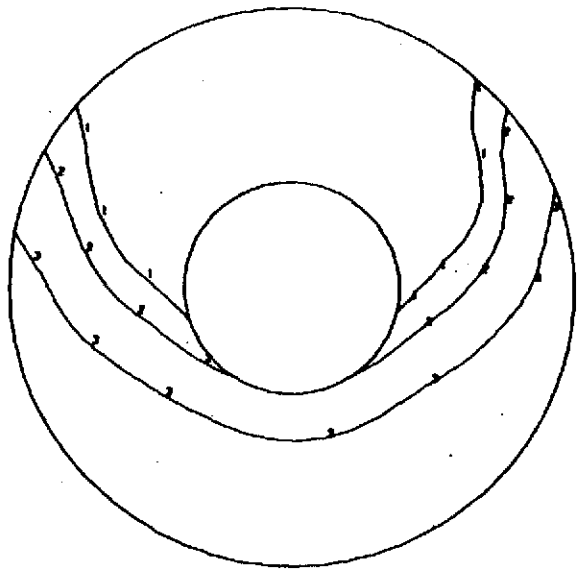


(a) Cowl

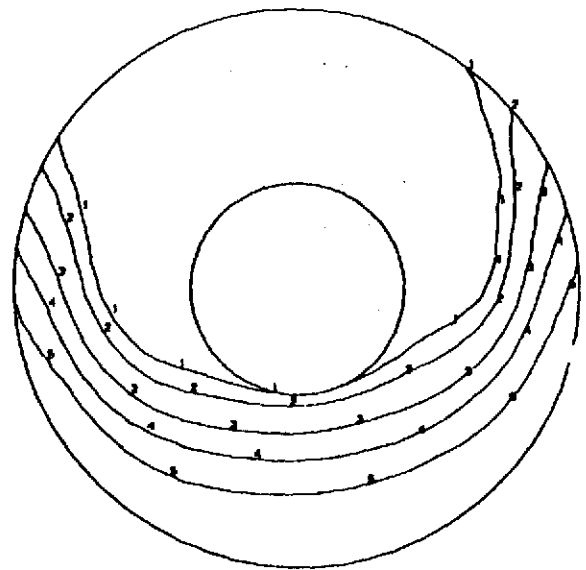


(b) Centerbody

Figure 51.—Boundary Layer Profiles for Translating Centerbody Inlet A1 at Takeoff— $\alpha = 90^\circ$, $V = 65 \text{ km/h (35 kn)}$



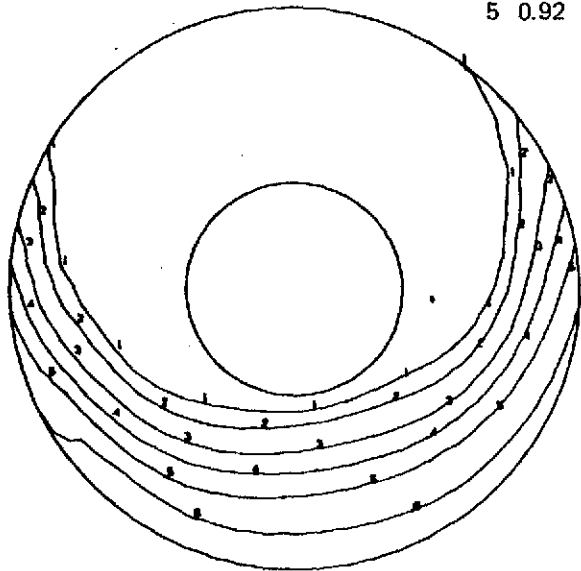
(a) $C_D^* = 0.284$
 $(M_{TH} = 0.168, \text{distortion} = 5.6\%, \text{recovery} = 0.9743)$



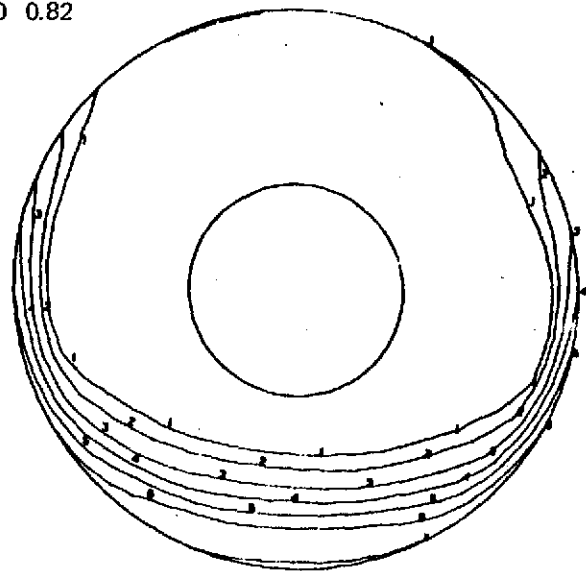
(b) $C_D^* = 0.572$
 $(M_{TH} = 0.356, \text{distortion} = 9.5\%, \text{recovery} = 0.9678)$

$P_T/P_{T REF}$

1	0.99	6	0.90
2	0.98	7	0.88
3	0.96	8	0.86
4	0.94	9	0.84
5	0.92	0	0.82

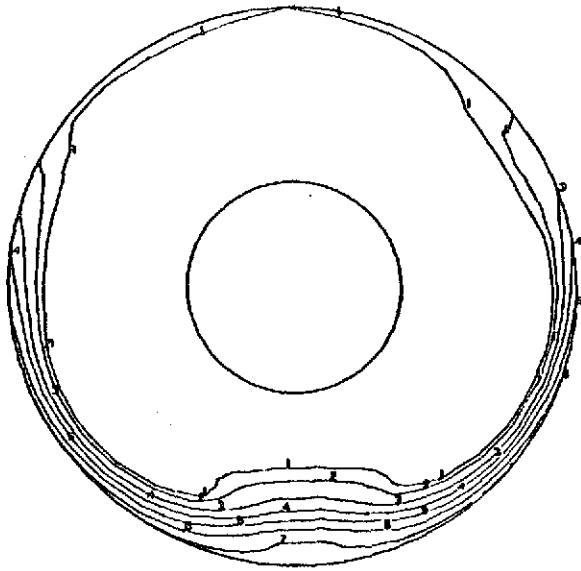


(c) $C_D^* = 0.657$
 $(M_{TH} = 0.422, \text{distortion} = 10.7\%, \text{recovery} = 0.9696)$



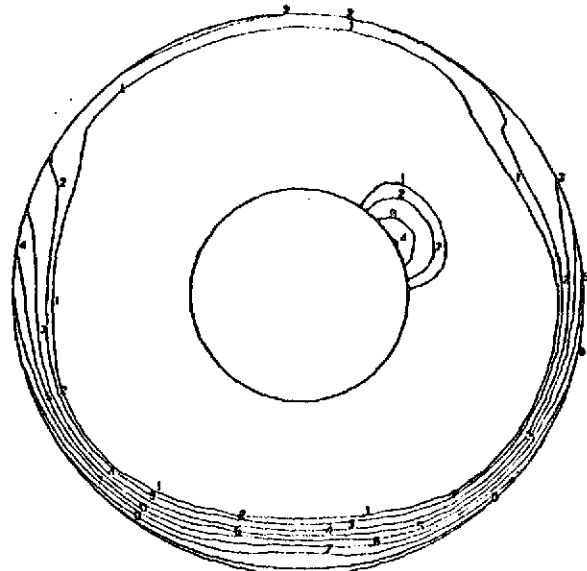
(d) $C_D^* = 0.783$
 $(M_{TH} = 0.536, \text{distortion} = 12.2\%, \text{recovery} = 0.9817)$

Figure 52.—Compressor Face Total Pressure Recovery Maps for Translating Centerbody Inlet A1 at Takeoff— $\alpha = 90^\circ$, $V = 65 \text{ km/h (35 kn)}$



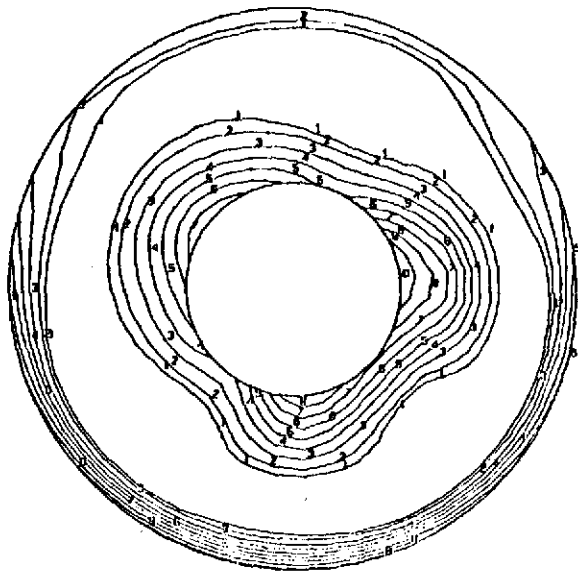
(e) $C_D^* = 0.872$

($M_{TH} = 0.637$, distortion = 12.9%, recovery = 0.9871)



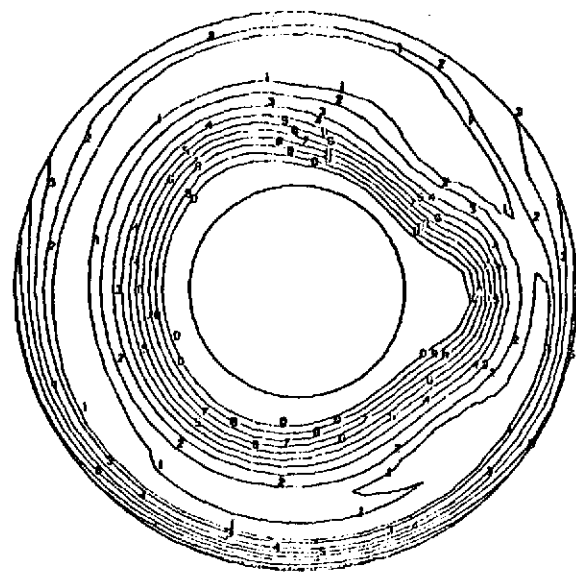
(f) $C_D^* = 0.928$

($M_{TH} = 0.722$, distortion = 13.8%, recovery = 0.9869)



(g) $C_D^* = 0.966$

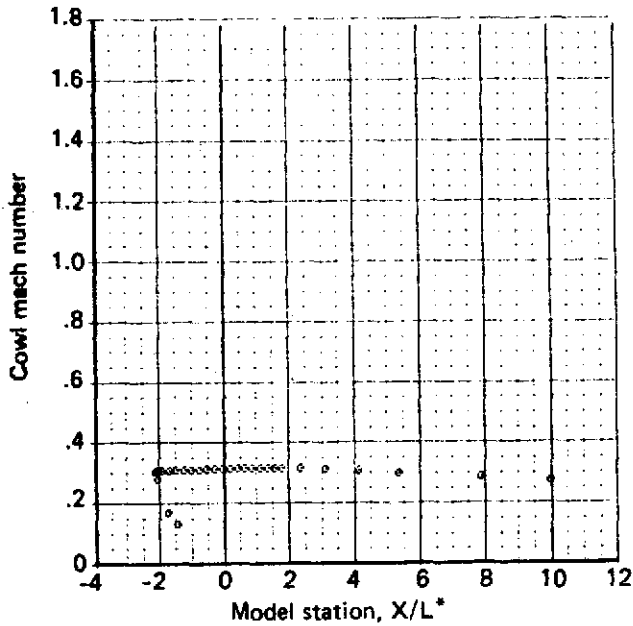
($M_{TH} = 0.804$, distortion = 15.5%, recovery = 0.9706)



(h) $C_D^* = 0.966$

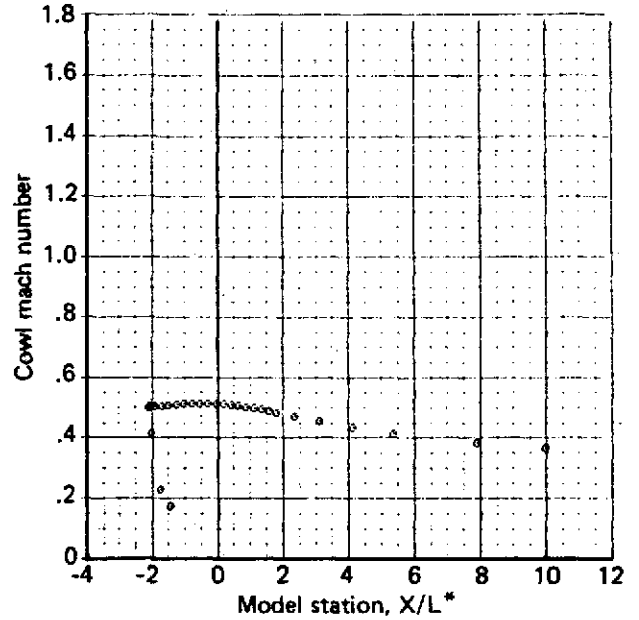
($M_{TH} = 0.806$, distortion = 26.3%, recovery = 0.9372)

Figure 52.—Concluded



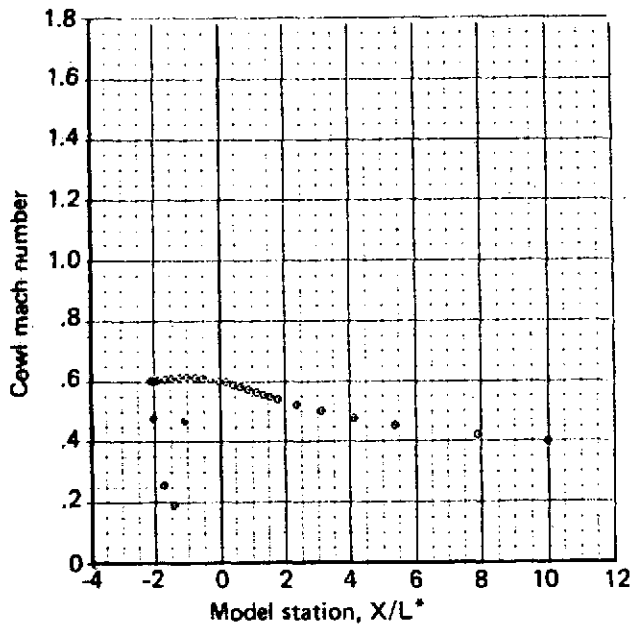
(a) $C_D^* = 0.284$

($M_{TH} = 0.168$, distortion = 5.6%, recovery = 0.9743)



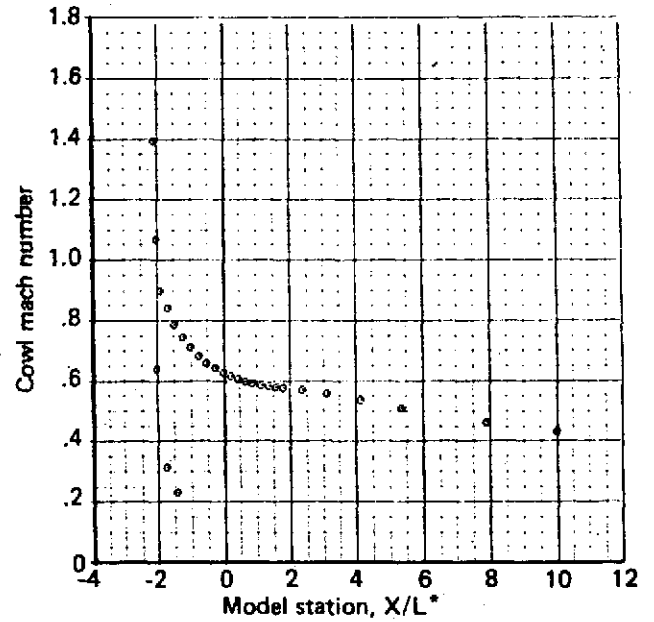
(b) $C_D^* = 0.572$

($M_{TH} = 0.356$, distortion = 9.5%, recovery = 0.9678)



(c) $C_D^* = 0.657$

($M_{TH} = 0.422$, distortion = 10.7%, recovery = 0.9696)

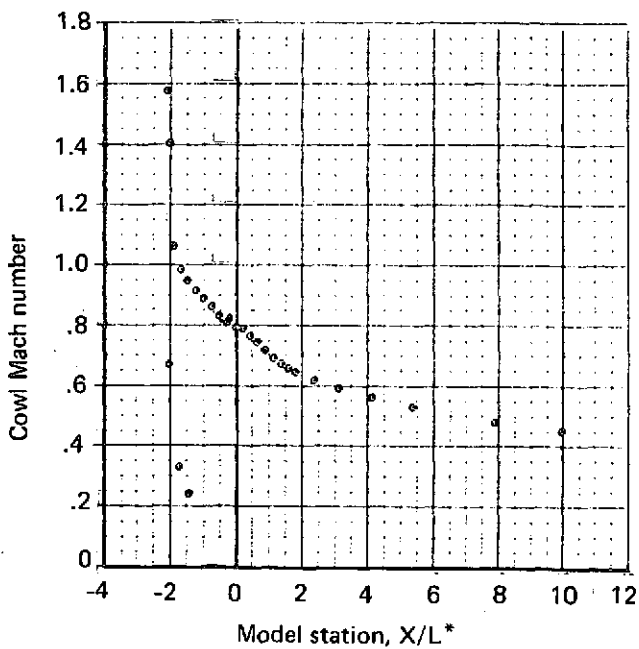


(d) $C_D^* = 0.783$

($M_{TH} = 0.536$, distortion = 12.2%, recovery = 0.9816)

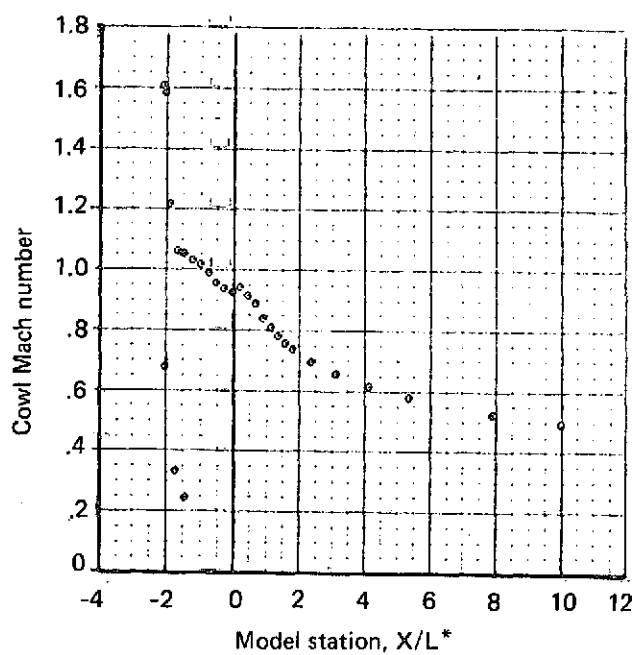
Notes: $L^* = 2.54$ cm Minimum cowl radius is at $X/L^* = 0$

Figure 53.—Inlet Cowl Mach Number Distribution for Translating Centerbody Inlet A1 at Takeoff— $\alpha = 90^\circ$, $V = 65$ km/h (35 kn)



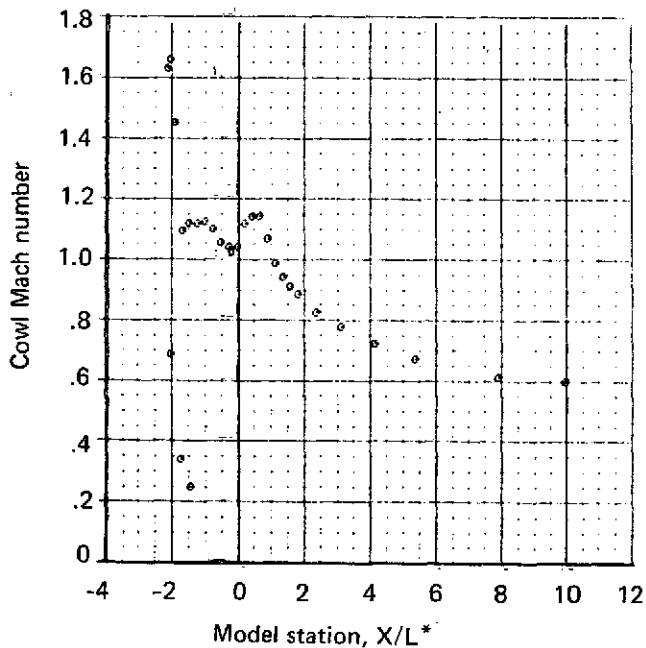
(e) $C_D^* = 0.872$

($M_{TH} = 0.637$, distortion = 12.9%, recovery = 0.9870)



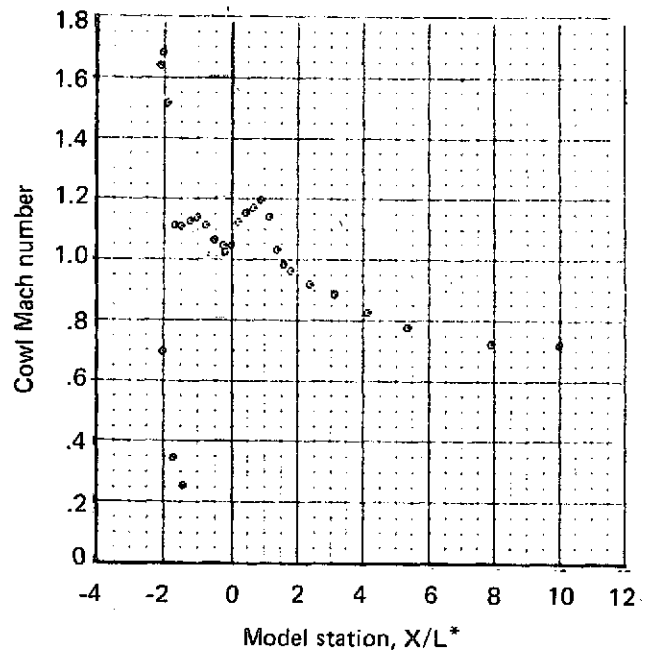
(f) $C_D^* = 0.928$

($M_{TH} = 0.722$, distortion = 13.8%, recovery = 0.9869)



(g) $C_D^* = 0.966$

($M_{TH} = 0.804$, distortion = 15.5%, recovery = 0.9706)



(h) $C_D^* = 0.966$

($M_{TH} = 0.806$, distortion = 26.3%, recovery = 0.9371)

Figure 53.—Concluded

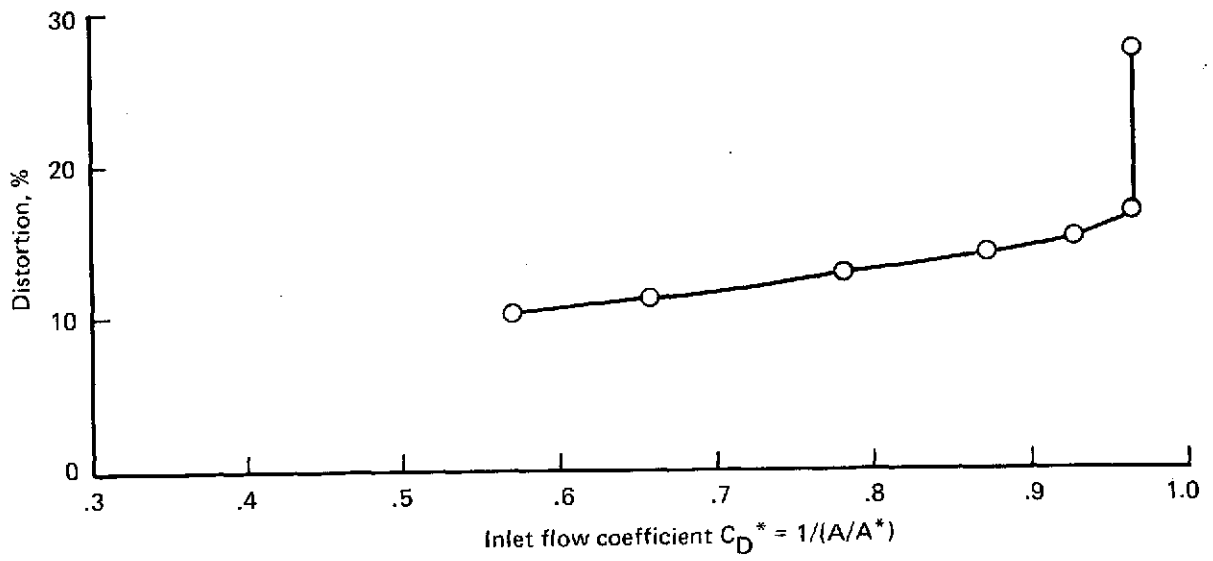
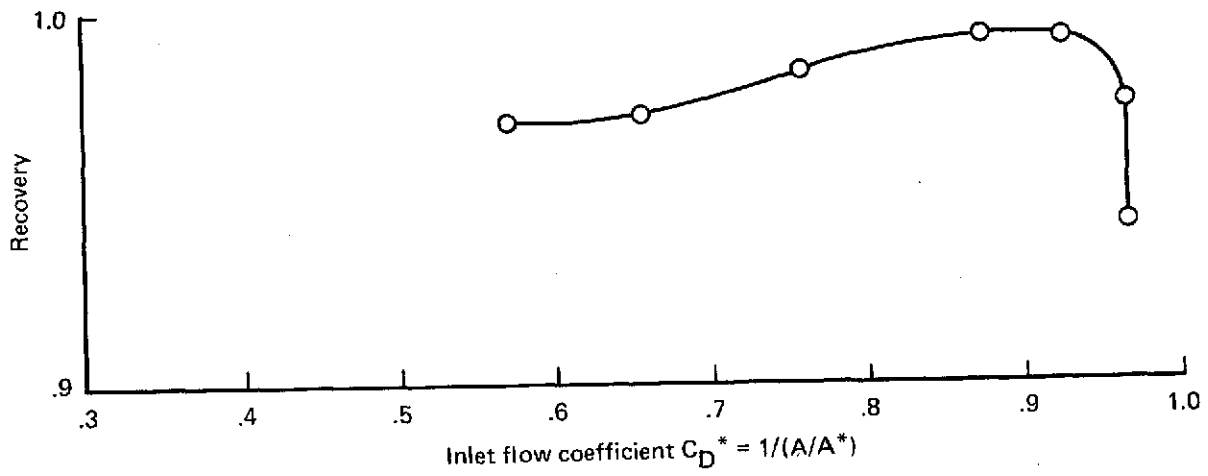
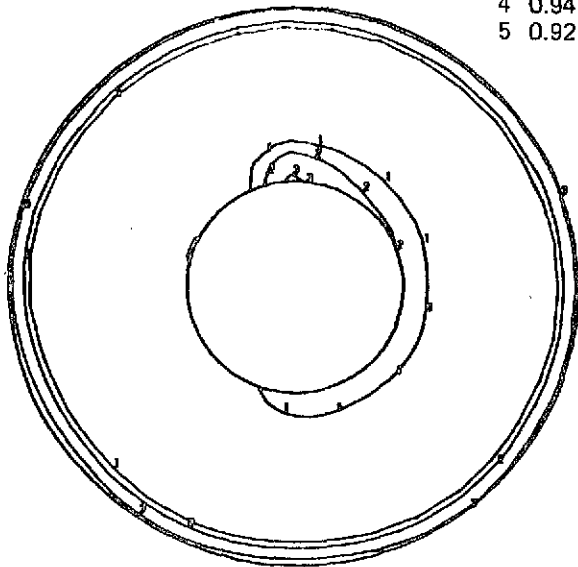


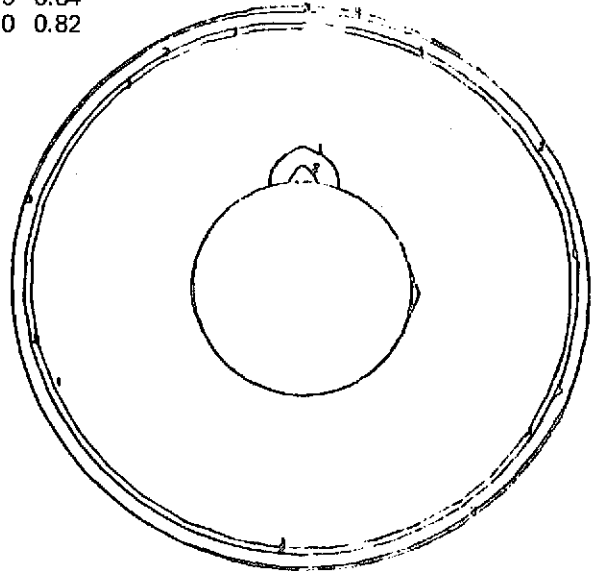
Figure 54.—Translating Centerbody Inlet A1 Distortion and Recovery Performance at Takeoff— $\alpha = 90^\circ$, $V = 65 \text{ km/h}$ (35 kn)

$P_T/P_{T REF}$

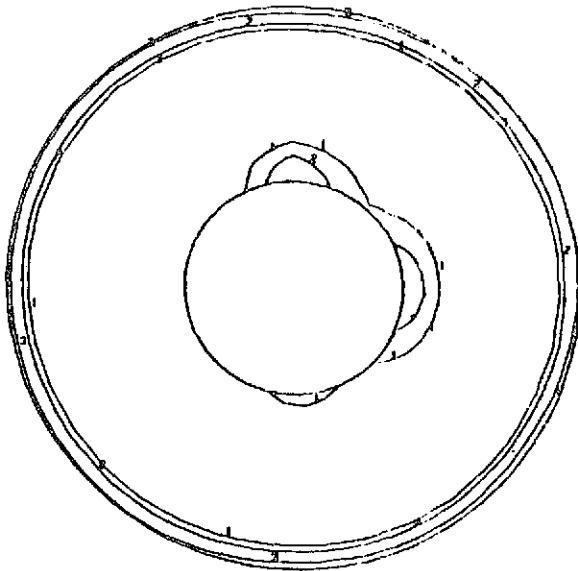
1	0.99	6	0.90
2	0.98	7	0.88
3	0.96	8	0.86
4	0.94	9	0.84
5	0.92	0	0.82



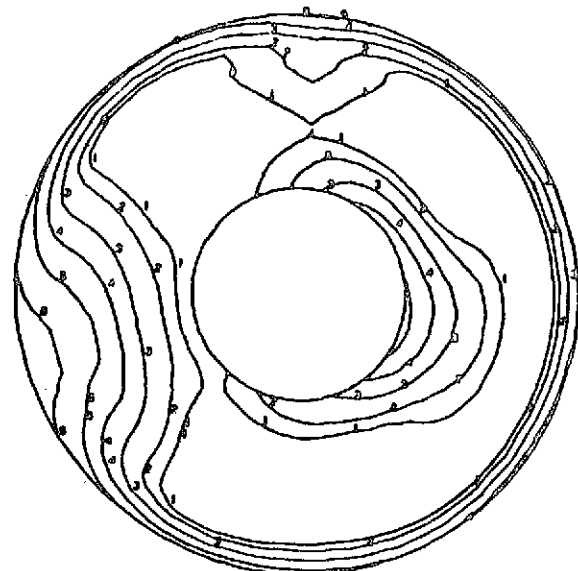
(a) $C_D^* = 0.975$, $V = 148$ km/h (80 kn)
 $(M_{TH} = 0.834, \text{distortion} = 3.8\%, \text{recovery} = 0.9934)$



(b) $C_D^* = 0.947$, $V = 185$ km/h (100 kn)
 $(M_{TH} = 0.763, \text{distortion} = 3.5\%, \text{recovery} = 0.9951)$



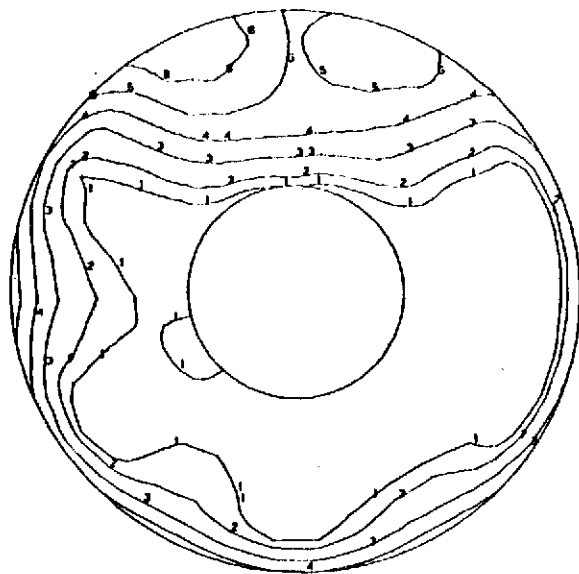
(c) $C_D^* = 0.952$, $V = 259$ km/h (140 kn)
 $(M_{TH} = 0.772, \text{distortion} = 3.7\%, \text{recovery} = 0.9937)$



(d) $C_D^* = 0.972$, $V = 259$ km/h (140 kn)*
 $(M_{TH} = 0.823, \text{distortion} = 10.3\%, \text{recovery} = 0.9756)$

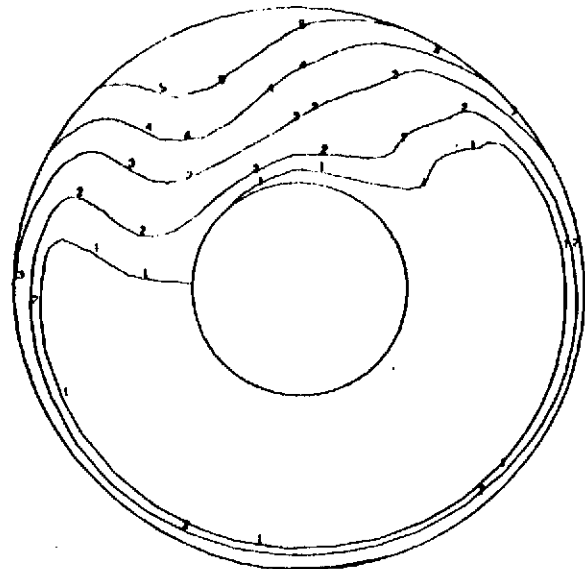
* (d) maps flow just beyond knee of recovery curve; (a), (b), and (c) map flow just prior to knee.

Figure 55.—Compressor Face Total Pressure Recovery Maps for Translating Centerbody Inlet A1 at Approach— $\alpha = 0^\circ$



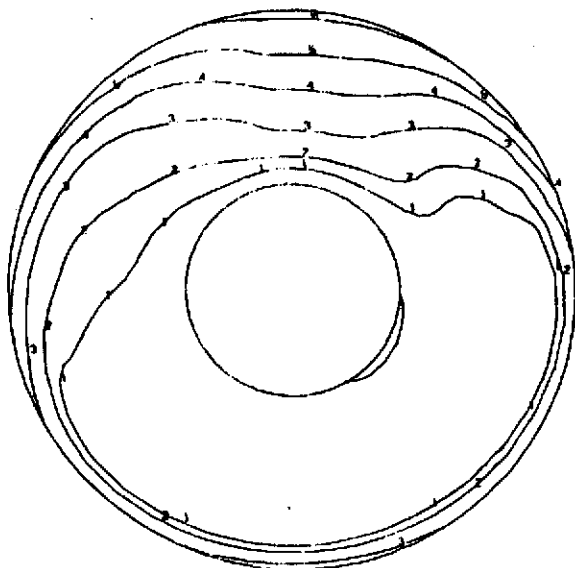
(a) $C_D^* = 0.925$, $\alpha = 0^\circ$

($M_{TH} = 0.712$, distortion = 11.3%, recovery = 0.9725)



(b) $C_D^* = 0.878$, $\alpha = 20^\circ$

($M_{TH} = 0.642$, distortion = 9.4%, recovery = 0.9808)



(c) $C_D^* = 0.925$, $\alpha = 35^\circ$

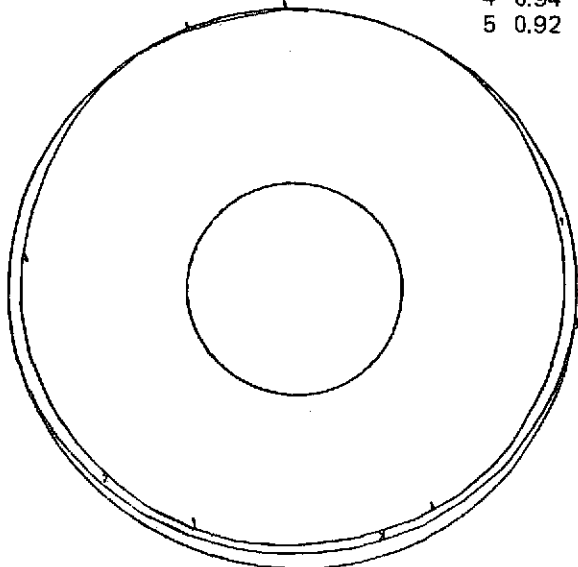
($M_{TH} = 0.715$, distortion = 10.2%, recovery = 0.9774)

$P_T/P_{T REF}$	
1	0.99
2	0.98
3	0.96
4	0.94
5	0.92
6	0.90
7	0.88
8	0.86
9	0.84
0	0.82

Figure 56.—Compressor Face Total Pressure Recovery Maps for Translating Centerbody Inlet A1 at Approach— $V = 0$

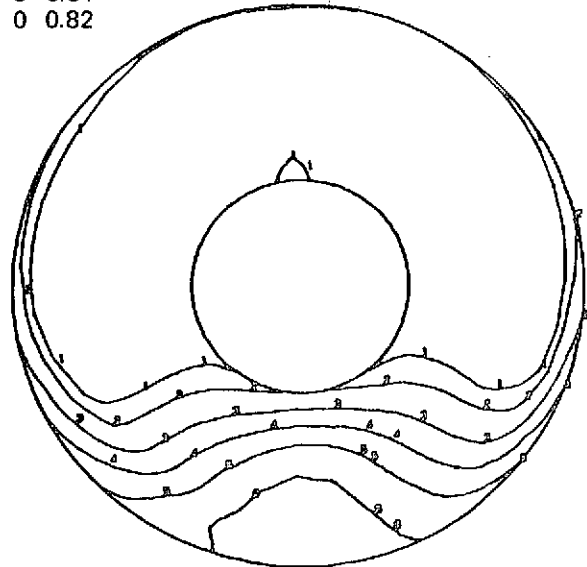
$P_T/P_{T REF}$

1	0.99	6	0.90
2	0.98	7	0.88
3	0.96	8	0.86
4	0.94	9	0.84
5	0.92	0	0.82



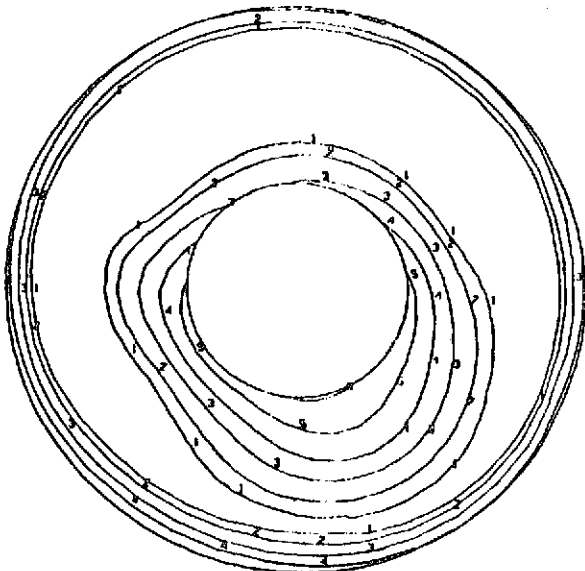
(a) $C_D^* = 0.798$

($M_{TH} = 0.551$, distortion = 2.8%, recovery = 0.9975)



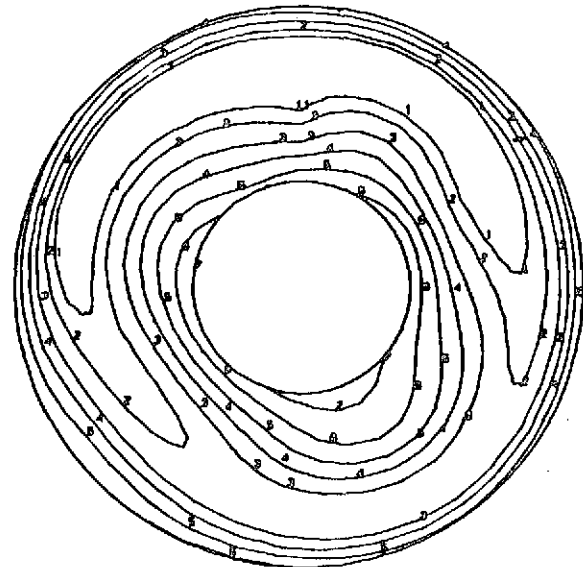
(b) $C_D^* = 0.864$

($M_{TH} = 0.627$, distortion = 11.2%, recovery = 0.9766)



(c) $C_D^* = 0.980$

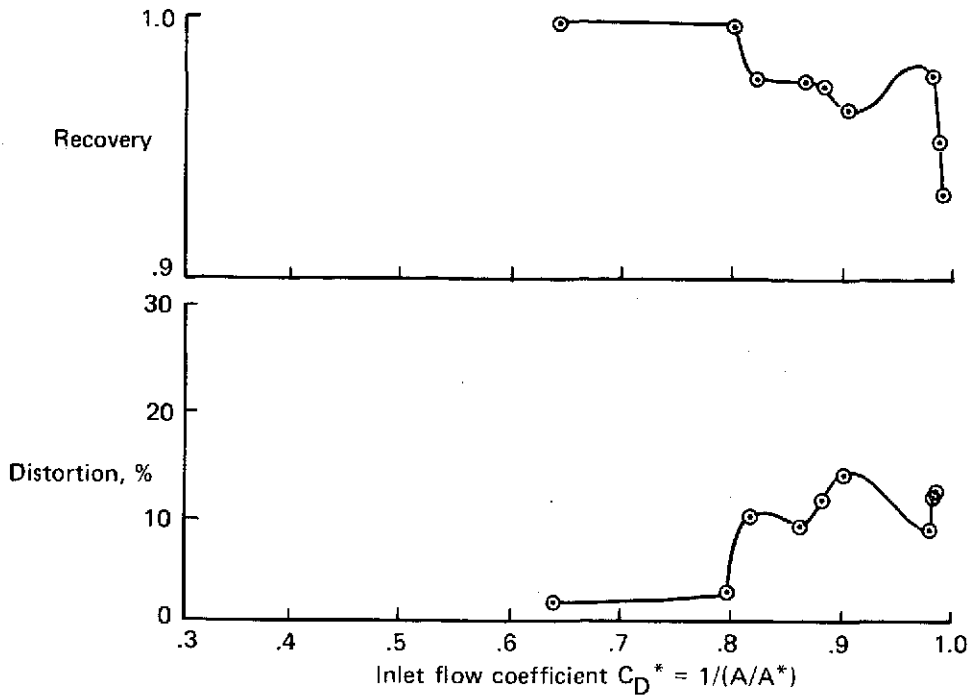
($M_{TH} = 0.850$, distortion = 9.1%, recovery = 0.9783)



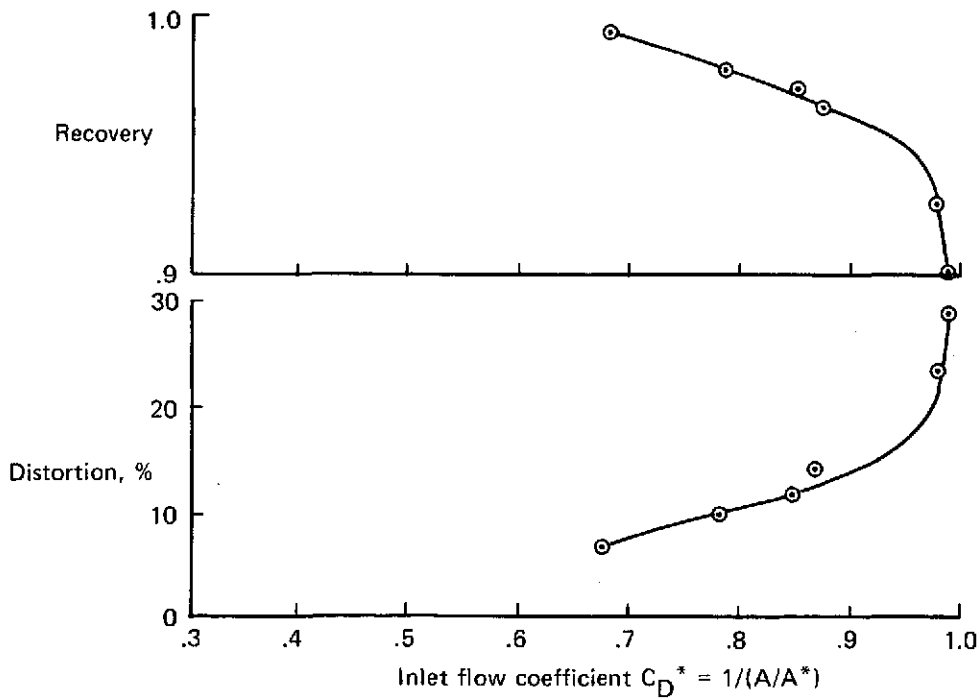
(d) $C_D^* = 0.986$

($M_{TH} = 0.875$, distortion = 12.4%, recovery = 0.9568)

Figure 57.—Compressor Face Total Pressure Recovery Maps for Translating Centerbody Inlet A1 at Approach— $\alpha = 20^\circ$, $V = 185$ km/h (100 kn)

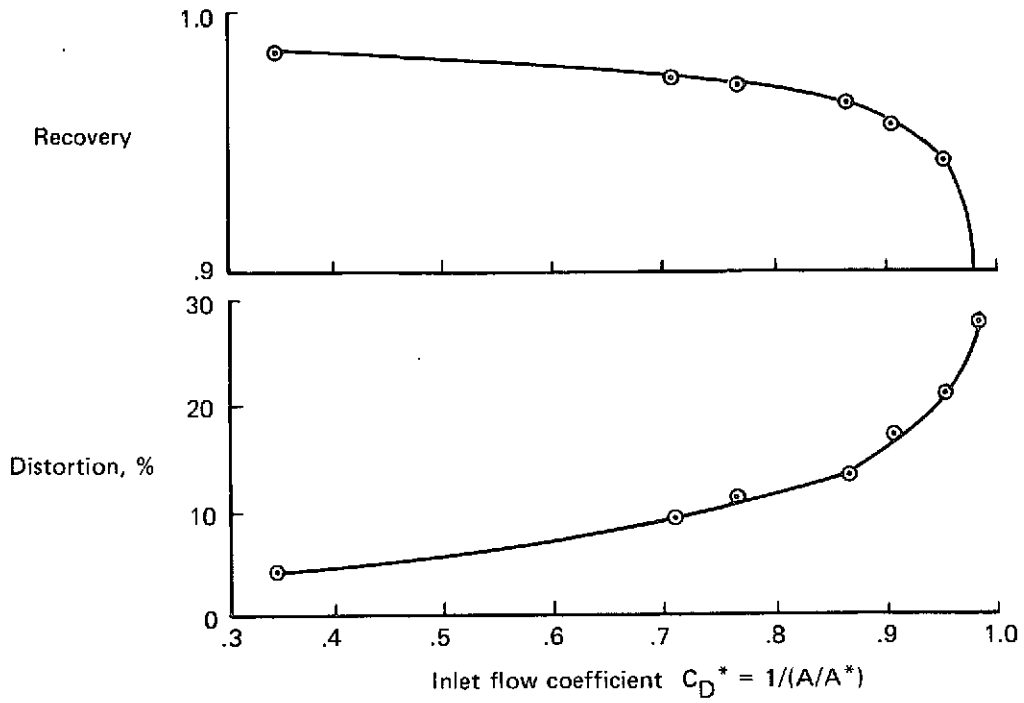


(a) $\alpha = 20^\circ$, $V = 185 \text{ km/h (100 kn)}$

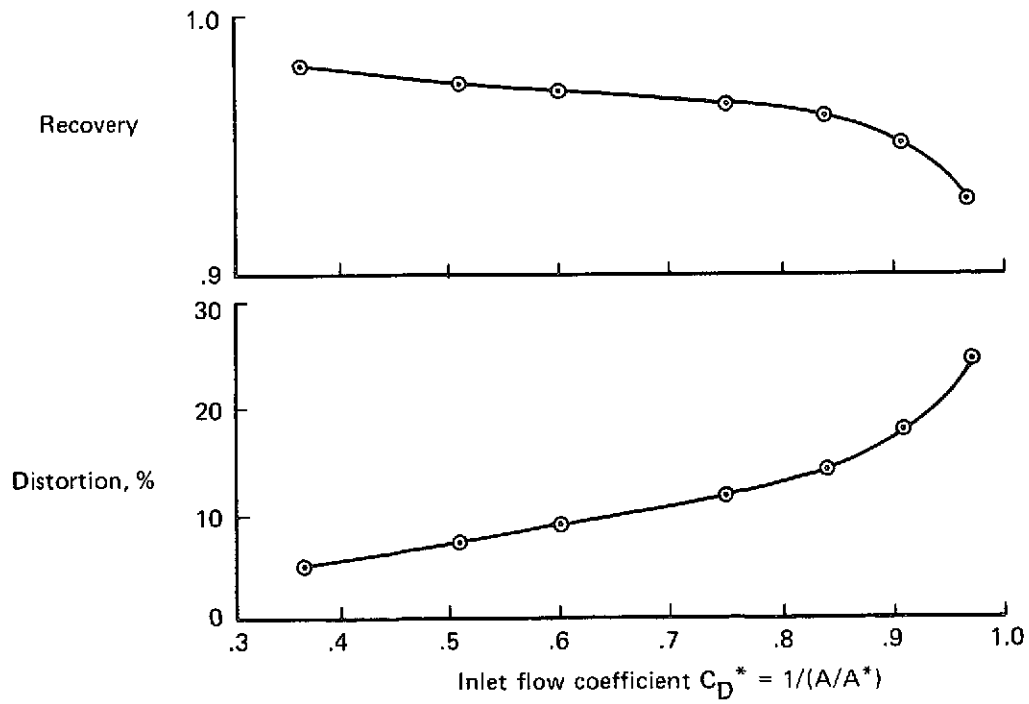


(b) $\alpha = 20^\circ$, $V = 259 \text{ km/h (140 kn)}$

Figure 58.—Translating Centerbody Inlet A1 Distortion and Recovery Performance at Approach



(c) $\alpha = 35^\circ$, $V = 148 \text{ km/h (80 kn)}$



(d) $\alpha = 35^\circ$, $V = 185 \text{ km/h (100 kn)}$

Figure 58.—Concluded

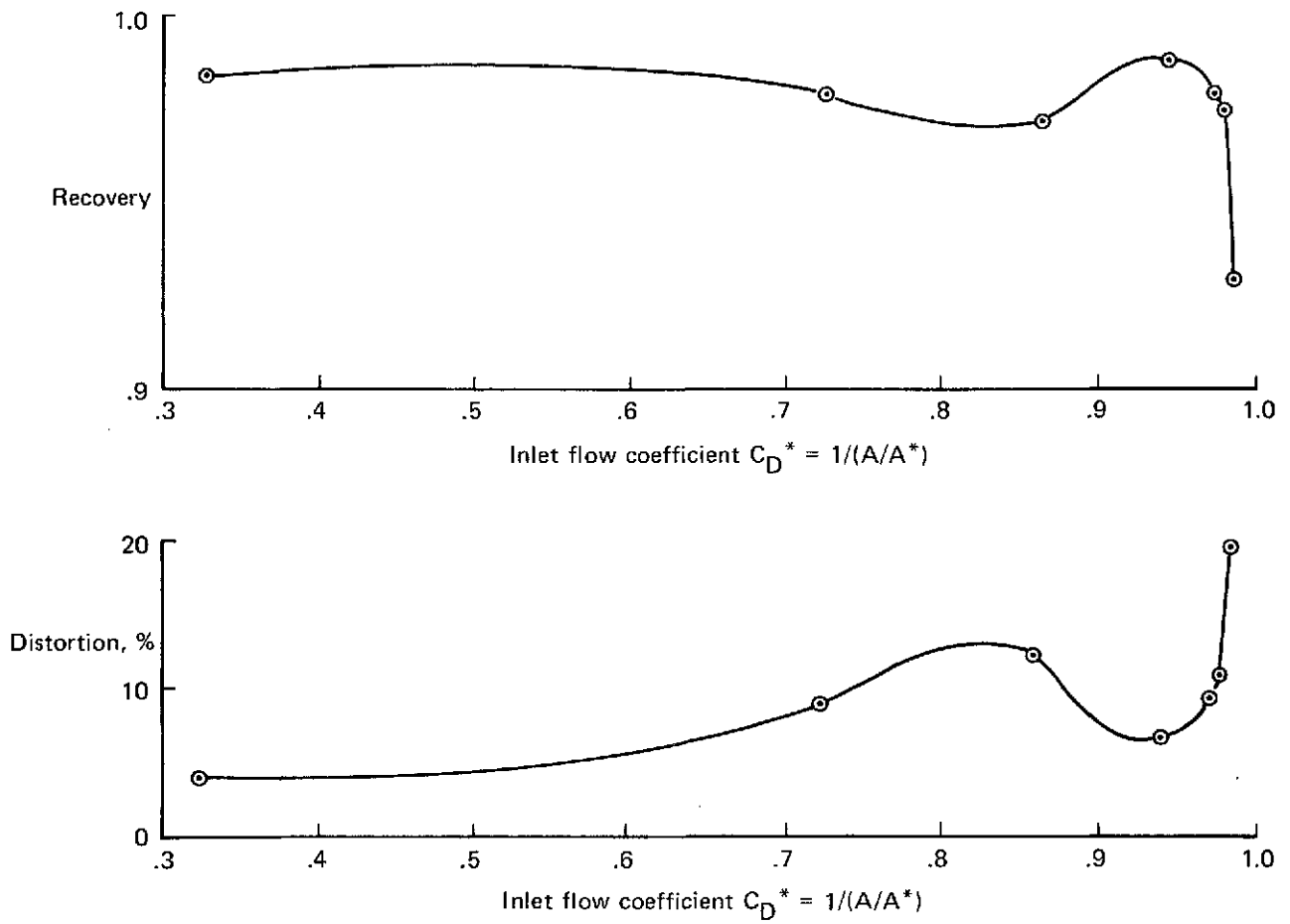
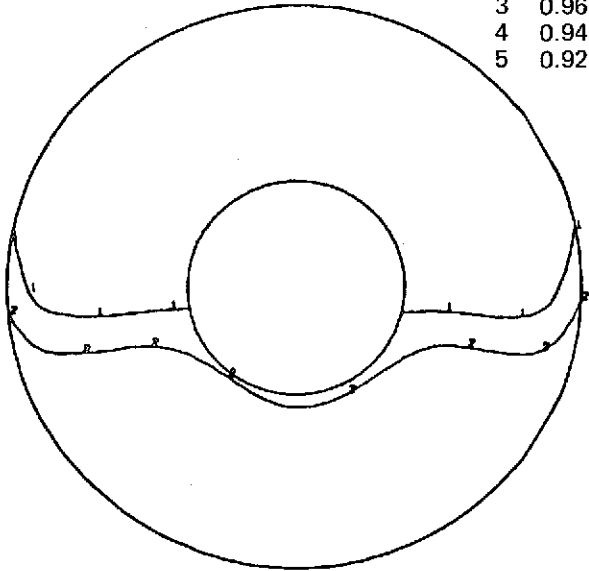


Figure 59.—Translating Centerbody Inlet A2 Distortion and Recovery Performance at Approach— $\alpha = 35^\circ$, $V = 148$ km/h (80 kn)

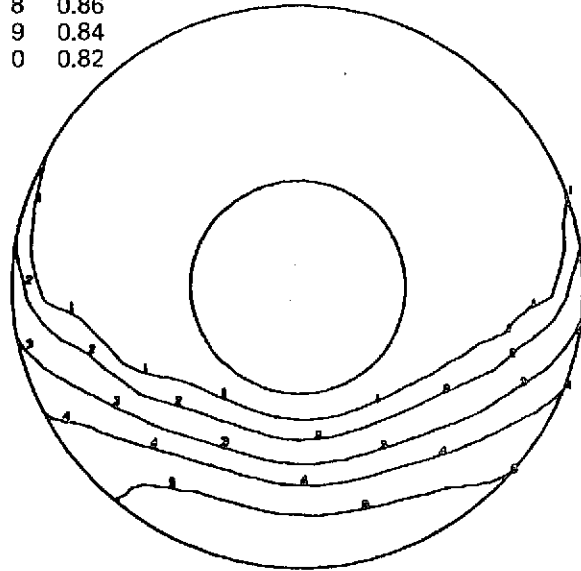
$P_T/P_{T REF}$

1	0.99	6	0.90
2	0.98	7	0.88
3	0.96	8	0.86
4	0.94	9	0.84
5	0.92	0	0.82



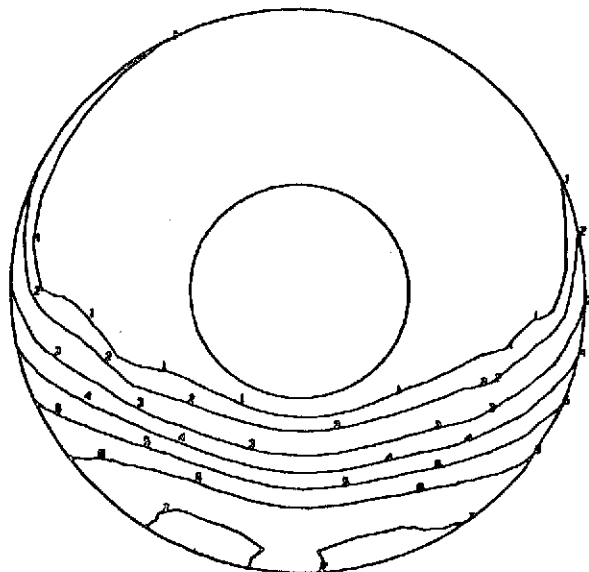
(a) $C_D^* = 0.323$

($M_{TH} = 0.191$, distortion = 4.0%, recovery = 0.9848)



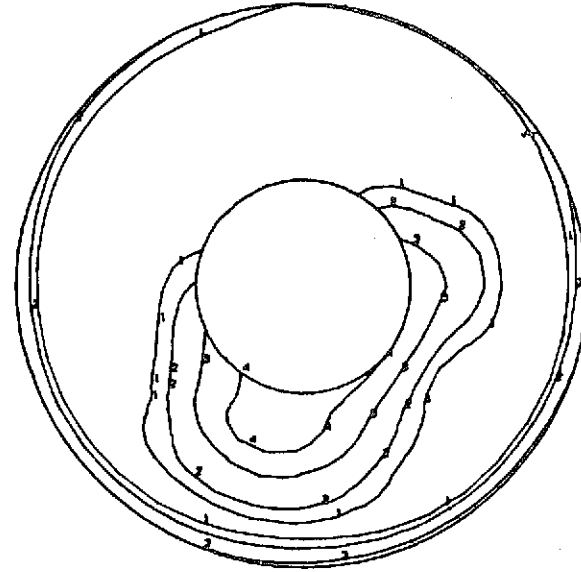
(b) $C_D^* = 0.725$

($M_{TH} = 0.480$, distortion = 9.1%, recovery = 0.9792)



(c) $C_D^* = 0.862$

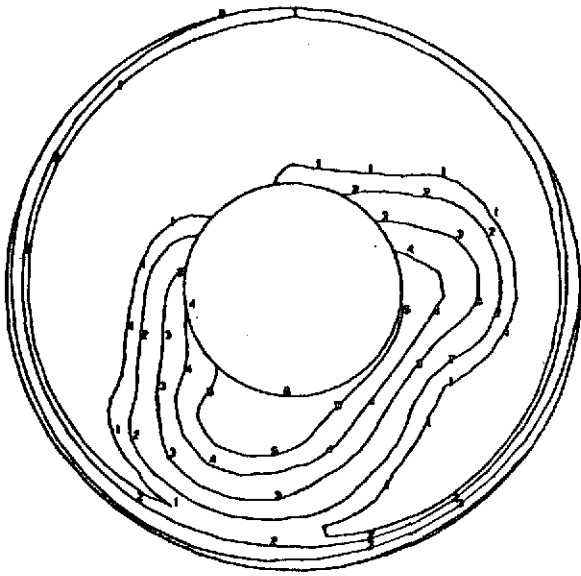
($M_{TH} = 0.626$, distortion = 12.5%, recovery = 0.9722)



(d) $C_D^* = 0.944$

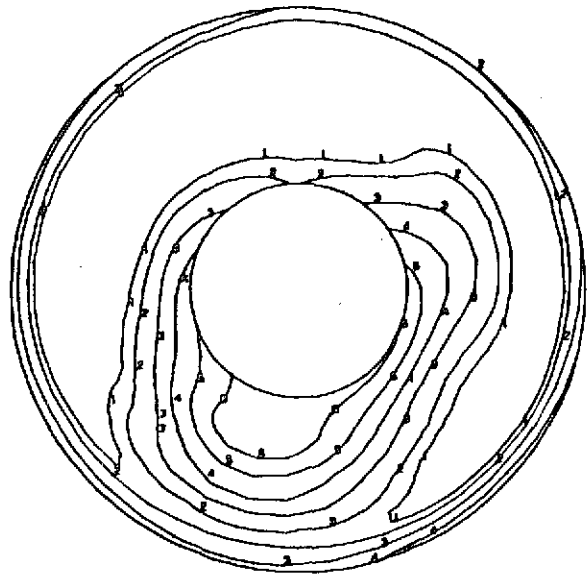
($M_{TH} = 0.757$, distortion = 6.6%, recovery = 0.9875)

Figure 60.—Compressor Face Total Pressure Recovery Maps for Translating Centerbody Inlet A2 at Approach— $\alpha = 35^\circ$, $V = 148$ km/h (80 kn)



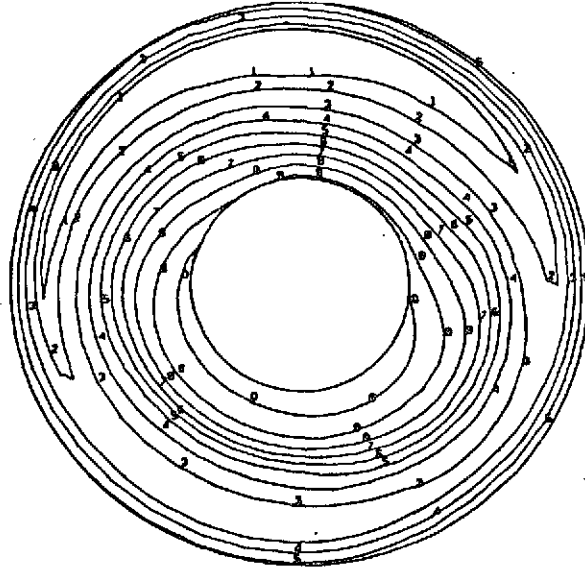
(e) $C_D^* = 0.973$

($M_{TH} = 0.830$, distortion = 9.5%, recovery = 0.9804)



(f) $C_D^* = 0.980$

($M_{TH} = 0.853$, distortion = 11.1%, recovery = 0.9753)



(g) $C_D^* = 0.985$

($M_{TH} = 0.874$, distortion = 19.6%, recovery = 0.9299)

Figure 60.—Concluded

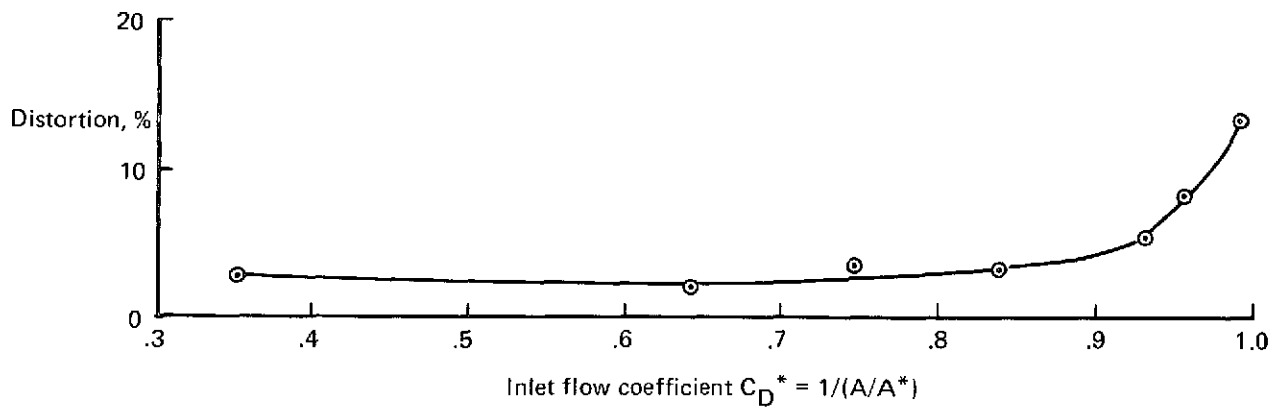
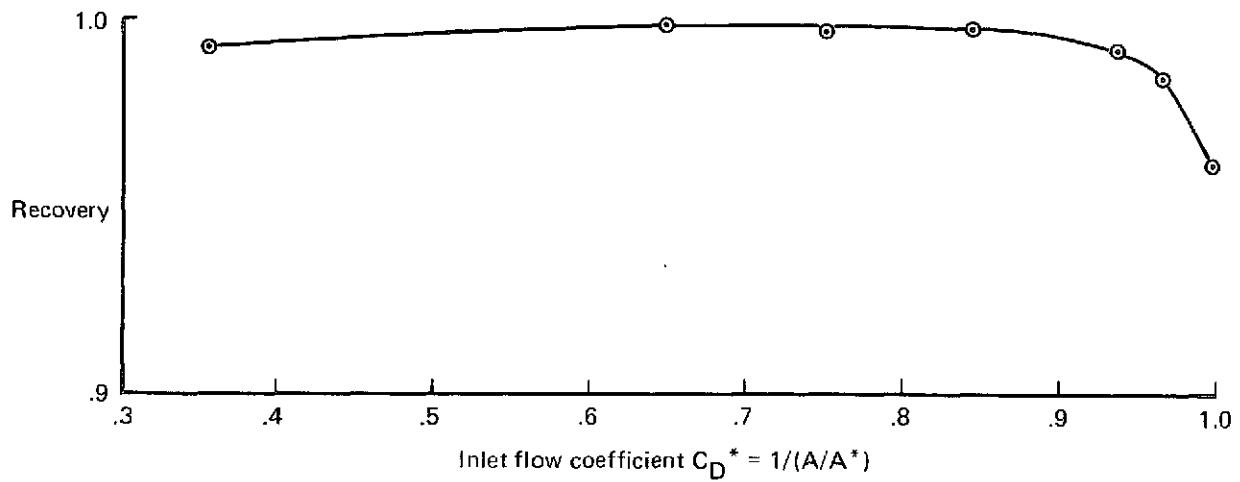


Figure 61.—Translating Centerbody Inlet A2 Distortion and Recovery Performance at Approach— $\alpha = 20^\circ$, $V = 259$ km/h (140 kn)

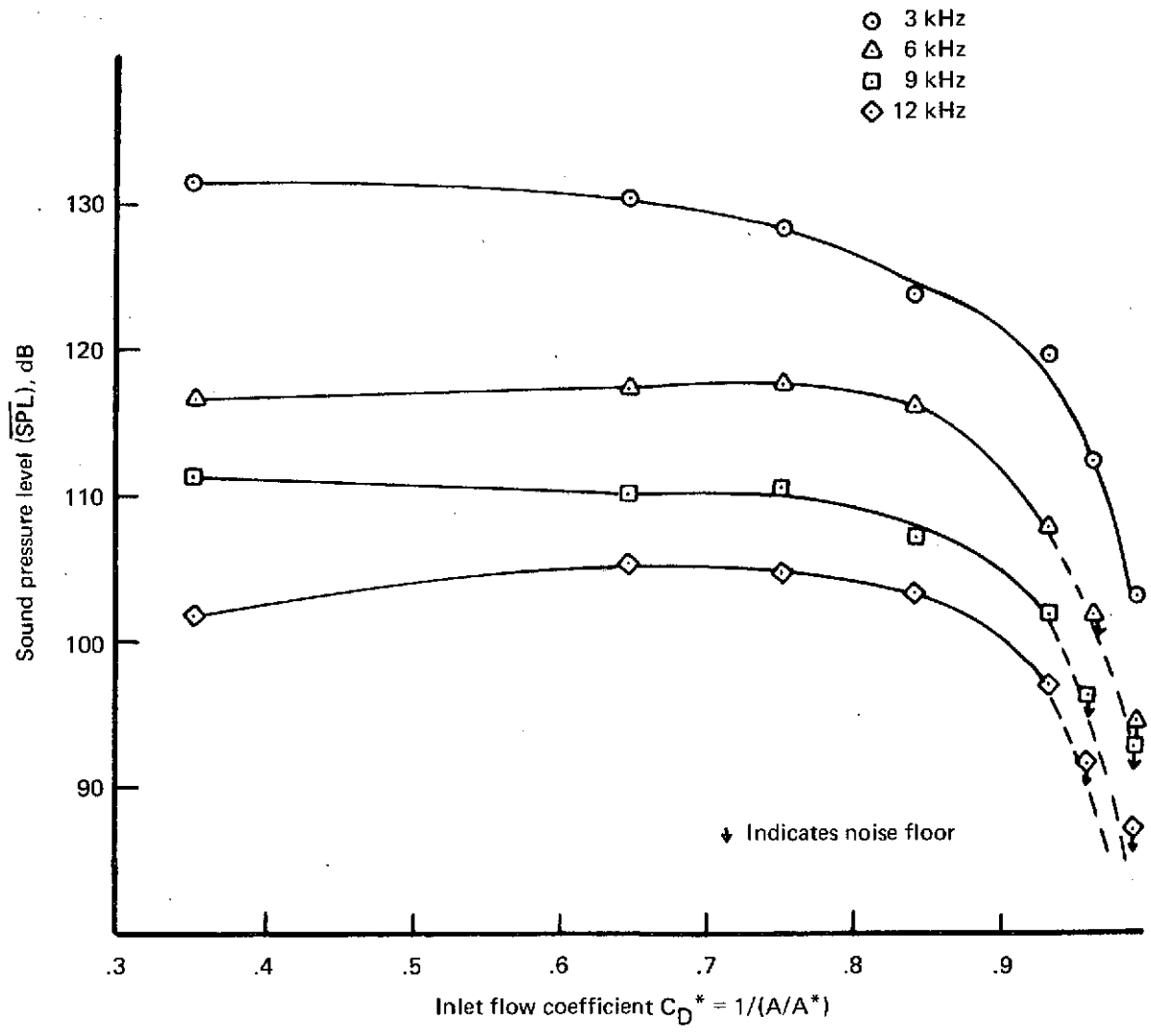
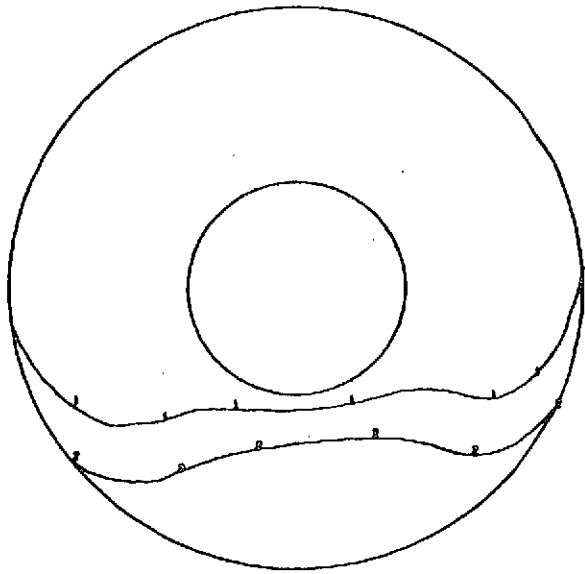
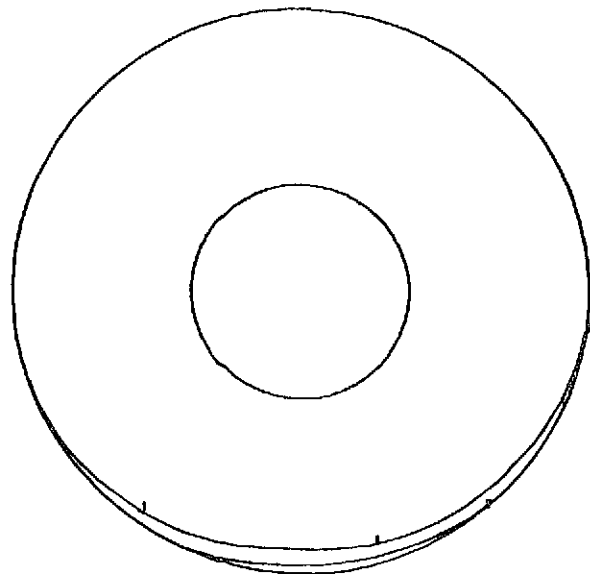


Figure 62.—Translating Centerbody Inlet A2 Acoustic Performance at Approach— $\alpha = 20^\circ$, $V = 259 \text{ km/h (140 kn)}$



(a) $C_D^* = 0.354$

($M_{TH} = 0.211$, distortion = 2.9%, recovery = 0.9927)

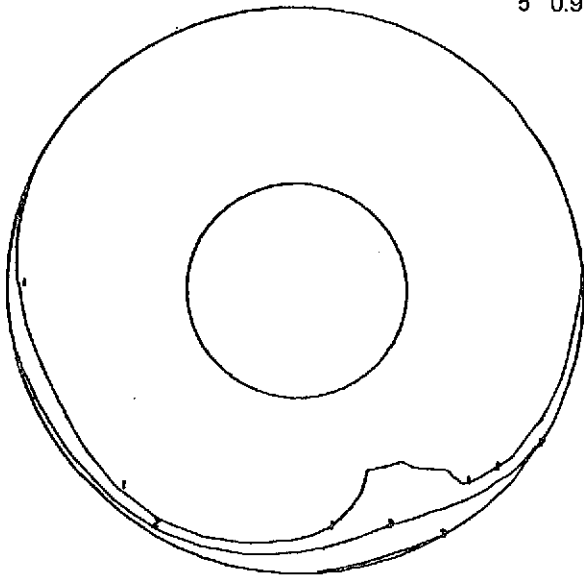


(b) $C_D^* = 0.647$

($M_{TH} = 0.414$, distortion = 2.0%, recovery = 0.9986)

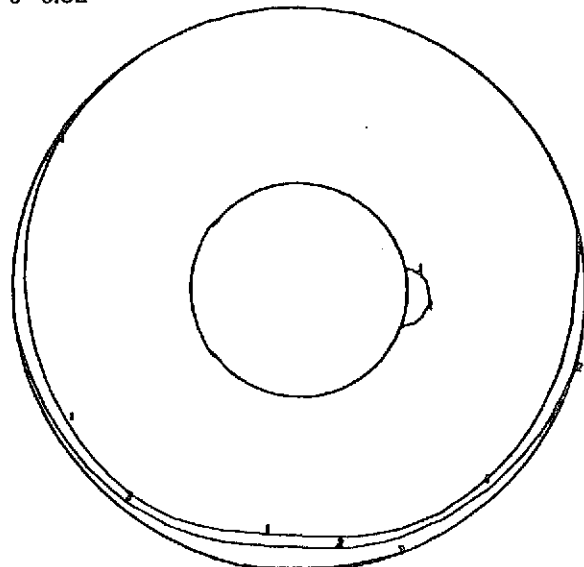
$P_T/P_{T REF}$

1	0.99	6	0.90
2	0.98	7	0.88
3	0.96	8	0.86
4	0.94	9	0.84
5	0.92	0	0.82



(c) $C_D^* = 0.751$

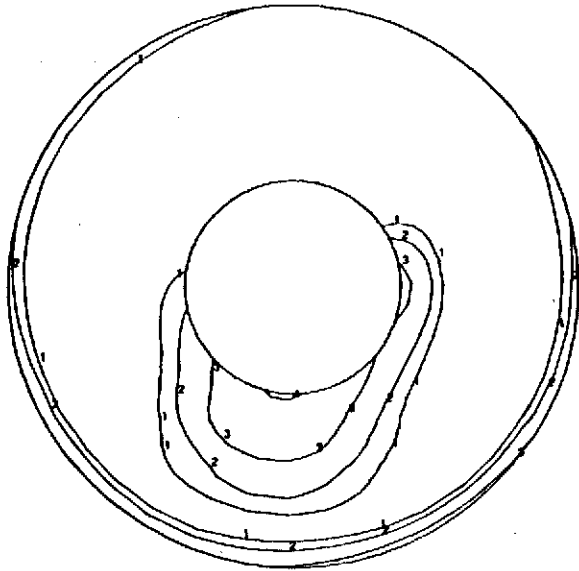
($M_{TH} = 0.504$, distortion = 3.6%, recovery = 0.9968)



(d) $C_D^* = 0.841$

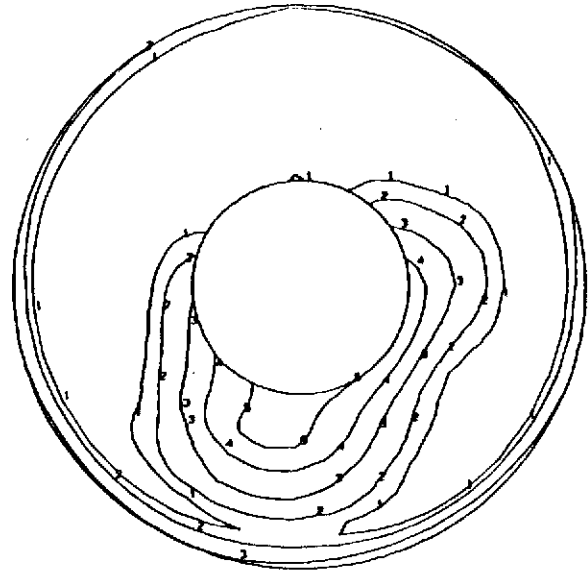
($M_{TH} = 0.599$, distortion = 3.5%, recovery = 0.9973)

Figure 63.—Compressor Face Total Pressure Recovery Maps for Translating Centerbody Inlet A2 at Approach— $\alpha = 20^\circ$, $V = 259$ km/h (140 kn)



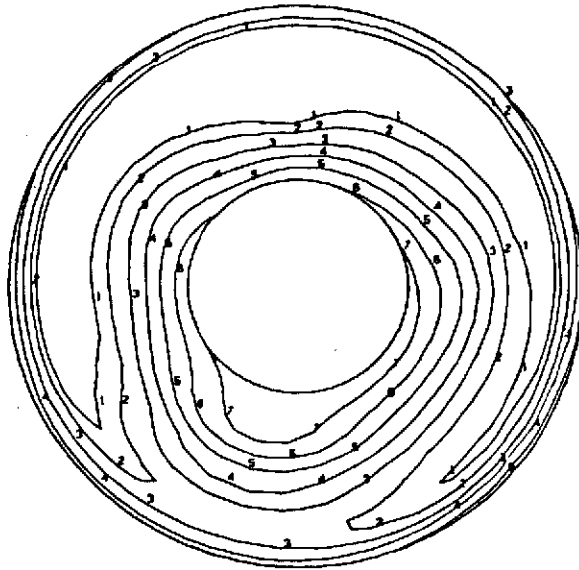
(e) $C_D^* = 0.934$

($M_{TH} = 0.734$, distortion = 5.6%, recovery = 0.9913)



(f) $C_D^* = 0.964$

($M_{TH} = 0.801$, distortion = 8.4%, recovery = 0.9843)



(g) $C_D^* = 0.996$

($M_{TH} = 0.928$, distortion = 13.4%, recovery = 0.9610)

Figure 63.—Concluded

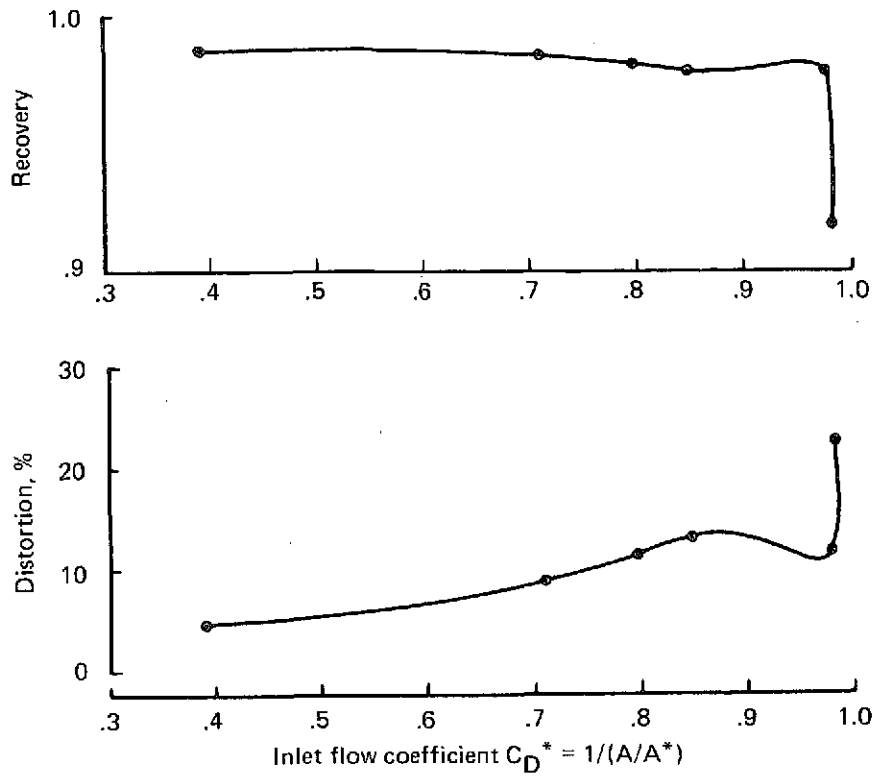


Figure 64.—Translating Centerbody Inlet A3 Distortion and Recovery Performance at Approach— $\alpha = 35^\circ$, $V = 148$ km/h (80 kn)

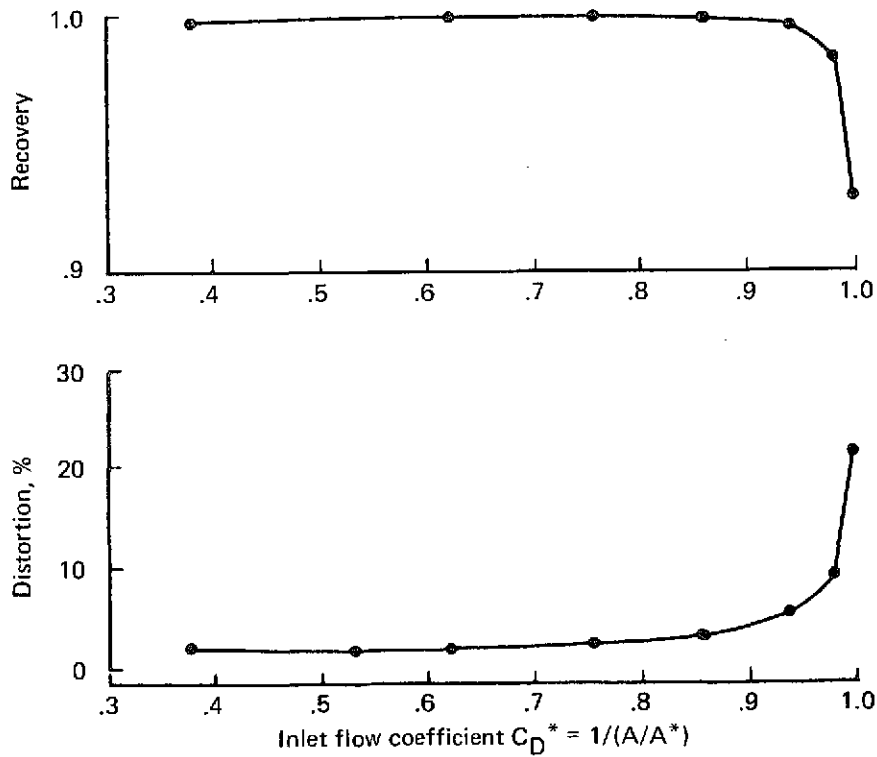


Figure 65.—Translating Centerbody Inlet A3 Distortion and Recovery Performance at Approach— $\alpha = 20^\circ$, $V = 259$ km/h (140 kn)

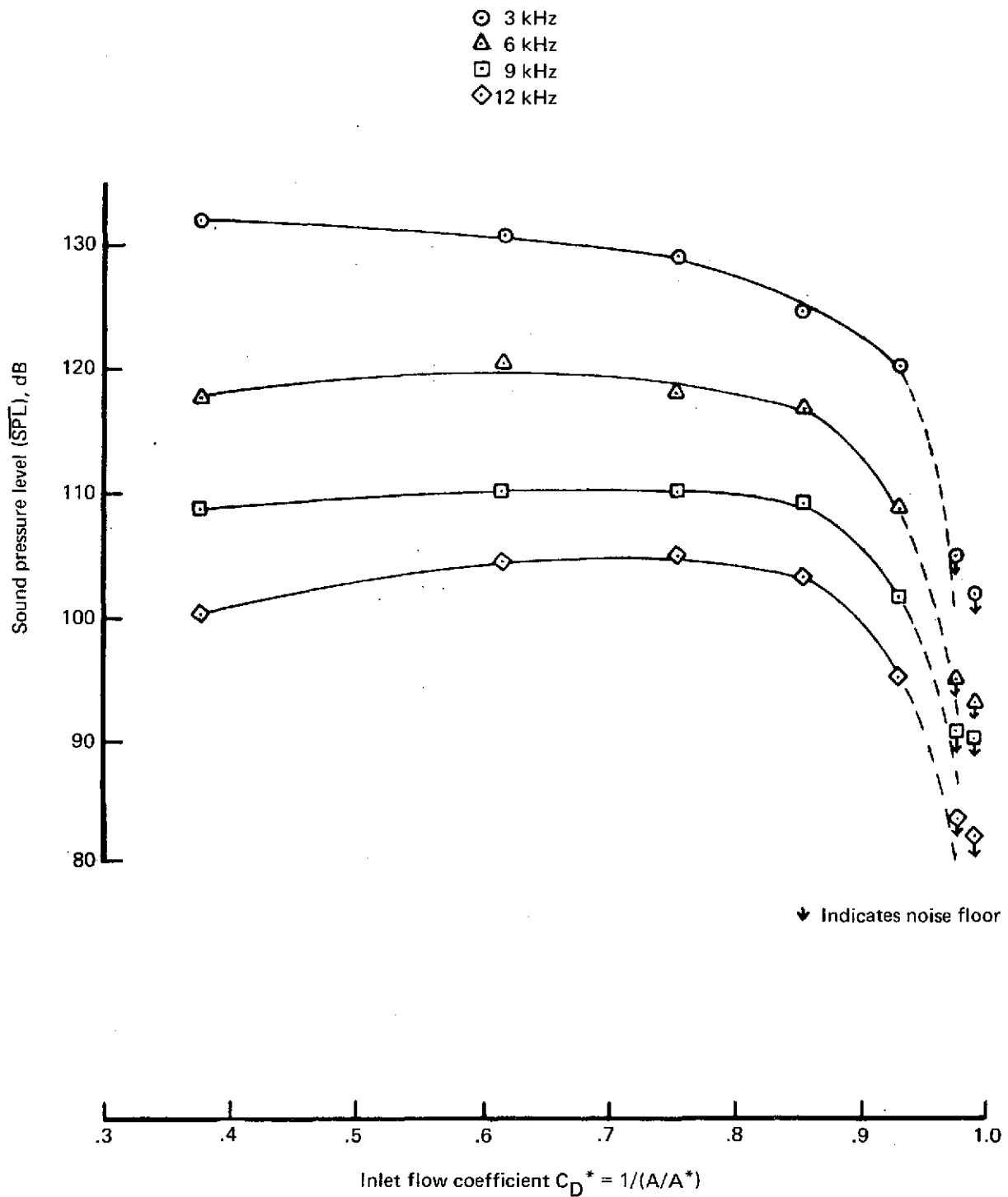


Figure 66.—Translating Centerbody Inlet A3 Acoustic Performance at Approach— $\alpha = 20^\circ$, $V = 259 \text{ km/h (140 kn)}$

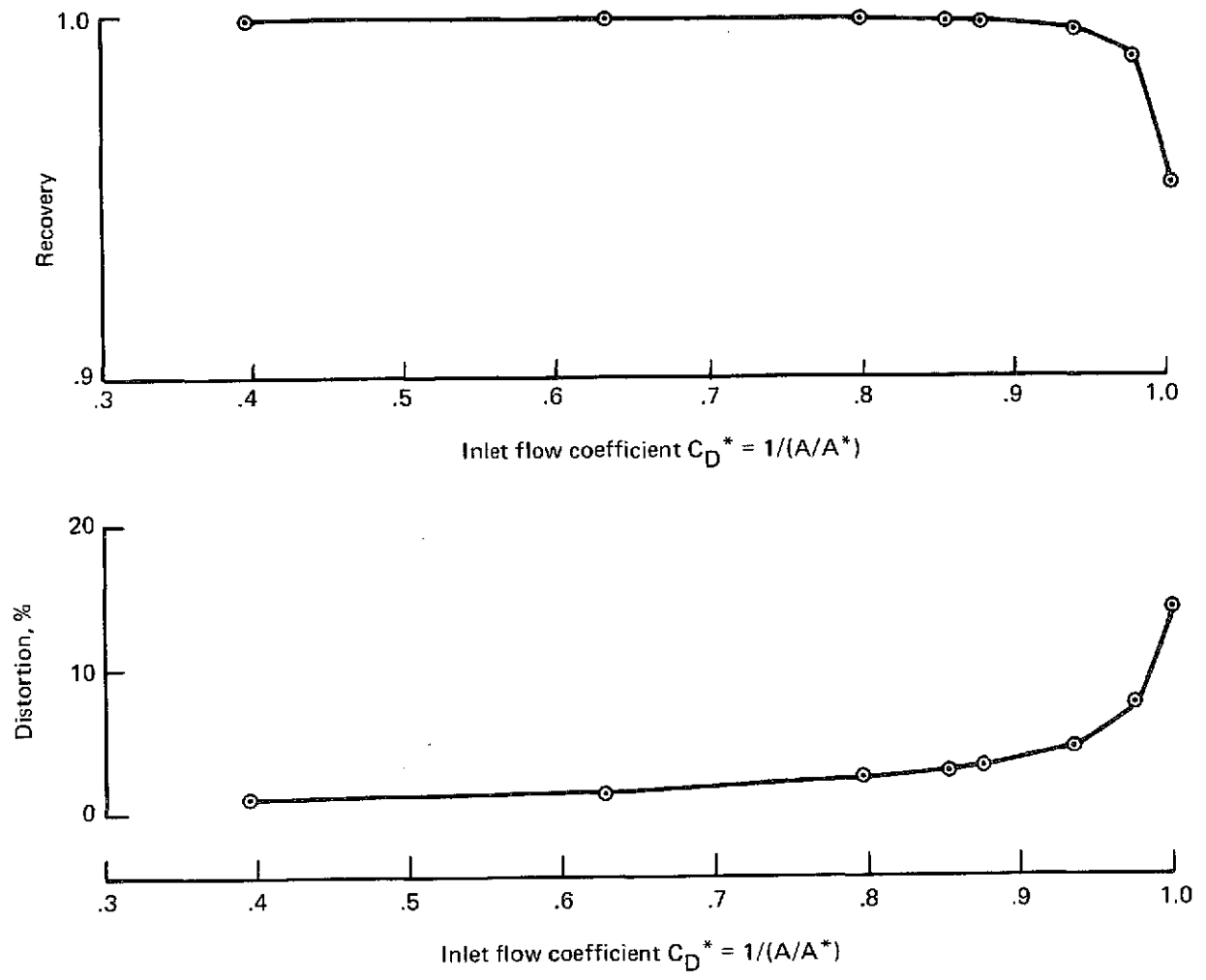


Figure 67.—Translating Centerbody Inlet A2 Distortion and Recovery Performance at Approach— $\alpha = 20^\circ$, $V = 185$ km/h (100 kn)

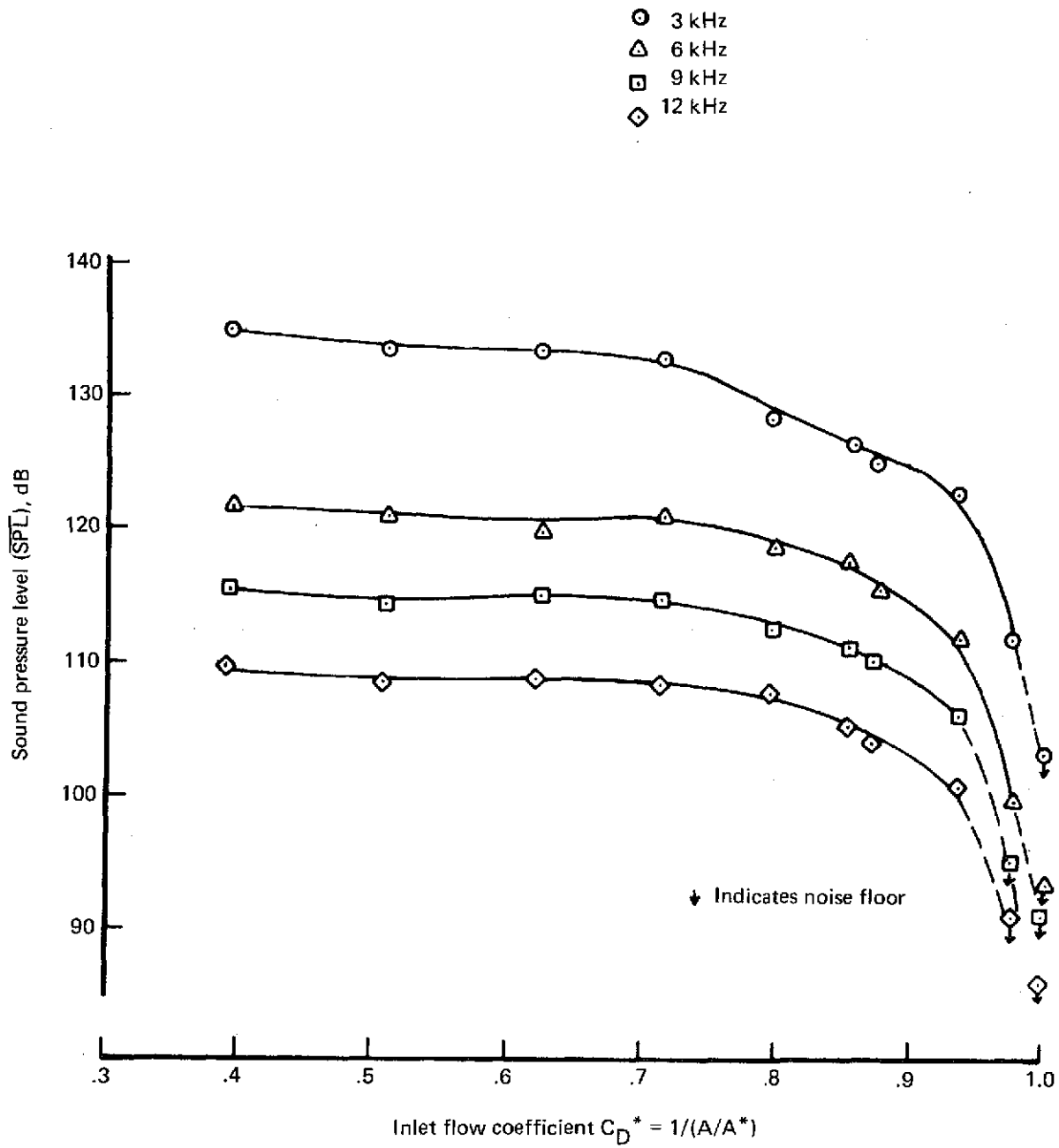


Figure 68.—Translating Centerbody Inlet A2 Acoustic Performance at Approach— $\alpha = 20^\circ$, $V = 185 \text{ km/h}$ (100 kn)

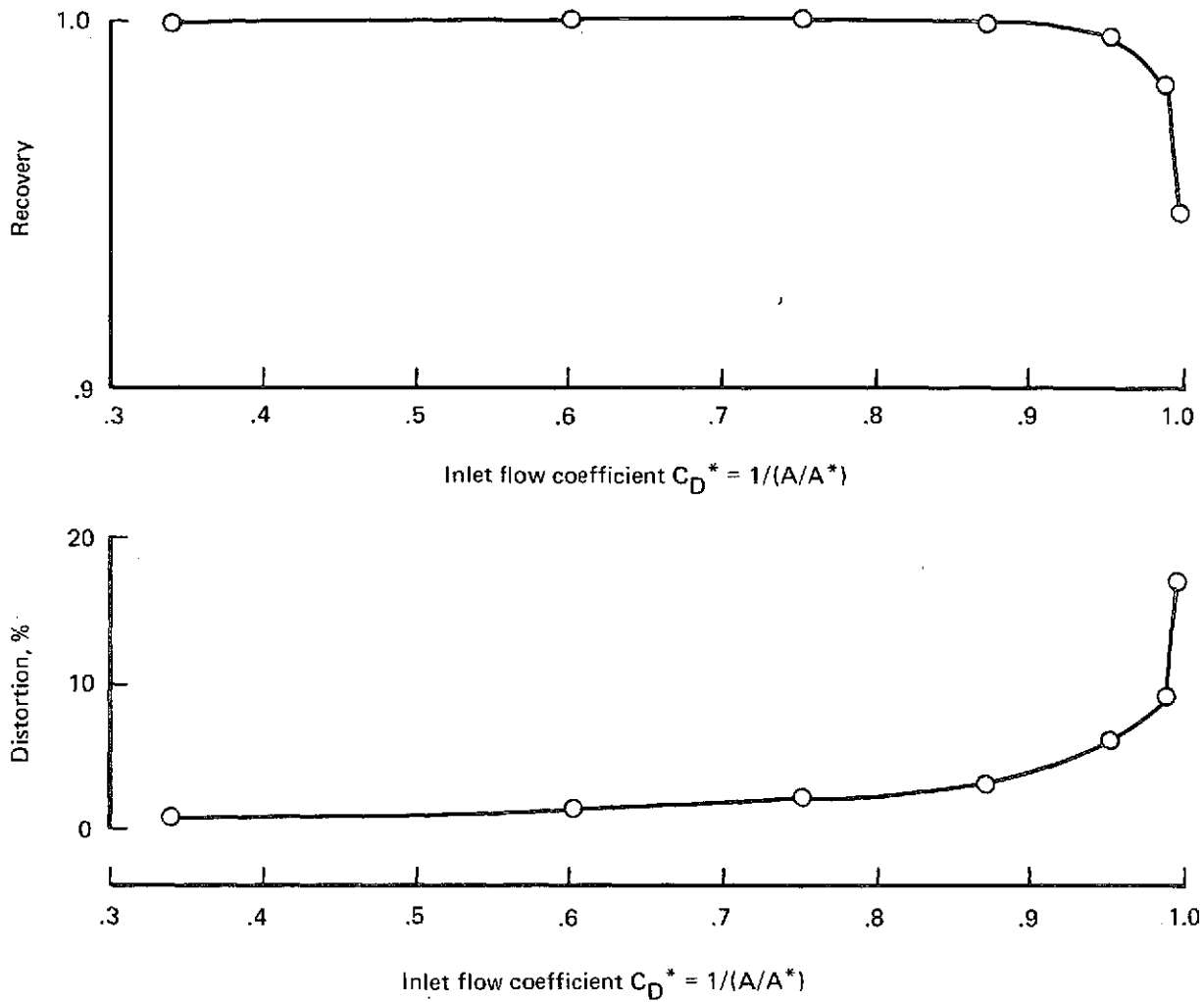


Figure 69.—Translating Centerbody Inlet A3 Distortion and Recovery Performance at Approach— $\alpha = 20^\circ$, $V = 185 \text{ km/h}$ (100 kn)

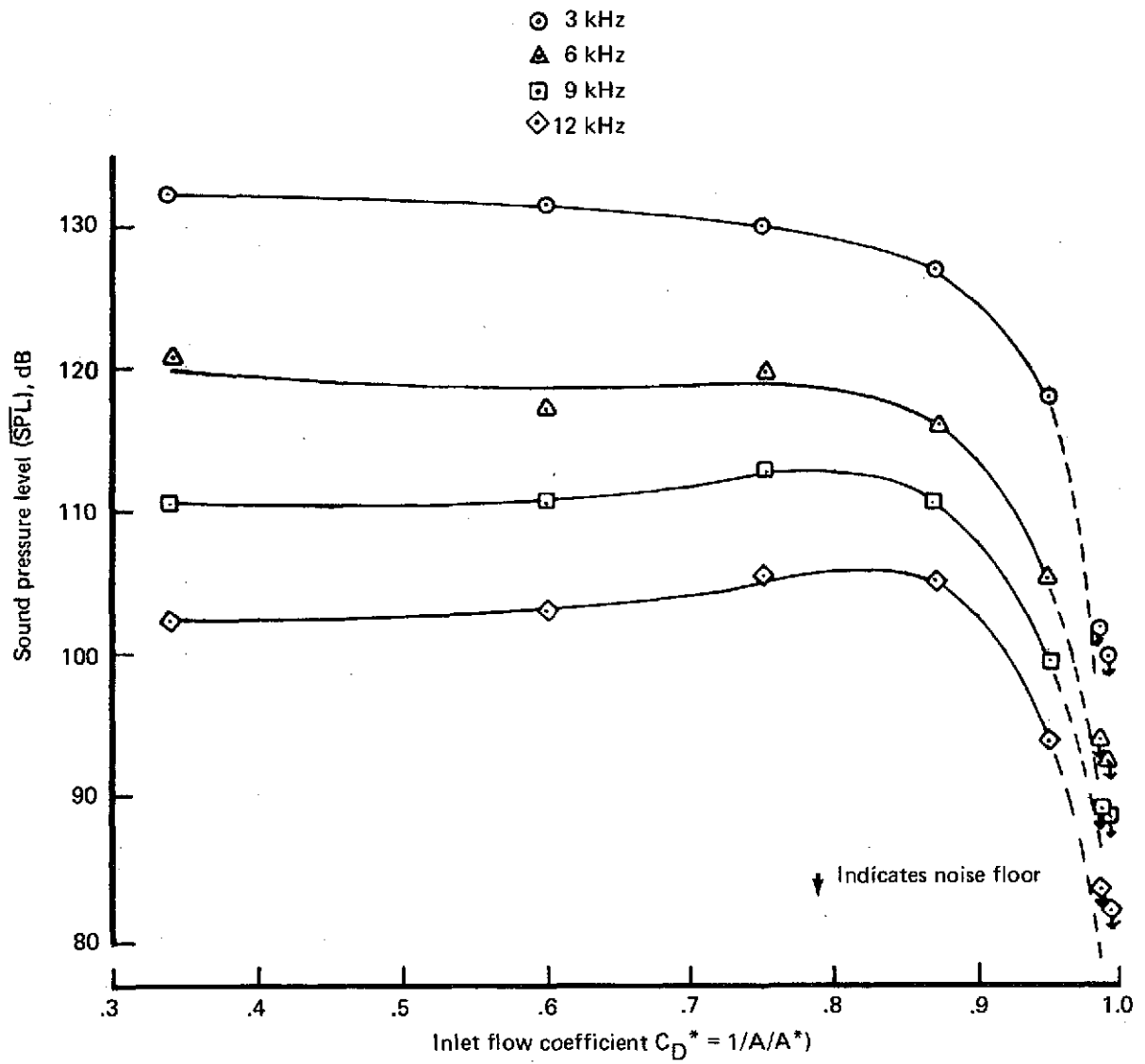


Figure 70.—Translating Centerbody Inlet A3 Acoustic Performance at Approach—
 $\alpha = 20^\circ$, $V = 185 \text{ km/h (100 kn)}$

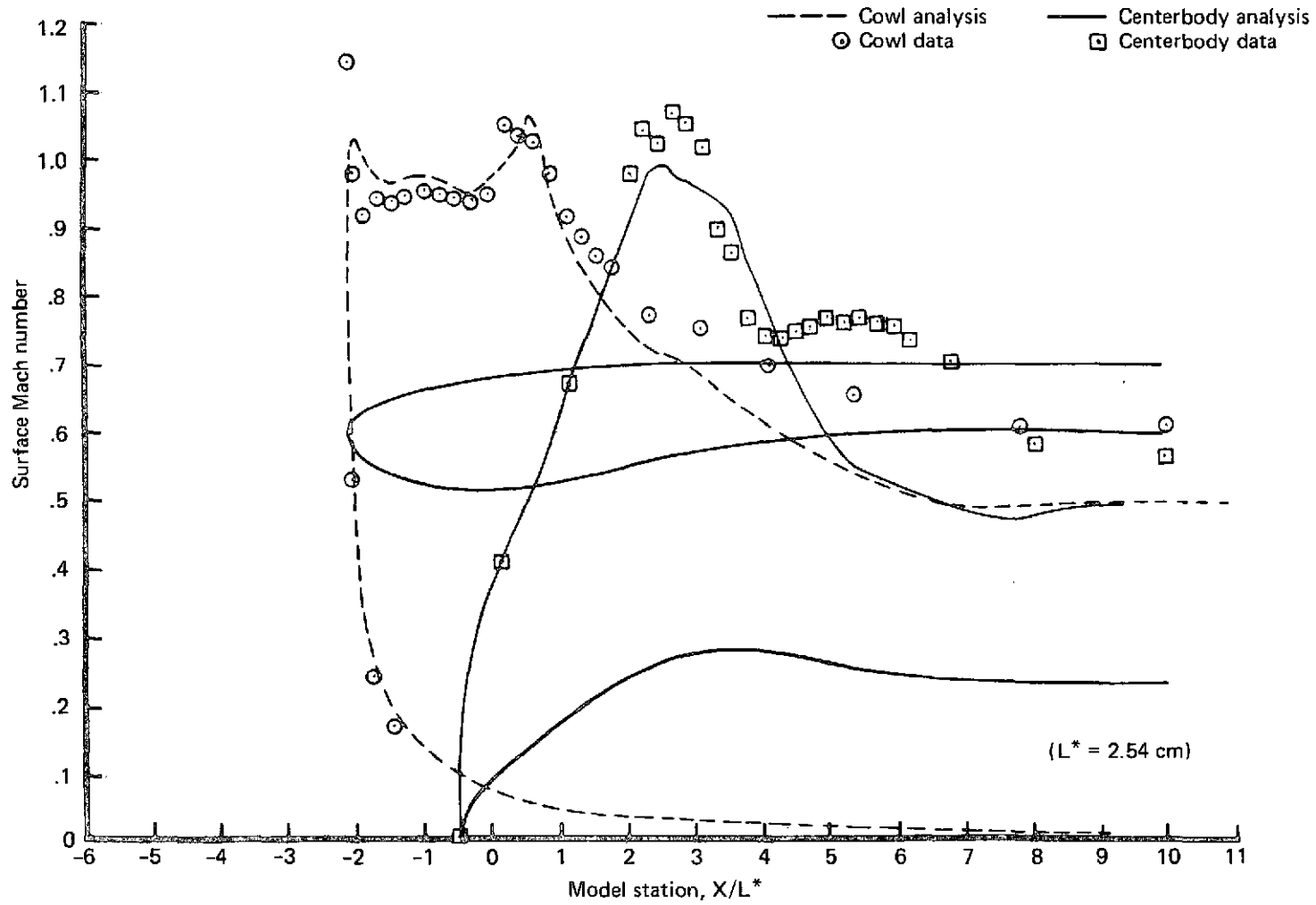


Figure 71.—Comparison of Analysis With Data for Translating Centerbody Inlet A1 at Takeoff—
 $V = 0$, $C_D^* = 0.963$

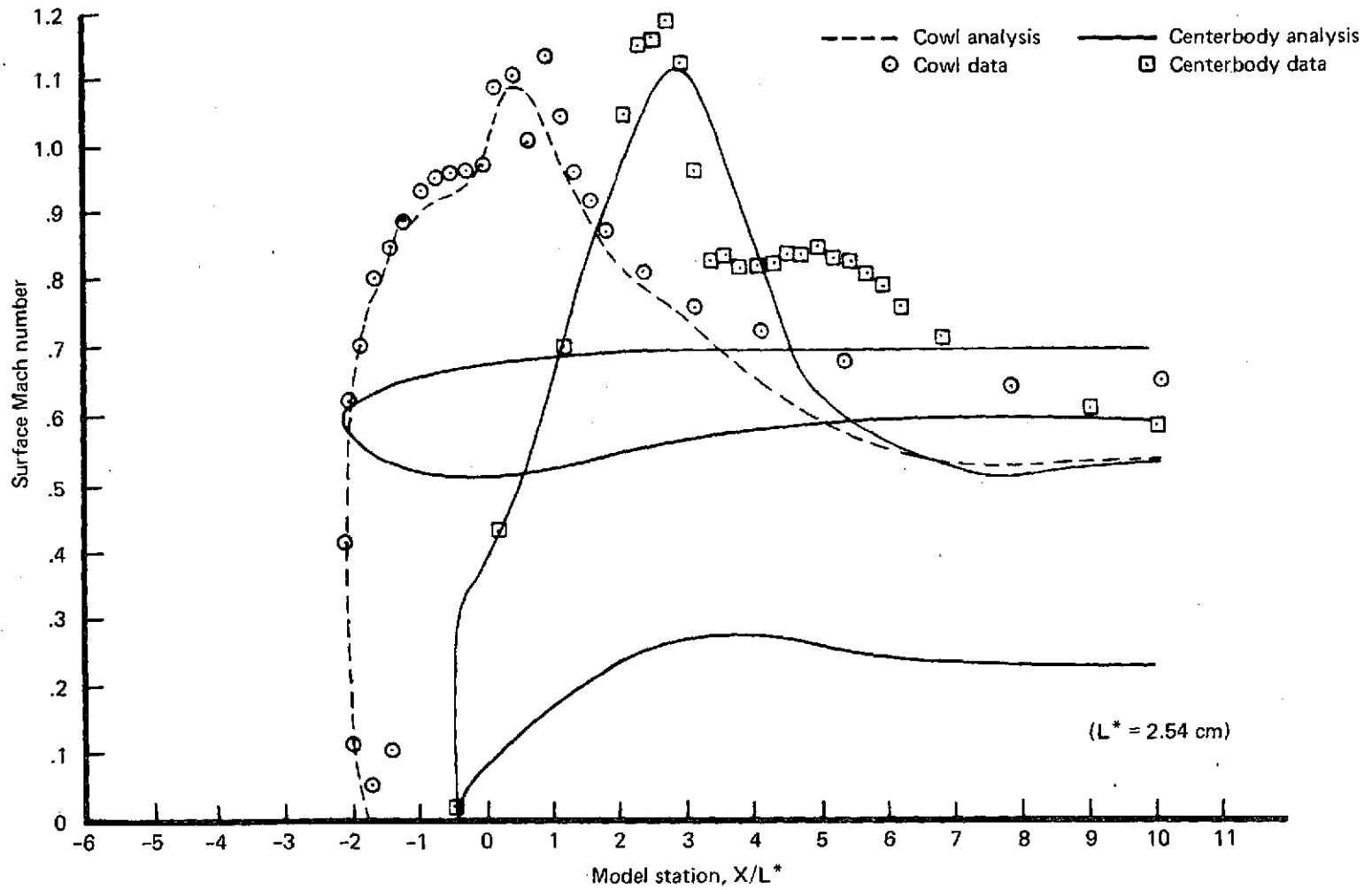


Figure 72.—Comparison of Analysis With Data for Translating Centerbody Inlet A1 at Takeoff—
 $V = 259 \text{ km/h (140 kn)}$, $C_D^* = 0.980$

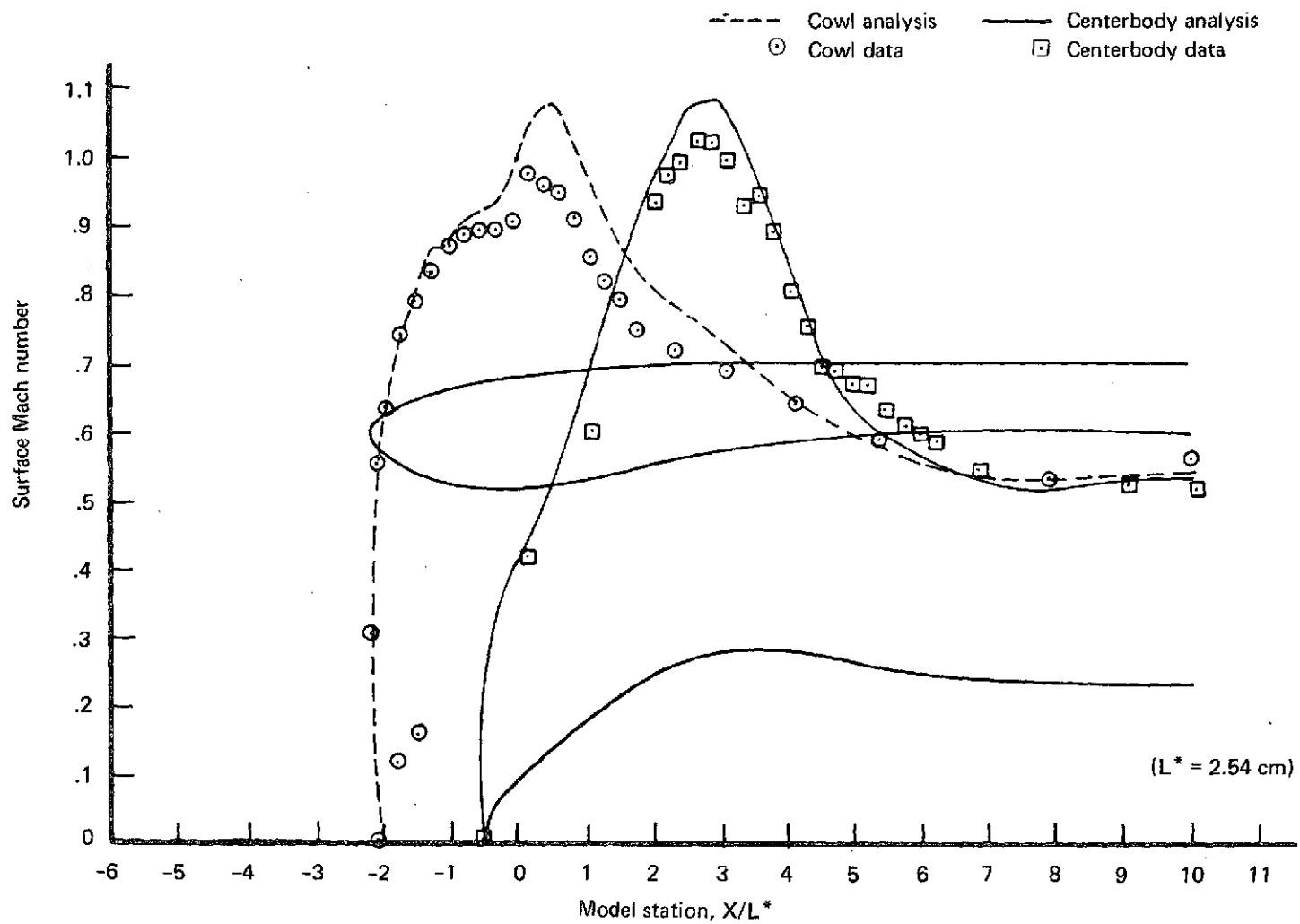


Figure 73.—Comparison of Analysis With Data for Translating Centerbody Inlet A1 at Takeoff—
 $V = 324 \text{ km/h}$ (175 kn) for Analysis, $V = 306 \text{ km/h}$ (165 kn) for Data; $C_D^* = 0.980$

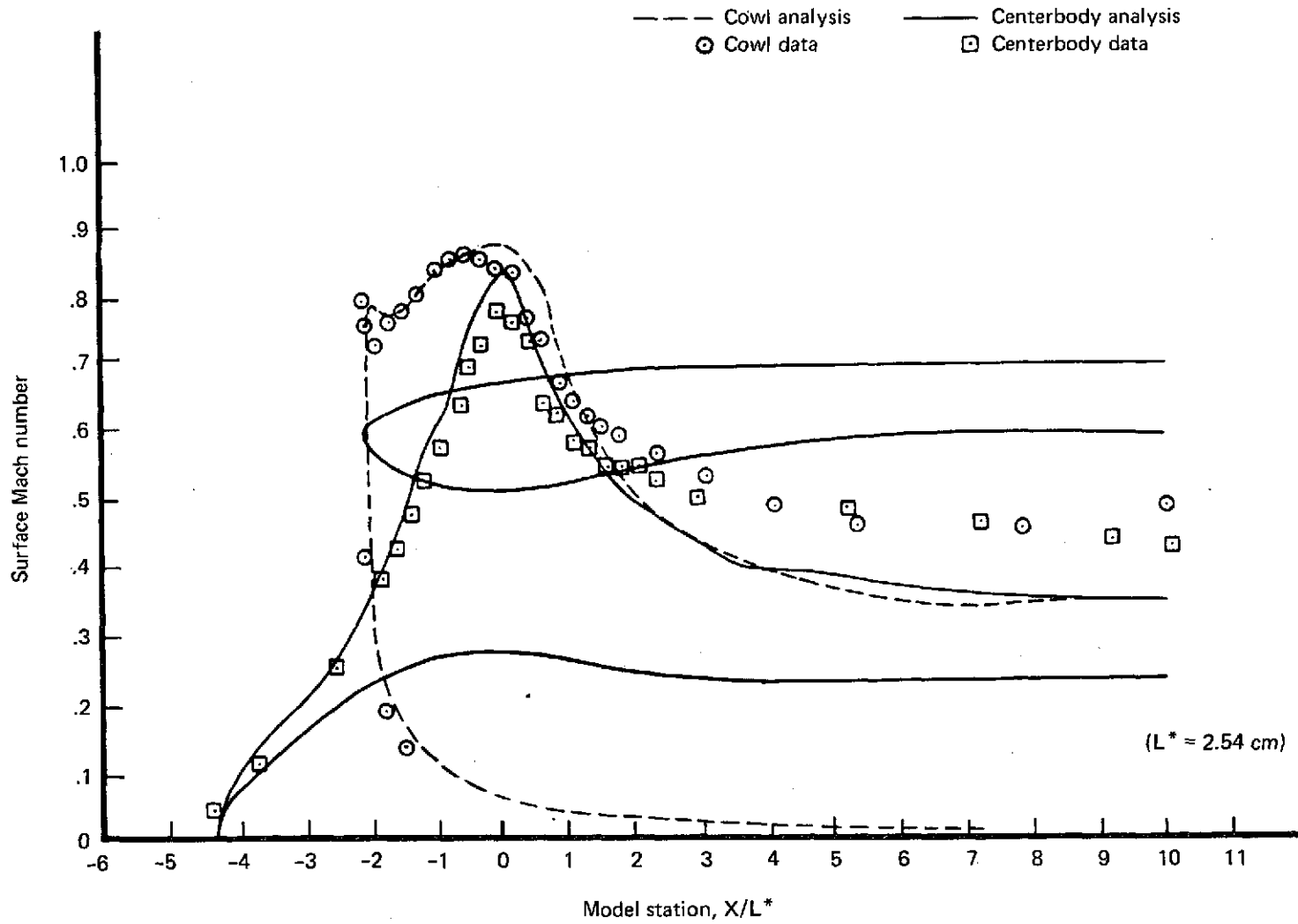


Figure 74.—Comparison of Analysis With Data for Translating Centerbody Inlet A1 at Approach—
 $V = 0, C_D^* = 0.914$

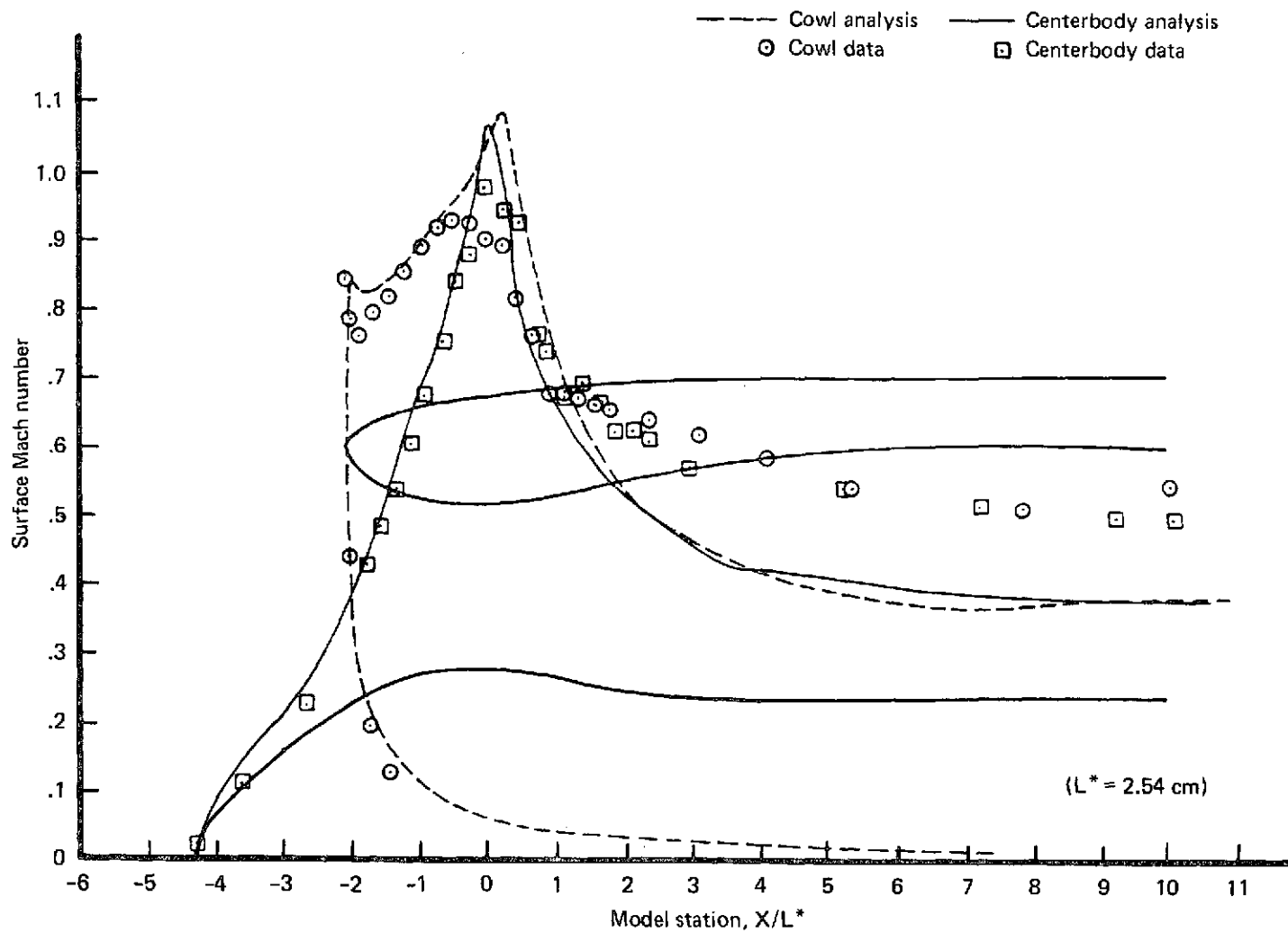


Figure 75.—Comparison of Analysis With Data for Translating Centerbody Inlet A1 at Approach—
 $V = 0$, $C_D^* = 0.963$

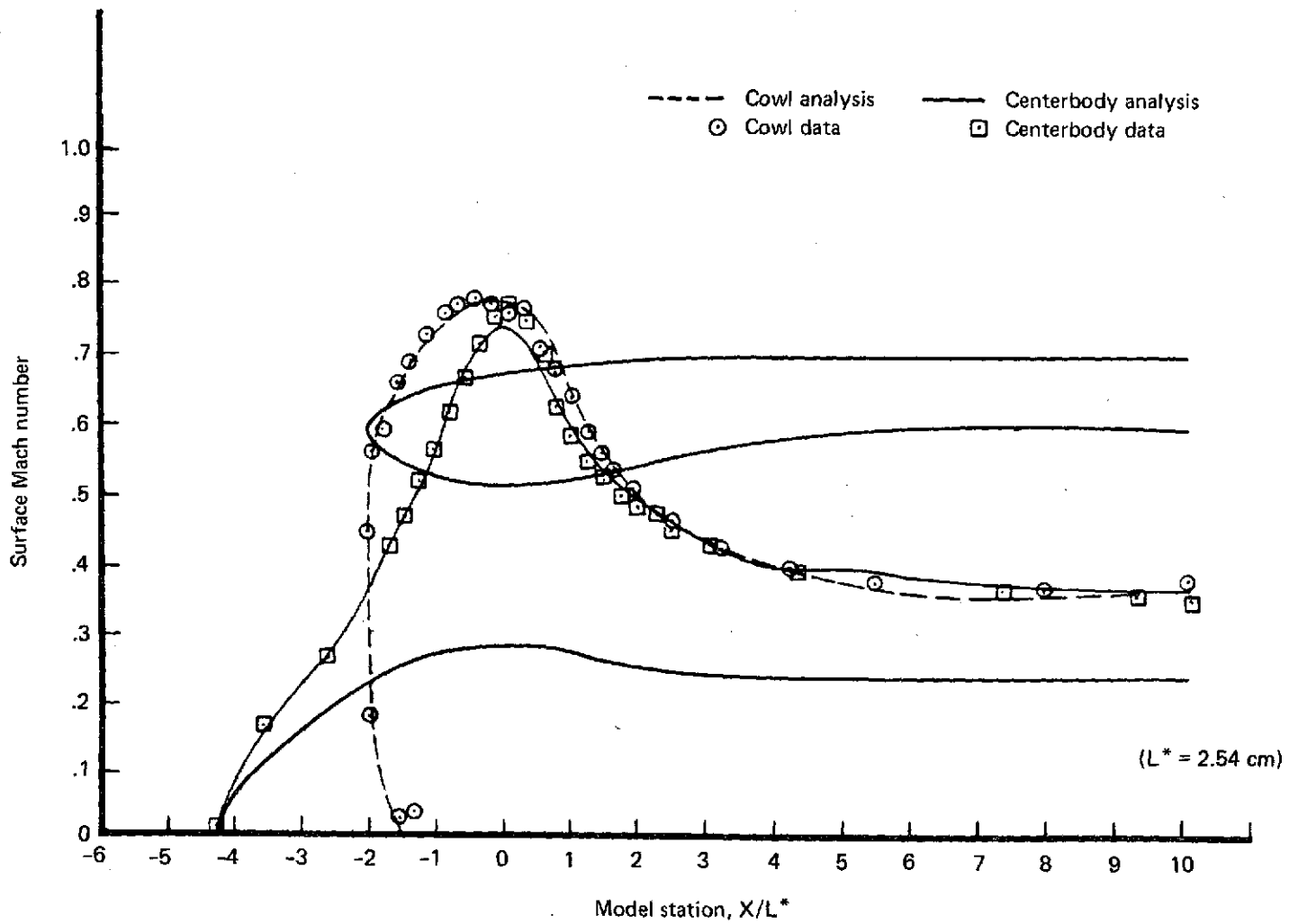


Figure 76.—Comparison of Analysis With Data for Translating Centerbody Inlet A1 at Approach—
 $V = 148 \text{ km/h (80 kn)}$, $C_D^* = 0.914$

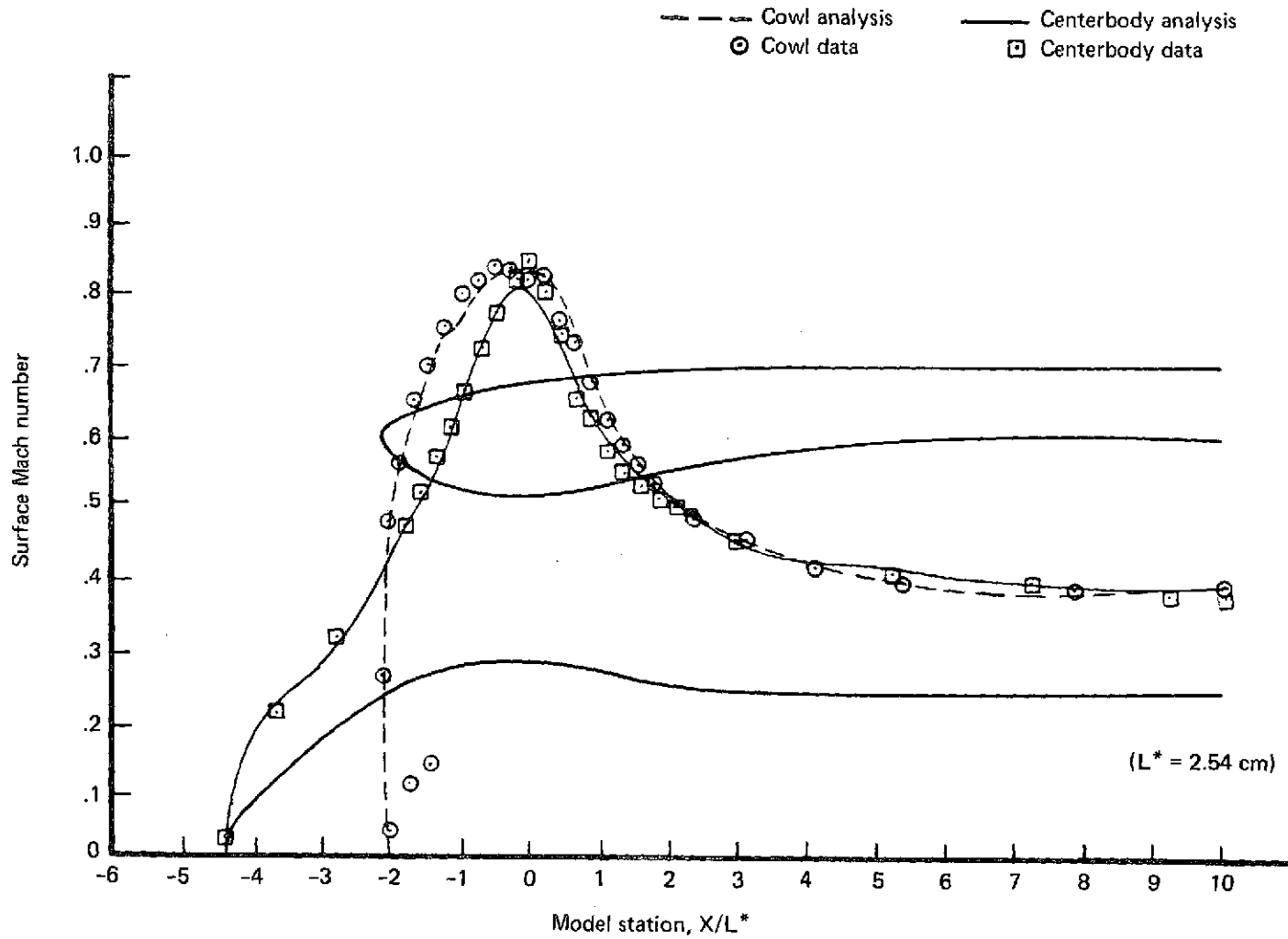
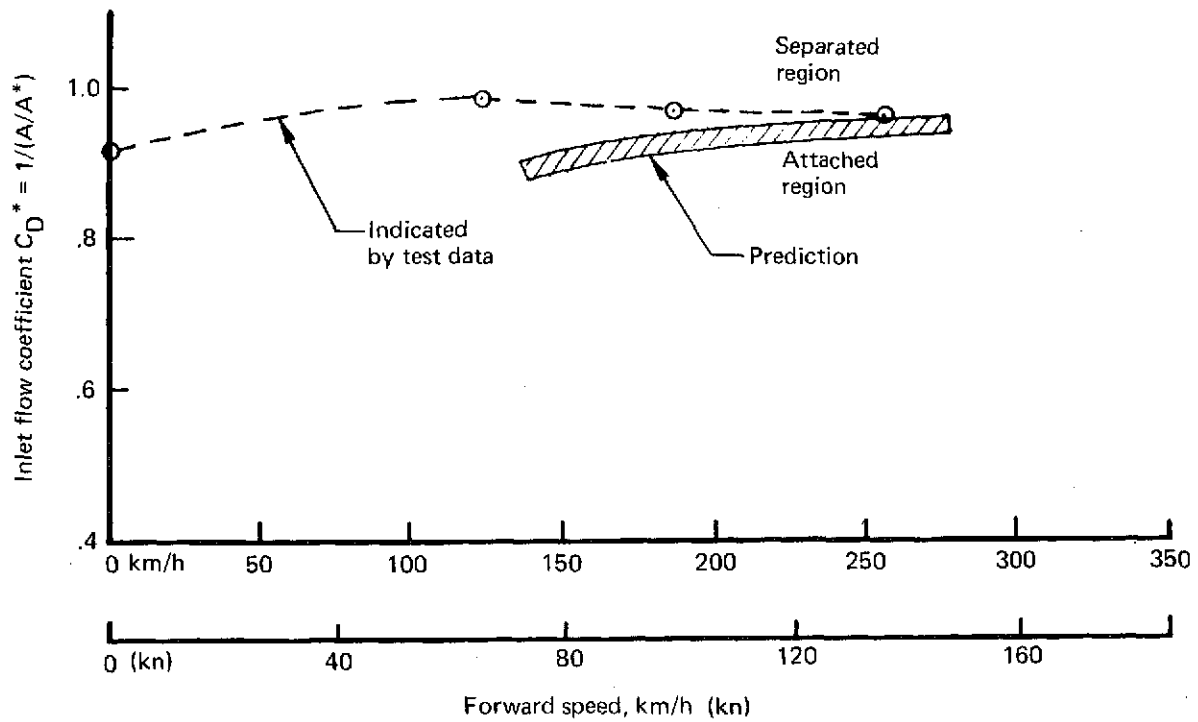
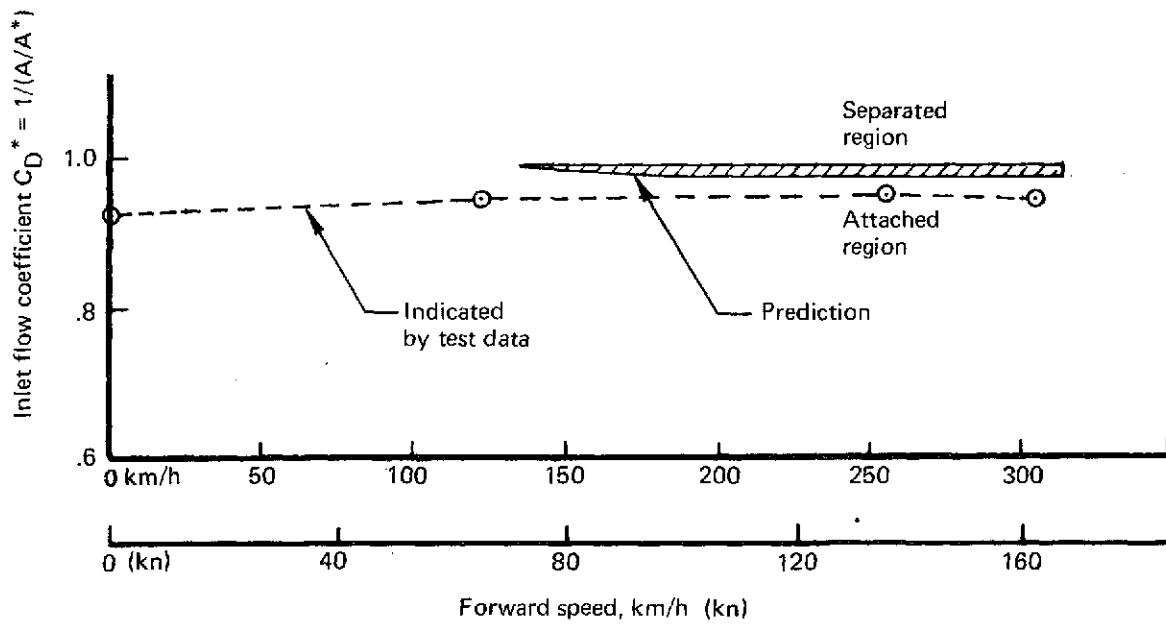


Figure 77.—Comparison of Analysis With Data for Translating Centerbody Inlet A1 at Approach—
 $V = 259$ km/h (140 kn), $C_D^* = 0.941$



(a) Approach-Cowl Separation



(b) Takeoff-Centerbody Separation

Figure 78.—Comparison of Analysis With Data for Translating Centerbody Inlet A1 Diffuser Separation— $\alpha = 0^\circ$

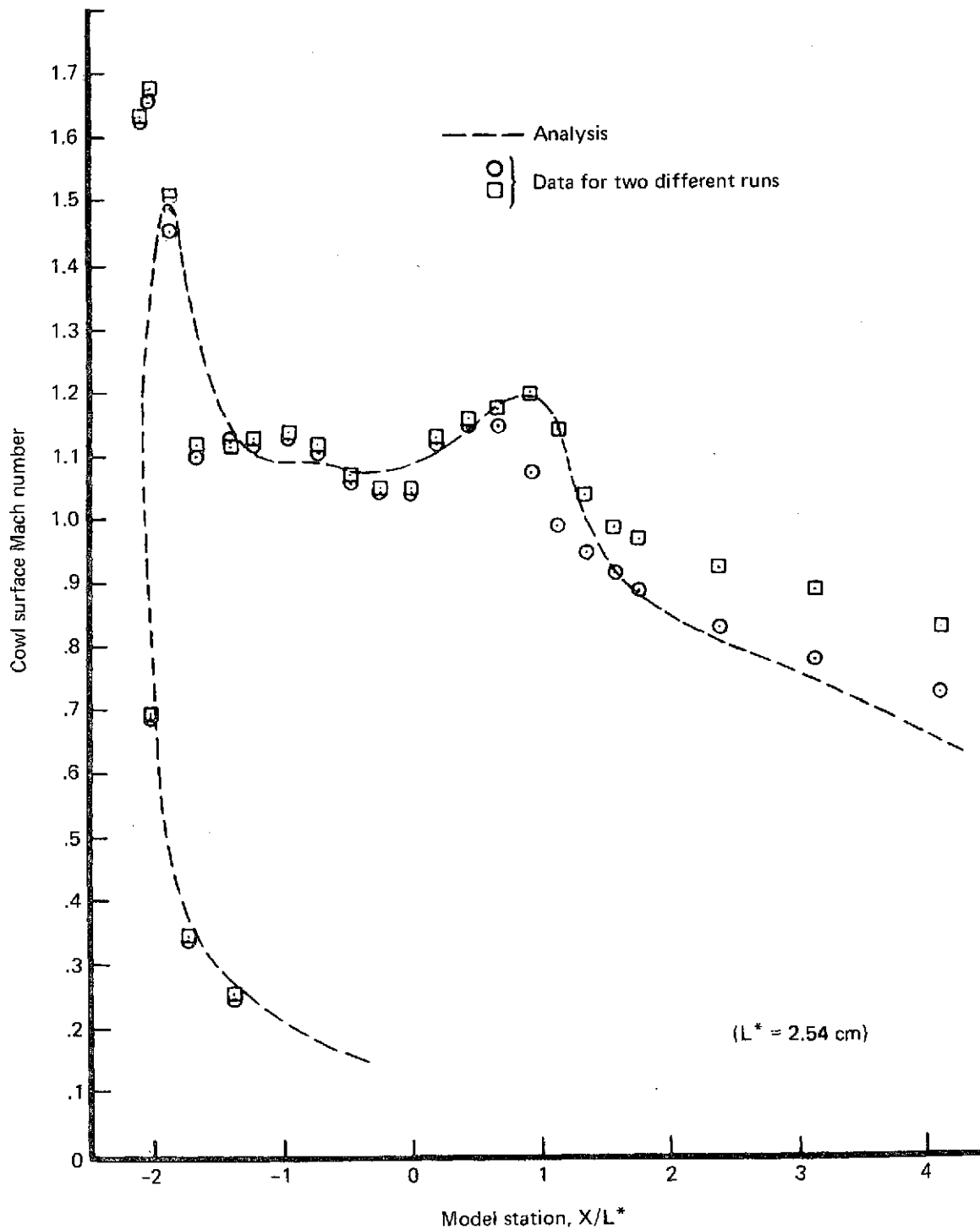


Figure 79.—Comparison of Analysis With Data for Translating Centerbody Inlet A1
 Cowl Surface Mach Number Distribution at Takeoff— $\alpha = 90^\circ$, $V = 65$ km/h (35 kn),
 $C_D^* = 0.963$

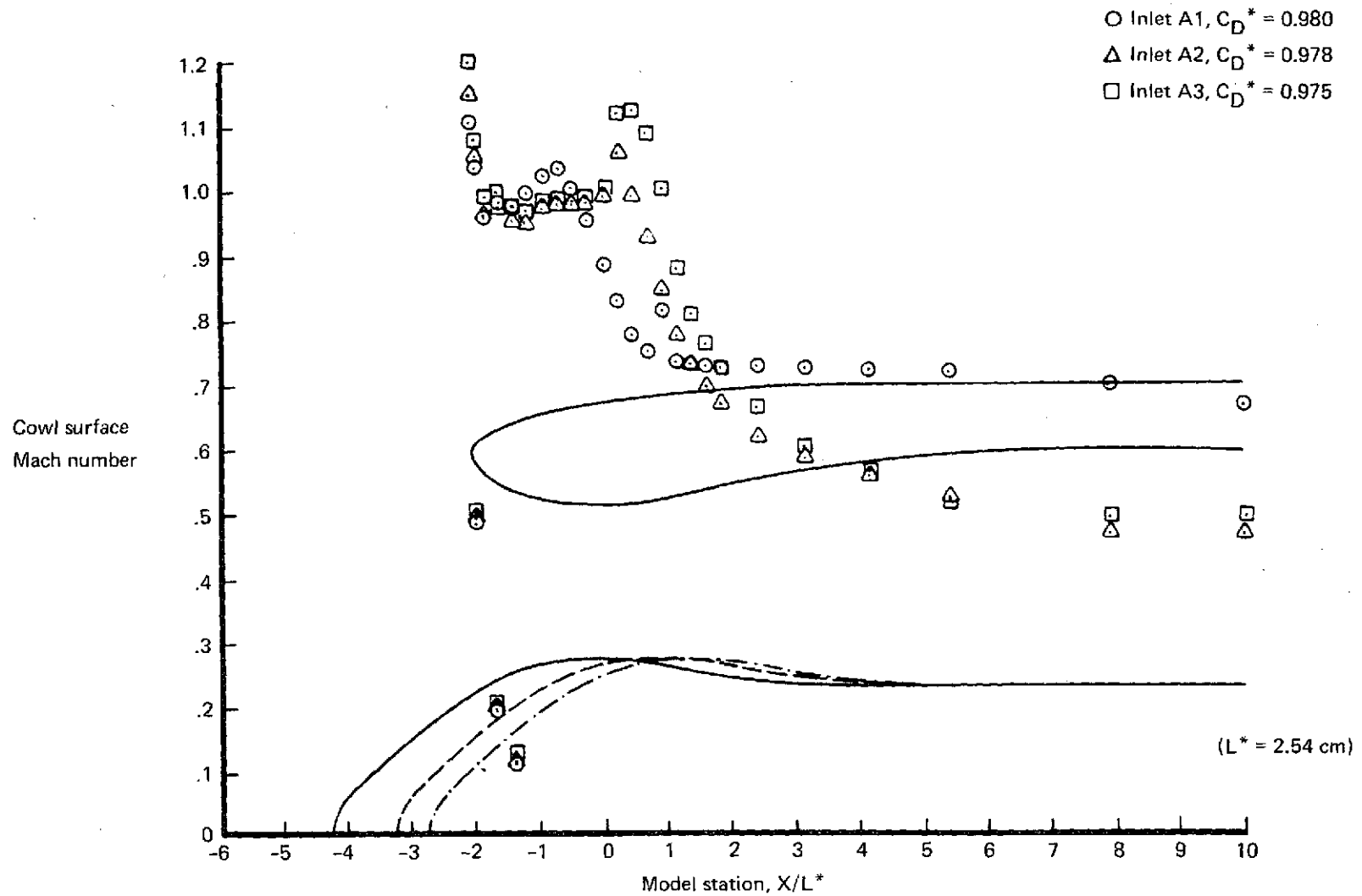


Figure 80.—Comparison of Cowl Surface Mach Number Distributions for Translating Centerbody Inlets A1, A2, and A3 at Approach, Windward Cowl— $\alpha = 35^\circ$, $V = 148 \text{ km/h (80 kn)}$

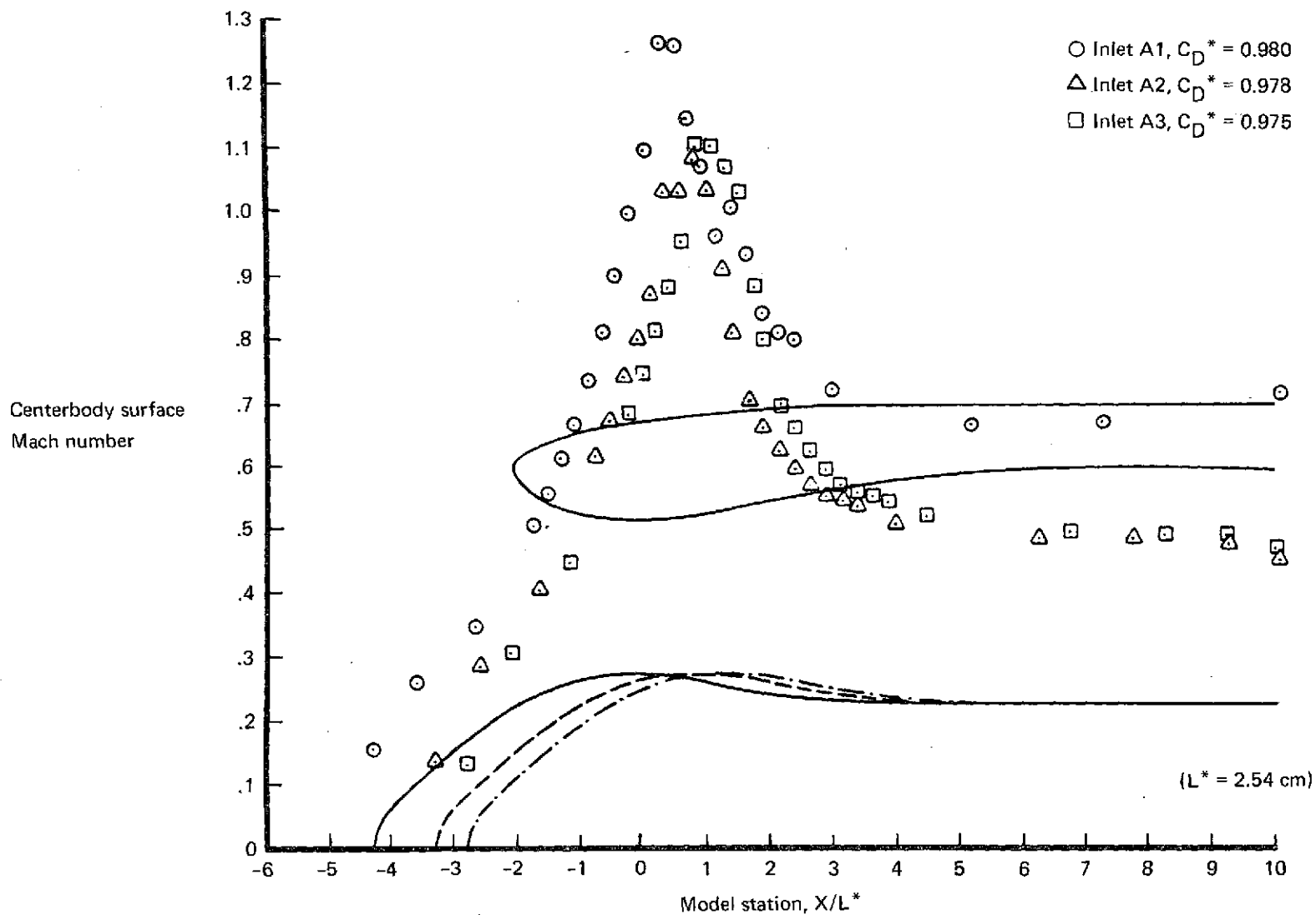


Figure 81.—Comparison of Centerbody Surface Mach Number Distributions for Translating Centerbody Inlets A1, A2, and A3 at Approach, Leeward Centerbody— $\alpha = 35^\circ$, $V = 148 \text{ km/h (80 kn)}$

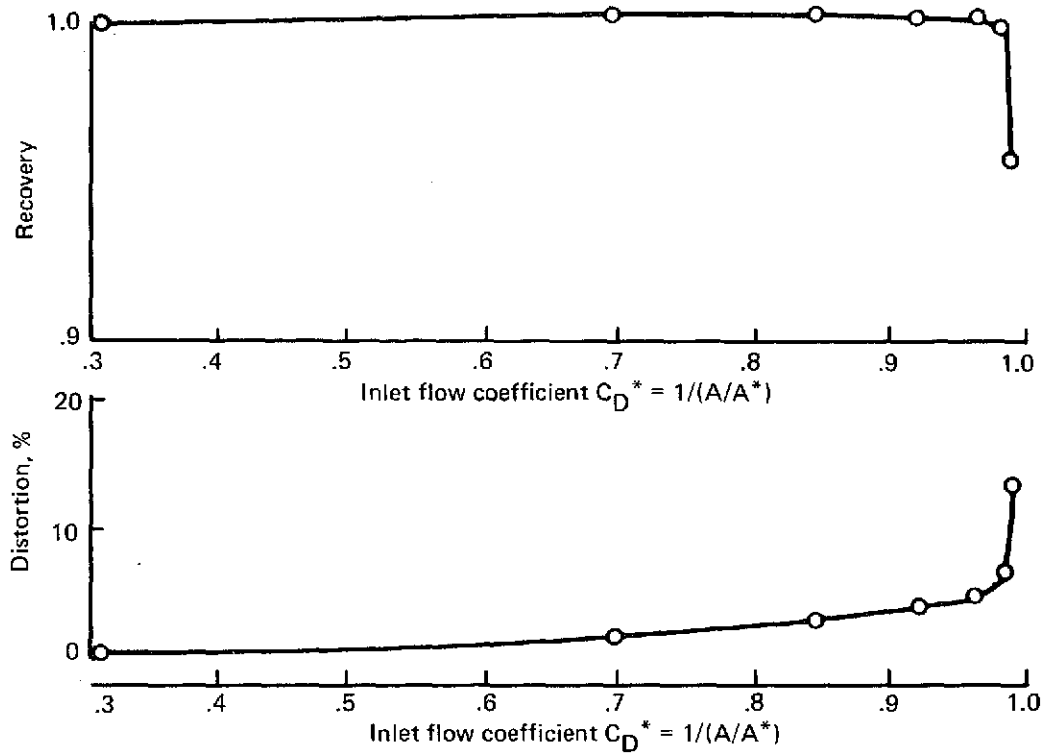


Figure 82.—Radial Vane Inlet B Distortion and Recovery Performance at Takeoff— $\alpha = 0^\circ$, $V = 315$ km/h (170 kn)

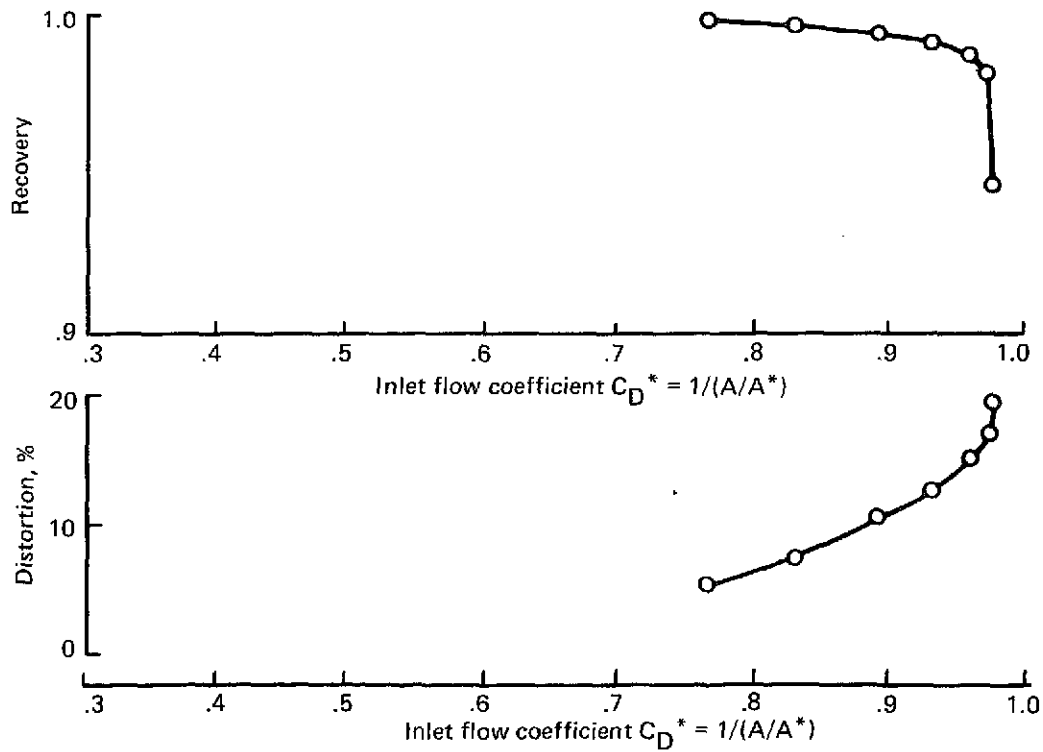


Figure 83.—Radial Vane Inlet B Distortion and Recovery Performance at Takeoff— $\alpha = 90^\circ$, $V = 65$ km/h (35 kn)

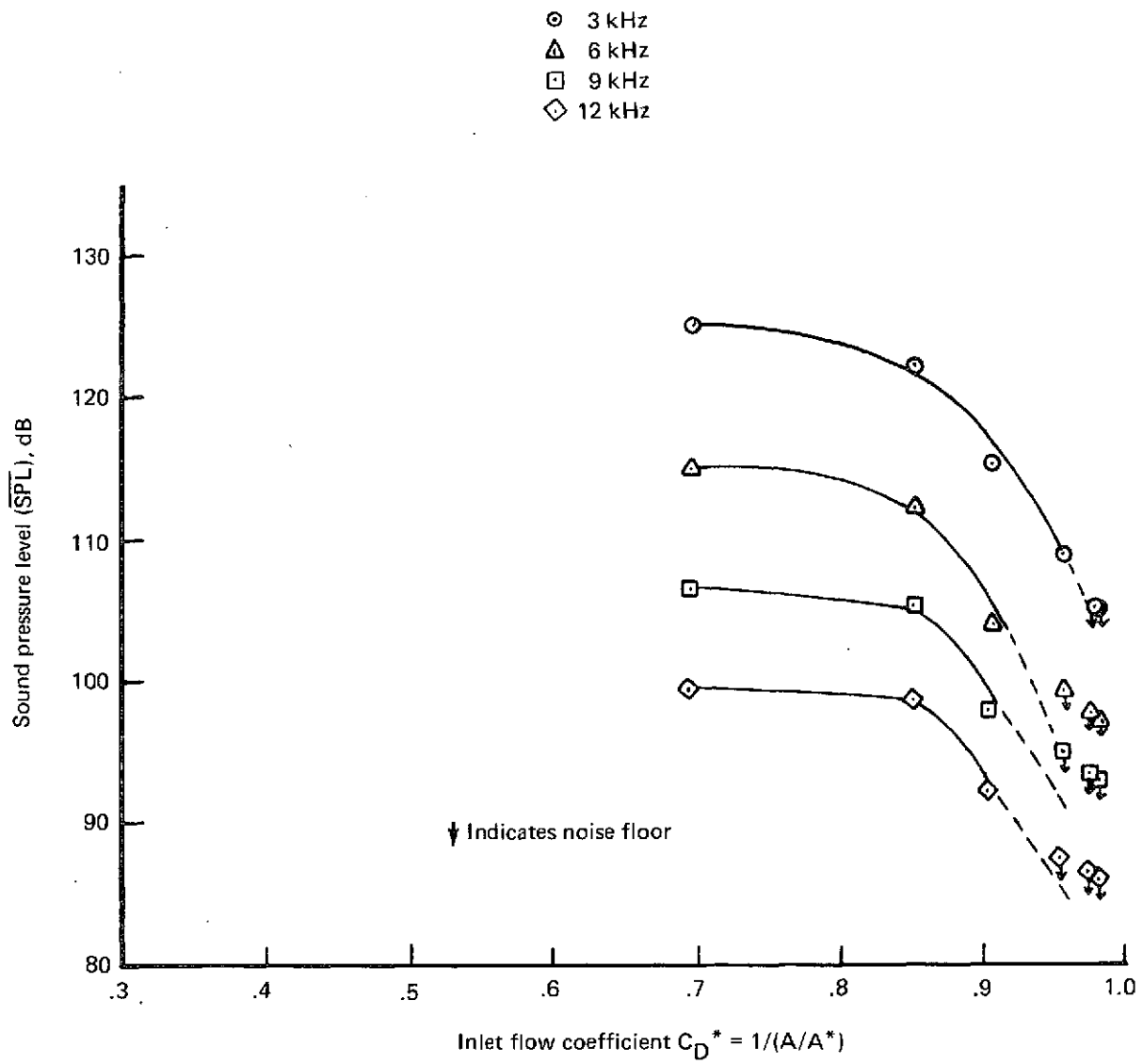


Figure 84.—Radial Vane Inlet B Acoustic Performance at Takeoff— $\alpha = 20^\circ$, $V = 315 \text{ km/h (170 kn)}$

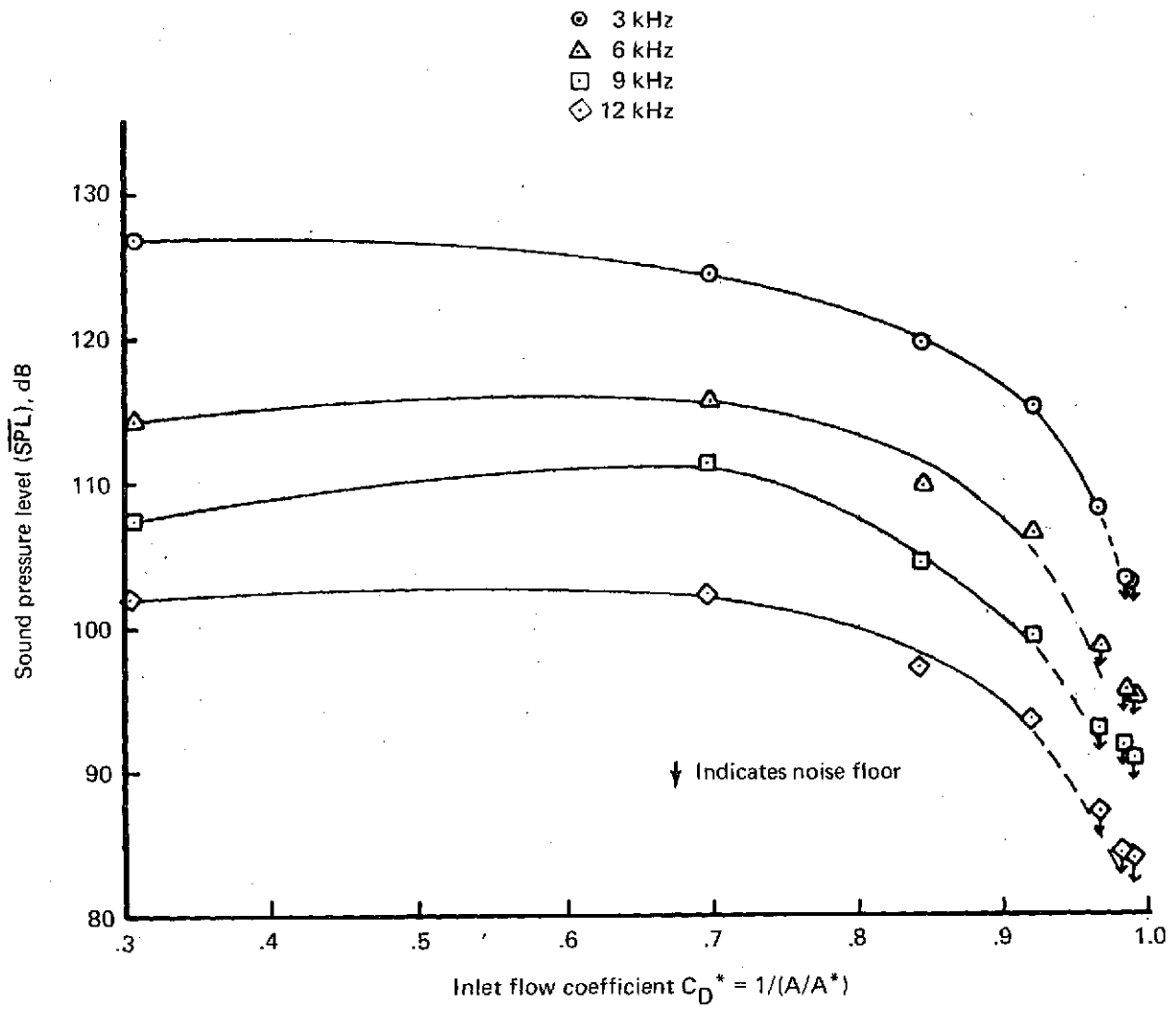


Figure 85.—Radial Vane Inlet B Acoustic Performance at Takeoff— $\alpha = 0^\circ$, $V = 315 \text{ km/h (170 kn)}$

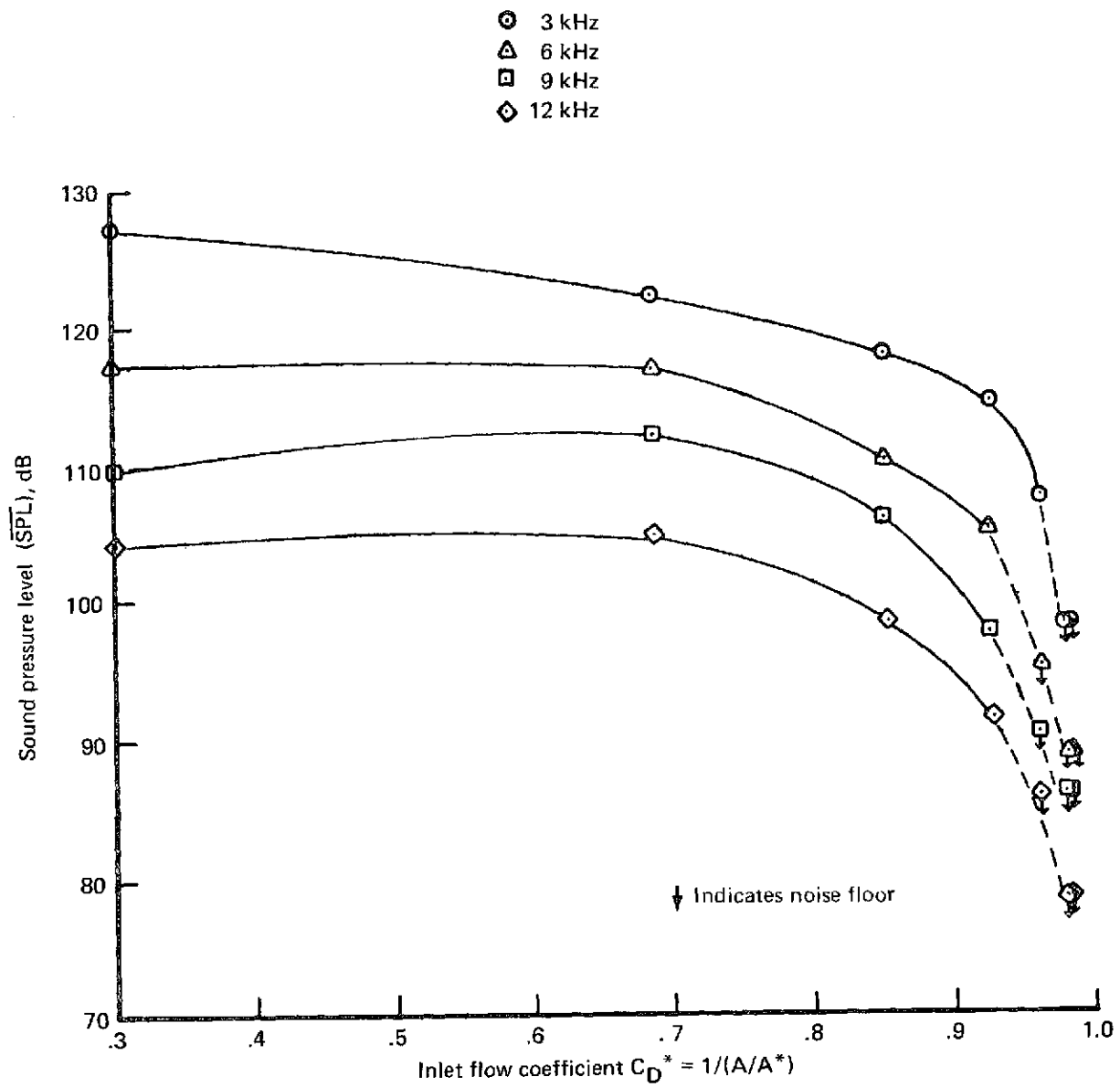


Figure 86.—Radial Vane Inlet B Acoustic Performance at Takeoff—
 $\alpha = 20^\circ$, $V = 259 \text{ km/h (140 kn)}$

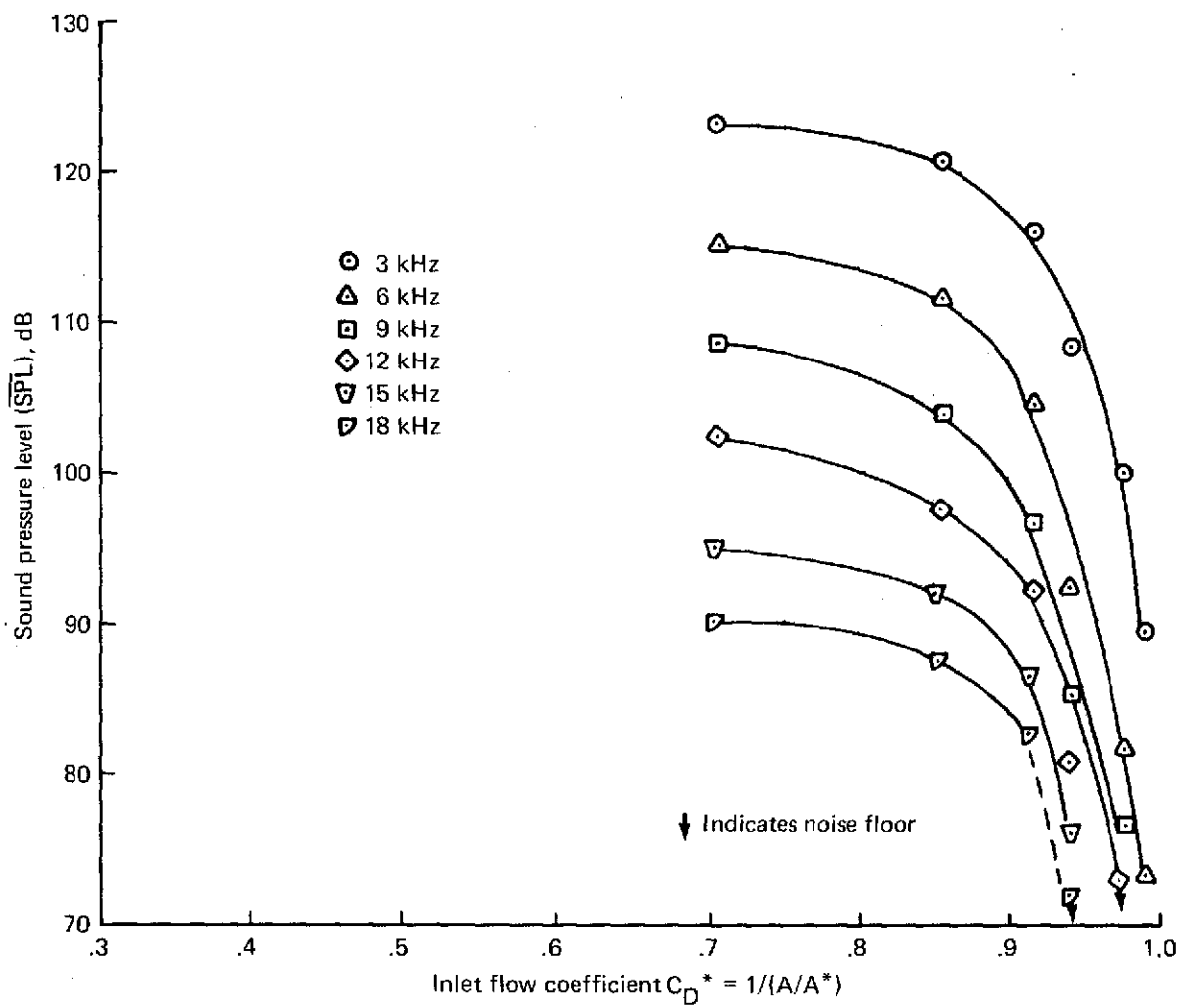
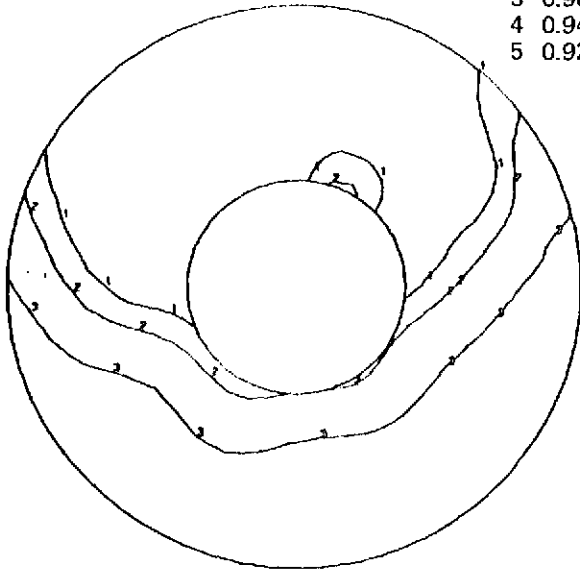


Figure 87.—Radial Vane Inlet B Acoustic Performance at Takeoff—
 $\alpha = 0^\circ, V = 0$

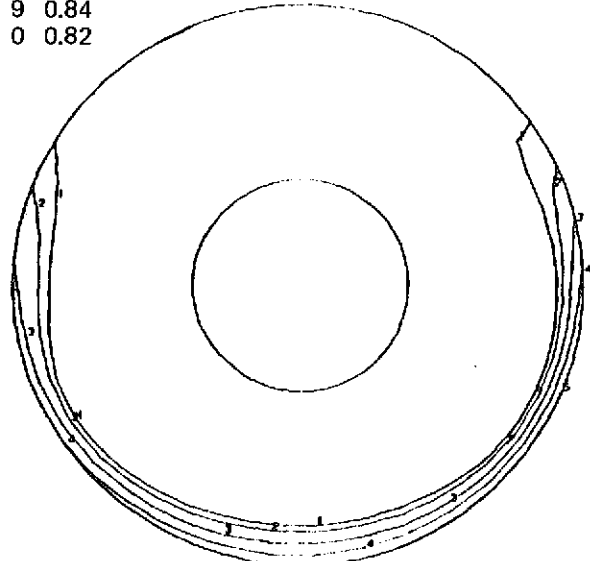
$P_T/P_{T REF}$

1	0.99	6	0.90
2	0.98	7	0.88
3	0.96	8	0.86
4	0.94	9	0.84
5	0.92	0	0.82



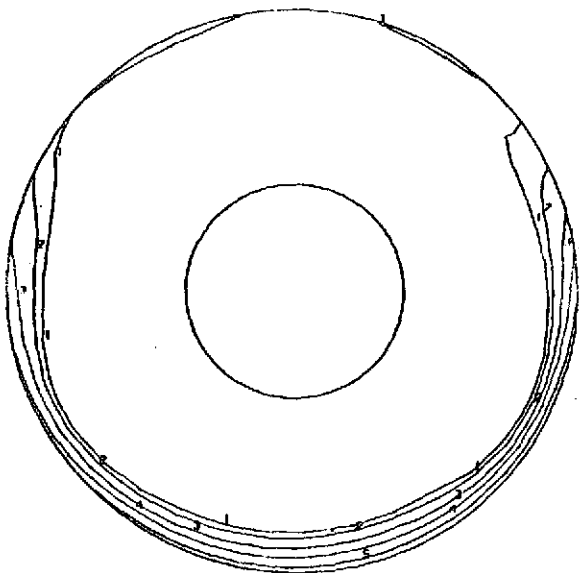
(a) $C_D^* = 0.277$

($M_{TH} = 0.163$, distortion = 5.4%, recovery = 0.9760)



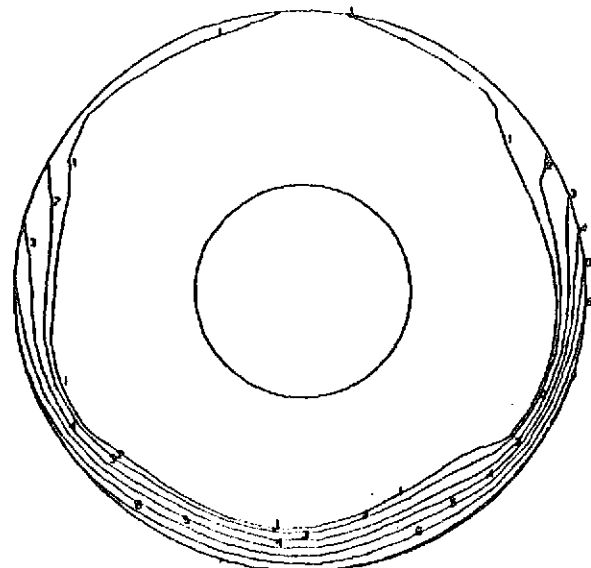
(b) $C_D^* = 0.767$

($M_{TH} = 0.520$, distortion = 6.3%, recovery = 0.9940)



(c) $C_D^* = 0.832$

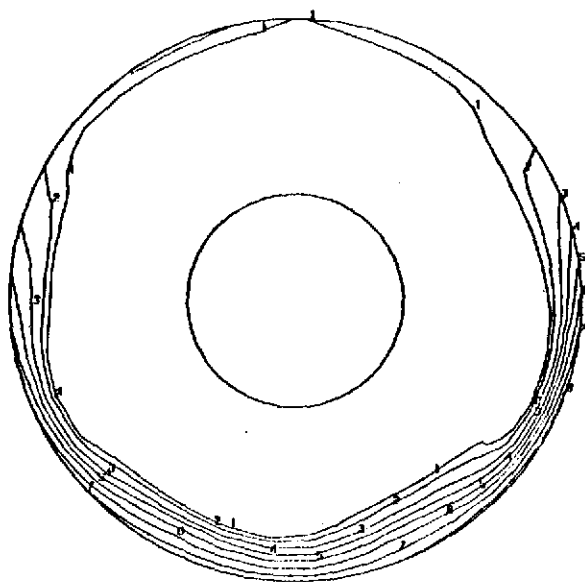
($M_{TH} = 0.589$, distortion = 7.6%, recovery = 0.9926)



(d) $C_D^* = 0.894$

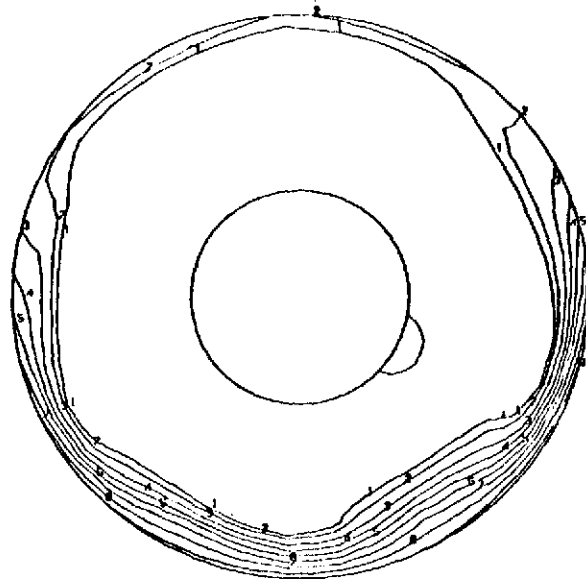
($M_{TH} = 0.669$, distortion = 10.8%, recovery = 0.9891)

Figure 88.—Compressor Face Total Pressure Recovery Maps for Radial Vane Inlet B at Takeoff— $\alpha = 90^\circ$, $V = 65$ km/h (35 kn)



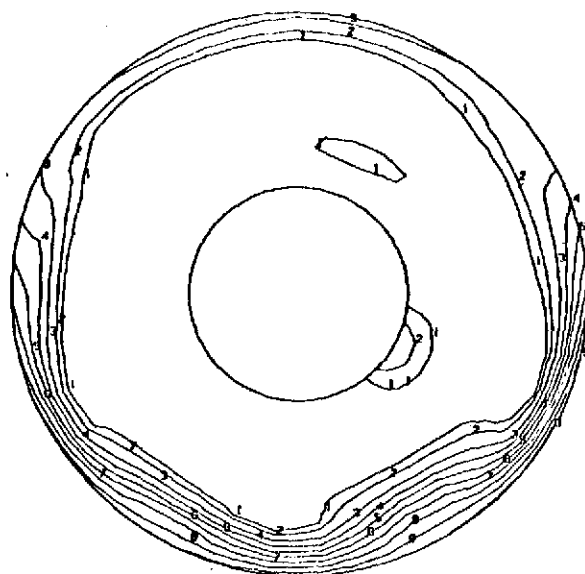
(e) $C_D^* = 0.931$

($M_{TH} = 0.731$, distortion = 12.8%, recovery = 0.9865)



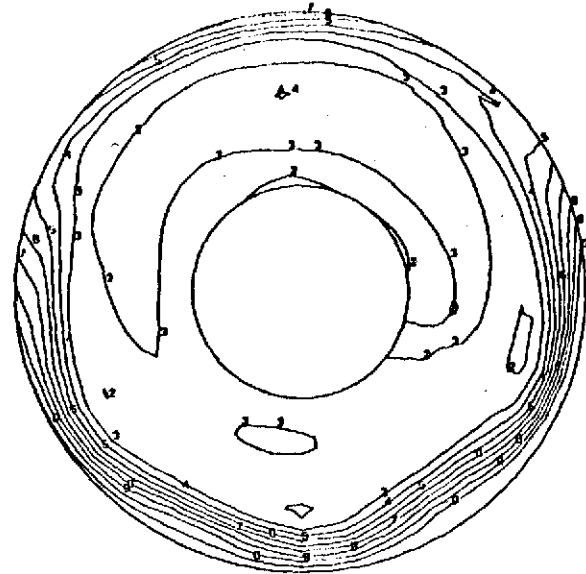
(f) $C_D^* = 0.960$

($M_{TH} = 0.793$, distortion = 15.2%, recovery = 0.9826)



(g) $C_D^* = 0.973$

($M_{TH} = 0.828$, distortion = 17.2%, recovery = 0.9763)



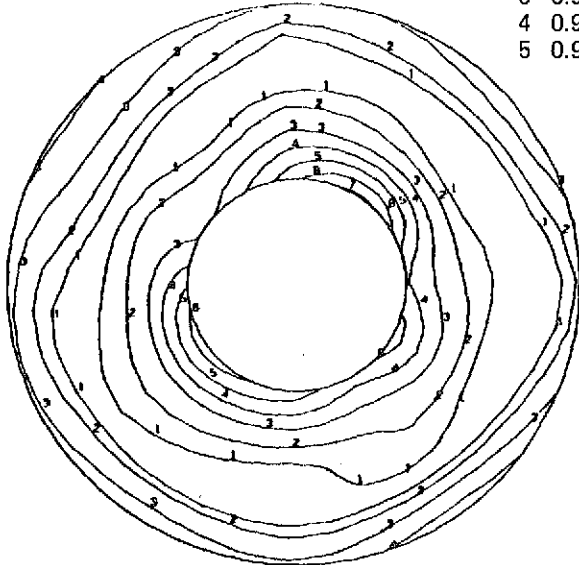
(h) $C_D^* = 0.976$

($M_{TH} = 0.837$, distortion = 19.8%, recovery = 0.9418)

Figure 88.—Concluded

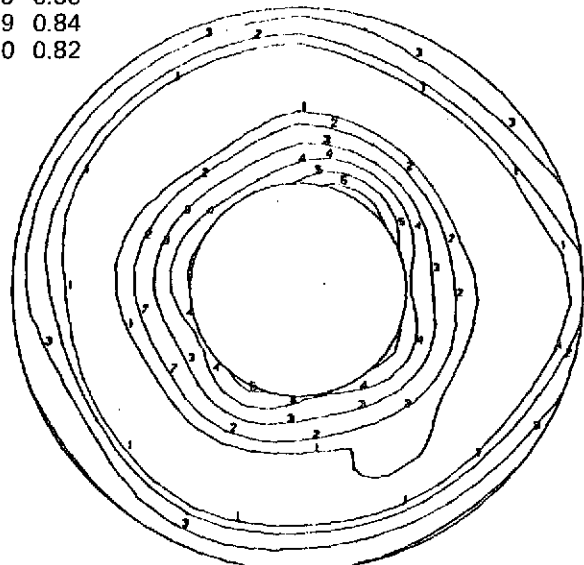
$P_T/P_{T REF}$

1	0.99	6	0.90
2	0.98	7	0.88
3	0.96	8	0.86
4	0.94	9	0.84
5	0.92	0	0.82



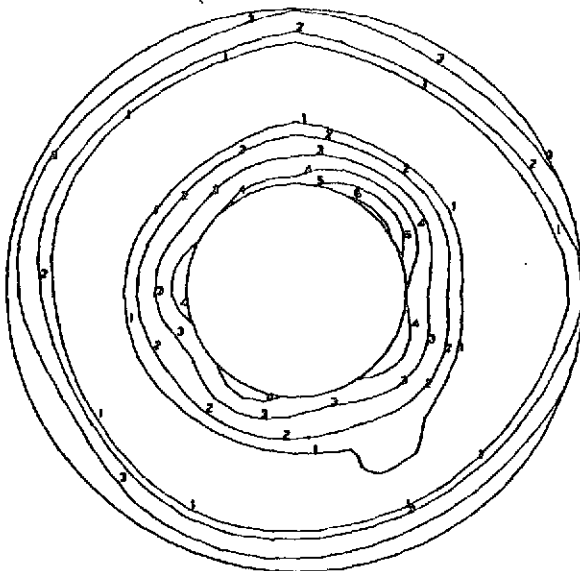
(a) $C_D^* = 0.937$, $\alpha = 0^\circ$, $V = 0$

($M_{TH} = 0.741$, distortion = 8.7%, recovery = 0.9740)



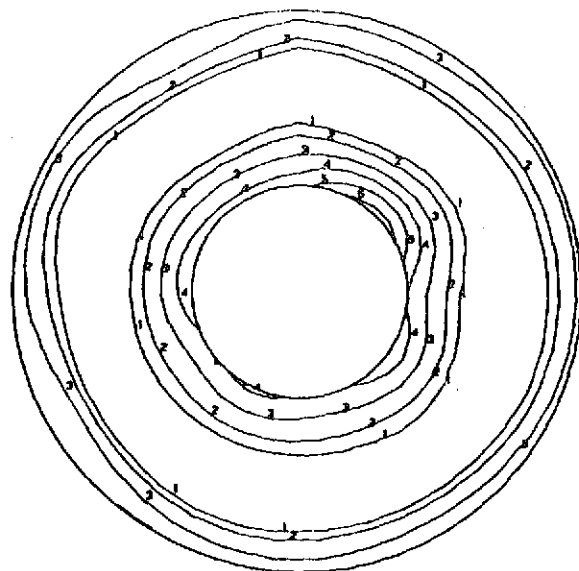
(b) $C_D^* = 0.921$, $\alpha = 0^\circ$, $V = 148 \text{ km/h (80 kn)}$

($M_{TH} = 0.713$, distortion = 8.0%, recovery = 0.9780)



(c) $C_D^* = 0.910$, $\alpha = 0^\circ$, $V = 185 \text{ km/h (100 kn)}$

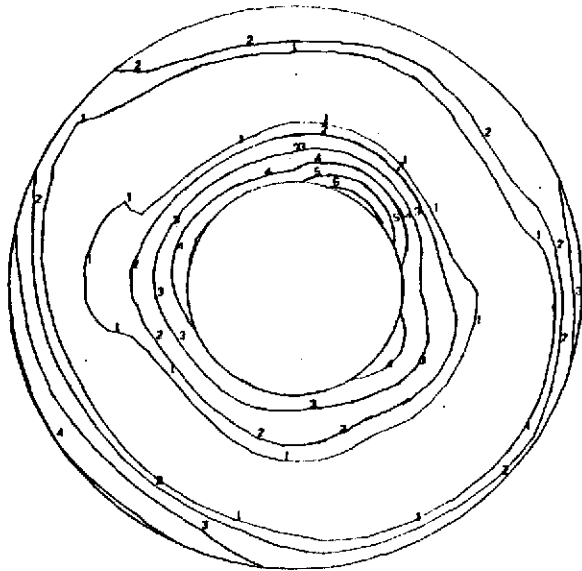
($M_{TH} = 0.693$, distortion = 7.0%, recovery = 0.9810)



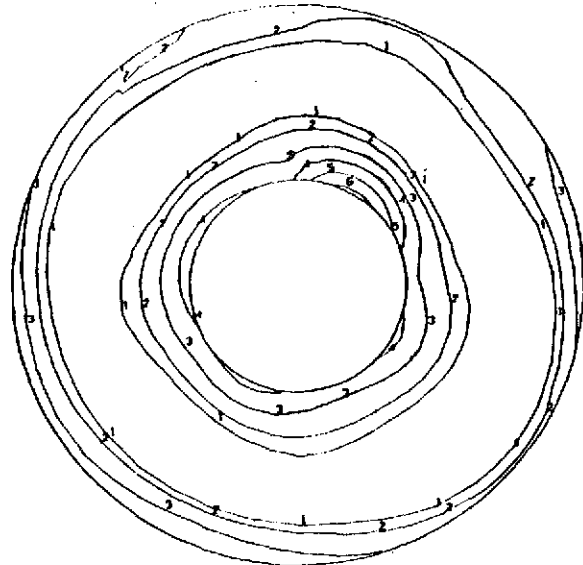
(d) $C_D^* = 0.914$, $\alpha = 0^\circ$, $V = 259 \text{ km/h (140 kn)}$

($M_{TH} = 0.701$, distortion = 7.4%, recovery = 0.9796)

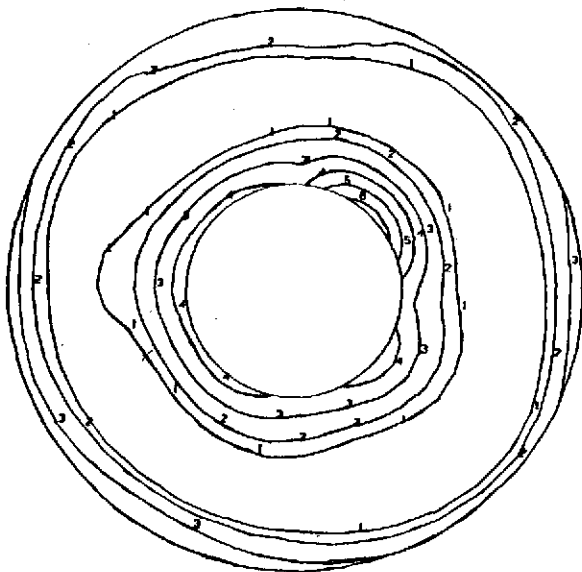
Figure 89.—Compressor Face Total Pressure Maps for Radial Vane Inlet B at Approach



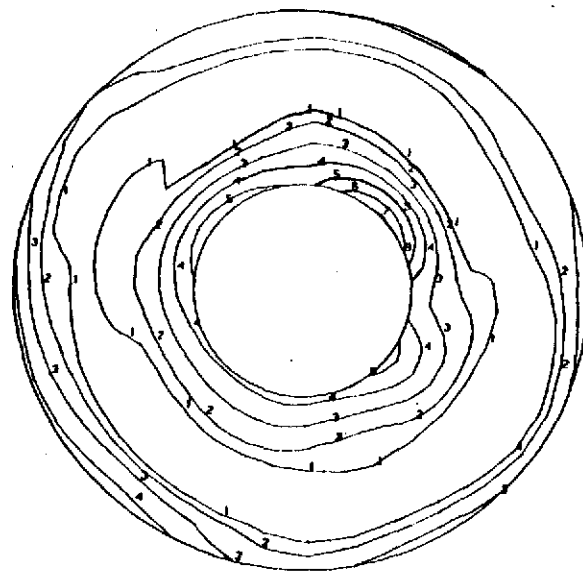
(e) $C_D^* = 0.892$, $\alpha = 35^\circ$, $V = 185 \text{ km/h (100 kn)}$
 $(M_{TH} = 0.664, \text{distortion} = 7.5\%, \text{recovery} = 0.9825)$



(f) $C_D^* = 0.895$, $\alpha = 20^\circ$, $V = 259 \text{ km/h (140 kn)}$
 $(M_{TH} = 0.671, \text{distortion} = 7.4\%, \text{recovery} = 0.9836)$

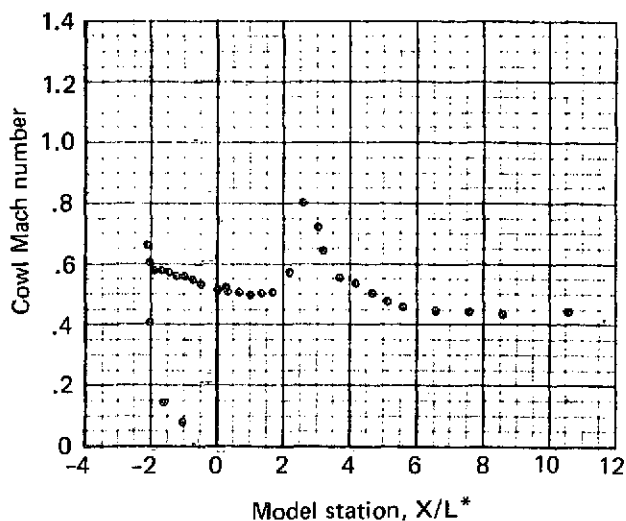


(g) $C_D^* = 0.901$, $\alpha = 20^\circ$, $V = 185 \text{ km/h (100 kn)}$
 $(M_{TH} = 0.680, \text{distortion} = 7.5\%, \text{recovery} = 0.9828)$



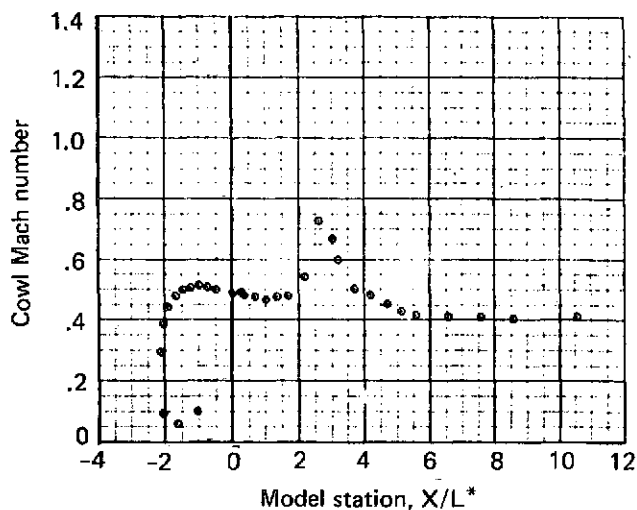
(h) $C_D^* = 0.917$, $\alpha = 35^\circ$, $V = 148 \text{ km/h (80 kn)}$
 $(M_{TH} = 0.705, \text{distortion} = 8.1\%, \text{recovery} = 0.9791)$

Figure 89.—Concluded



(a) $C_D^* = 0.937, \alpha = 0^\circ, V = 0$

($M_{TH} = 0.741, \text{distortion} = 8.7\%, \text{recovery} = 0.9740$)



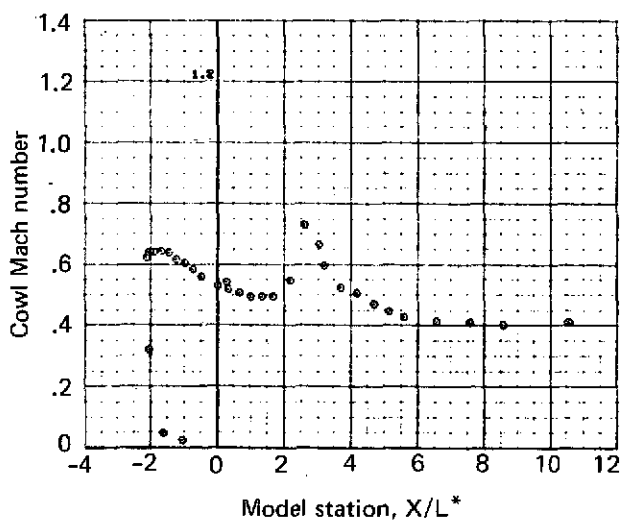
(b) $C_D^* = 0.909, \alpha = 0^\circ, V = 185 \text{ km/h (100 kn)}$

($M_{TH} = 0.693, \text{distortion} = 7.0\%, \text{recovery} = 0.9809$)

Notes:

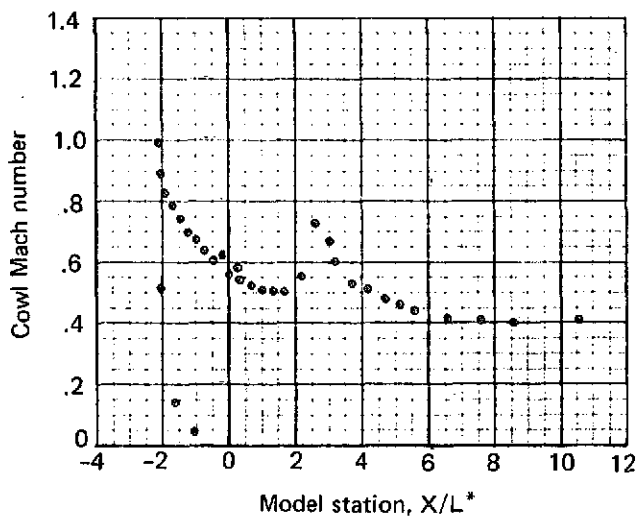
$L^* = 2.54 \text{ cm}$

Minimum cowl radius is at $X/L^* = 0$



(c) $C_D^* = 0.901, \alpha = 20^\circ, V = 185 \text{ km/h (100 kn)}$

($M_{TH} = 0.680, \text{distortion} = 7.5\%, \text{recovery} = 0.9827$)



(d) $C_D^* = 0.892, \alpha = 35^\circ, V = 185 \text{ km/h (100 kn)}$

($M_{TH} = 0.664, \text{distortion} = 7.5\%, \text{recovery} = 0.9825$)

Figure 90.—Inlet Cowl Mach Number Distribution for Radial Vane Inlet B at Approach

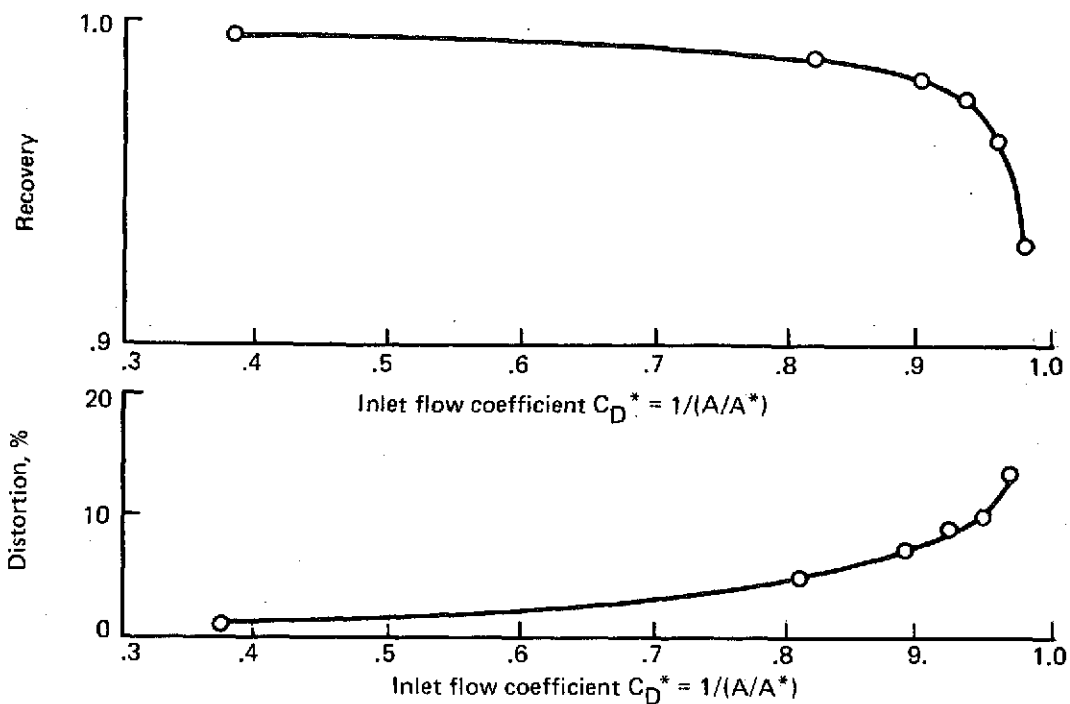


Figure 91.—Radial Vane Inlet B Distortion and Recovery Performance at Approach— $\alpha = 0^\circ$, $V = 148$ km/h (80 kn).

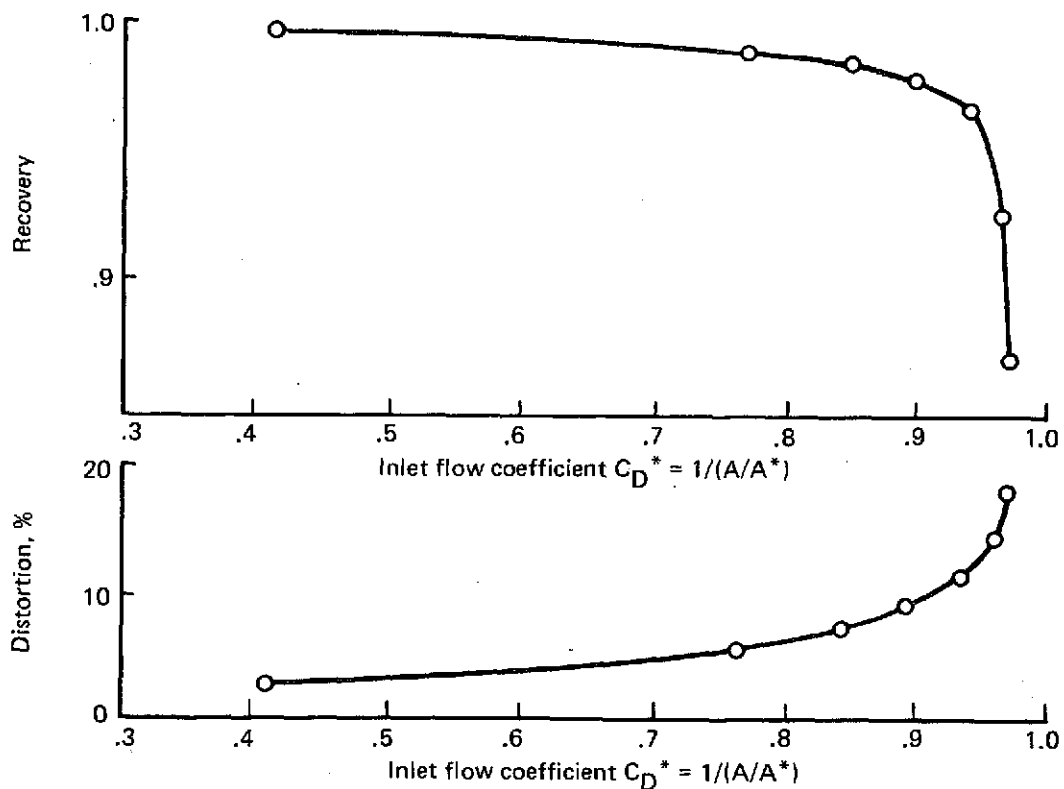


Figure 92.—Radial Vane Inlet B Distortion and Recovery Performance at Approach— $\alpha = 35^\circ$, $V = 185$ km/h (100 kn).

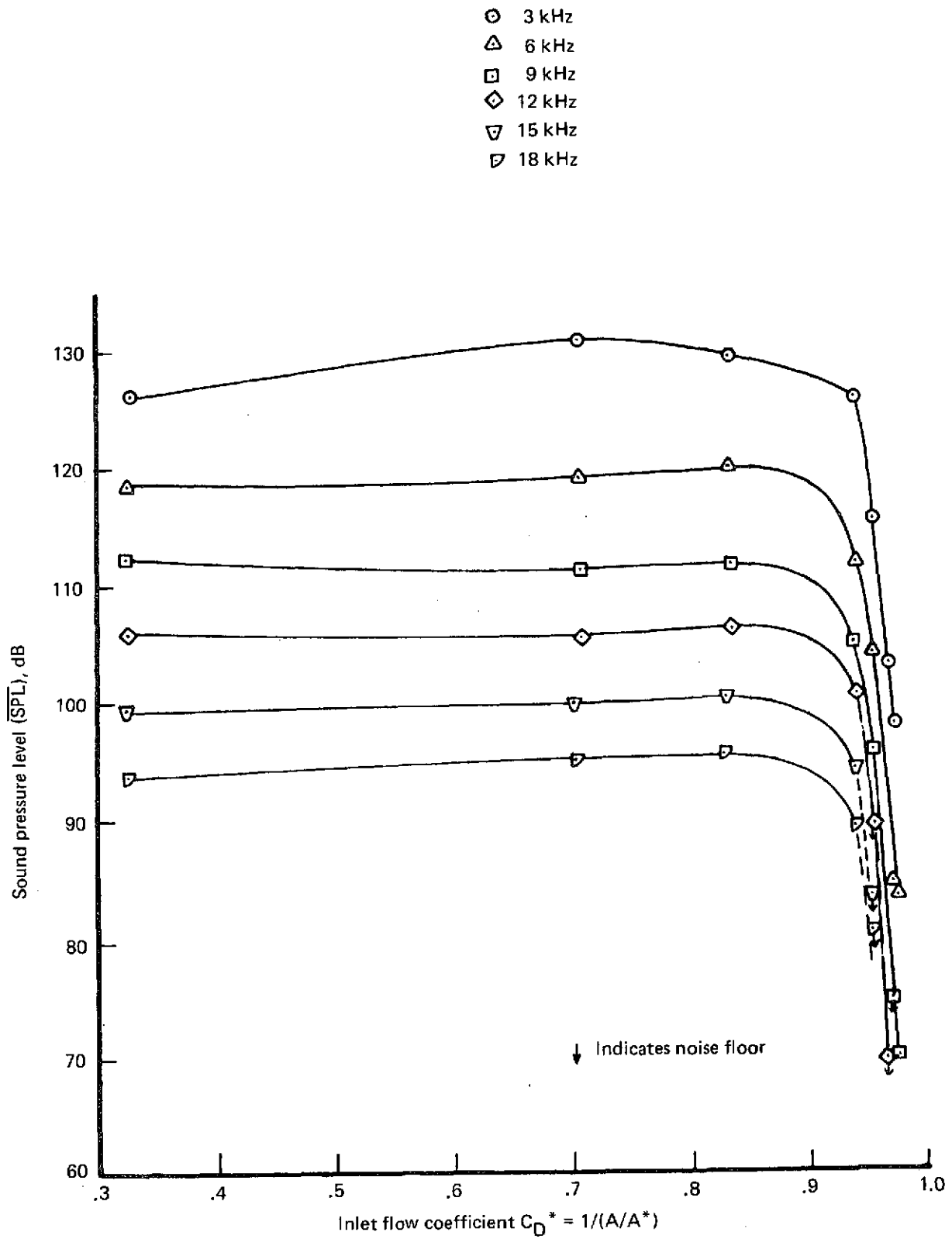


Figure 93.—Radial Vane Inlet B Acoustic Performance at Approach— $\alpha = 0^\circ$, $V = 0$

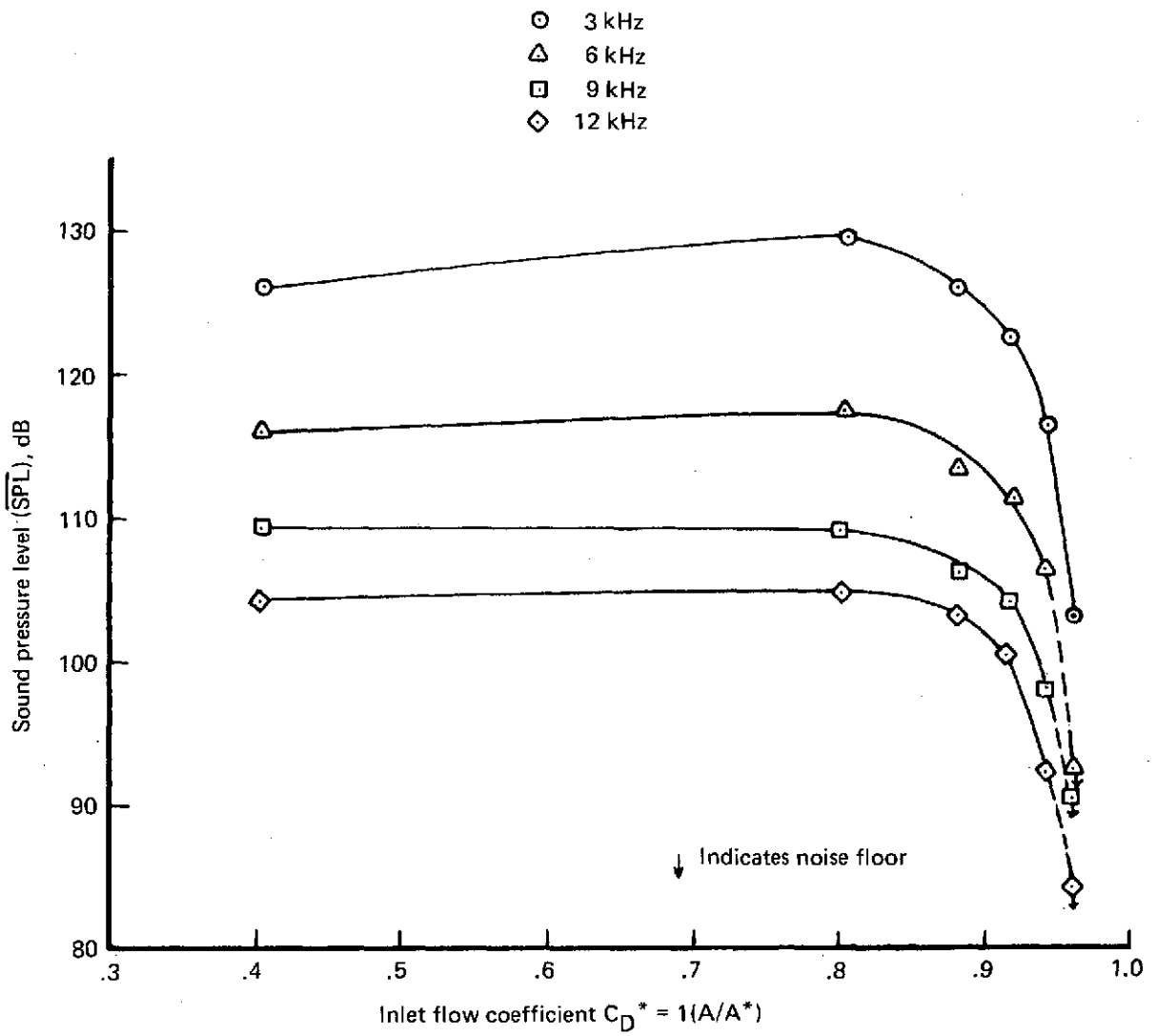


Figure 94.—Radial Vane Inlet B Acoustic Performance at Approach $-\alpha = 0^\circ$, $V = 148 \text{ km/h (80 kn)}$

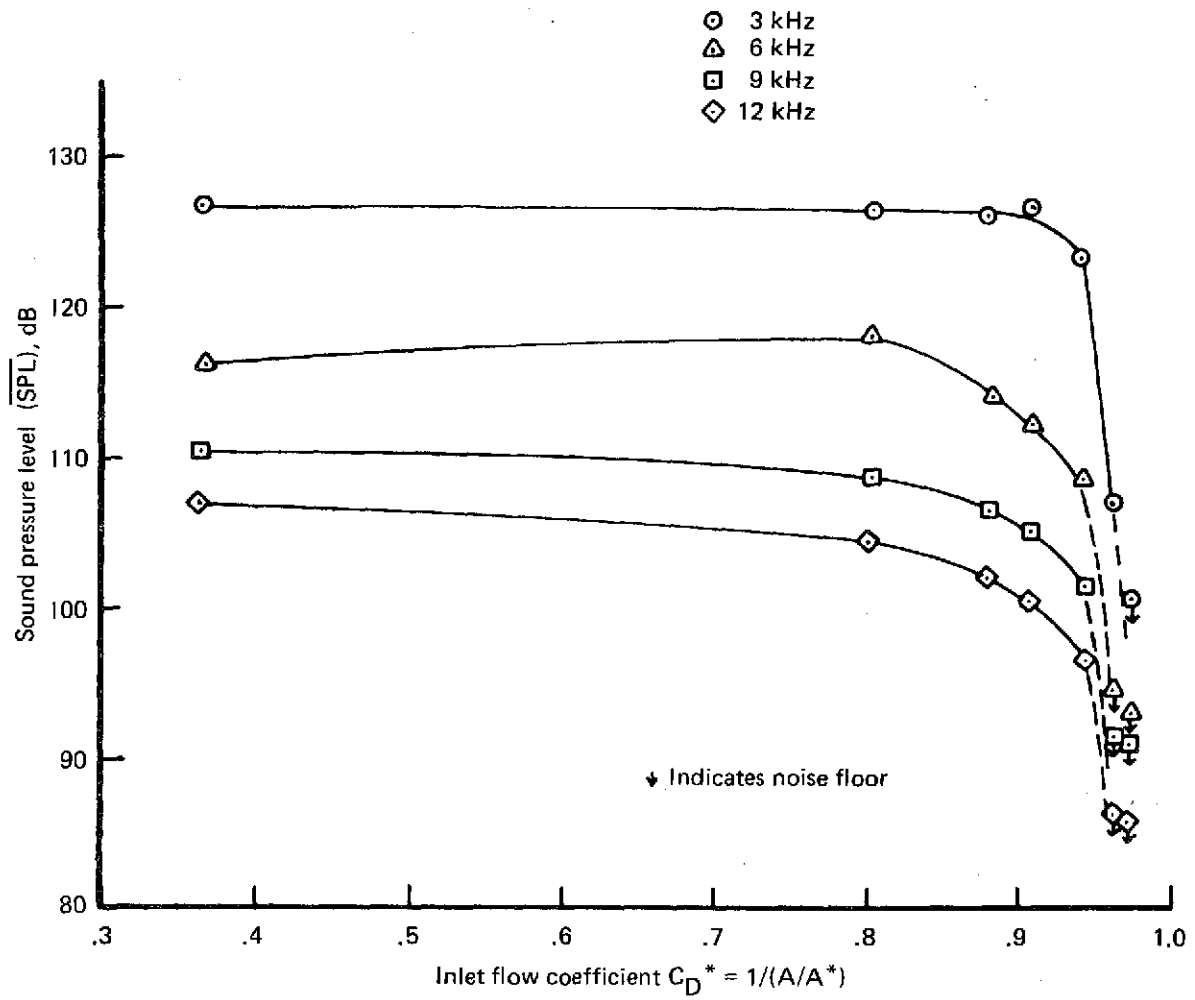


Figure 95.—Radial Vane Inlet B Acoustic Performance at Approach— $\alpha = 0^\circ$, $V = 185 \text{ km/h}$ (100 kn)

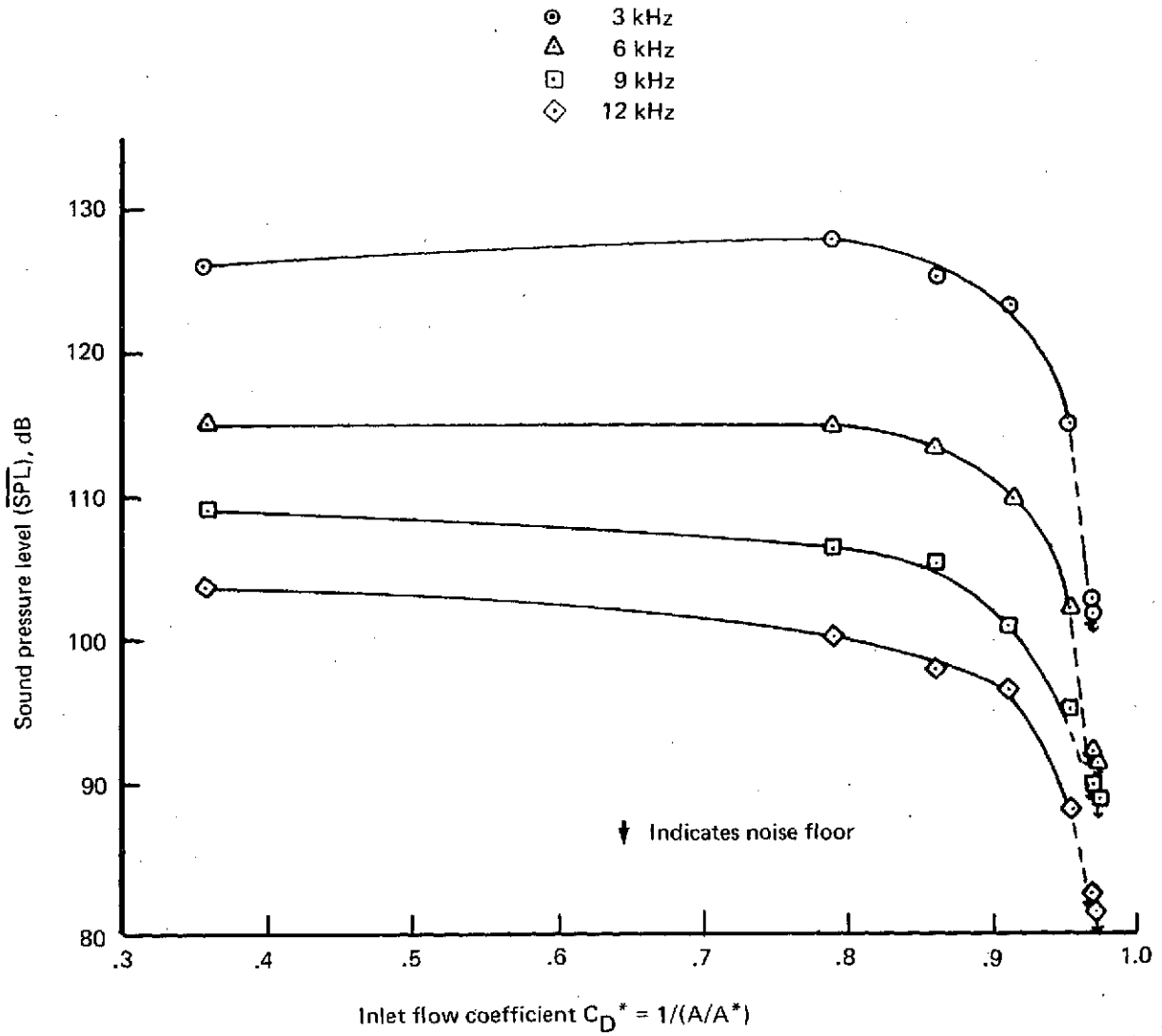


Figure 96.—Radial Vane Inlet B Acoustic Performance at Approach— $\alpha = 0^\circ$, $V = 259 \text{ km/h (140 kn)}$

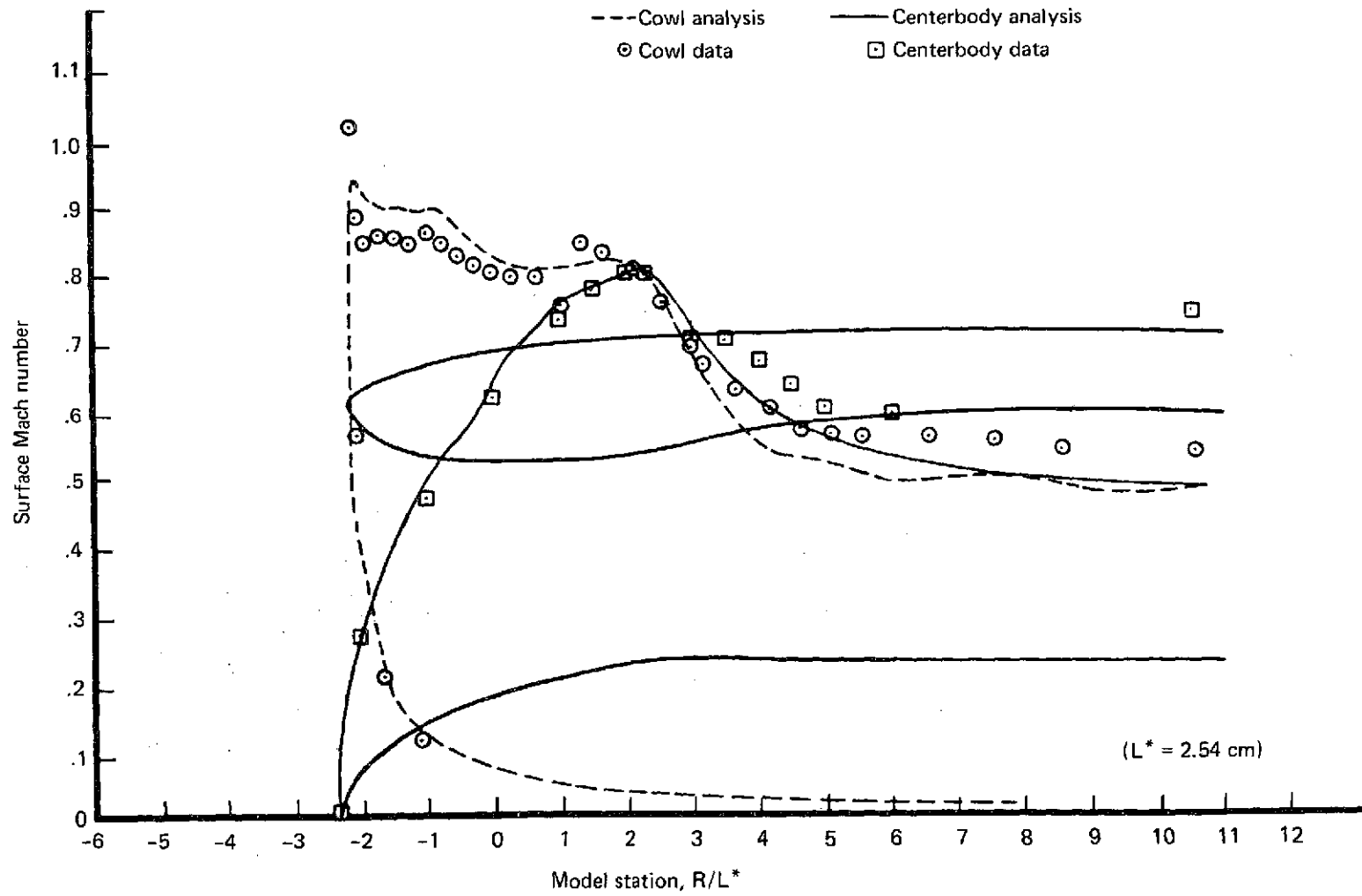


Figure 97.—Comparison of Analysis With Data for Radial Vane Inlet B at Takeoff—
 $V = 0, C_D^* = 0.941$

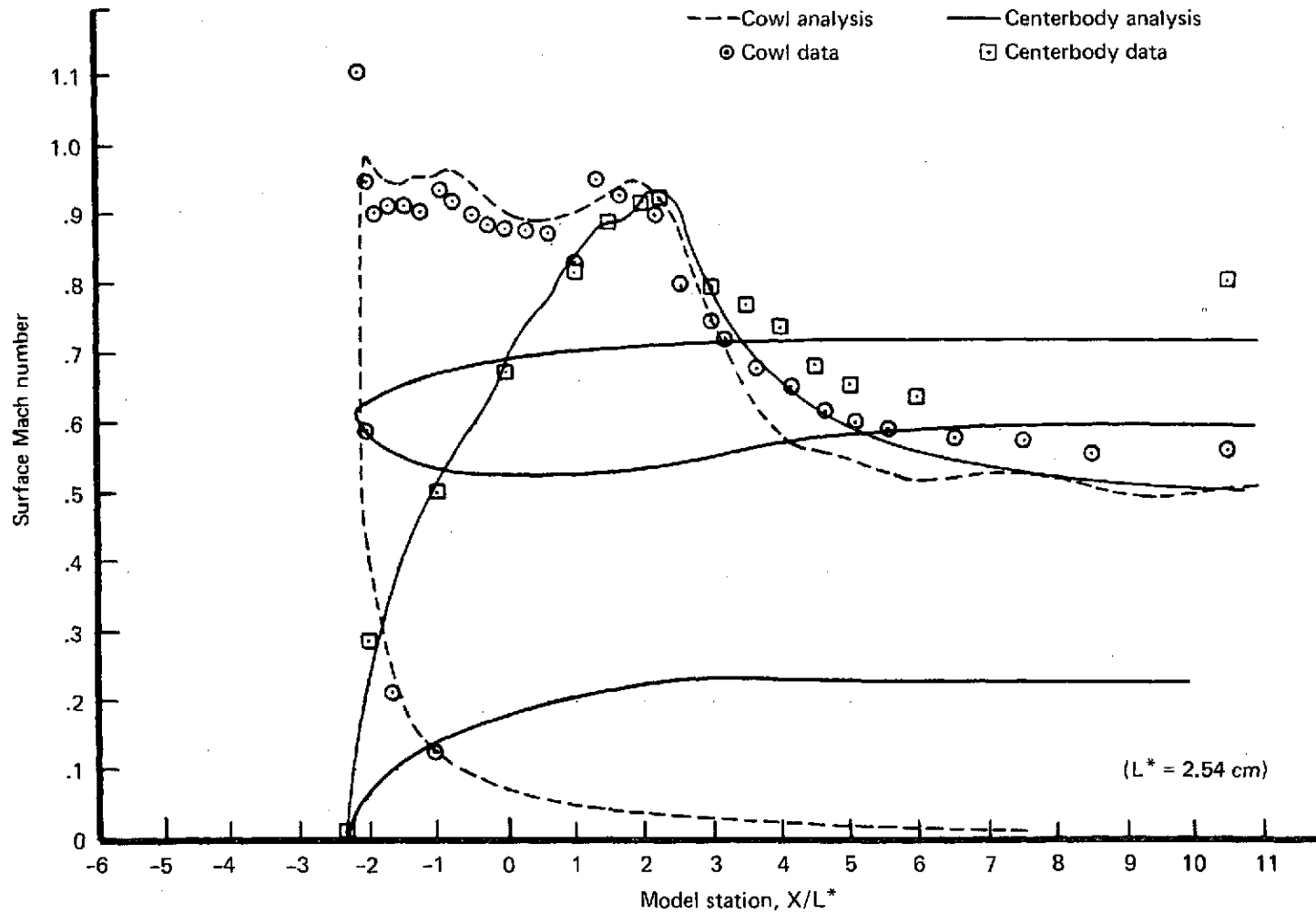


Figure 98.—Comparison of Analysis With Data for Radial Vane Inlet B at Takeoff—
 $V = 0$, $C_D^* = 0.980$

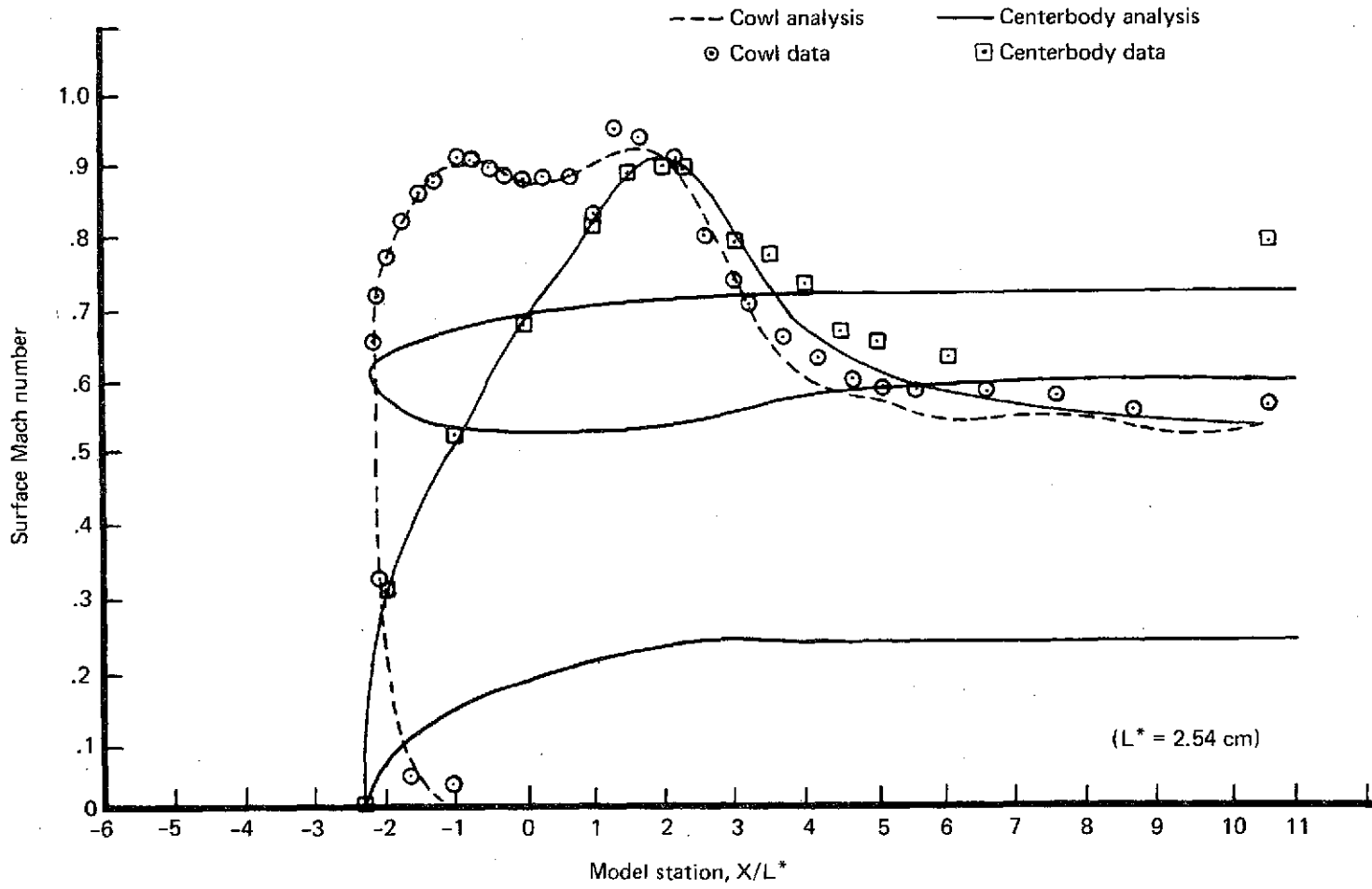


Figure 99.—Comparison of Analysis With Data for Radial Vane Inlet B at Takeoff—
 $V = 148$ km/h (80 kn), $C_D^* = 0.970$

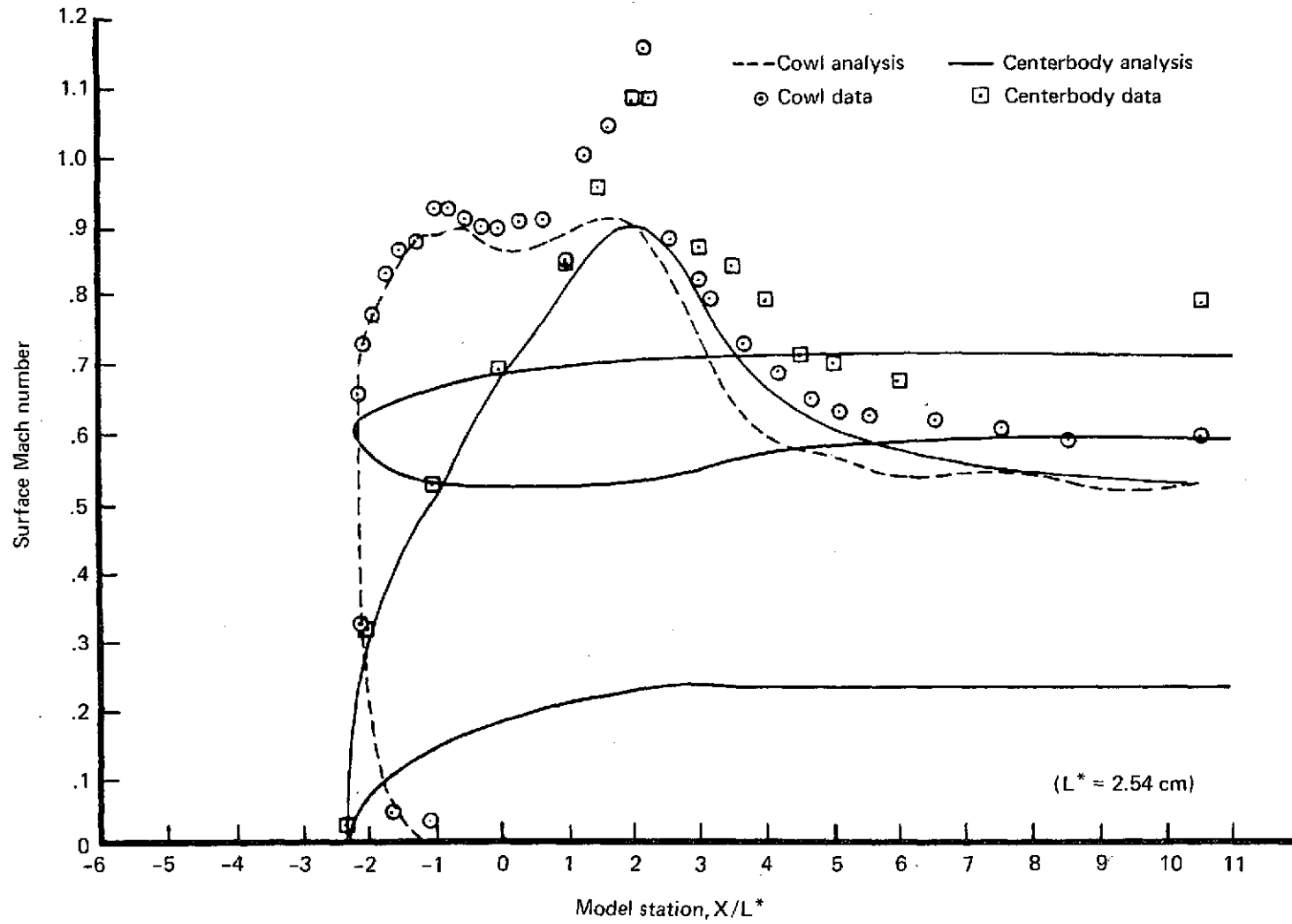


Figure 100.—Comparison of Analysis With Data for Radial Vane Inlet B at Takeoff—
 $V = 148 \text{ km/h (80 kn)}$, $C_D^* = 0.982$

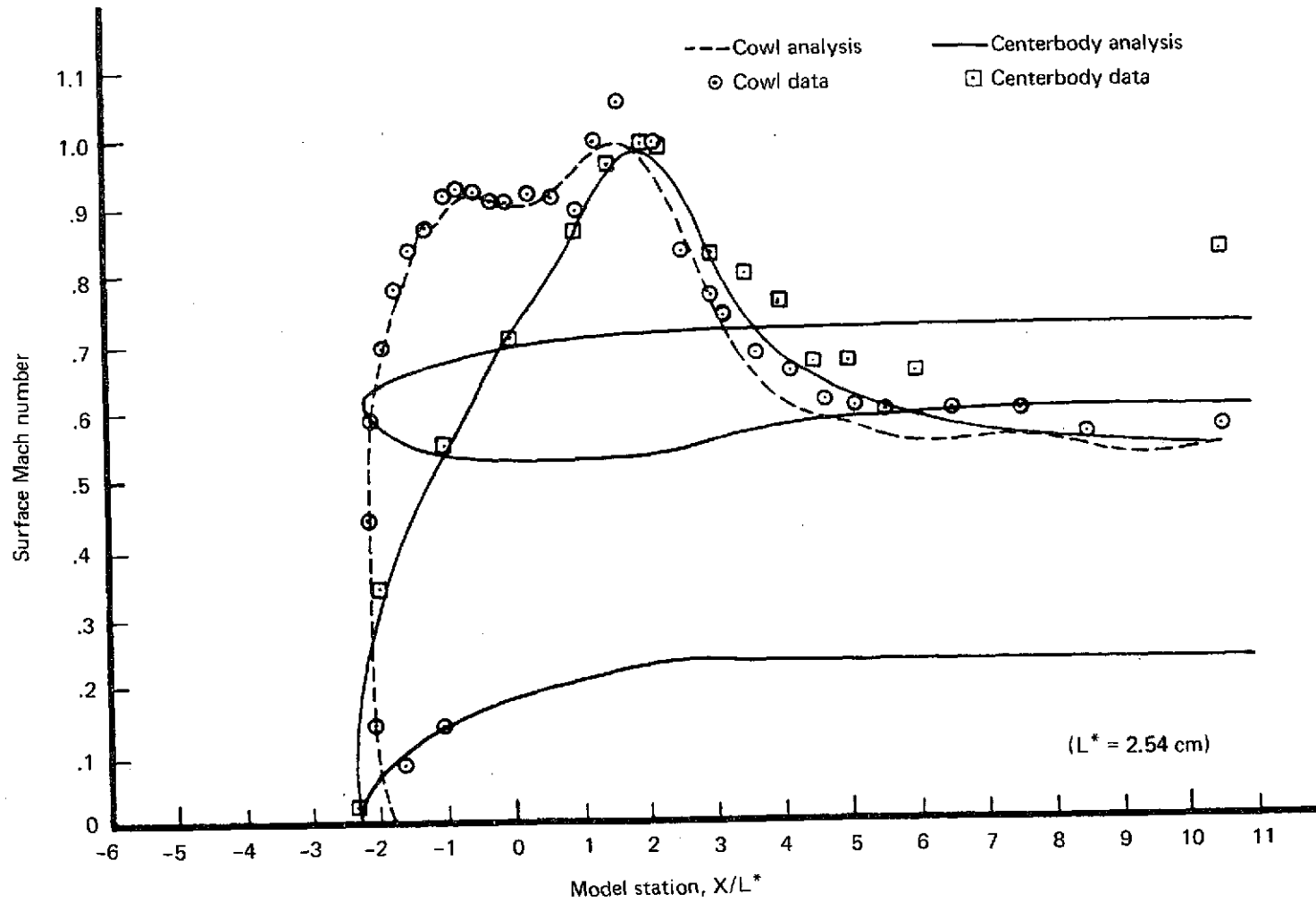


Figure 101.—Comparison of Analysis With Data for Radial Vane Inlet B at Takeoff—
 $V = 259$ km/h (140 kn), $C_D^* = 0.991$

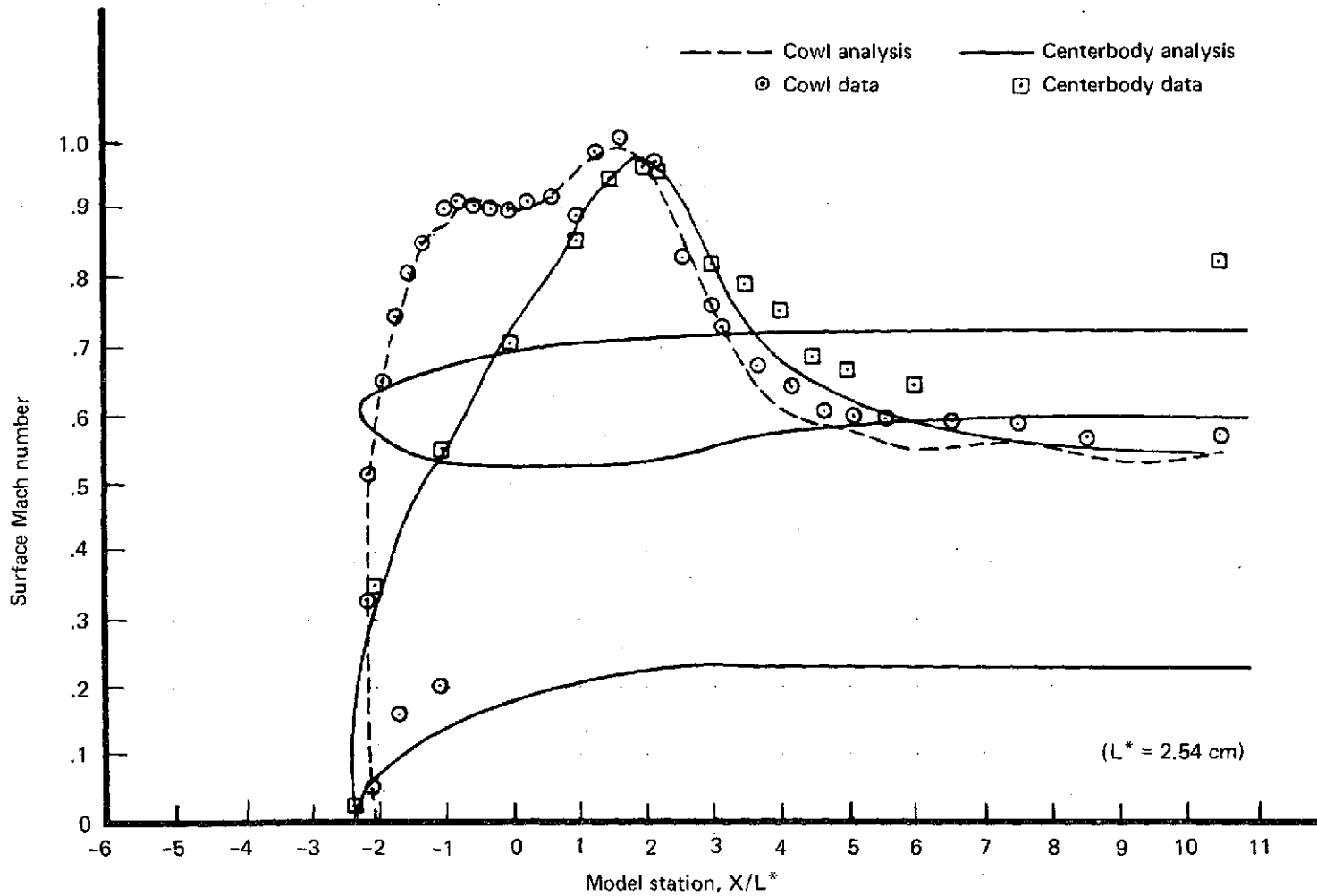


Figure 102.—Comparison of Analysis With Data for Radial Vane Inlet B at Takeoff—
 $V = 324$ km/h (175 kn), $C_D^* = 0.991$

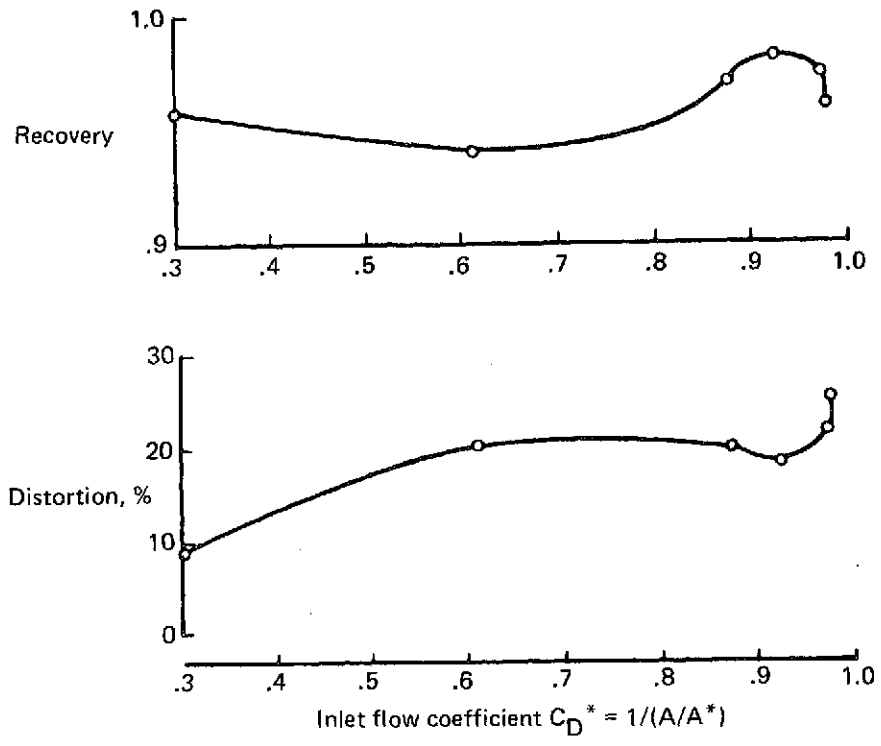


Figure 103.—QCSEE High Mach Number Inlet CI Distortion and Recovery Performance— $\alpha = 50^\circ$, $V = 148$ km/h (80 kn)

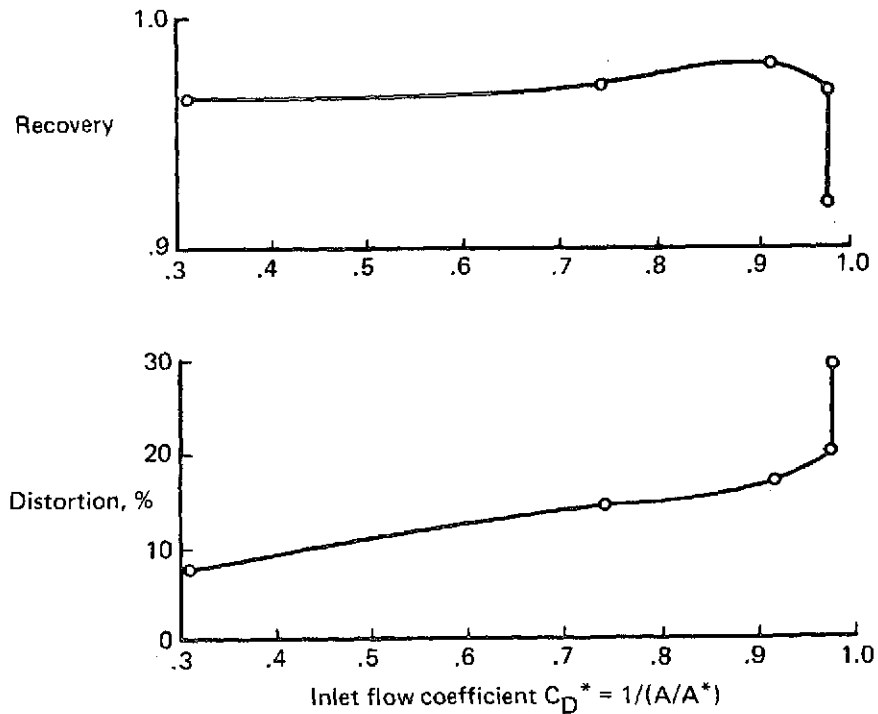
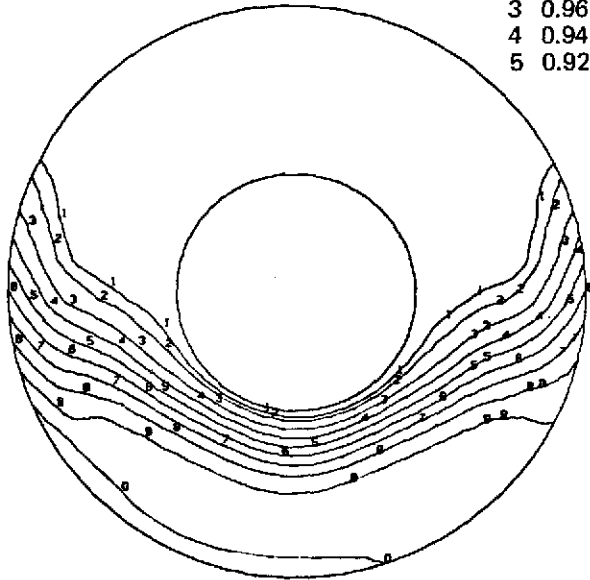


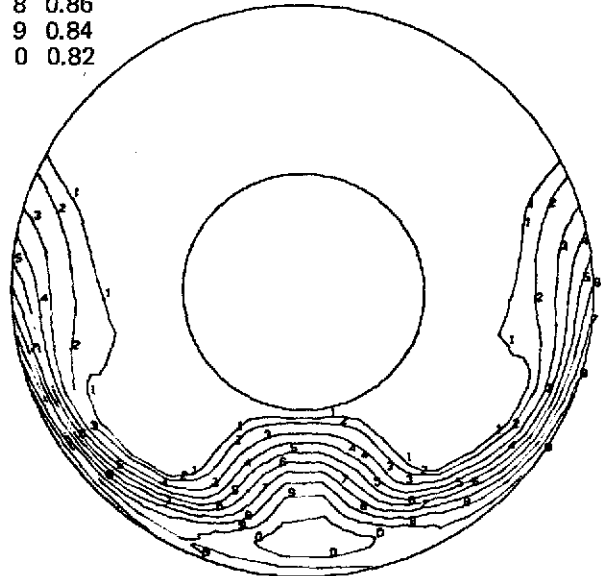
Figure 104.—QCSEE High Mach Number Inlet CI Distortion and Recovery Performance— $\alpha = 90^\circ$, $V = 65$ km/h (35 kn)

$P_T/P_{T REF}$			
1	0.99	6	0.90
2	0.98	7	0.88
3	0.96	8	0.86
4	0.94	9	0.84
5	0.92	0	0.82



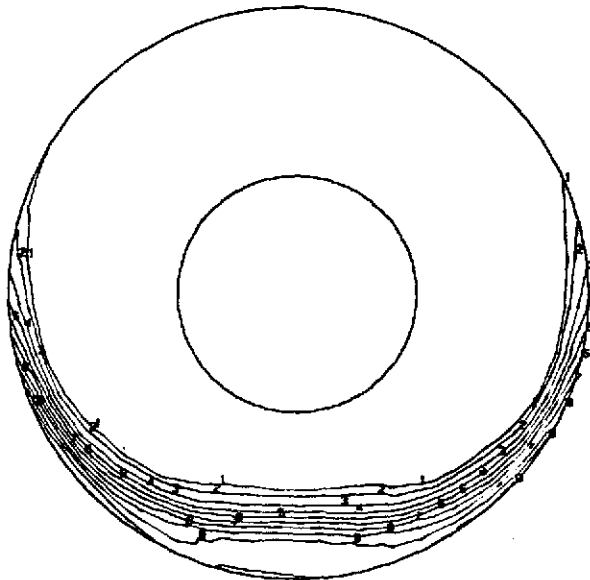
(a) $C_D^* = 0.609$

($M_{TH} = 0.385$, distortion = 20.3%, recovery = 0.9387)



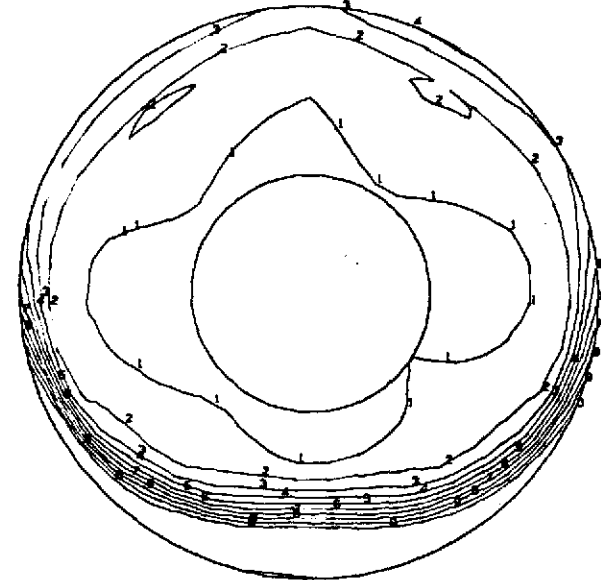
(b) $C_D^* = 0.873$

($M_{TH} = 0.639$, distortion = 20.0%, recovery = 0.9686)



(c) $C_D^* = 0.919$

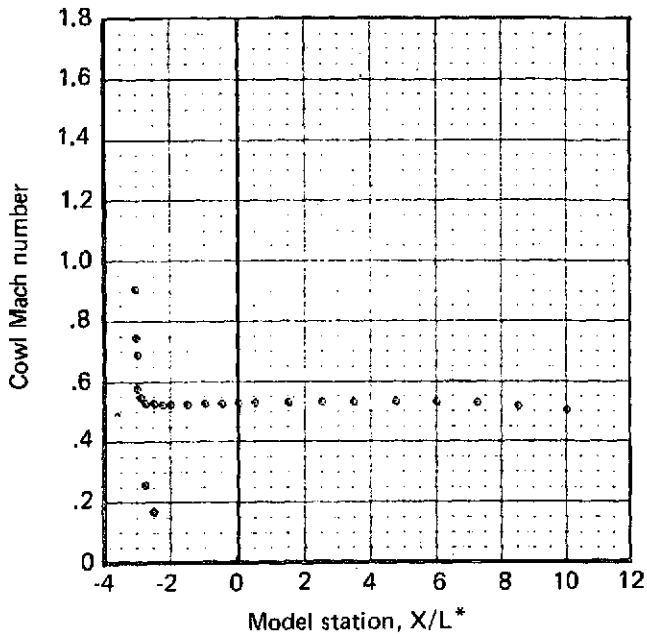
($M_{TH} = 0.709$, distortion = 18.2%, recovery = 0.9743)



(d) $C_D^* = 0.972$

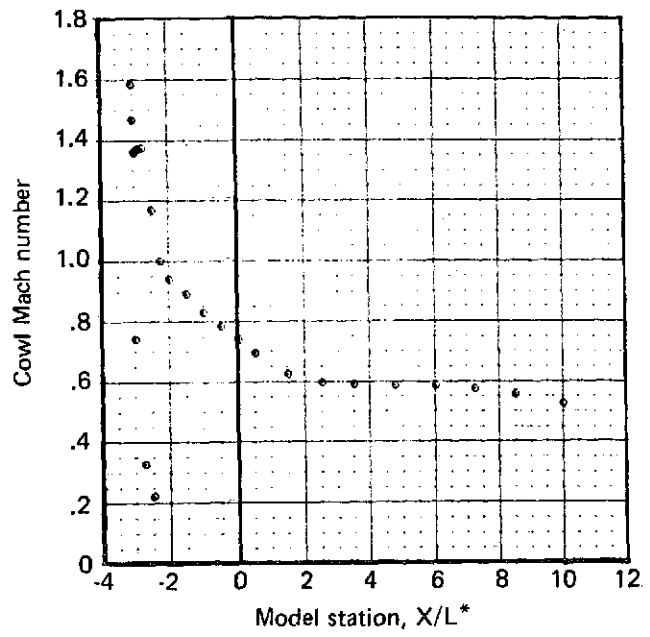
($M_{TH} = 0.824$, distortion = 25.5%, recovery = 0.9583)

Figure 105.—Compressor Face Total Pressure Recovery Maps for QCSEE
High Mach Number Inlet $C1-\alpha = 50^\circ$, $V = 148$ km/h (80 kn)



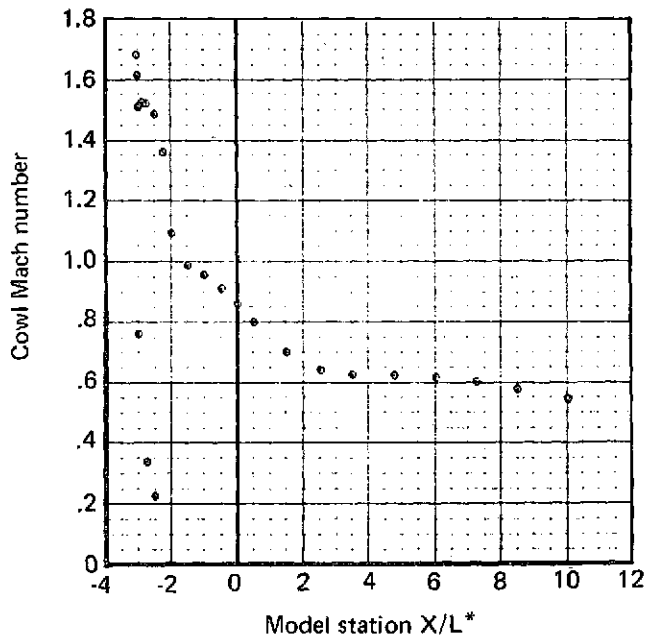
(a) $C_D^* = 0.609$

($M_{TH} = 0.385$, distortion = 20.3%, recovery = 0.9387)



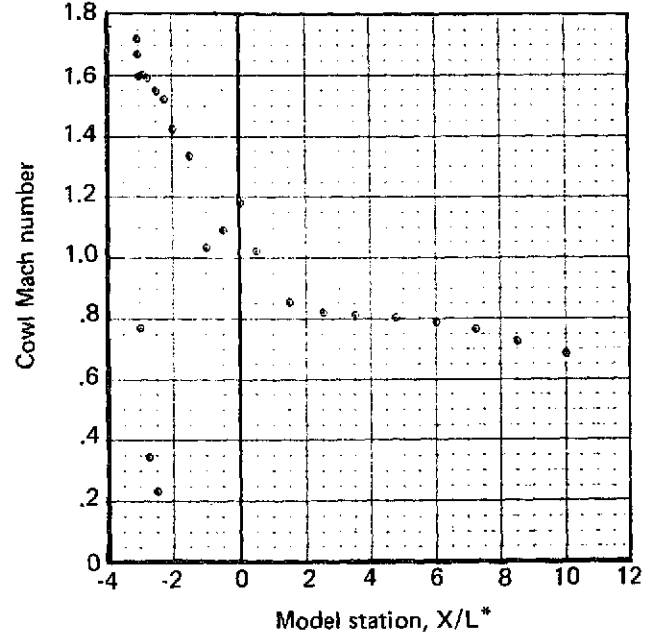
(b) $C_D^* = 0.873$

($M_{TH} = 0.639$, distortion = 20.0%, recovery = 0.9686)



(c) $C_D^* = 0.919$

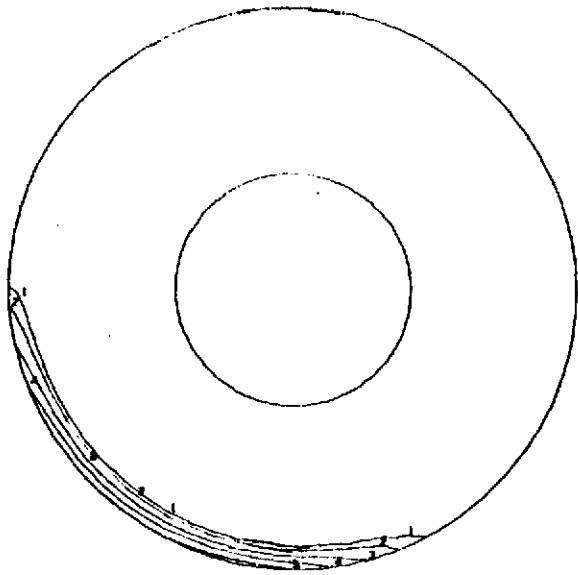
($M_{TH} = 0.709$, distortion = 18.2%, recovery = 0.9743)



(d) $C_D^* = 0.972$

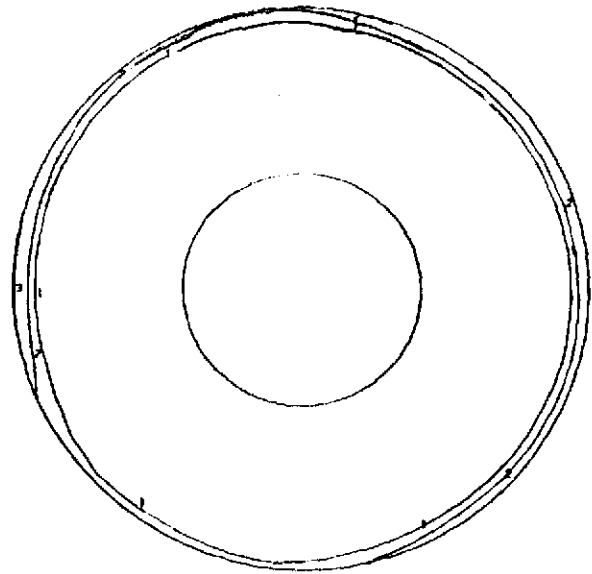
($M_{TH} = 0.824$, distortion = 25.5%, recovery = 0.9583)

Figure 106.—Inlet Cowl Mach Number Distribution for QCSEE High Mach Number Inlet C1—
 $\alpha = 50^\circ$, $V = 148$ km/h (80 kn)



(a) $C_D^* = 0.333$

($M_{TH} = 0.197$, distortion = 5.9%, recovery = 0.9975)

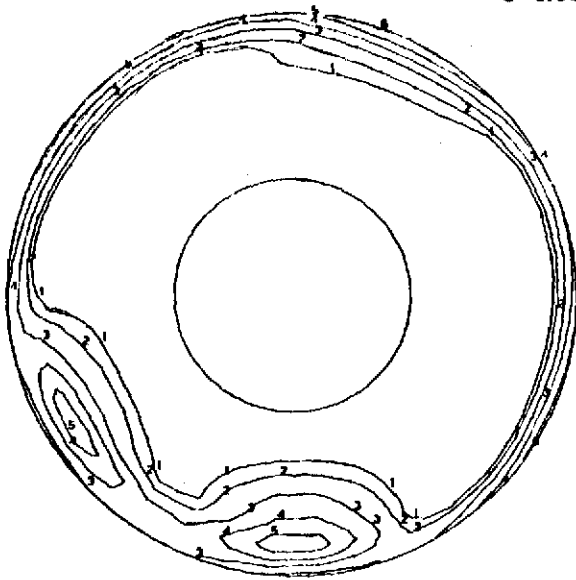


(b) $C_D^* = 0.739$

($M_{TH} = 0.492$, distortion = 2.9%, recovery = 0.9972)

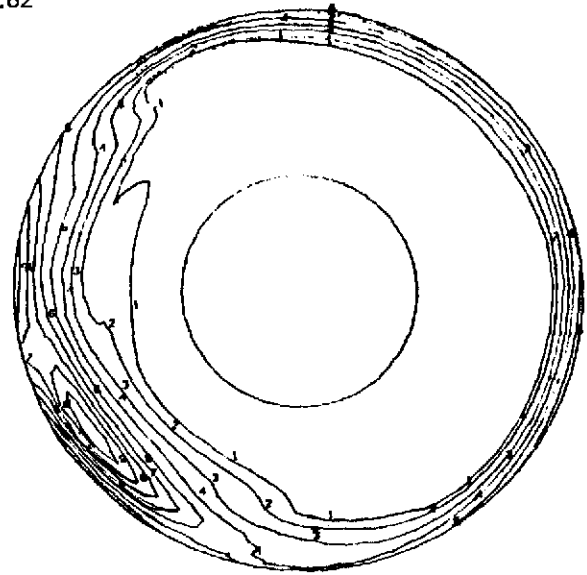
$P_T/P_{T REF}$

1	0.99	6	0.90
2	0.98	7	0.88
3	0.96	8	0.86
4	0.94	9	0.84
5	0.92	0	0.82



(c) $C_D^* = 0.966$

($M_{TH} = 0.808$, distortion = 9.7%, recovery = 0.9845)



(d) $C_D^* = 0.990$

($M_{TH} = 0.891$, distortion = 18.2%, recovery = 0.731)

Figure 107.—Compressor Face Total Pressure Recovery Maps for QCSEE High Mach Number Inlet C1— $\alpha = 0^\circ$, $V = 0$

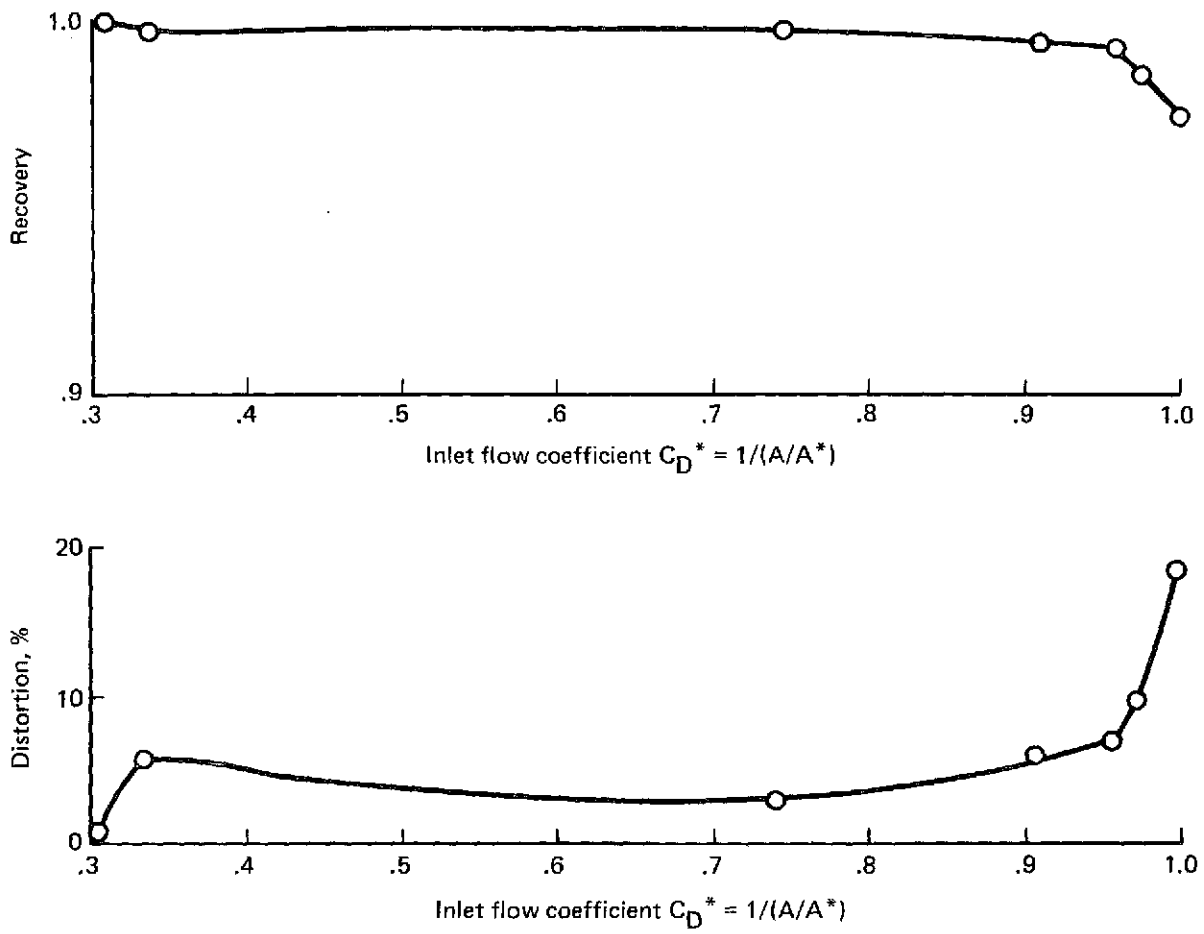


Figure 108.—QCSEE High Mach Number Inlet C1 Distortion and Recovery Performance— $\alpha = 0^\circ$, $V = 0$

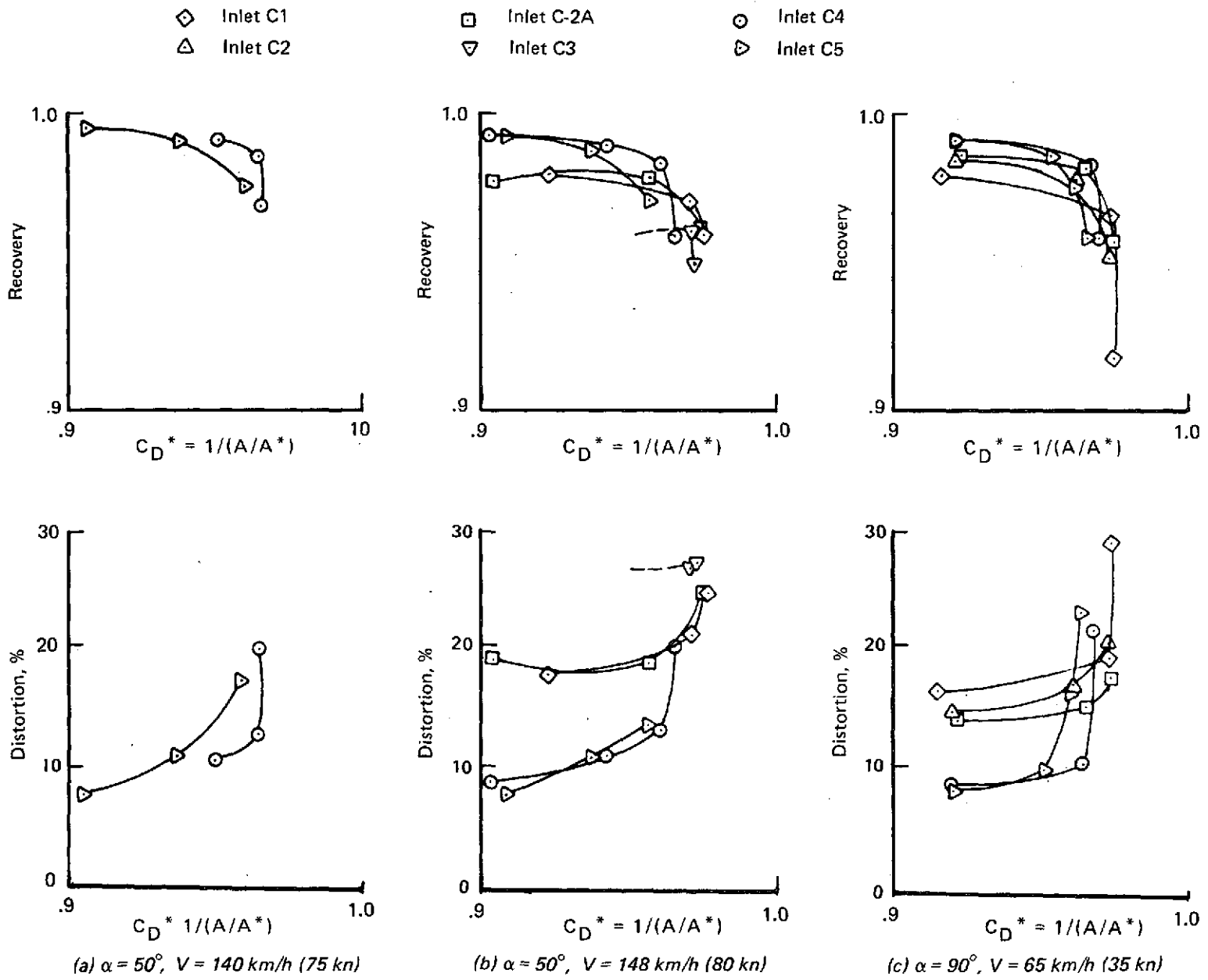


Figure 109.—QCSEE High Mach Number Inlet C Performance Summary— $\alpha = 50^\circ$, $\alpha = 90^\circ$

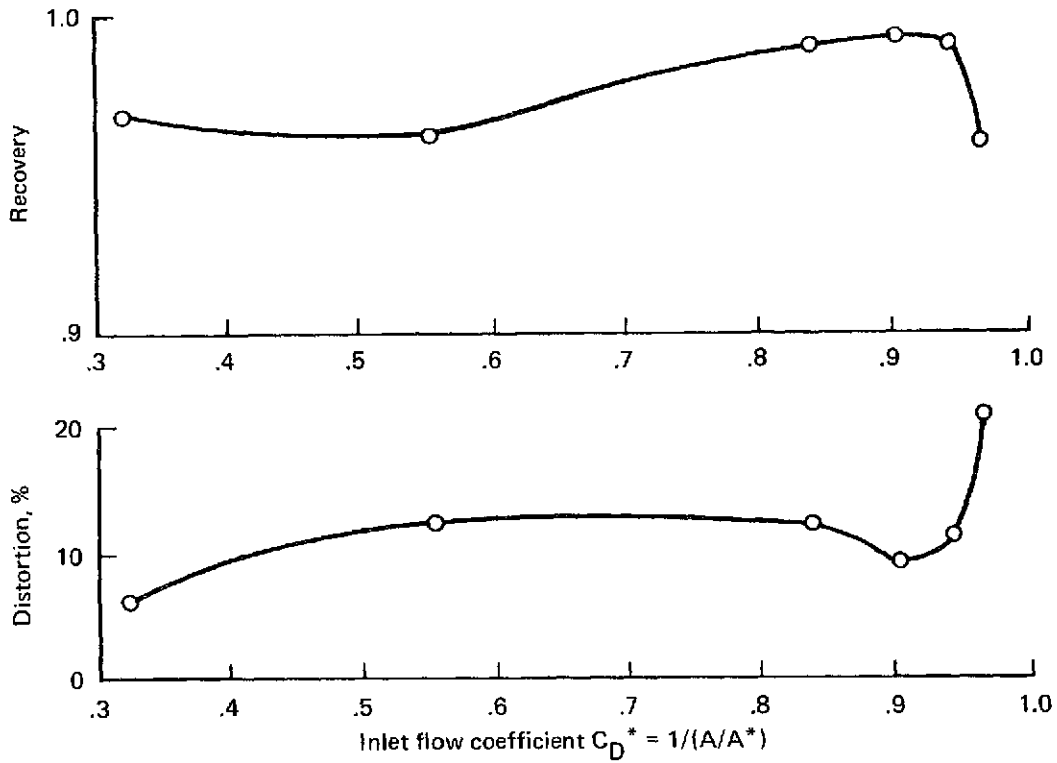


Figure 110.—QCSEE High Mach Number Inlet C4 Distortion and Recovery Performance— $\alpha = 50^\circ$, $V = 148$ km/h (80 kn)

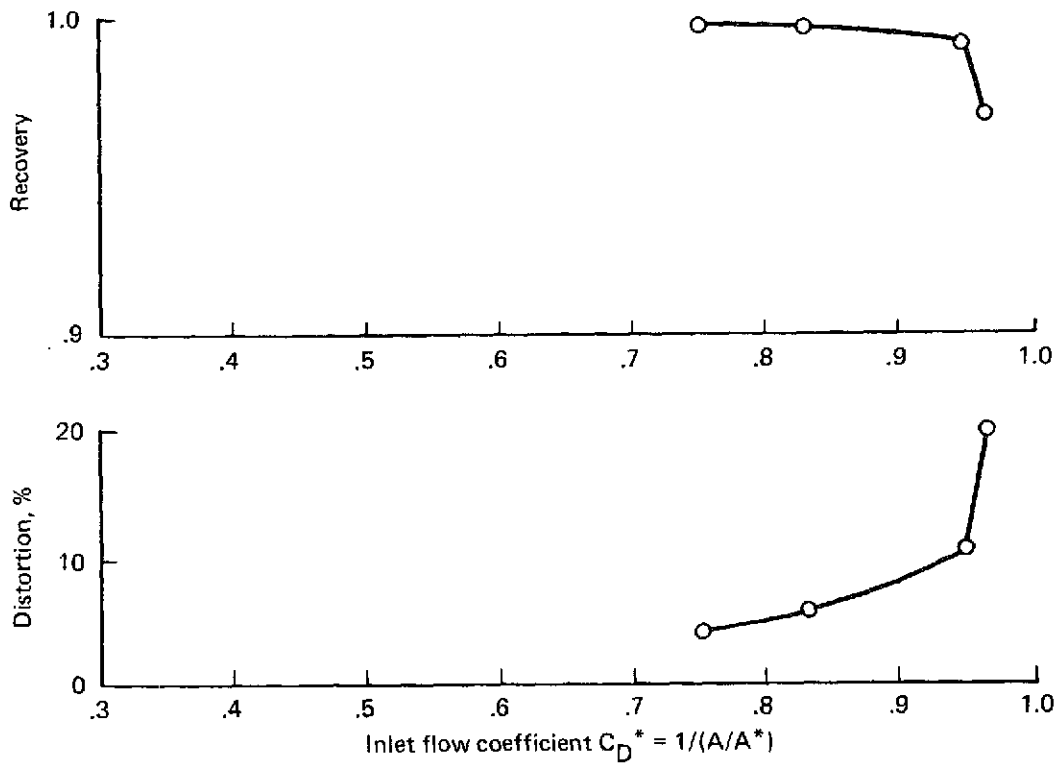
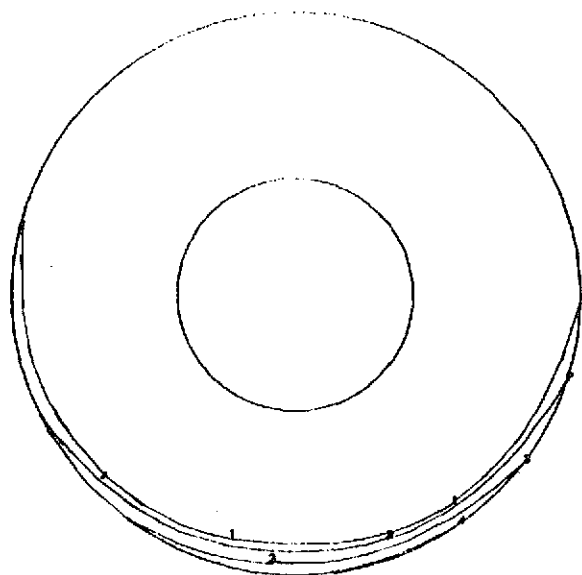
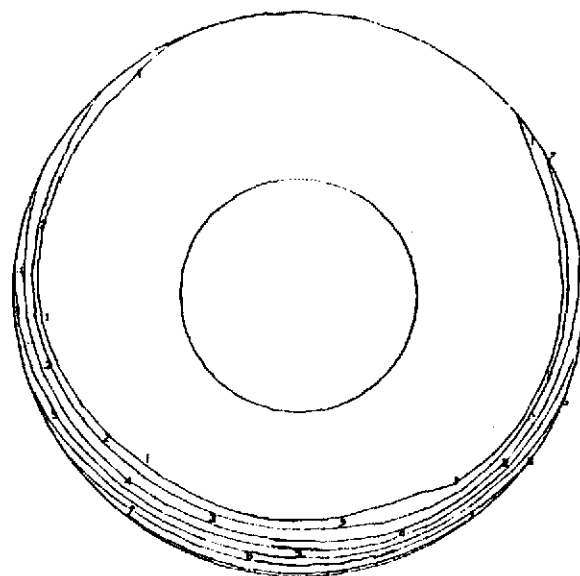


Figure 111.—QCSEE High Mach Number Inlet C4 Distortion and Recovery Performance $\alpha = 50^\circ$, $V = 140$ km/h (75 kn)



(a) $C_D^* = 0.755$

($M_{TH} = 0.508$, distortion = 4.4%, recovery = 0.9978)

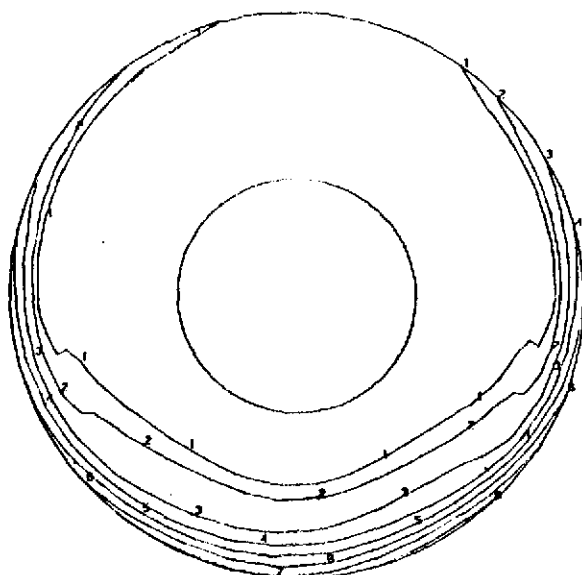


(b) $C_D^* = 0.948$

($M_{TH} = 0.764$, distortion = 10.6%, recovery = 0.9902)

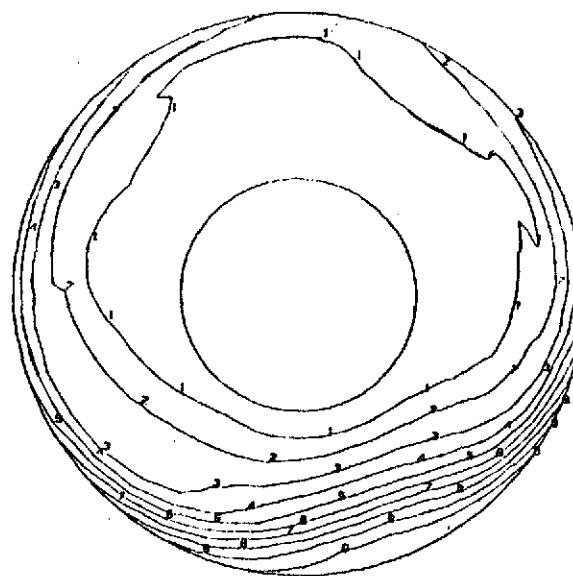
$P_T/P_{T REF}$

1	0.99	6	0.90
2	0.98	7	0.88
3	0.96	8	0.86
4	0.94	9	0.84
5	0.92	0	0.82



(c) $C_D^* = 0.962$

($M_{TH} = 0.798$, distortion = 12.9%, recovery = 0.9841)



(d) $C_D^* = 0.962$

($M_{TH} = 0.798$, distortion = 20.0%, recovery = 0.9673)

Figure 112.—Compressor Face Total Pressure Recovery Maps for QCSEE
High Mach Number Inlet C4— $\alpha = 50^\circ$, $V = 140$ km/h (75 kn)

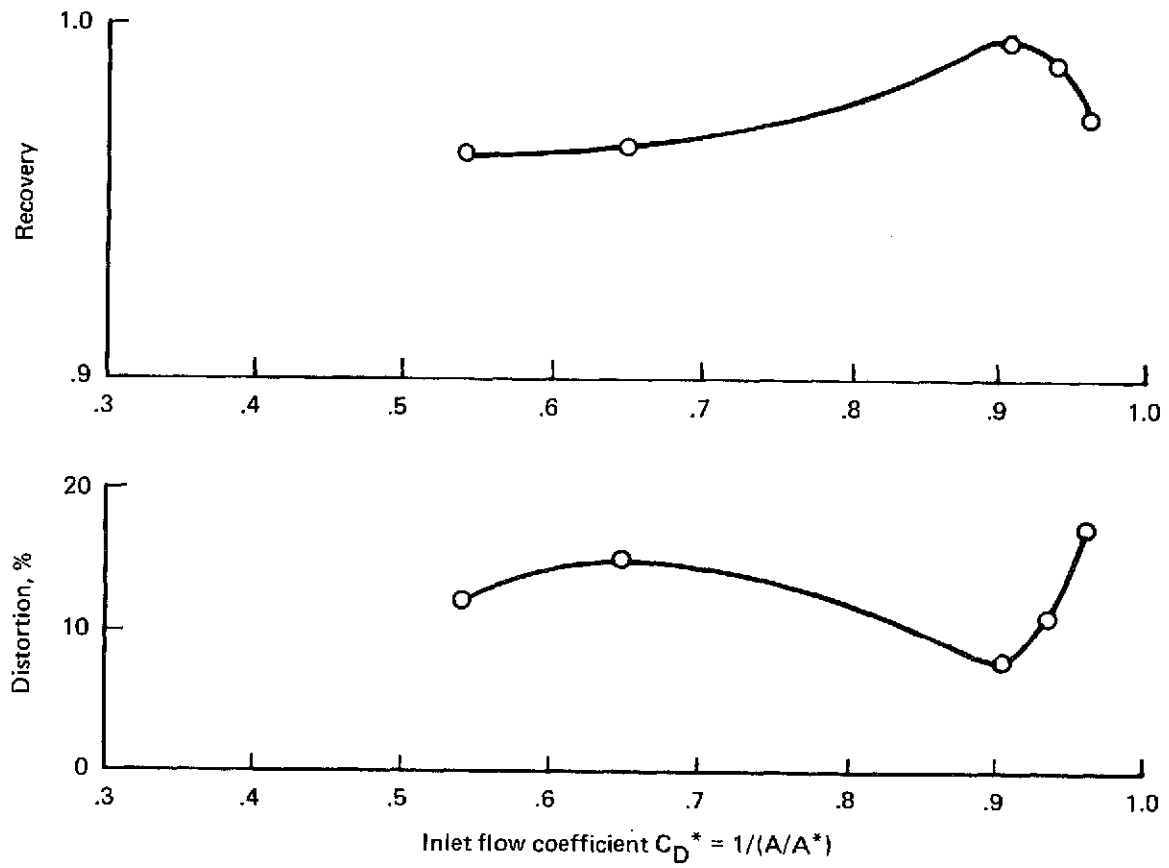


Figure 113.—QCSEE High Mach Number Inlet C5 Distortion and Recovery Performance
 $-\alpha = 50^\circ, V = 140 \text{ km/h (75 kn)}$

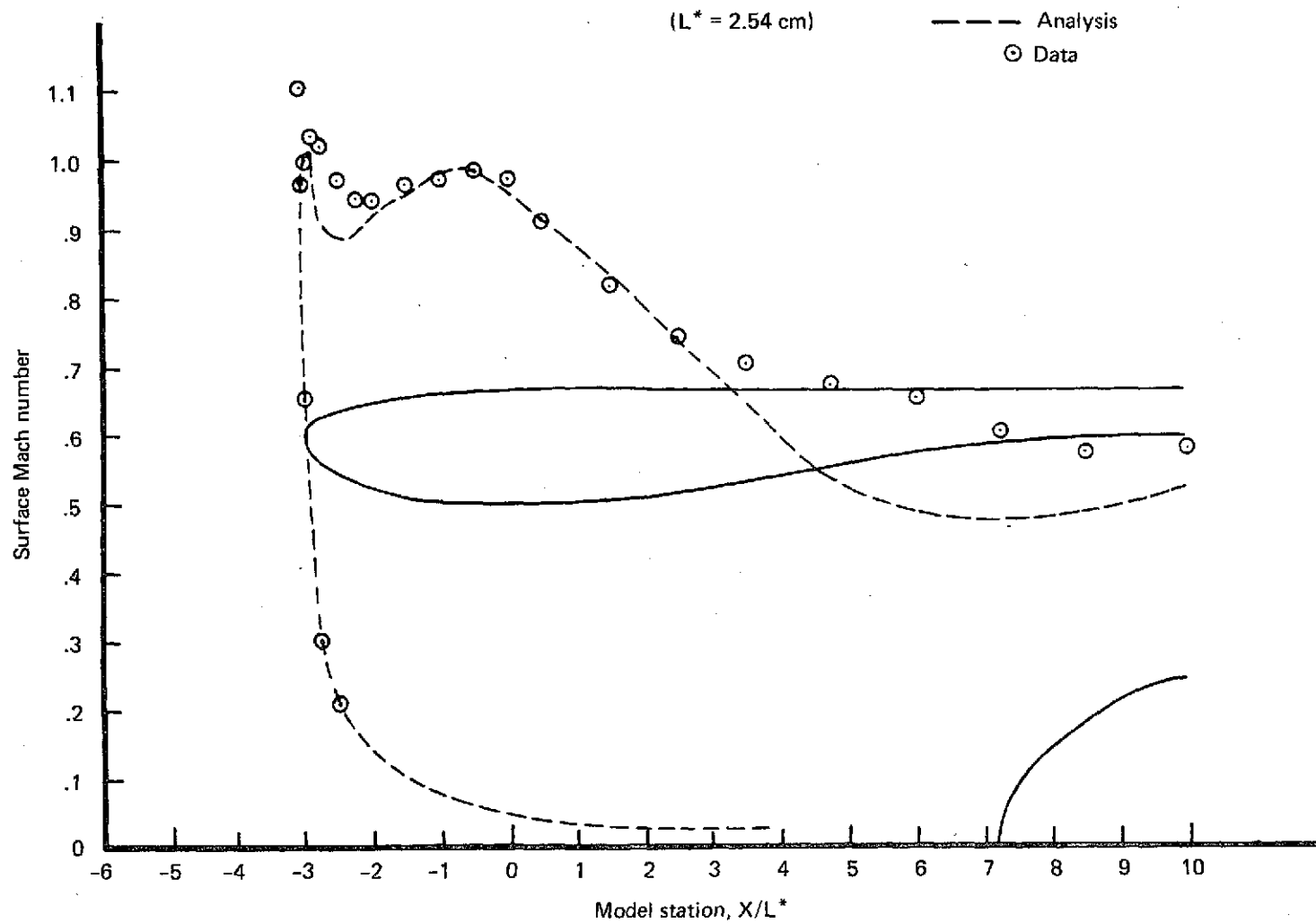


Figure 114.—Comparison of Analysis With Data for QCSEE High Mach Number
Inlet $C_1 - V = 0$, $C_D^* = 0.959$

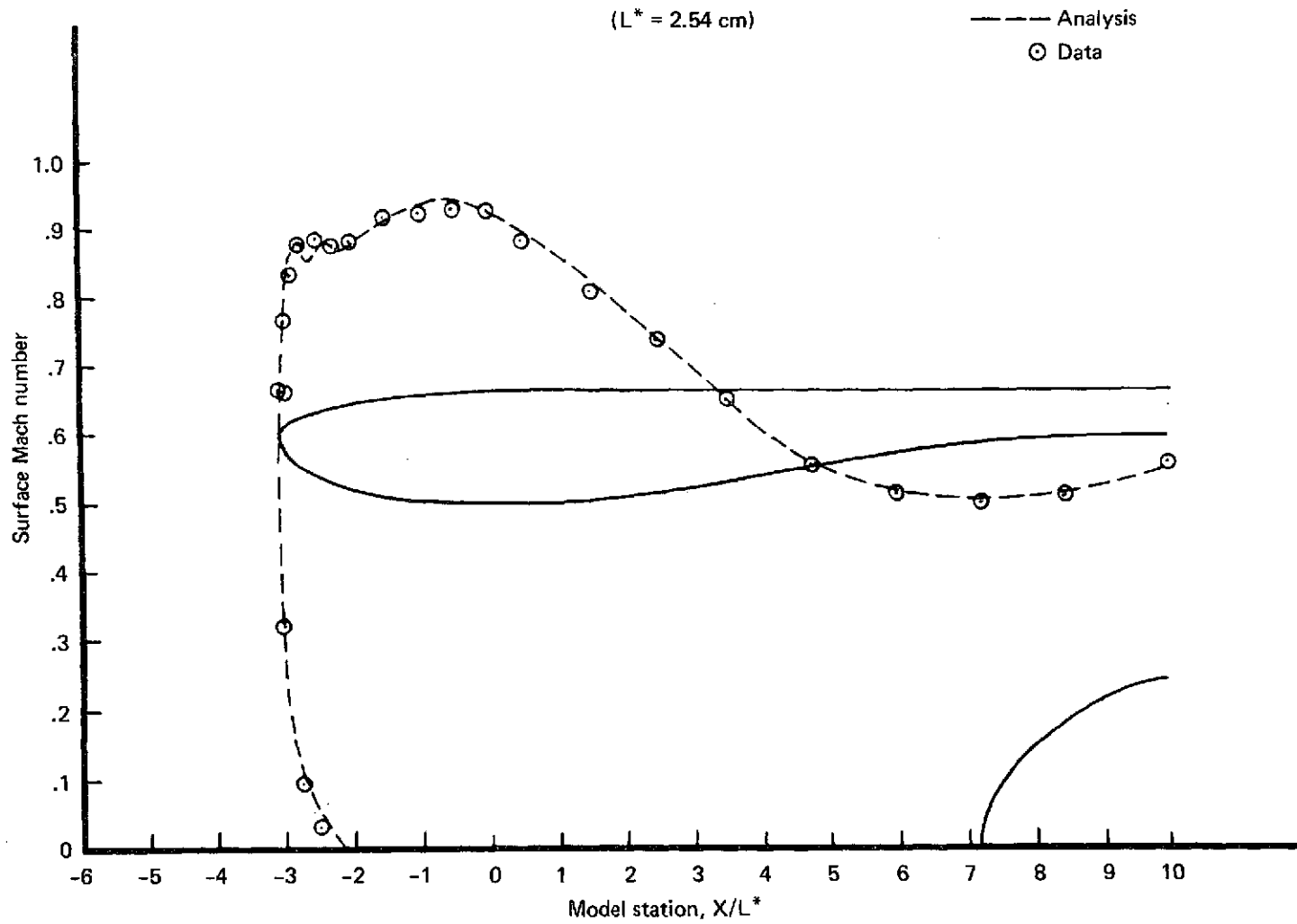


Figure 115.—Comparison of Analysis With Data for QCSEE High Mach Number Inlet C1— $V = 148 \text{ km/h (80 kn)}$, $C_D^* = 0.959$

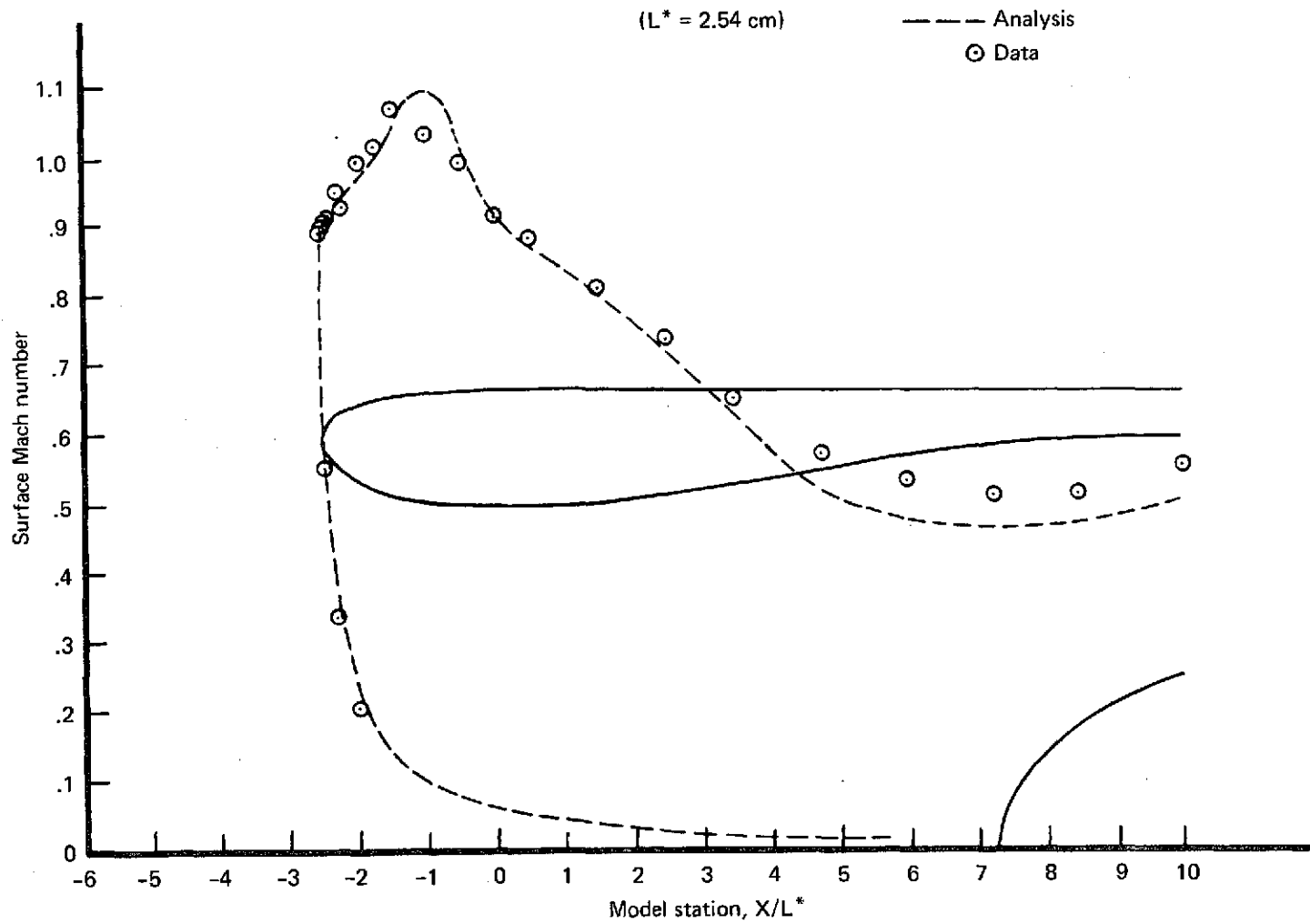


Figure 116.—Comparison of Analysis With Data for QCSEE High Mach Number
Inlet $C_4-V = 0$, $C_D^* = 0.959$

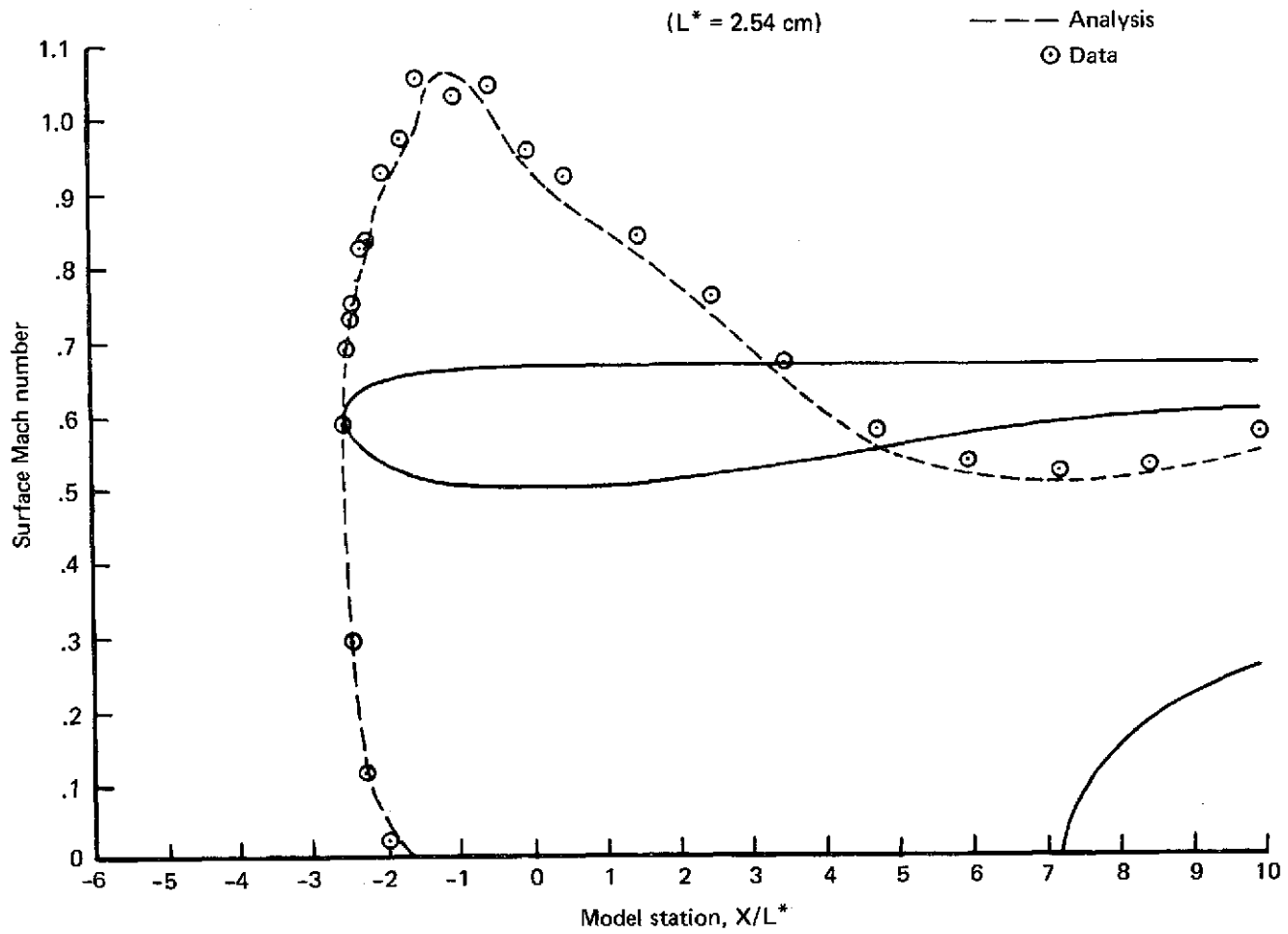


Figure 117.—Comparison of Analysis With Data for QCSEE High Mach Number Inlet C4-V = 148 km/h (80 kn), $C_D^* = 0.959$

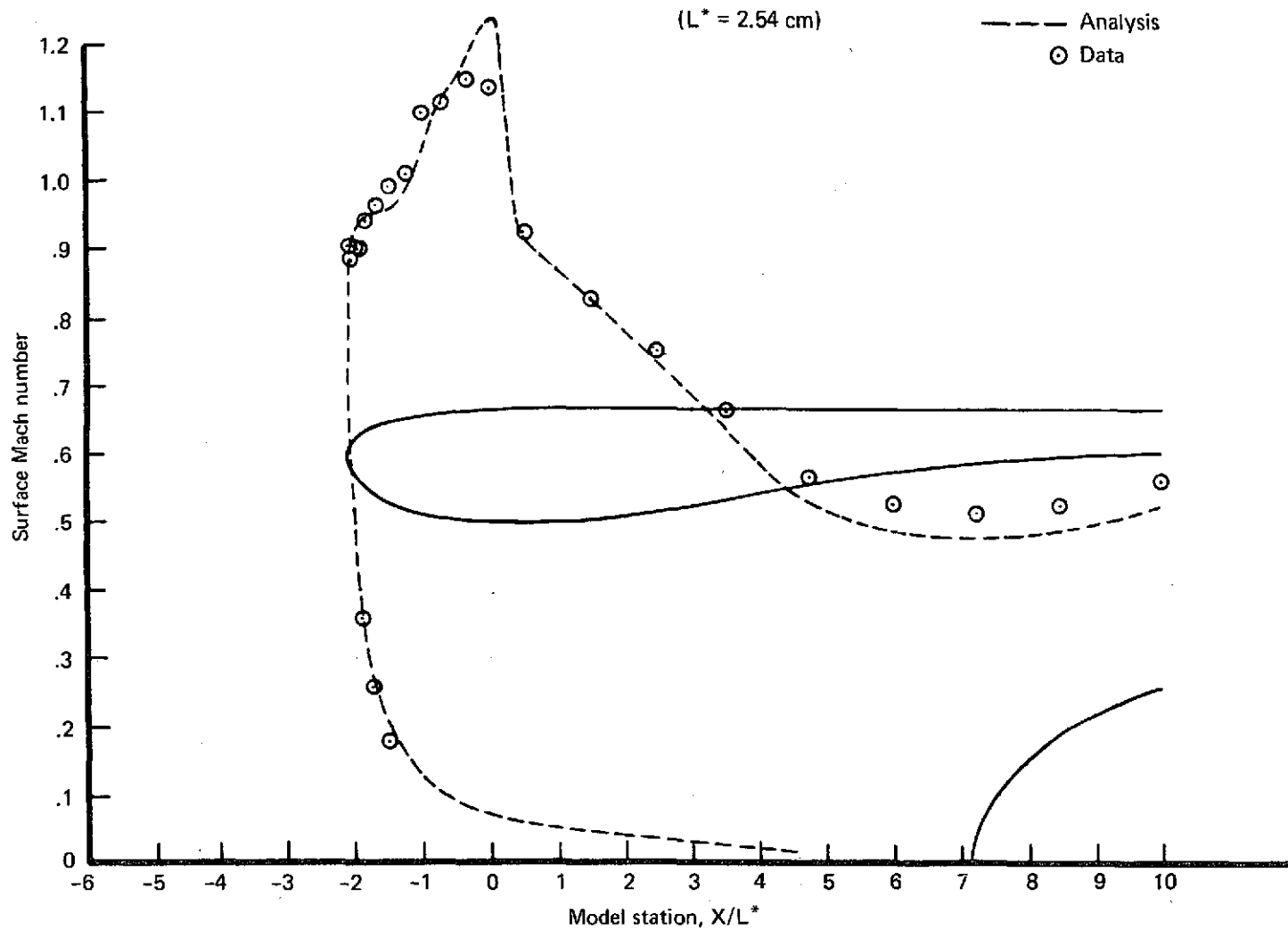


Figure 118.—Comparison of Analysis With Data for QCSEE High Mach Number.
 Inlet $C_5-V = 0$, $C_D^* = 0.959$

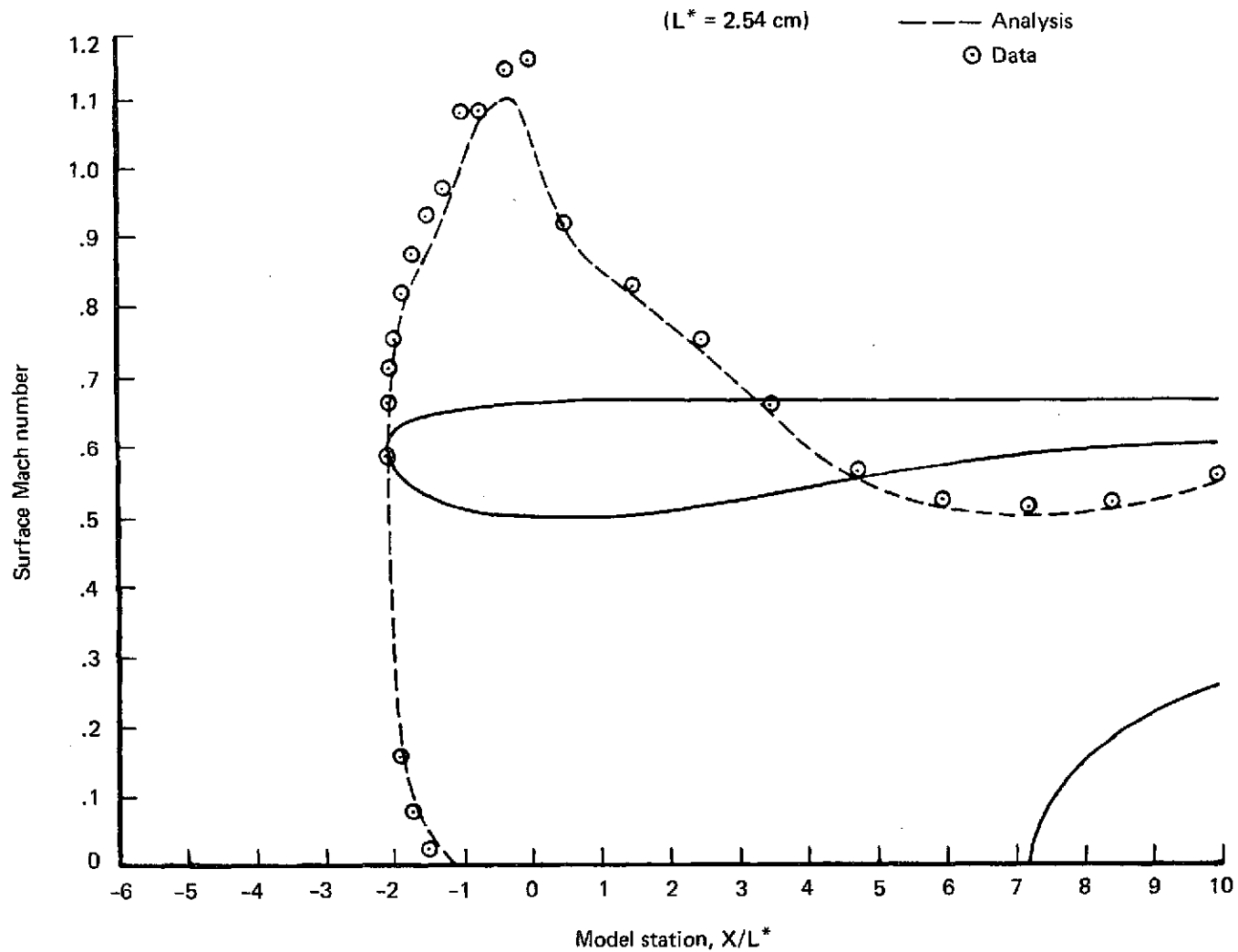


Figure 119.—Comparison of Analysis With Data for QCSEE High Mach Number Inlet C5— $V = 148 \text{ km/h}$ (80 kn), $C_D^* = 0.959$

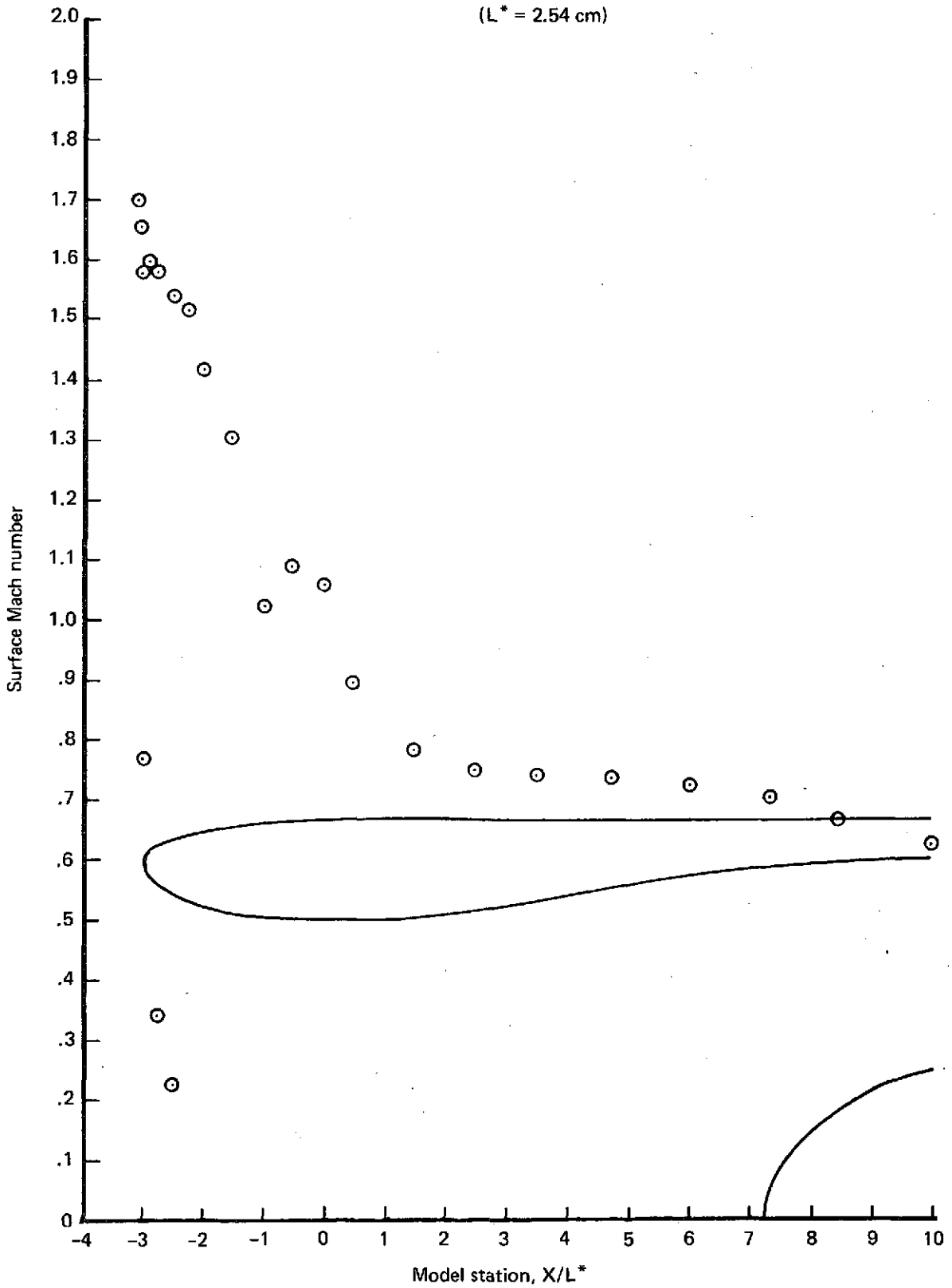


Figure 120.—Cowl Mach Number Distributions for QCSEE High Mach Number Inlet C1— $\alpha = 50^\circ$, $V = 148 \text{ km/h (80 kn)}$, $C_D^* = 0.963$

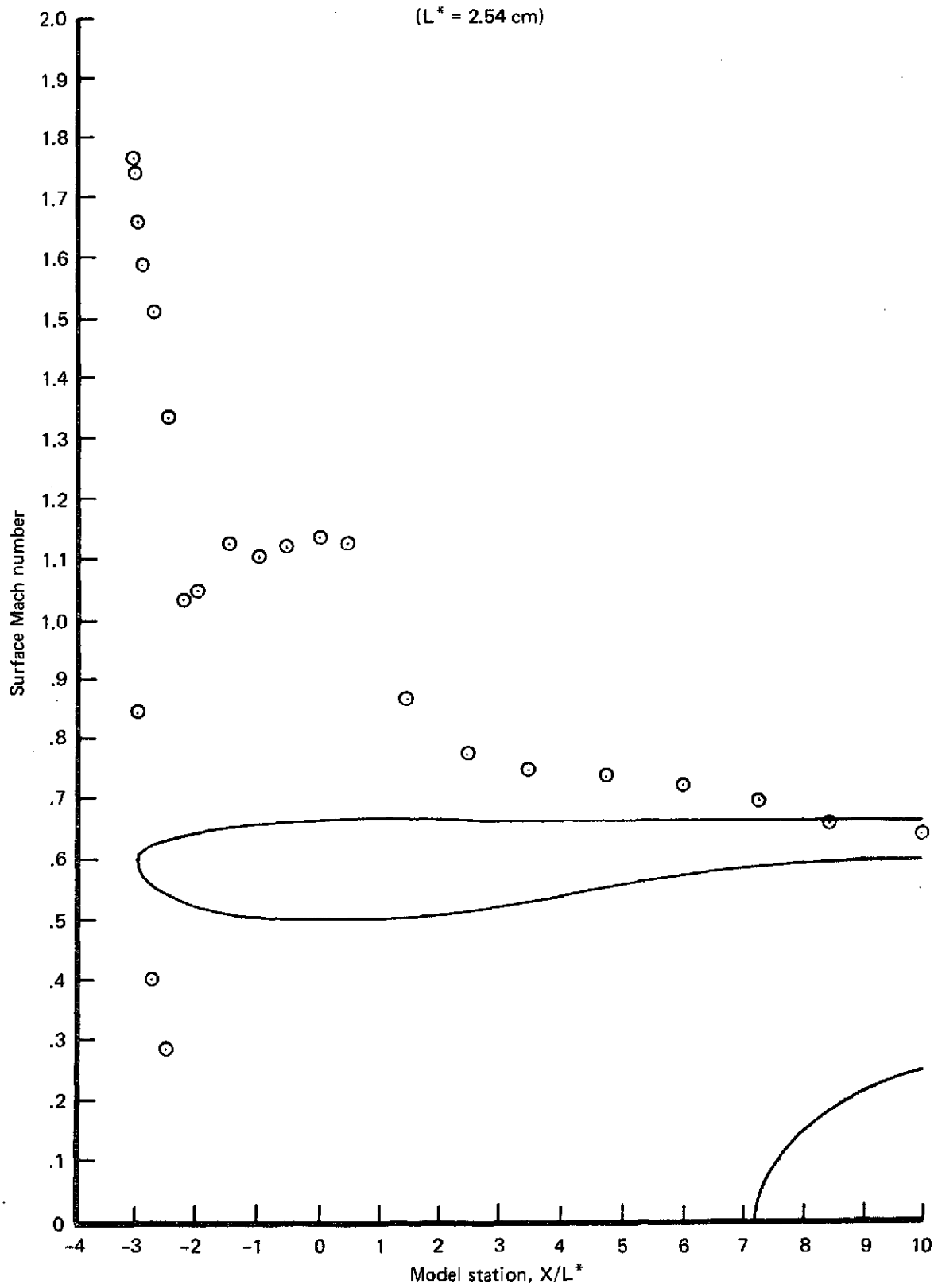


Figure 121.—Cowl Mach Number Distributions for QCSEE High Mach Number Inlet C1— $\alpha = 90^\circ$, $V = 65 \text{ km/h}$ (35 kn), $C_D^* = 0.963$

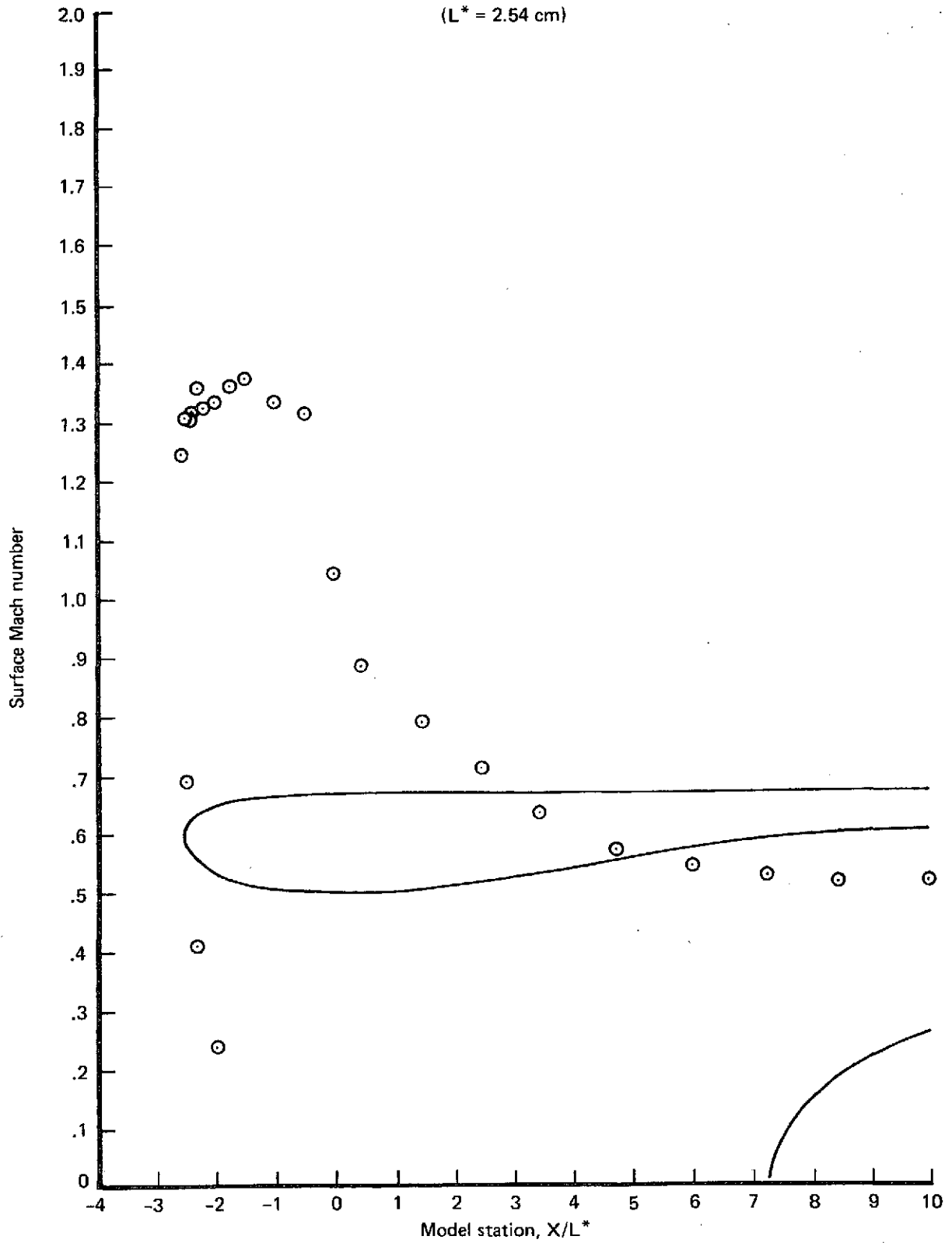


Figure 122.—Cowl Mach Number Distributions for QCSEE High Mach Number Inlet C4— $\alpha = 50^\circ$, $V = 148 \text{ km/h (80 kn)}$, $C_D^* = 0.941$

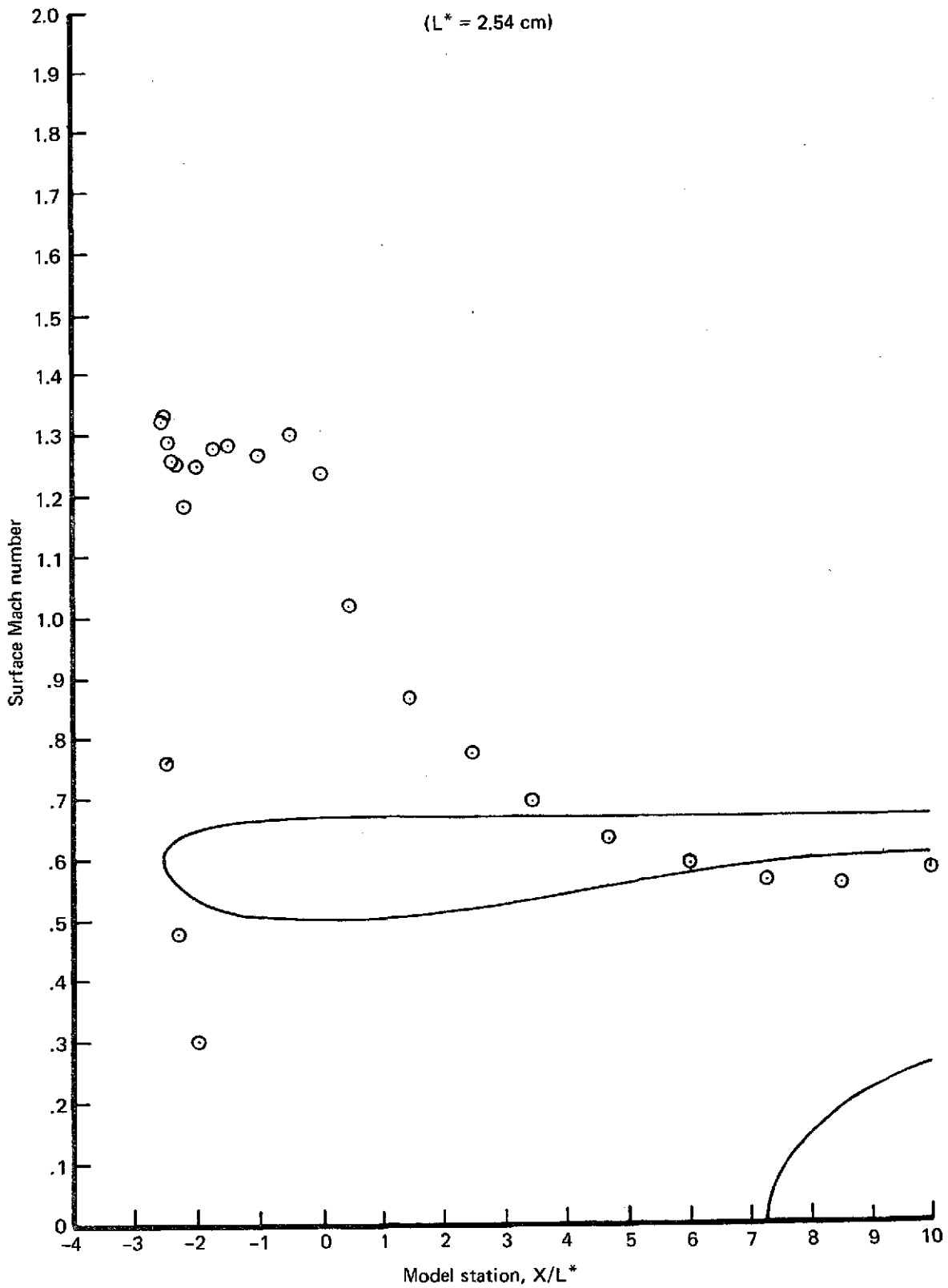


Figure 123.—Cowl Mach Number Distributions for QCSEE High Mach Number Inlet C4— $\alpha = 90^\circ$, $V = 65 \text{ km/h}$ (35 kn), $C_D^* = 0.963$

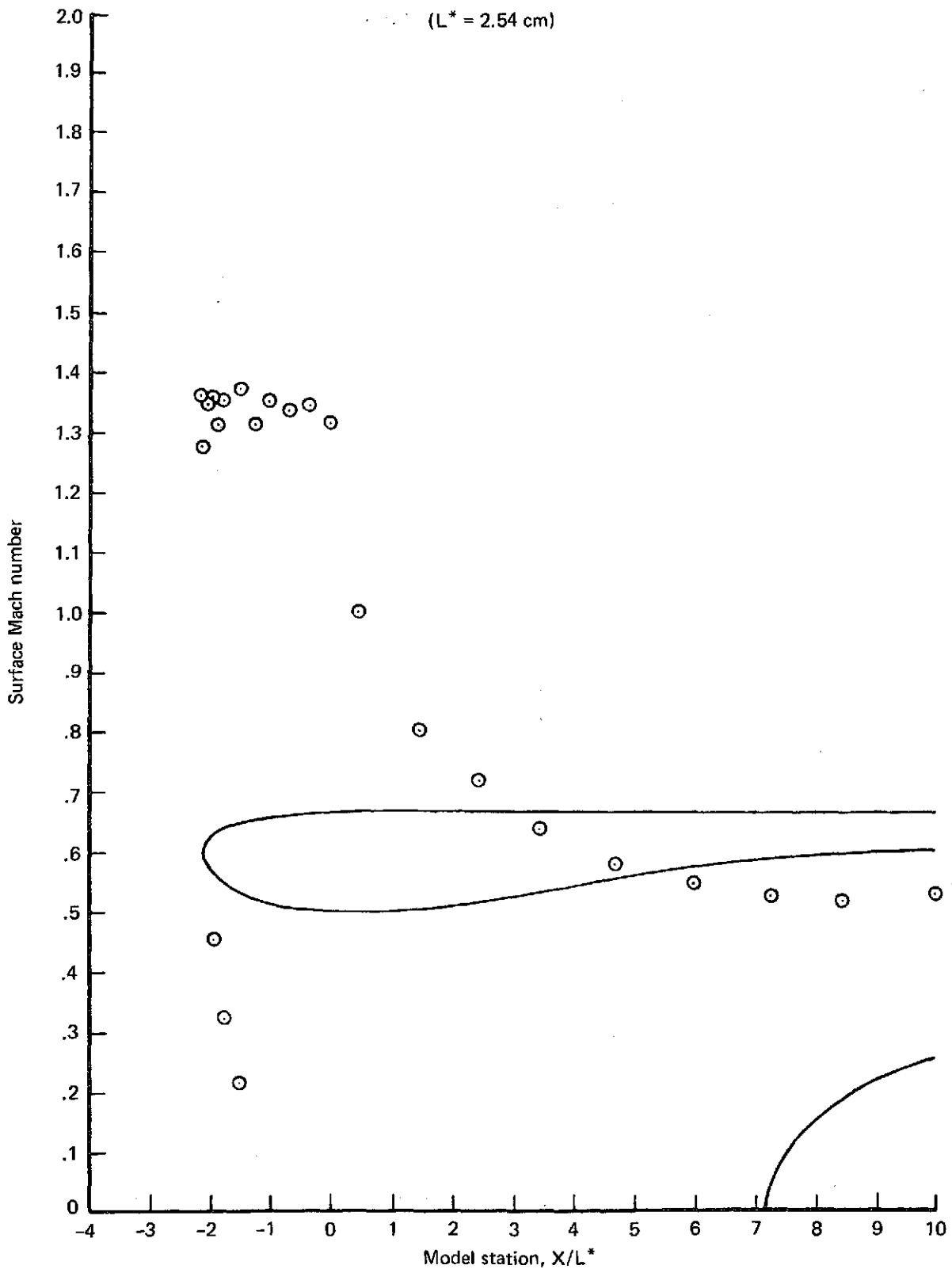


Figure 124.—Cowl Mach Number Distributions for QCSEE High Mach Number Inlet C5— $\alpha = 50^\circ$, $V = 148 \text{ km/h (80 kn)}$, $C_D^* = 0.931$

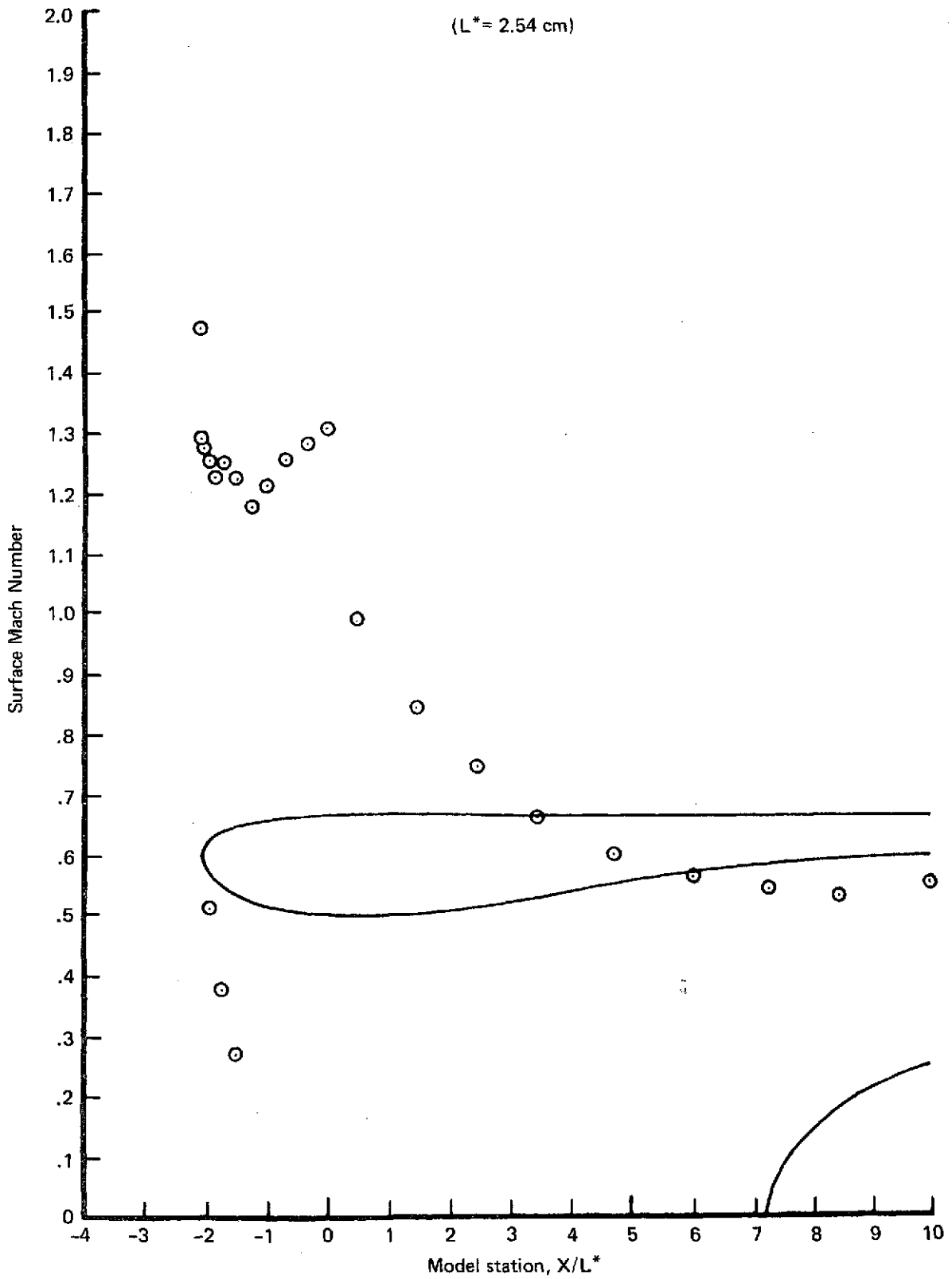


Figure 125.—Cowl Mach Number Distributions for QCSEE High Mach Number Inlet $C5-\alpha = 90^\circ$, $V = 65 \text{ km/h}$ (35 kn), $C_D^* = 0.946$

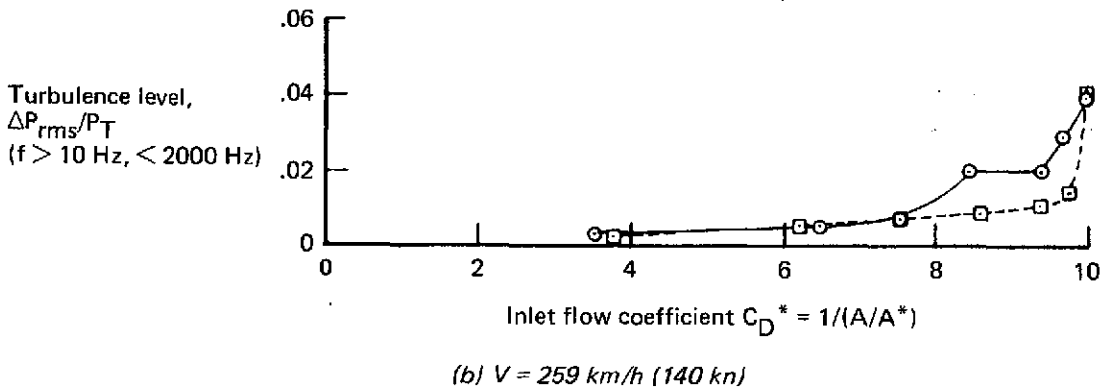
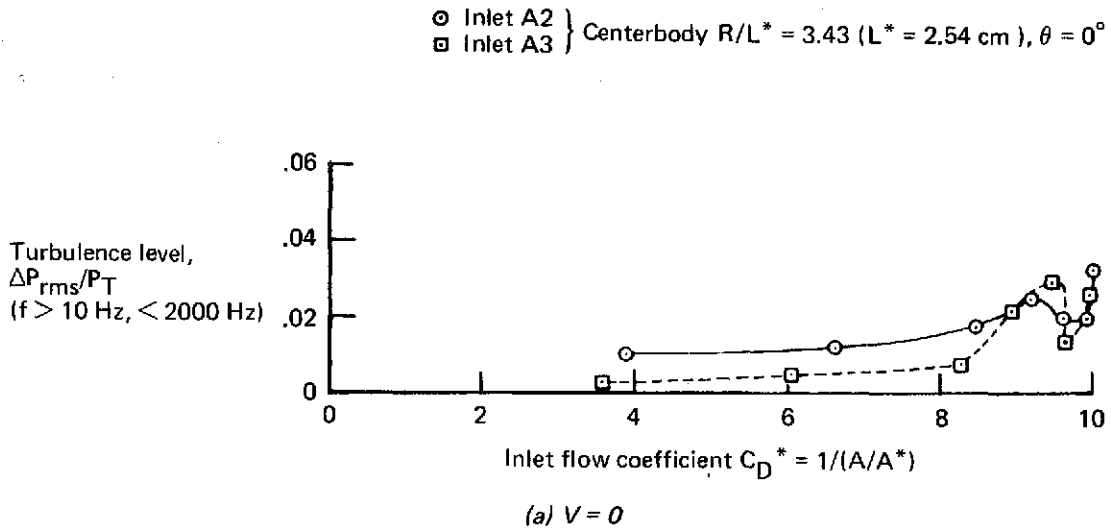


Figure 126.—Effect of C_D^* on ΔP_{rms} for Translating Centerbody Inlets A2 and A3 at Approach— $\alpha = 20^\circ$

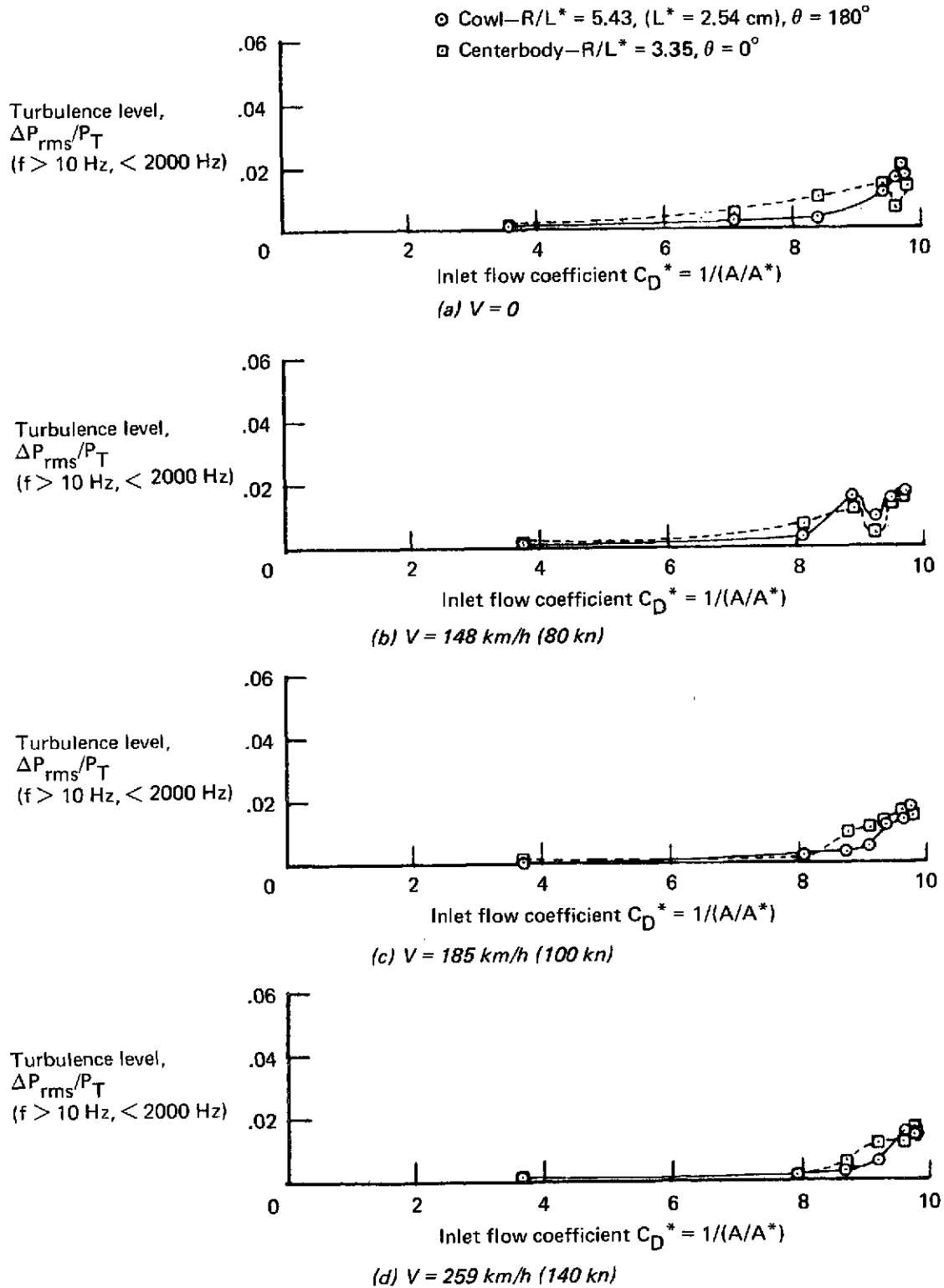
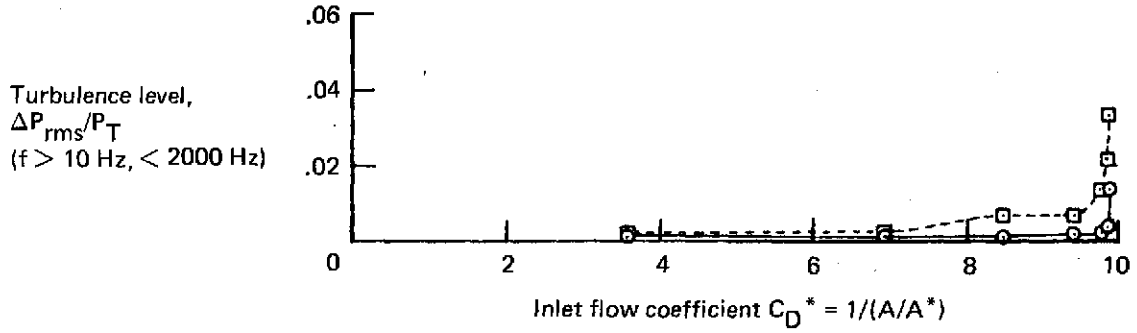
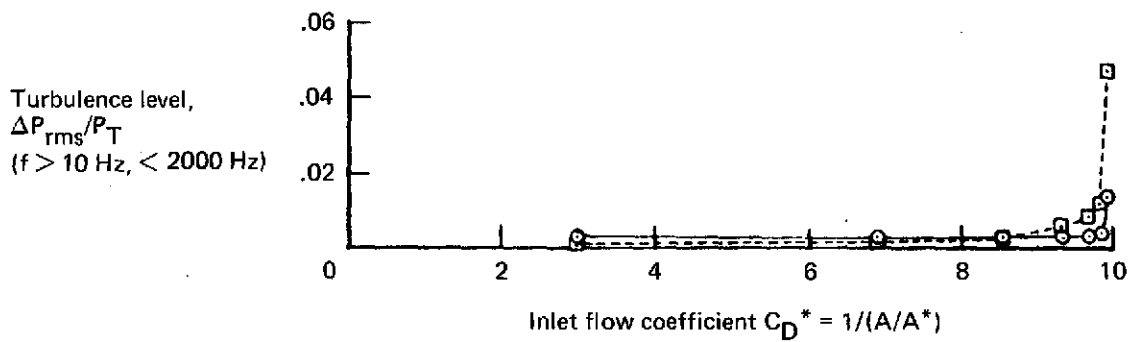


Figure 127.—Effect of C_D^* on ΔP_{rms} for Radial Vane Inlet B at Approach— $\alpha = 0^\circ$

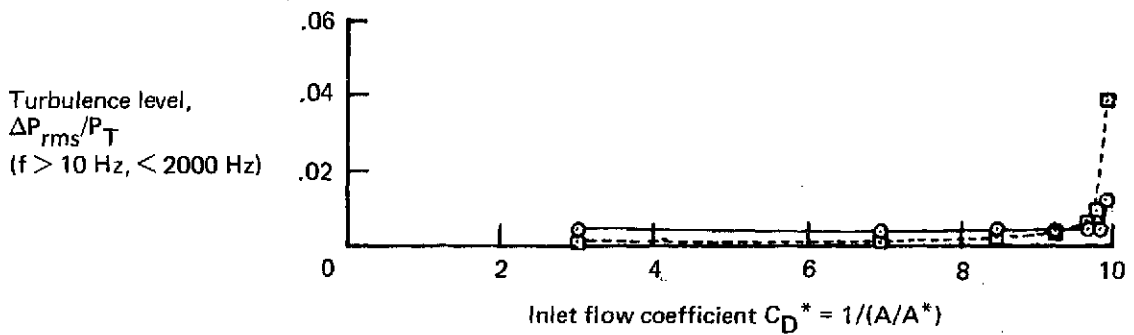
- Cowl— $R/L^* = 5.43$ ($L^* = 2.54$ cm), $\theta = 180^\circ$
- Centerbody— $R/L^* = 3.35$, $\theta = 0^\circ$



(a) $V = 0$



(b) $V = 259$ km/h (140 kn)



(c) $V = 315$ km/h (170 kn)

Figure 128.—Effect of C_D^* on ΔP_{rms} for Radial Vane Inlet B at Takeoff— $\alpha = 0^\circ$

- ⊙ Cowl— $R/L^* = 5.43$ ($L^* = 2.54$ cm), $\theta = 180^\circ$
- ⊠ Centerbody— $R/L^* = 3.35$, $\theta = 0^\circ$

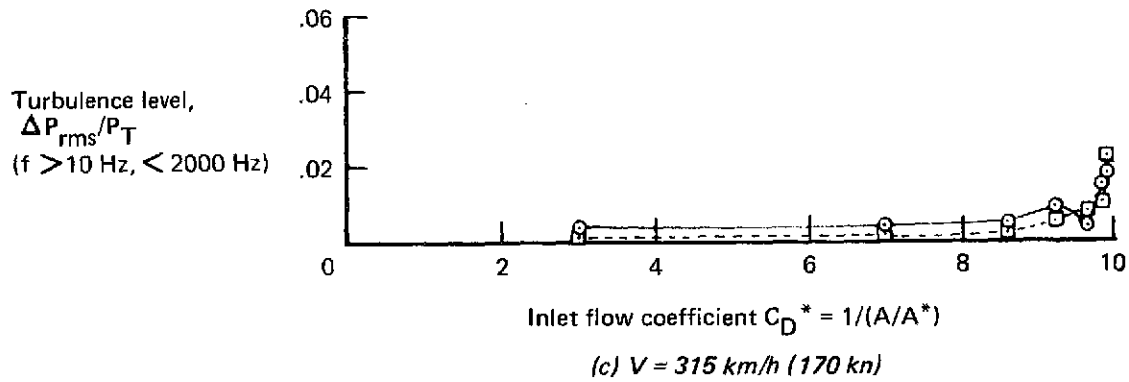
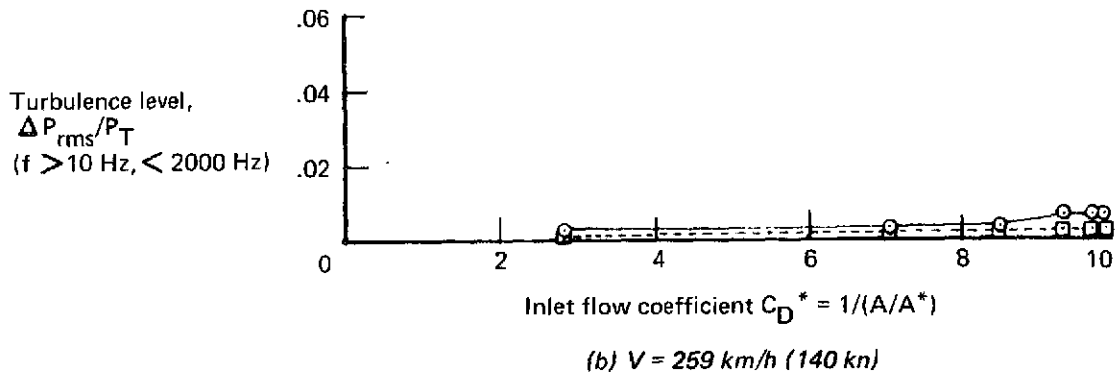
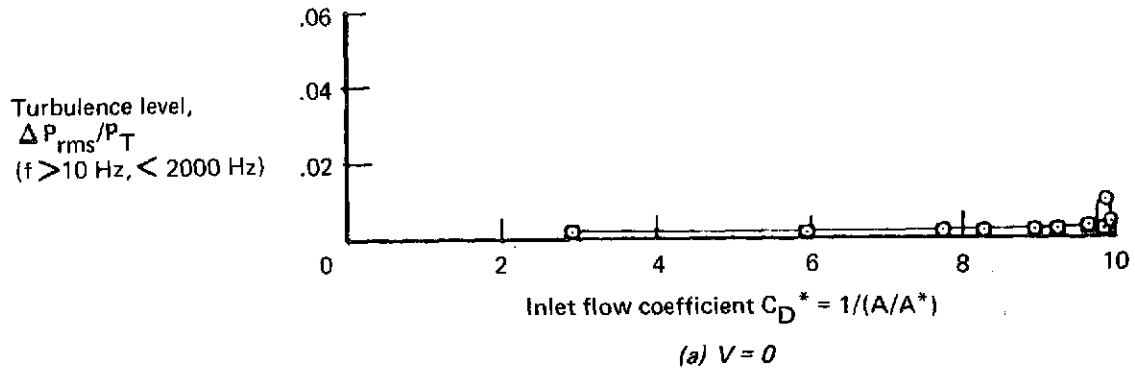
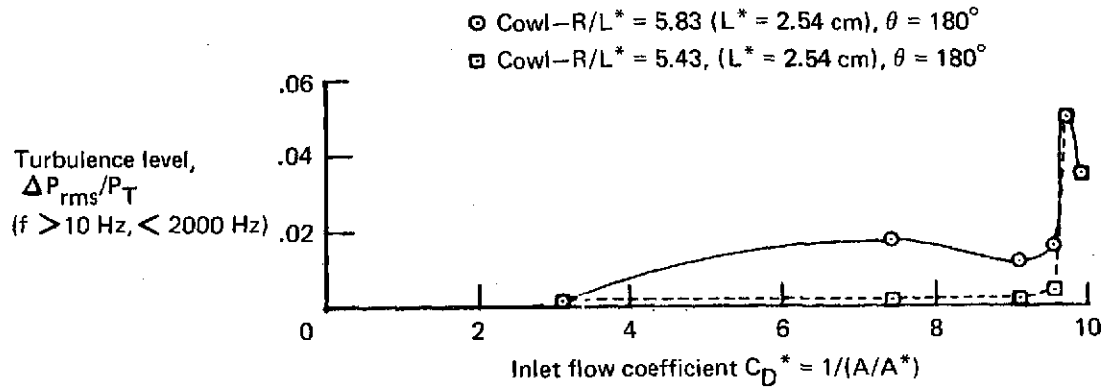
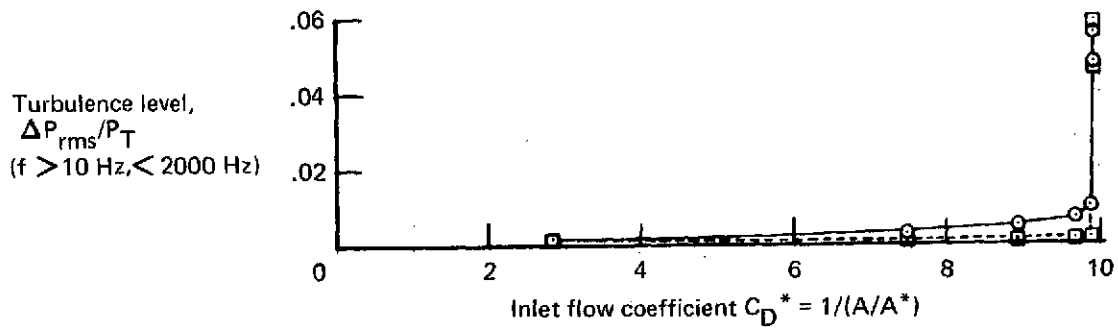


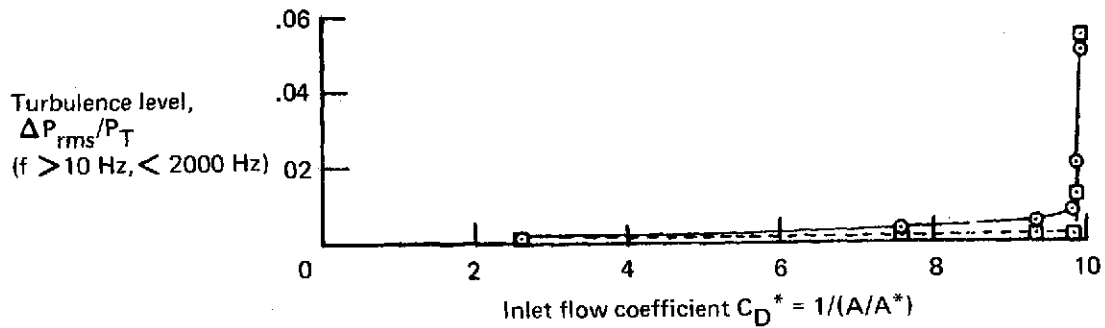
Figure 129.—Effect of C_D^* on ΔP_{rms} for Radial Vane Inlet B at Takeoff— $\alpha = 20^\circ$



(a) $V = 0$



(b) $V = 148 \text{ km/h (80 kn)}$



(c) $V = 315 \text{ km/h (170 kn)}$

Figure 130.—Effect of C_D^* on ΔP_{rms} for QCSEE High Mach Number Inlet C1— $\alpha = 0^\circ$

Table 1.—Translating Centerbody Inlet A Coordinates and Centerbody Translations

Cowl			Centerbody—A1 approach				
X/L*	R/L*	Remarks	X/L*	R/L*	Remarks		
4.474	7.000	External cowl lip	-4.290	0.000	Nose		
3.817	6.995		-4.096	0.519			
3.161	6.980		-3.417	1.202			
2.504	6.954		-2.525	1.914			
1.848	6.917		-1.850	2.312			
1.190	6.867		-1.360	2.520			
-0.534	6.801		-0.854	2.670			
-0.123	6.716		-0.422	2.743			
-0.780	6.602		0.000	2.767			
-1.108	6.529		Hilite	0.450		2.723	Approach throat
-1.436	6.439	0.900		2.642			
-1.765	6.316	1.350		2.563			
-1.962	6.203	1.800		2.496			
-2.027	6.145	2.250		2.439			
-2.093	6.005	2.700		2.383			
-2.051	5.848	3.150		2.339			
-2.009	5.776	3.700		2.287			
-1.967	5.721	6.671		2.287			
-1.926	5.674	10.186		2.287	Compressor face		
-1.800	5.565	Internal cowl lip					
-1.674	5.483						
-1.465	5.381						
-1.256	5.307						
-1.047	5.254						
-0.837	5.216						
-0.628	5.191						
-0.419	5.156						
-0.209	5.169						
0.000	5.168				Min cowl dia		
0.450	5.185						
0.900	5.255						
1.350	5.341						
1.800	5.432						
2.250	5.518						
2.700	5.592						
3.150	5.661						
4.162	5.798						
5.175	5.902	Cowl diffuser					
6.187	5.975						
7.200	6.015						
7.847	6.018						
10.186	6.018						
					Compressor face		

Condition	Centerbody translation
A1 takeoff	$X/L^* = X/L^*_{A1 APP} + 3.85$
A2 approach	$X/L^* = X/L^*_{A1 APP} + 1.00$
A3 approach	$X/L^* = X/L^*_{A1 APP} + 1.50$

Internal lip contour equation: $(X/a)^{2.5} + (R/b)^{1.8} = 1$ $a/b = 2.5$ $(a/L^*) = 2.093$ $(b/L^*) = 0.837$
External lip contour equation: $(X/a)^2 + (R/b)^2 = 1$ $a/b = 6.6$ $(a/L^*) = 6.567$ $(b/L^*) = 0.995$
Contraction ratio: $100 (A_{HI}/A_{MIN Cowl} - 1) = 35\%$

Note: $L^* = 2.54$

Table 2.—Translating Centerbody Inlet A Cross-Sectional Areas

Inlet	Hilite area cm ² (in ²)	Throat area cm ² (in ²)	Compressor face area cm ² (in ²)
A1 approach	730.90 (113.28)	386.13 (59.85)	628.03 (97.35)
A2 approach	730.90 (113.28)	390.49 (60.53)	628.03 (97.35)
A3 approach	730.90 (113.28)	401.19 (62.18)	628.03 (97.35)
A1 takeoff	730.90 (113.28)	482.00 (74.71)	628.03 (97.35)

Table 3.—Translating Centerbody Inlet A1 Static Pressure Taps
(a) Cowl Taps

Tap no.	Radius, R/L*	Axial dist from model throat—approach, X_T/L^*	Axial dist from comp face—approach, $X_{C APP}/L^*$	Surface dist from cowl hilite, S_H/L^*	Circumferential position, $(\theta),^\circ$	Remarks	Axial dist from comp face, takeoff, $X_{C TO}/L^*$
1	6.005	-1.4	12.279	-0.86	180	External cowl lip Hilite Internal cowl lip Cowl throat Cowl throat Diffuser (Part line) Cowl BL rake Compressor face (Nominal)	Same as approach
2		-1.7		-0.54	180		
3		2.015		-0.17	180		
4		-2.093		0	180		
5		-2.015		0.168	180		
6		-1.855		0.467	180		
7		-1.650		0.723	180		
8		-1.430		0.966	180		
9		-1.200		1.208	180		
10		-0.960		1.454	180		
11		-0.720		1.697	180		
12		-0.487		1.932	180		
13		-0.247		2.172	180		
14		5.168		0	10.186		
30	5.168	0	10.186	2.419	0		
15	6.018	0.230	7.786 (7.936)	2.649	180		
16		0.460		2.880	180		
17		0.690		3.112	180		
18		0.920		3.345	180		
19		1.150		3.579	180		
20		1.375		3.808	180		
21		1.605		4.043	180		
22		1.840		4.282	180		
23		2.400		4.851	180		
24		3.150		5.611	180		
25		4.150		6.620	180		
26		5.400		7.877	180		
27		7.900		10.379	180		
28		10.017		0.169	12.496	180	
29	6.108	10.017	0.169	12.496	270		
31	6.018	10.017	0.169	12.496	90		
32	6.018	10.017	0.169	12.496	90		

Notes:

$L^* = 2.54$ cm

Compressor face is 10.186 (X/L^*) downstream from cowl throat (min cowl radius), and is the location of P_{T2} probes.

Compressor face is 10.186 (X/L^*) downstream from centerbody max radius at approach and 6.336 (X/L^*) downstream from centerbody max radius at takeoff.

Table 3.—Concluded
(b) Centerbody Taps

Tap no.	Radius, R/L*	Axial dist from model throat—approach, X_T/L^*	Axial dist from comp face—approach, $X_{C APP}/L^*$	Surface dist from centerbody nose S_N/L^*	Circumferential position, (θ) , °	Remarks	Axial dist from comp face, takeoff, $X_{C TO}/L^*$	
1	0	-3.630	13.816	-1.189	180		9.966	
2		-4.290	14.476	0	—		10.626	
3		-3.630	13.816	1.189	0		9.966	
4		-2.680	12.866	2.449	0		9.016	
5		1.749	11.935	3.540	0		8.085	
6		-1.540	11.726	3.769	0		7.876	
7		-1.327	11.513	3.997	0		7.663	
8		-1.111	11.297	4.224	0		7.447	
9		-0.893	11.079	4.450	0		7.229	
10		-0.673	10.859	4.675	0		7.009	
11		-0.450	10.636	4.902	0		6.786	
12		-0.225	10.411	5.126	0		6.561	
13	2.767	0	10.186	5.352	0	6.336		
30	2.767	0	10.186	5.352	190	6.336		
14	2.642	0.250	9.936	5.603	0	Max R ↑ Diffuser Centerbody BL rake (-5°) ↓	6.086	
15		0.400	9.686	5.855	0		5.836	
16		0.700	9.486	6.057	0		5.636	
17		0.900	9.286	6.266	10		5.436	
18		1.150	9.036	6.515	0		5.186	
19		1.400	8.786	6.768	10		4.936	
20		1.650	8.536	7.021	0		4.686	
21		1.900	8.286	7.274	0		4.436	
22			2.150	8.036	7.525		0	4.186
23			2.400	7.786	7.777		10	3.936
24			3.000	7.186	8.381		0	3.336
25		2.287	5.281	4.905	10.664		0	1.055
26 App	2.287	7.281	2.905	12.664	0	—		
27 App	2.287	9.281	0.905	14.664	0	—		
28 App	2.287	10.131	0.055	15.515	13	—		
29 App	2.287	10.131	0.055	15.515	93	—		
31 App	2.287	10.131	0.055	15.515	195	—		
32 App	2.287	10.131	0.055	15.515	284	—		
28 T/O	2.287	—	—	—	0	Comp. face (Takeoff only)	-0.435	
29 T/O	2.287	—	—	—	80	—	-0.435	
31 T/O	2.287	—	—	—	180	—	-0.435	
32 T/O	2.287	—	—	—	270	—	-0.435	

Note: $L^* = 2.54$ cm

Table 4.—Radial Vane Inlet B Coordinates

Cowl			Centerbody		
X/L*	R/L*	Remarks	X/L*	R/L*	Remarks
4.816	7.200		-2.32	0	Nose
4.120	7.195		-2.00	0.680	
3.425	7.179		-1.50	1.100	
2.729	7.151		-1.00	1.370	
2.034	7.112		-0.50	1.570	
1.338	7.059		0	1.750	
0.642	6.989		0.50	1.890	
-0.053	6.899		1.00	2.010	
-0.749	6.778		1.50	2.120	
-1.097	6.701		2.00	2.200	
-1.444	6.605		2.50	2.270	
-1.792	6.475		3.00	2.285	Vane throat
-2.001	6.356		5.00	2.285	
-2.070	6.295		10.54	2.285	Compressor face
-2.140	6.146				
-2.097	5.985				
-2.054	5.912				
-2.012	5.855				
-1.969	5.808				
-1.840	5.696				
-1.712	5.612				
-1.498	5.507				
-1.284	5.432				
-1.070	5.378				
-0.856	5.339				
-0.642	5.314				
-0.428	5.299				
-0.214	5.292				
0.000	5.290	Throat			
1.000	5.310				
1.500	5.335				
2.000	5.370				
2.500	5.430				
3.000	5.520				
4.000	5.710	Cowl diffuser			
5.000	5.820				
6.000	5.900				
7.000	5.930				
8.000	5.960				
9.000	6.000				
10.090	6.016				
10.540	6.016	Compressor face			

Internal lip contour equation:
 $(X/a)^{2.5} + (R/b)^{1.8} = 1$ $a/b = 2.5$
 $(a/L^*) = 2.14$ $(b/L^*) = 0.856$

External lip contour equation:
 $(X/a)^2 + (R/b)^2 = 1.0$ $a/b = 6.6$
 $(a/L^*) = 6.956$ $(b/L^*) = 1.054$

Contraction ratio (cowl only):
 $100 (A_{HI}/A_{MIN \text{ cowl}} - 1) = 35\%$

Note: L* = 2.54 cm

Table 5.—Radial Vane Inlet B Static Pressure Taps
(a) Cowl Taps

Tap no.	Radius, R/L*	Axial dist from min cowl radius ref, X _R /L*	Axial dist from comp face, X _C /L*	Circumferential position (θ), °	Remarks	Surface dist from cowl hilite, S _H /L*	Axial dist from vane throat, X _{VT} /L*	Axial dist from hilite, X _{H1} /L*
1	6.146	-1.050	11.590	180	External cowl lip	-1.26	-5.14	1.090
2		-1.650	11.190	180		0.627		0.490
3		-2.071	12.611	180		-0.118		0.069
4		-2.140	12.680	180	Hilite	0		0
5		-2.071	12.611	180	Internal cowl lip	0.162		0.069
6		-1.908	12.448	180		0.468		0.232
7		-1.703	12.243	180		0.725		0.437
8		-1.473	12.013	180		0.976		0.667
9		-1.241	11.781	180		1.222		0.849
10	-0.996	11.536	180	1.475		1.144		
11	-0.748	11.288	180	1.726	1.392			
12	-0.498	11.038	180	1.977	1.642			
13	-0.252	10.792	180	2.223	1.888			
14	0	10.540	180	Min cowl dia	2.476	-3.00	2.140	
15	-0.334	10.206	180	(Part line)	2.809	2.474		
16	-0.668	9.872	180		3.143	2.808		
17	1.002	9.538	180		3.478	3.142		
18	1.336	9.204	180		3.812	3.476		
19	1.670	8.870	180		4.147	-1.33	3.810	
20	2.170	8.370	180		4.648	-0.83	4.310	
21	2.585	7.955	180		5.068	4.725		
22	5.520	3.000	7.540		180	Vane throat	5.489	0
34	5.520	3.000	7.540	0	Vane throat	5.489	0	5.140
23	3.170	7.370	180	Cowl BL rake (175°)	5.662	0.17	5.310	
24	3.670	6.870	180		6.172	0.67	5.810	
25	4.170	6.370	180	Diffuser	6.678	6.210		
26	4.670	5.870	180		7.182	1.67	6.810	
27	5.110	5.430	180		7.623	7.250		
28	5.550	4.990	180		8.065	2.55	7.690	
29	6.550	3.990	180		9.066	3.55	8.690	
30	7.550	2.990	180		10.068	4.55	9.690	
31	8.550	1.990	180		11.068	5.55	10.690	
32	6.017	10.540	0		180	13.058	7.54	12.680
33	6.017	10.540	0		270	13.058	7.54	12.680
35	6.017	10.540	0		0	13.058	7.54	12.680
36	6.017	10.540	0	90	13.058	7.54	12.680	

Note: L* = 2.54 cm

Table 5.—Concluded
(b) Centerbody taps

Tap no.	Radius, R/L*	Axial dist from min cowl radius ref, X _R /L*	Axial dist from comp face X _C /L*	Circumferential position (θ), °	Remarks	Surface dist from centerbody nose, S _N /L*	Axial dist from vane throat, X _{VT} /L*
1	0.680	-2.00	12.54	180	Centerbody nose	0.780	-5.00
2	0	-2.32	12.86	—		0	-5.32
3	0.680	-2.00	12.54	0		0.780	-5.00
4	1.370	-1.00	11.54	0		1.996	-4.00
5	1.750	0	10.54	0		3.068	-3.00
6	2.01	1.00	9.54	0		4.104	-2.00
7	2.120	1.50	9.04	0		4.614	-1.50
8	2.200	2.00	8.54	0		5.122	-1.00
9		2.25	8.29	0		5.374	-0.75
10	2.270	2.50	8.04	0		5.626	-0.50
11	2.285	3.00	7.54	0	6.126	0	
19	2.285	3.00	7.54	180	Vane throat	6.126	0
12	2.285	3.50	7.04	0		6.627	0.50
13	2.285	4.00	6.54	0		7.127	1.00
14	2.285	4.50	6.04	0		7.627	1.50
15	2.285	5.00	5.54	0		8.127	2.00
16	2.285	6.00	4.54	0		9.126	3.00
17	2.285	10.54	0	0	↑	13.667	7.54
18	2.285	10.54	0	90	Compressor face	13.667	7.54
20	2.285	10.54	0	180		13.667	7.54
21	2.285	10.54	0	270	↓	13.667	7.54

Note: Takeoff locations same as approach

L* = 2.54 cm

Table 6.—Principal Geometric Characteristics of QCSEE Inlets C1 Through C5

Inlet	Internal lip			External lip		
	CR, %	a/b	Shape	FR	a/b	Shape
C1	45	3.0	$(R/a)^{2.2} + (Y/b)^{2.2} = 1$	0.902	6.60	$(X/a)^2 + (R/b)^2 = 1$
C2	45	3.0	$(R/a)^{2.2} + (Y/b)^{2.2} = 1$	0.902	4.55	Arbitrary
C2-A	45	3.0	$(R/a)^{2.2} + (Y/b)^{2.2} = 1$	0.902	4.55	Arbitrary
C3	42	3.0	$(R/a)^{2.2} + (Y/b)^{2.2} = 1$	0.894	4.17	Arbitrary
C4	45	2.5	$(R/a)^{2.7} + (Y/b)^{1.8} = 1$	0.902	4.55	Arbitrary
C5	46	2.0	$(R/a)^2 + (Y/b)^2 = 1$	0.906	4.15	Arbitrary

Notes:

Arbitrary shape means not represented by an equation.

C2-A is same as C2 but with hilite smoothed (C2 had a small ridge due to fabrication error).

Table 7.—QCSEE High Mach Number Inlet C Coordinates
(a) Inlet C1

Cowl					
X/L*	R/L*	Remarks	X/L*	R/L*	Remarks
1.244	6.679		2.0	5.104	
0.813	6.676		2.2	5.125	
0.382	6.666		2.4	5.148	
-0.049	6.652		2.6	5.173	
-0.480	6.625		2.8	5.200	
-0.911	6.592		3.0	5.229	
-1.342	6.548		3.2	5.260	
-1.773	6.492	External cowl lip	3.4	5.293	
-2.204	6.418		3.6	5.328	
-2.420	6.370		3.8	5.365	
-2.635	6.311		4.0	5.404	
-2.851	6.230		4.2	5.443	
-2.980	6.156		4.4	5.481	
-3.023	6.118		4.6	5.518	
-3.066	6.026	Hilite	4.8	5.553	
-3.035	5.846		5.0	5.588	
-3.005	5.780		5.2	5.620	
-2.913	5.656		5.4	5.652	
-2.759	5.527		5.6	5.682	Diffuser
-2.606	5.434		5.8	5.711	
-2.448	5.361	Internal cowl lip	6.0	5.739	
-2.146	5.251		6.2	5.765	
-1.840	5.171		6.4	5.790	
-1.553	5.112		6.6	5.814	
-1.226	5.068		6.8	5.836	
-0.920	5.038		7.0	5.857	
-0.613	5.018		7.2	5.877	
-0.307	5.007		7.4	5.896	
0	5.004	Throat	7.6	5.913	
0.200	5.005		7.8	5.929	
0.400	5.008	Diffuser	8.0	5.943	
0.600	5.013		8.2	5.957	
0.800	5.020		8.4	5.969	
1.000	5.029	Part line	8.6	5.979	
1.200	5.040		8.8	5.989	
1.400	5.053		9.0	5.997	
1.600	5.068		9.4	6.009	
1.800	5.085		10.0	6.018	Compressor face

Spinner		
X/L*	R/L*	Remarks
7.288	0	Nose
7.542	0.875	
8.051	1.482	
8.559	1.868	
9.068	2.156	
9.577	2.383	
9.763	2.455	
9.949	2.495	
10.000	2.500	Compressor face

Note: $L^* = 2.54$ cm

Table 7.—Continued
 (b) Inlets C2-A and C2

External lip		
X/L*	R/L*	Remarks
-3.066	6.026	Hilite
-3.040	6.130 (6.110)	
-3.000	6.202 (6.180)	
-2.900	6.309 (6.300)	
-2.800	6.382 (6.375)	
-2.600	6.471 (6.465)	
-2.400	6.525 (6.520)	
-2.200	6.559	
-2.000	6.585	
-1.800	6.607	
-1.600	6.625	
-1.400	6.639	
-1.200	6.650	
-1.000	6.658	
-0.800	6.664	
-0.600	6.669	
-0.400	6.673	
-0.200	6.677	
-0.100	6.679	





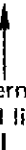

Notes:

Coordinates in parentheses are for inlet C2.

All C2 and C2-A coordinates are identical to C1 coordinates except as shown.

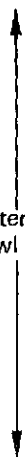
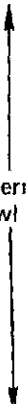
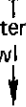
C-3

Table 7.—Continued
(c) Inlet C3

X/L*	R/L*	Remarks	X/L*	R/L*	Remarks
0	5.004	Throat	-2.011	6.547	 External cowl lip 
-0.288	5.007	 Internal cowl lip 	-1.811	6.576	
-0.575	5.017		-1.611	6.600	
-0.863	5.035		-1.411	6.620	
-1.151	5.064		-1.211	6.635	
-1.439	5.105		-1.011	6.647	
-1.726	5.161		-0.811	6.656	
-2.014	5.236		-0.611	6.663	
-2.302	5.339		-0.411	6.668	
-2.445	5.408		-0.211	6.673	
-2.589	5.494		-0.011	6.677	
-2.733	5.616		0.089	6.679	
-2.819	5.732				
-2.848	5.794				
-2.877	5.963	Hilite			
-2.851	6.055	 External cowl lip 			
-2.811	6.132				
-2.711	6.263				
-2.611	6.346				
-2.411	6.444				
-2.211	6.505				

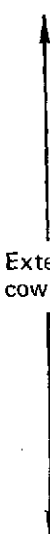

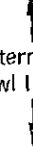
Note: C3 coordinates are same as C1 coordinates downstream of the throat.

Table 7.—Continued
(d) Inlet C4

X/L*	R/L*	Remarks	X/L*	R/L*	Remarks
0	5.004	Throat	-2.089	6.470	 External cowl lip
-0.256	5.005	 Internal cowl lip	-1.889	6.520	
-0.511	5.011		-1.689	6.559	
-0.767	5.026		-1.489	6.585	
-1.022	5.053		-1.289	6.607	
-1.278	5.095		-1.089	6.625	
-1.533	5.156		-0.889	6.639	
-1.789	5.244		-0.689	6.650	
-2.044	5.368		-0.489	6.658	
-2.197	5.470		-0.289	6.664	
-2.351	5.606		-0.089	6.669	
-2.402	5.665	-0.111	6.673		
-2.453	5.735	-0.311	6.677		
-2.504	5.826	-2.289	6.679		
-2.555	6.026	Hilite			
-2.529	6.143	 External cowl lip			
-2.489	6.215				
-2.389	6.320				
-2.289	6.388				

Note: C4 coordinates are same as C1 coordinates downstream of the throat.

Table 7.—Concluded
(e) Inlet C5

X/L*	R/L*	Remarks	X/L*	R/L*	Remarks
0	5.0040	Throat	-1.9944	6.2438	 External cowl lip
-0.2272	5.0101	 Internal cowl lip	-1.9142	6.3012	
-0.4518	5.0286		-1.8071	6.3562	
-0.6710	5.0590		-1.6733	6.4087	
-0.8824	5.1012		-1.5395	6.4501	
-1.0834	5.1544		-1.4058	6.4841	
-1.2717	5.2183		-1.2987	6.5076	
-1.4452	5.2919		-1.1648	6.5333	
-1.6017	5.3745		-0.9775	6.5645	
-1.7393	5.4651		-0.8706	6.5798	
-1.8566	5.5626		-0.7635	6.5941	
-1.9522	5.6658	-0.4959	6.6255		
-1.9915	5.7193	-0.2818	6.6466		
-2.0738	5.8848	-0.0678	6.6641		
-2.0984	5.9979	0.1464	6.6778		
-2.1014	6.0547	0.3604	6.6870		
-2.0998	6.0794	0.5744	6.6904		
-2.0907	6.1158	 External cowl lip			
-2.0800	6.1409				
-2.0614	6.1722				
-2.0212	6.2195				

Note: C5 coordinates are same as C1 coordinates downstream of the throat.

Table 8.—QCSEE High Mach Number Inlet C Static Pressure Taps
(a) Inlets C1, C2, and C2-A

Tap no.	X/L*	Remarks	Circumferential position (θ), ^o
1	-2.500	↑ External cowl lip	180
2	-2.750		180
3	-3.000	↓ Hilite	180
4	-3.066		
5	-3.050	↑	180
6	-3.000		180
7	-2.900	↑	180
8	-2.750		180
9	-2.500	Internal cowl lip	180
10	-2.250		180
11	-2.000	↓	180
12	-1.500		180
13	-1.000	↓	180
14	-0.500		180
15	0	Throat	180
16	0.500	↑	180
17	1.500		180
18	2.500	↑	180
19	3.500		180
20	4.750	↑	180
21	6.000		180
22	7.250	Diffuser	180
23	8.500	↑	180
24	10.000		180
25	10.000	Cowl	270
26	10.000	↓	0
27	10.000		Compressor face
28	10.000	↑	180
29	10.000		270
30	10.000	Spinner	0
31	10.000	↓	90

Note: L* = 2.54 cm

Table 8.—Continued
(b) Inlet C3

Tap no.	X/L*	Remarks	Circumferential position (θ), °
1	-2.400	↑ External cowl lip	180
2	-2.650		180
3	-2.800	↓ Hilite	180
4	-2.877		180
5	-2.860	↑	180
6	-2.810		180
7	-2.750	↓	180
8	-2.650		180
9	-2.500	Internal cowl lip	180
10	-2.250		180
11	-2.000	↓	180
12	-1.500		180
13	-1.000	↓	180
14	-0.500		180
15	0	Throat	180

Note: C3 uses same instrumentation as C1 except for new cowl static taps 1 through 15.

Table 8.—Continued
(c) Inlet C4

Tap no.	X/L*	Remarks	Circumferential position (θ), °
1	-2.000	↑ External cowl lip	180
2	-2.300		180
3	-2.475	↓ Hilite	180
4	-2.555		180
5	-2.500	↑	180
6	-2.450		180
7	-2.400	↓	180
8	-2.300		180
9	-2.200	Internal cowl lip	180
10	-2.000		180
11	-1.750	↓	180
12	-1.500		180
13	-1.000	↓	180
14	-0.500		180
15	0	Throat	180

Note: C4 uses same instrumentation as C1 except for new cowl static taps 1 through 15.

Table 8.—Concluded
(d) Inlet C5

Tap no.	X/L*	Remarks	Circumferential position (θ), °
1	-1.5000	↑	180
2	-1.7500	External cowl lip	180
3	-1.9000	↓	180
4	-2.1014	Hi-lite	180
5	-2.0800	↑	180
6	-2.0400		180
7	-1.9750		180
8	-1.8500		180
9	-1.7000	Internal cowl lip	180
10	-1.5000		180
11	-1.2500		180
12	-1.0000		180
13	-0.7000		180
14	-0.3500	↓	180
15	0	Throat	180

Note: C5 uses same instrumentation as C1 except for new cowl static taps 1 through 15.

Table 9.—Microphone Locations Relative to Inlet Entrance Center

Microphone location	Distance r, cm (in)	Angle ϕ , °
01	315 (124.0)	25
02	188 (74.0)	45
03	138 (54.5)	74
04	133 (52.5)	90
05F	255 (100.5)	2
05S	83 (32.5)	68
201	343 (135.0)	26
202	191 (75.0)	45
203	142 (56.0)	70
204	133 (52.5)	92
205	168 (66.0)	2

Table 10.—Translating Centerbody Inlet A1 Operating Characteristics at Takeoff

α , °	V km/h (kn)	Recovery at knee	Distortion at knee, %	Inlet airflow	$\overline{\Delta\text{SPL}}$, dB	C_D^*	Inlet operation
0	0	0.99	10	Stable	16	0.93	Good
0	259 (140)	0.99	10	Stable	24	0.94	Good
0	306 (165)	0.99	10	Stable	16	0.92	Good
20	259 (140)	0.99	10	Stable	10	0.92	Good
20	306 (165)	0.99	10	Stable	19	0.94	Good
35	148 (80)	0.99	10	Stable	—	0.95	Good
90	65 (35)	0.99	14	Stable	—	0.93	Marginal

Notes:

$\overline{\Delta\text{SPL}}$ is the noise reduction, in dB, at the knee from the biggest observed SPL at lower airflow for 3 kHz; based on 4-microphone average; not available for $\alpha > 20^\circ$.

C_D^* is the inlet flow coefficient—ratio of actual inlet airflow to maximum airflow, one-dimensional choke, at the throat: $C_D^* = 1/(A/A^*)$.

C_D^* is chosen where recovery ≥ 0.98 and/or distortion $\leq 10\%$.

*Table 11.—Translating Centerbody Inlet A1 Airflow Characteristics at Takeoff—
 $\alpha = 90^\circ$, $V = 65 \text{ km/h (35 kn)}$*

C_D^*	Boundary layer separation			Inlet airflow (on-line observation)
	Hilite	Cowl diffuser	Centerbody diffuser	
0.284	Yes	Yes	No	Stable
0.572	Yes	No	No	Stable
0.657	Yes	No	No	Stable
0.784	No	No	No	Stable
0.872	No	No	No	Fairly stable
0.928	No	No	No	Fairly stable
0.966	No	No	No	Stable
0.966	No	No	Yes	Stable

Table 12.—Translating Centerbody Inlet A1 Operating Characteristics at Approach

$\alpha, ^\circ$	$V, \text{ km/h (kn)}$	Recovery at knee	Distortion at knee, %	Inlet airflow	$\overline{\Delta\text{SPL}}, \text{ dB}$	C_D^*	Inlet operation
0	0	0.97	10	Unstable	13	0.910	Marginal
0	148 (80)	0.98	5	Stable	24	0.990	Good
0	185 (100)	0.98	9	Stable	30	0.975	Good
0	259 (140)	0.98	10	Stable	26	0.970	Good
20	185 (100)	1.00	3	Unstable above $C_D^* = 0.8$	1	0.800	Poor
20	259 (140)	0.98	10	Unstable and separated	2	0.780	Poor
35	148 (80)	0.97	10	Unstable and separated	—	0.740	Poor
35	185 (100)	0.97	10	Unstable and separated	—	0.640	Poor

See notes for table 10.

Table 13.—Translating Centerbody Inlets A2 and A3 Operating Characteristics at Approach

(a) Inlet A2

$\alpha, ^\circ$	V, km/h (kn)	Recovery at knee	Distortion at knee, %	Inlet airflow	$\overline{\Delta SPL}$, dB	C_D^*	Inlet operation
20	0	0.98	10	Unstable, low airflow	20	0.940	Marginal
20	185 (100)	0.97	10	Stable	30	0.990	Good
20	259 (140)	0.98	10	Unstable, low airflow	22	0.975	Good
35	148 (80)	0.98	10	Unstable, low airflow	—	0.975	Marginal
35	185 (100)	0.97	11	Unstable, low airflow	—	0.710	Poor

(b) Inlet A3

$\alpha, ^\circ$	V km/h (kn)	Recovery at knee	Distortion at knee, %	Inlet airflow	$\overline{\Delta SPL}$, dB	C_D^*	Inlet operation
20	0	0.970	10	Unstable, low airflow	24	0.980	Marginal
20	185 (100)	0.970	10	Stable	32 +	0.990	Good
20	259 (140)	0.980	10	Stable	29 +	0.980	Good
35	148 (80)	0.980	10	Unstable, low airflow	—	0.775	Marginal
35	185 (100)	0.975	10	Stable	—	0.700	Poor

See notes for table 10.

Table 14.—Radial Vane Inlet B Operating Characteristics

(a) Takeoff

$\alpha, ^\circ$	V, km/h (kn)	Recovery at knee	Distortion at knee, %	Inlet airflow	$\overline{\Delta\text{SPL}}, \text{dB}$	C_D^*	Inlet operation
0	0	0.980	8	Stable	24	0.980	Good
0	148 (80)	0.980	10	Stable	Lost	0.985	Good
0	259 (140)	0.990	10	Stable	29 +	0.990	Good
0	315 (170)	0.990	7	Stable	24 +	0.985	Good
20	259 (140)	0.990	10	Stable	30 +	0.985	Good
20	315 (170)	0.990	10	Stable	20 +	0.970	Good
35	148 (80)	0.990	10	Stable	—	0.975	Good
90	65 (35)	0.985	10	Stable	—	0.885	Good

(b) Approach

$\alpha, ^\circ$	V, km/h (kn)	Recovery at knee	Distortion at knee, %	Inlet airflow	$\overline{\Delta\text{SPL}}, \text{dB}$	C_D^*	Inlet operation
0	0	0.97	9	Stable	11	0.950	Marginal
0	148 (80)	0.97	8	Stable	12	0.940	Marginal
0	185 (100)	0.97	9	Stable	3*	0.940	Marginal
0	259 (140)	0.97	8	Stable	9	0.940	Marginal
20	185 (100)	0.97	9	Stable	10	0.945	Marginal
20	259 (140)	0.97	10	Stable	11	0.945	Marginal
35	148 (80)	0.97	9	Stable	—	0.935	Good
35	185 (100)	0.97	10	Stable	—	0.940	Good

*9 dB at 6 kHz

See notes for table 10.

Table 15.—QCSEE High Mach Number Inlet C Operating Characteristics

(a) Inlet C1

$\alpha, ^\circ$	V, km/h (kn)	Recovery at knee	Distortion at knee, %	Inlet airflow	$\overline{\Delta SPL}$, dB	C_D^*	Inlet operation
0	0	0.985	10	Unstable, high airflows	28	0.970	Good
0	148 (80)	0.980	6	Stable	30 +	0.990	Good
0	315 (170)	0.980	9	Stable	25 +	0.990	Good
20	0	0.985	10	Stable	34	0.985	Good
20	306 (165)	0.980	Not avail	Stable	26 +	0.985	Good
50	148 (80)	0.980	17	Unstable	—	0.920	Poor
90	65 (35)	0.980	17	Unstable	—	0.910	Poor

(b) Inlet C4

$\alpha, ^\circ$	V km/h (kn)	Recovery at knee	Distortion at knee, %	Inlet airflow	$\overline{\Delta SPL}$, dB	C_D^*	Inlet operation
0	0	0.980	10	Stable	32	0.98 +	Good
0	148 (80)	0.985	7	Stable	28 +	0.98	Good
0	306 (165)	0.980	10	Stable	23 +	0.98	Good
20	306 (165)	0.985	10	Stable	25 +	0.97	Good
50	148 (80)	0.990	10	Unstable, low airflows	—	0.93	Marginal
50	140 (75)	0.990	10	Stable	—	0.94	Good
90	65 (35)	0.990	10	Stable	—	0.95	Good

(c) Inlet C5

$\alpha, ^\circ$	V km/h (kn)	Recovery at knee	Distortion at knee, %	Inlet airflow	$\overline{\Delta SPL}$, dB	C_D^*	Inlet operation
0	0	0.980	8	Stable	31	0.980	Good
0	148 (80)	0.980	8	Stable	28 +	0.985	Good
0	306 (165)	0.980	6	Stable	24 +	0.980	Good
20	306 (165)	0.985	10	Stable	22 +	0.950	Good
50	148 (80)	0.990	10	Unstable, low airflows	—	0.930	Marginal
50	140 (75)	0.990	10	Unstable low airflows	—	0.930	Marginal
90	65 (35)	0.990	10	Stable	—	0.950	Good

See notes for table 10.